2022-3
Tagungsbericht

Conference Proceedings
The Role of Catalysis for the Energy Transition

October 5 - 7, 2022 | Ludwigshafen

DGMK

Umschlaggestaltung: DIE NEUDENKER®, Darmstadt | DGMK e.V., Hamburg
Titelfotografie: opyright (c) 2020 SMAK_Photo/Shutterstock.

ISSN 1433-9013
ISBN 978-3-947716-45-6

https://www.dgmk.de

C O N T E N T S

Page

Postersession

Petrochemicals in the Refinery Network

H. Blanke,
BP Europa SE, Advanced Fuels Products

Abstract

The reduction of global CO_2 emissions is key to meet the climate change in the future and the present. bp's purpose is reimagining energy. We want to become a net zero company by 2050 or sooner and help the world get to net zero. The company has set short-term (to 2025) and medium-term aims (to 2030).
These targets also include bp's petrochemical operations. In cooperation with other companies, bp is developing solutions to use feedstock from the circular economy and other sustainable products such as bio-based feedstock in the plants of bp's refineries.

Today, bp produces more than 4 mio. tons of petrochemicals per year at its German refineries in Gelsenkirchen and Lingen. Main products are ethylene, propylene, methanol, cumene, cyclohexane and LPG-streams with properties to be of interest for subsequent processing in the chemical industry.

One way to reduce the carbon footprint of refinery products is coprocessing with sustainable biogenic feedstock. Lately, UCO (used cooking oil) has become a promising candidate for this. Various units in the refinery can be used for coprocessing: e.g., hydrocracker, FCC and hydrotreater. To prove and control bio-origin in outcome streams of the units, bp uses C14-test method that was developed in bp laboratory in Bochum.

An alternative way to reduce CO_2, especially for petrochemical products, was investigated using pyrolysis oil from waste plastics at low concentration in a steam cracker.
In a second pathway, pyrolysis oil originating from tyres was taken for lab investigation for possible future use in a coker unit.

Summarizing, coprocessing of pyrolysis oil aimed for petrochemical products looks attractive and means a start on circular economy, net zero ambitions and saving of CO_2.

Efficient Direct-DME Synthesis; a BASF-Linde Joint Development

H. Ahi[1], K. Braunsmann[1], M. G. Schwab[1], N. Bottke[1], A. Behrens[2], A. Peschel[2]
[1]BASF SE, [2]Linde GmbH

Abstract

Dimethyl ether (DME) has diverse applications in various fields, namely as blending in liquefied petroleum gas (LPG) to improve its burning properties, and also to minimize the impact of deficit of LPG. It has also the potential to be used as biofuel in transportation segment. Conventionally, DME is produced in a two-step process via MeOH, being limited by thermodynamics. BASF-Linde Direct-DME technology is focused on direct conversion of syn gas to DME, taking the advantages of favorable thermodynamics, leading to higher syngas conversion. This process is applicable to medium to large scale DME production and can be operated with a flexible syngas feedstock. A reduced OPEX and lower CAPEX is expected when the proper process condition is applied. Taking the environmental aspect into consideration, this technology can lower CO_2 footprint and it has synergies with dry-reforming technology allowing for further CO_2 import.

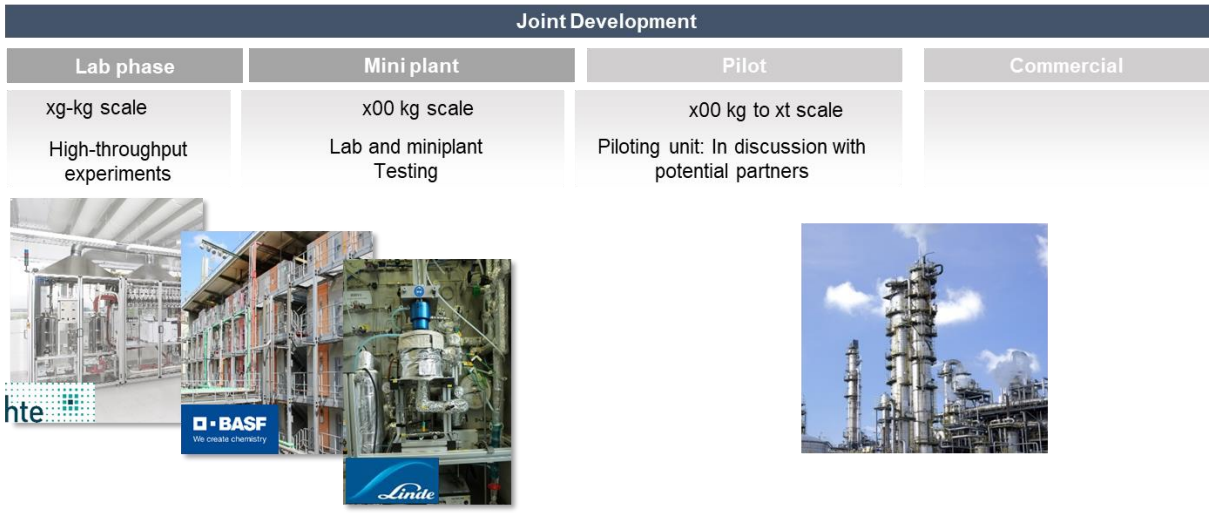

For this purpose, there was a need for development of a specific catalyst as well as determining the best process concept. Therefore, a joint development of BASF and Linde on a new technology for the direct synthesis of dimethyl ether from syngas was started more than five years a go where BASF is responsible for the development of catalyst system and Linde dealing with process design.

The BASF-Linde Direct-DME catalyst is a combination of two catalysts, methanol synthesis catalyst and dehydration catalyst in bifunctional catalysis. By optimization of individual catalysts and optimization of catalyst bed structure via individual kinetics of bifunctional catalyst, best configuration for long-term operation and maximum yield identified.

The BASF Direct-DME mini-plant has been running steadily for more than 3500 hours revealing high conversion, high stability, low level of by-product formation.

Experimental and Simulation Studies of Methanol and DME Synthesis from CO_2-rich Syngas on Cu/ZnO/ZrO_2 Catalysts

M. Herfet[1], B. Lacerda de Oliveira Campos [1], K. Herrera Delgado[1], D. Guse[2], M. Kind[2], I. Dessel[1], L. Warmuth[1], S. Wild[1], T. Zevaco[1], S. Pitter[1] and J. Sauer[1]
Karlsruhe Institute of Technology - [1] Institute of Catalysis Research and Technology - [2] Institute of Thermal Process Engineering

Abstract

Central elements for a climate-neutral energy system are processes that ensure the efficient use of available raw material resources and enable the cross-sectoral application of sustainable technologies. Here, an efficient CZZ methanol synthesis catalyst prepared using a scalable coprecipitation method was used in combination with H-FER-20 as dehydration catalyst to perform experimental kinetics studies and model-based optimization for the direct synthesis of dimethyl ether (DME) in a wide range of variable process conditions. This, in order to improve the DME productivity using various CO/CO_2 gas feeds such as those that could be used in Power-to-fuels technologies. Additionally, other dehydration catalysts (i.e. MFI zeolite type) were investigated to study the catalytic performance during the direct DME synthesis especially at CO_2-enriched syngas feeds. In order to get knowledge of the catalyst stability, long-term experiments were also performed until 250 h time on stream (TOS). Hereby, we focus on the determination of product selectivity and catalysts productivity.

1. Introduction

Due to the ongoing climate change, the European Green Deal has been adopted in 2019 as a concept to phase out the use of fossil fuels by 2050. Thus, climate neutrality is to be achieved in the European Union by reducing greenhouse gas emissions. [1] The greenhouse gas carbon dioxide (CO_2) contributes the most to global warming and is currently the largest driver of climate change. [2,3,4] In recent years, CO_2 concentration in the atmosphere has increased sharply due to the use of fossil fuels for power generation and heating. [5]

The future strategy envisages decarbonization in order to effectively reduce carbon dioxide emissions and thus achieve a carbon-free economy. Optimized carbon neutral chemical processes that use energy sources based on sustainable raw materials [1, 6-8] would help to reduce or compensate the impact of such emissions in the atmosphere. [1,3]
With the possibility of using renewable sources, the carbon cycle can be closed so that no additional carbon is emitted into the atmosphere but it is used instead. Synthetic carbon-neutral hydrocarbons would also significantly contribute to the future energy system. [9] Innovative schemes such as the Power-to-X (PtX) approach is of high importance to establish alternative production processes, where the sector of renewable electrical energy is couple with the chemical industry. [10] Methanol (MeOH) and dimethyl ether (DME) are examples of chemical energy carriers that can be produced in a sustainable way. Both can be directly synthesized from synthesis gas streams. Synthesis gas (H_2/CO) is an important intermediate in the chemical industry for manufacturing valuable basic chemicals and synthetic fuels that can be

derived from a variety of feedstocks (Figure 1). [11, 12] Currently, the main manufacturing processes are steam reforming of natural gas and coal gasification. [13,14] However, these processes are characterized by high specific CO_2 emissions. [9] Therefore, efforts are being made to find more eco-friendly alternative processes [1, 13] such as biomass pyrolysis and gasification, hydrothermal gasification of biomass, or even methane pyrolysis. [15, 16, 17]

Methanol and DME can be also produced from CO_2 extracted from the atmosphere via a direct air capture process (DAC) and green hydrogen produced via water electrolysis. [13,18,19,20] However, this process presents some challenges due to the fluctuating nature of renewable energies, which can cause the deactivation of the catalyst and thus a decrease in productivity.

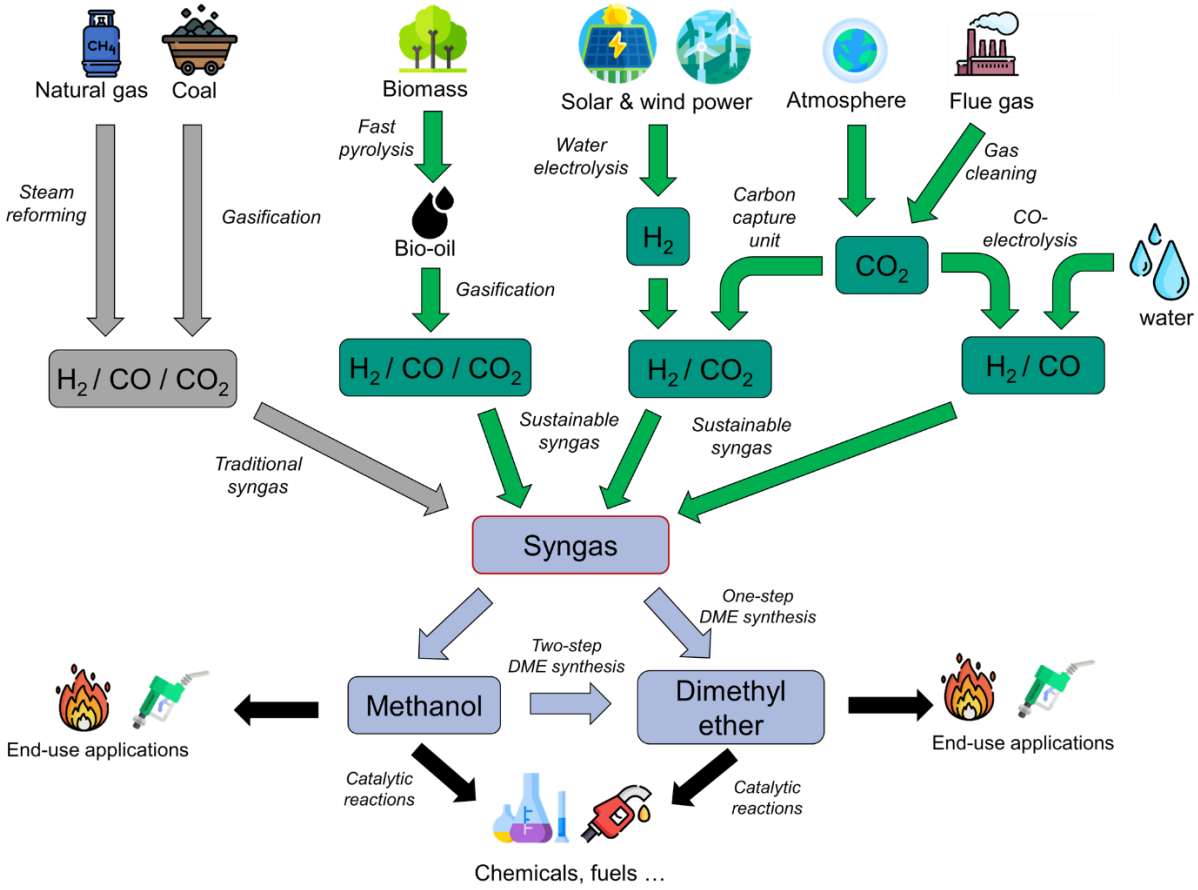

Figure 1: Schematic representation of the renewable syngas production process routes to produce methanol and dimethyl ether compared to the fossil syngas process route. Images: Freepik, Flaticon [21].

The research in our group focuses on the study of the effects of variable reaction conditions (i.e. CO_x/H_2 stream compositions, pressure, temperature) on the catalyst and the overall process efficiency for the methanol and direct dimethyl ether synthesis.
We are working in the optimization of catalytic materials in order to increase its activity and long-term stability. Process conditions are also optimized through model-based optimization using own developed kinetic models of both reactions.
In the following, some excerpts from our current research on catalyst preparation, kinetic measurements, modeling and model-based optimization will be presented.

2. Continuous coprecipitation method for the synthesis of highly productive Cu/Zn/Zr-based catalyst

To fulfil the demand for high quality Cu/Zn/Zr-based (CZZ) catalysts, methods to date need optimization. Synthesis should yield the optimal precursor for methanol formation catalysts, rosasite ($Cu_{1-x}Zn_x(OH)_2CO_3$, with x=0.15-0.31. [22] The subsequent calcination of this precursor leads to an oxidic compound with a close contact between Cu and Zn. A close contact of the active species is further enhanced by interparticular homogeneity. Additionally, a promotor like Al or Zr is added. Zirconia as promoter is especially efficient in long-term conversion of varying CO_2/CO_x feeds. [35] Usually, methanol formation catalysts are synthesized by batch coprecipitation and subsequent ageing in a stirred tank reactor. [23] This method is time- and material-intensive and delivers inhomogeneous materials due to temperature and concentration gradients within the reactor. [23,24]

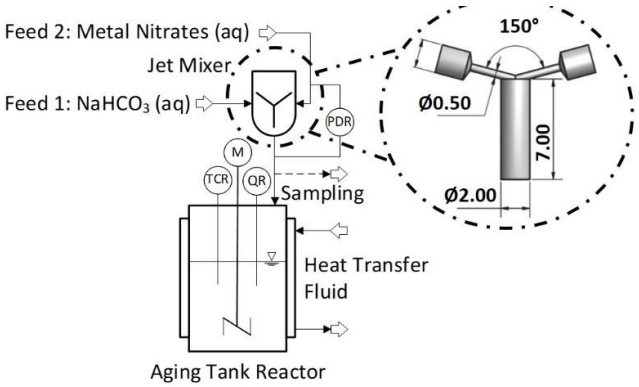

Figure 2: Optimized continuous coprecipitation experimental setup with a Y-mixer to blend the educts [24]

Therefore, an optimized continuous method has been developed in which a Y-mixer is used to blend the educts rapidly and uniformly (Figure 2). In this continuous coprecipitation, the initial seed formation takes place in the mentioned Y-mixer. A rapid nucleation guarantees small and monodisperse particles. These particles in suspension are then immediately transferred to a stirred double-jacketed reactor, in which the subsequent ageing takes place. The high speed of stirring and the relatively small diameter of this reactor ensures the evolution of a highly homogenous material (Figure 3). [25] The subsequent ageing step is necessary to yield the mentioned rosasite phase.

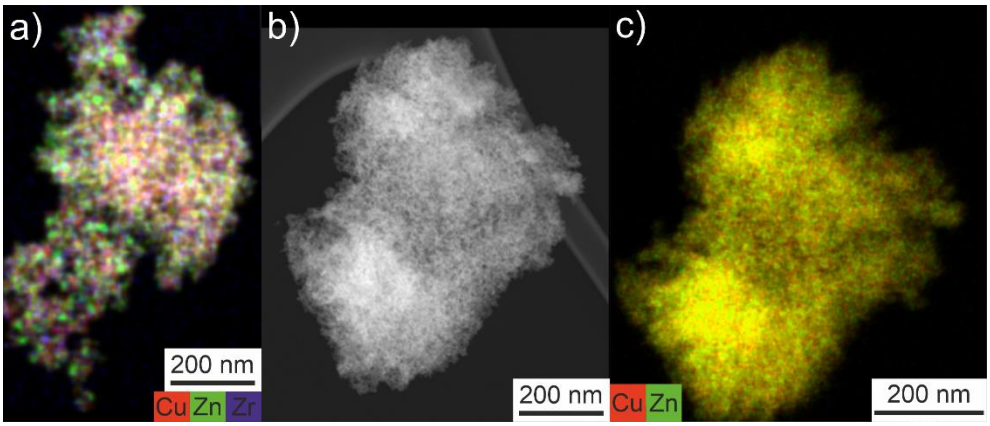

Figure 3: Homogeneity of CZZ-based materials synthesized with different methods, investigated by STEM-EDX measurements. Batch precipitation, STEM-EDX map (a), Continuous coprecipitation HAADF-STEM (b) and STEM-EDX map (c)

Furthermore, the material obtained by continuous coprecipitation shows a significant smaller particle size distribution than for the batch precipitated samples, indicated by H_2-TPR measurements (Figure 4). This leads to a higher catalytic activity observed in the direct dimethyl ether synthesis (catalyst mixed with acidic zeolithe; Figure 5). Thus, a new scalable method for obtaining high quantities of an efficient methanol synthesis catalyst has been developed in which a reproducible high quality can be ensured.

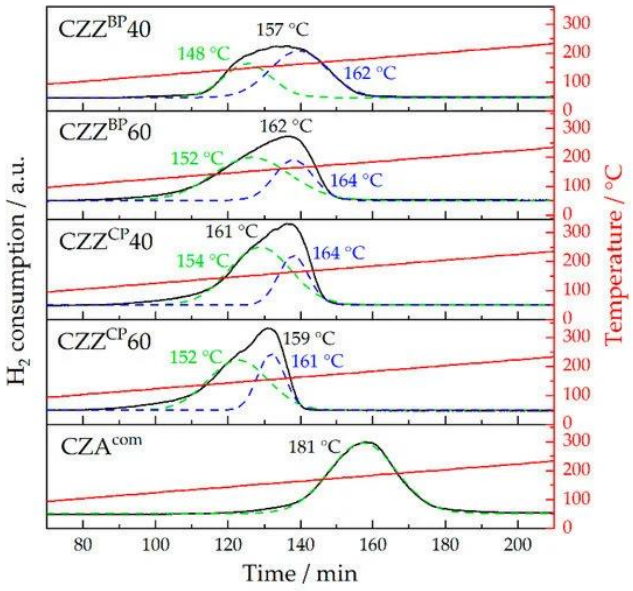

Figure 4: H_2-TPR profiles of the calcined CZZ pre-catalysts and CZAcom (H_2-TPR: 5% H_2/Ar, 1 °C min^{-1}, RT–300 °C). BP: Batch coprecipitation; CP: Continuous coprecipitation; com: commercial. The number in CZZBP/CP x corresponds to the respective ageing temperature. Figure taken from Polierer et al.[25]

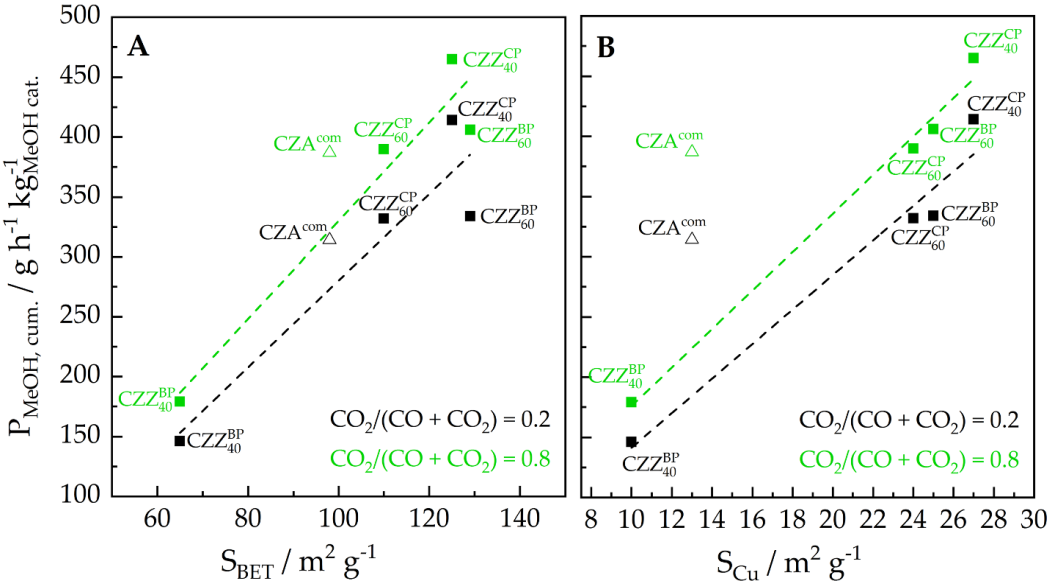

Figure 5: Cumulative MeOH productivity P_{MeOH}, cum. of CZZ/FER and CZA/FER catalysts as a function of (A) the specific BET surface area SBET and (B) the specific copper surface area SCu. CZAcom was not considered in linear fitting. Conditions productivity tests: CO_2/(CO + CO_2) = 0.2 (black) (H_2:CO:CO_2:N_2:Ar = 37.5:12:3:15:32.5 vol%) and 0.8 (green) (H_2:CO:CO_2:N_2:Ar = 46.5:3:12:15:23.5 vol%), 230 °C, 50 bar, GHSV = 36,000 mL h−1 g−1. Figure taken from Polierer et al.[25]

3. Kinetic studies on the optimum catalyst bed composition of CZZ to H-FER-20

For the kinetic studies on bed variation, CZZ in-house synthesized catalysts have been used, which were aged at a temperature of 40 °C during continuous co-precipitation. [26] The procedure used to prepare the CZZ catalysts and the characterization methods used are described in one of our publications Polierer et al. [25] A commercial zeolite H-FER-20 from an industrial partner was used for the dehydration step of MeOH to DME.
For the catalytic studies, both catalyst systems had a sieve fraction of 250-500 µm and the physical mixtures studied had different mass ratios, as reported by Wild et al. [26]

For the studies on direct DME synthesis, a 6-fold parallel reactor system has been used. Each reactor has the same volume flow distribution as well as pressure and temperature. A wide range of process conditions for different CuO/ZnO/ZrO_2 (CZZ) to H-FER-20 (FER) ratios have been investigated. The experiments were performed at a constant pressure of 30 bar and a temperature range of 210 °C to 240 °C. The gas hourly space velocity (GHSV) used in these experiments were 2.78 and 3.57 s^{-1} with regard to the catalyst volume. In addition, the CO_2/CO_x gas compositions (CO_2/CO_x = 0.4-0.9) were adjusted to investigate the optimal bed composition of the two catalysts.

Kinetic modeling

Recently, a microkinetic model of the methanol synthesis on Cu/Zn-based catalysts was developed in our group [27], which was based on ab initio density functional theory (DFT) calculations from Studt et al. [28,29] With this theoretical model, it was possible to identify the main reaction paths, the rate determining steps (RDS), and the most abundant surface species (see scheme in Figure 6).

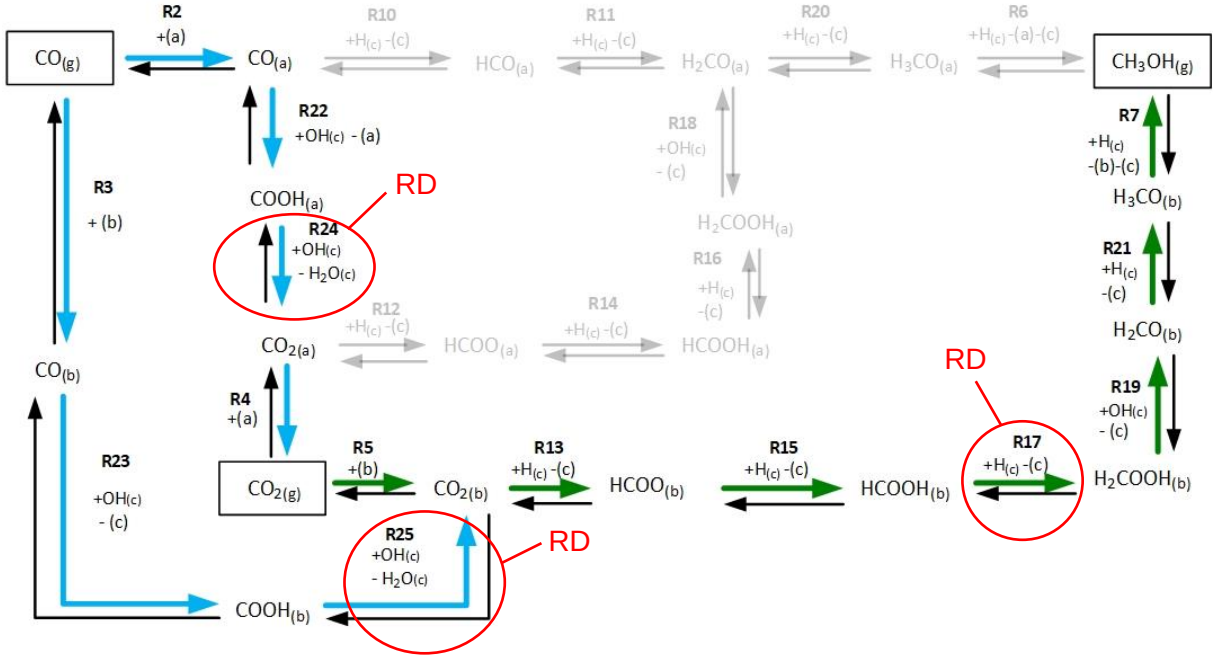

Figure 6: Considered reaction network of the methanol synthesis and the water-gas shift reaction. (a): pure Cu (211) site, (b): Cu/Zn (211) site, (c): Cu or Cu/Zn sites only for H_2 or H_2O adsorption, (g): gas phase. Adapted from [27] with permission from the Royal Society of Chemistry.

In the following step, these results were used to develop a formal kinetic model [30], as this

type of model is less complex to implement and requires a much lower computational effort than the microkinetic model. This model considers two global reactions: the CO_2 hydrogenation to methanol and the water-gas shift reaction (WGSR). The reaction rate equations ($\dot{r}$) are the following:

$$\dot{r}_{CO_2\ hyd.} = \exp\left(A_1 - \frac{E_{A,2}}{R \cdot T}\right) \cdot \phi_{Zn} \cdot \theta_b \cdot \theta_c \cdot f_{H_2}^{1.5} \cdot f_{CO} \cdot \left(1 - \frac{f_{MeOH} \cdot f_{H_2O}}{f_{H_2}^3 \cdot f_{CO_2} \cdot K^0_{P,CO_2\ hyd.}}\right) \quad (1)$$

$$\dot{r}_{rWGSR} = \exp\left(A_2 - \frac{E_{A,2}}{R \cdot T}\right) \cdot \phi_{Zn} \cdot \theta_b \cdot \theta_c \cdot f_{CO_2} \cdot f_{H_2O} \cdot \left(1 - \frac{f_{CO} \cdot f_{H_2O}}{f_{H_2} \cdot f_{CO_2} \cdot K^0_{P,rWGSR}}\right) \quad (2)$$

Here, A_{1-2} are pre-exponential factors, $E_{A,1-2}$ are global activation energies, R is the universal gas constant, T is the temperature, ϕ_{Zn} is the zinc coverage, θ_b is the coverage of free Cu/Zn sites, θ_c is the coverage of free sites for H_2 and H_2O, f_j is the fugacity of component j, and $K^0_{P,k}$ is the equilibrium constant of global reaction k. The zinc coverage is assumed to be 0.50 for the operating conditions studied.
The fugacity coefficients are calculated considering the Peng-Robinson equation of state, using binary interaction parameters and other parameters from the literature. [31,32] The free sites θ_b and θ_c are calculated as follows:

$$\theta_b = \left(\overline{K_1} \cdot f_{H_2}^{0.5} \cdot f_{CO_2} + 1\right)^{-1} \quad (3)$$

$$\theta_c = \left(\overline{K_2} \cdot f_{H_2}^{-0.5} \cdot f_{H_2O} + 1\right)^{-1} \quad (4)$$

Where $\overline{K_{1-2}}$ are the adsorption constants.

In order to simulate the methanol dehydration to DME, the associative mechanism was considered to be dominant, in accordance with theoretical results from Arvidsson et al. [33] The reaction rate equation is given as follows [26]:

$$\dot{r}_{Dehyd.} = \exp\left(A_3 - \frac{E_{A,3}}{R \cdot T}\right) \cdot \theta_d \cdot f_{MeOH}^2 \cdot \left(1 - \frac{f_{DME} \cdot f_{H_2O}}{f_{MeOH}^2 \cdot K^0_{P,Dehyd}}\right) \quad (5)$$

Here, θ_d is the coverage of free zeolite sites, which is calculated as follows:

$$\theta_d = \left(\overline{K_3} \cdot f_{MeOH} + 1\right)^{-1} \quad (6)$$

The kinetic model of the direct DME synthesis consists in merging the methanol synthesis (Eqs. 1-4) and the methanol dehydration to DME (Eqs. 5-6), and has nine parameters (A_{1-3}, $E_{A,1-3}$, $\overline{K_{1-3}}$). [26] In order to estimate the kinetic parameters, experiments at various compositions of CZZ/FER and various operating conditions were performed in a lab plant with parallel reactors, totalizing 240 steady-state data points. Then, an optimization problem was solved, in which the sum of normalized squared errors (χ^2) was minimized:

$$f_{min} = \chi^2 = \sum_{i=1}^{N_p} \left[\frac{\left(y^i_{out,CO} - \hat{y}^i_{out,CO}\right)^2}{\left(y^i_{out,CO}\right)^2} + \frac{\left(y^i_{out,CO_2} - \hat{y}^i_{out,CO_2}\right)^2}{\left(y^i_{out,CO_2}\right)^2} + \frac{\left(y^i_{out,MeOH} - \hat{y}^i_{out,MeOH}\right)^2}{\left(y^i_{out,MeOH}\right)^2} + \frac{\left(y^i_{out,DME} - \hat{y}^i_{out,DME}\right)^2}{\left(y^i_{out,DME}\right)^2} \right] \quad (7)$$

The estimated parameters and the corresponding confidence intervals are summarized in Table 1. The activation energy of the methanol dehydration was not statistically relevant, and the total number of parameters were reduced to eight. Despite the low amount of parameters, the model adequately simulated the experiments, as shown for some data points in Figure 7.

Table 1: Parameters of the kinetic model of the direct DME synthesis. Reproduced from [26] with permission from the Royal Chemistry Society.

Parameters	Value	Unit
$\boldsymbol{A_1}$	9.57 ± 0.44	–
$\boldsymbol{A_2}$	26.23 ± 2.43	–
$\boldsymbol{A_3}$	3.08 ± 0.54	–
$\boldsymbol{E_{A,1}}$	75.53 ± 2.29	kJ·mol^{-1}
$\boldsymbol{E_{A,2}}$	119.71 ± 9.44	kJ·mol^{-1}
$\boldsymbol{E_{A,3}}$	Not statistically relevant	
$\boldsymbol{K_1}$	0.38 ± 0.14	bar$^{-1.5}$
$\boldsymbol{K_2}$	8.28 ± 0.90	bar$^{-0.5}$
$\boldsymbol{K_3}$	52.92 ± 30.14	bar^{-1}

For these operating conditions, both the simulations and the experiments point to an optimal catalyst bed distribution close to CZZ/FER = 90/10 vol.%. The validated kinetic model is then used to investigate the influence of temperature, gas hourly space velocity (GHSV), and CO_2/CO_X ratio in the optimal FER composition. For all investigated conditions, the optimal FER was always below 12 vol.%, with temperature and CO_2/CO_X ratio having little influence, while a reduction in GHSV (that is, higher residence times) shift the optimum to lower values of FER composition. By extrapolating the model to "high performance" conditions (i.e., 60 bar, feed: $H_2/CO/CO_2$ = 70/12/18 vol.%), the same tendency is maintained, but even lower optimal values were found.

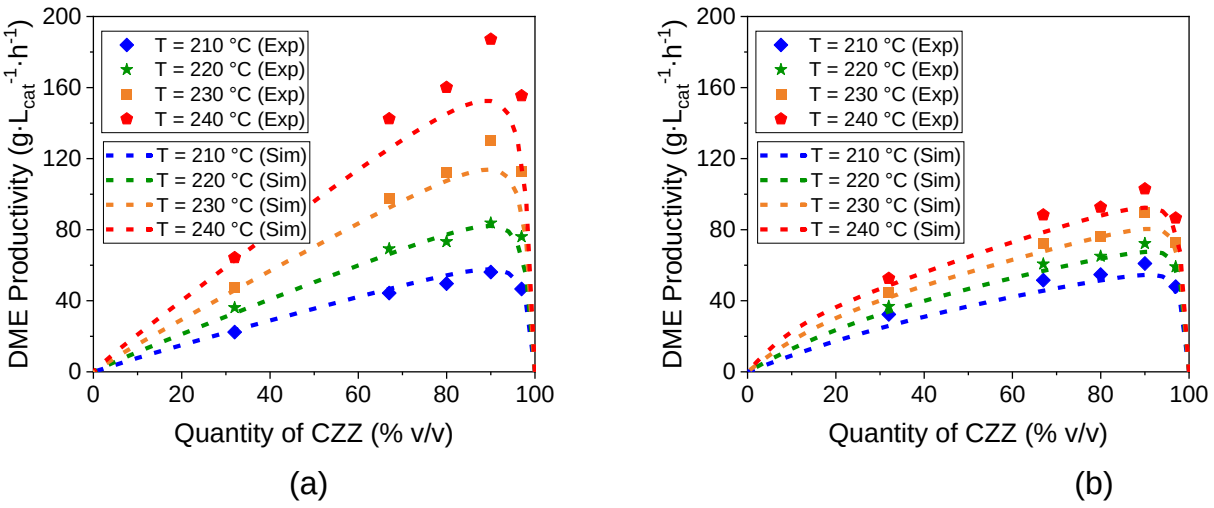

Figure 7: DME productivity as a function of the CZZ quantity and temperature: experimental points (dots) and simulation curves (lines). Operating conditions: 31 bar, 2.78 s^{-1}. (a) Feed: $H_2/CO/CO_2/N_2$ = 45/12/8/35 vol.%. (b) Feed: $H_2/CO/CO_2/N_2$ = 45/2/18/35 vol.%. Adapted from [26] with permission from the Royal Chemistry Society.

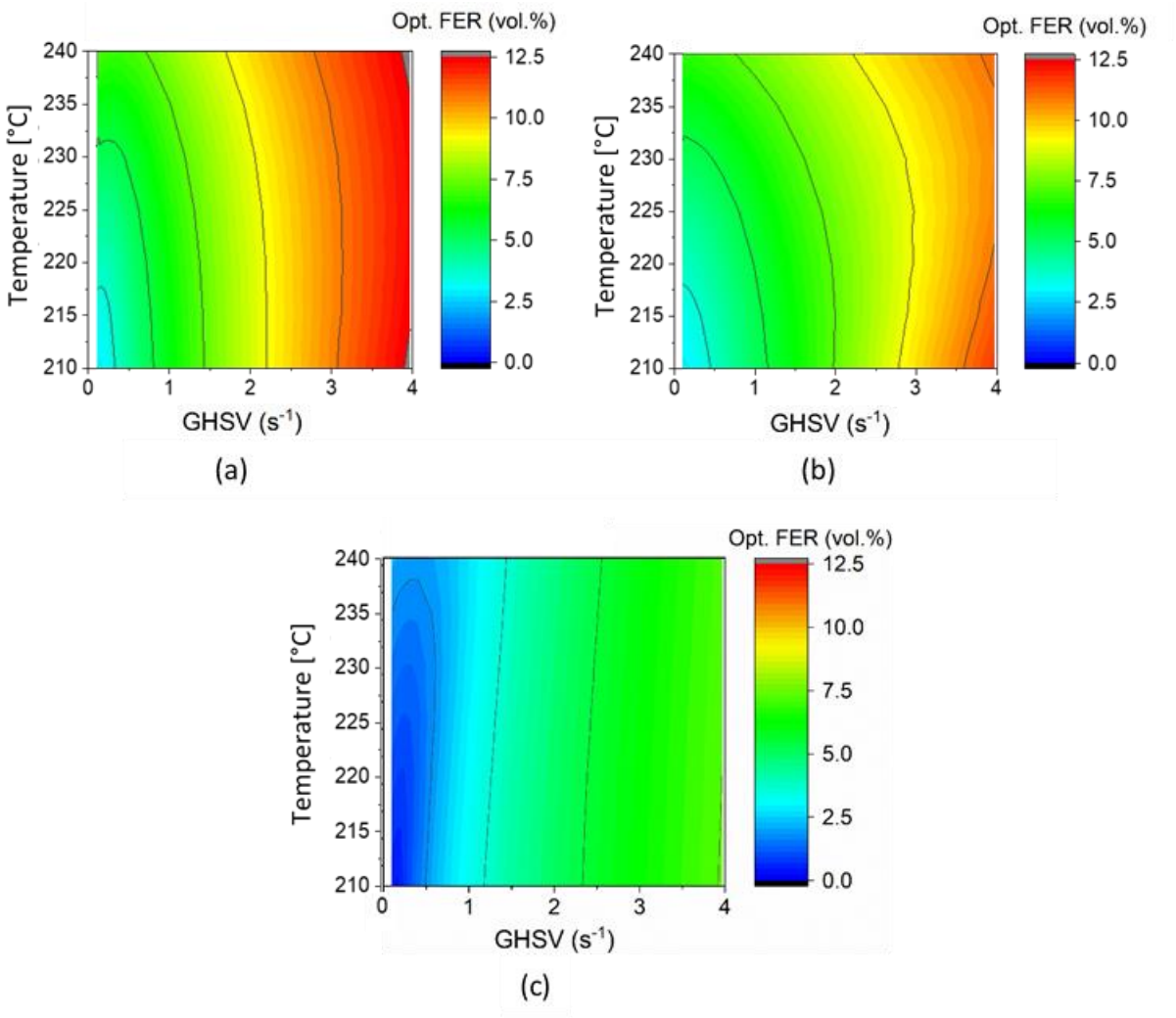

Figure 8: Optimal fraction of FER in the catalyst bed composition. (a) 31 bar, feed: $H_2/CO/CO_2/N_2$ = 45/12/8/35 vol.%; (b) 31 bar, feed: $H_2/CO/CO_2/N_2$ = 45/2/18/35 vol. %; (c) 60 bar, feed: $H_2/CO/CO_2$ = 70/12/18 vol.%. Reproduced from [26] with permission from the Royal Chemistry Society.

4. Comparison between FER and MFI catalysts as dehydration catalyst for the direct DME synthesis

Based on the kinetic studies of Wild et. al [26], other zeolite catalysts have been tested and compared to H-FER 20.
For these studies, a CZZ to zeolite ratio of 90:10 vol.% was chosen, which is based on optimum ratio find previously.
Compared to the previous methanol catalyst, an optimized version of the CZZ catalyst prepared at an aging temperature of 60 °C has been used for the new experiments. Since this catalyst has a higher activity, the catalyst ratio does not quite match anymore and is thus sub-stoichiometric. The sub-stoichiometric ratio of the catalysts has been an additional comparison parameter between the activity of the different zeolite catalysts, this in order to identify the differences in performance by using the same amount.

Two commercial MFI structure-based zeolites with different acidities (H-MFI-80 and H-MFI-30) were used as acidic catalysts. The same ferrierite catalyst (H-FER-20) presented in chapter 3 was used for comparison.
The experimental test series of the direct DME synthesis have been carried out in a single tubular reactor with a fixed catalyst bed. The identical process conditions have been chosen for each series of experiments, ensuring comparability. The experiments have been performed at a constant gas hourly-space-velocity (GHSV) of 4.52 s^{-1} with regard to the catalyst volume. The process pressure (i.e. 30 bar) and temperature (i.e. 230 °C) were kept constant. For the long-term experiment with a process duration of 250 h, the CO_2/CO_x concentration was also kept constant at a ratio of 0.5. Here, the change in catalyst activity as well as the experimental reproducibility in terms of methanol productivity has been investigated.

For the evaluation of the different tests with respect to the catalyst systems, known performance characteristics such as productivity and selectivity have been defined in Eqs. 8-10.
In the long-term experiments over 250 h time on stream (TOS), the total methanol productivity $P_{MeOH,ges}$ and the dimethyl ether productivity P_{DME} are used as parameters to evaluate the catalyst performance.

$$P_{MeOH,ges} = \frac{\dot{n}_{gesamt,out}\ \widetilde{M}_{MeOH}\ (y_{MeOH} + 2 \cdot y_{DME})}{m_{Kat}} \qquad (g_{MeOH,ges}/(kg_{Kat}*h)) \qquad (8)$$

$$P_{DME} = \frac{\dot{n}_{DME,out} \cdot \widetilde{M}_{DME}}{m_{MeOH-Katalysator}} \qquad (g_{DME}/(kg_{Kat}*h)) \qquad (9)$$

$$S_{DME} = \frac{\nu_{DME}\ \dot{n}_{DME,out}}{\sum_{i=1}^{j} \nu_i\ \dot{n}_{i,out}} \qquad (mol\text{-}\%) \qquad (10)$$

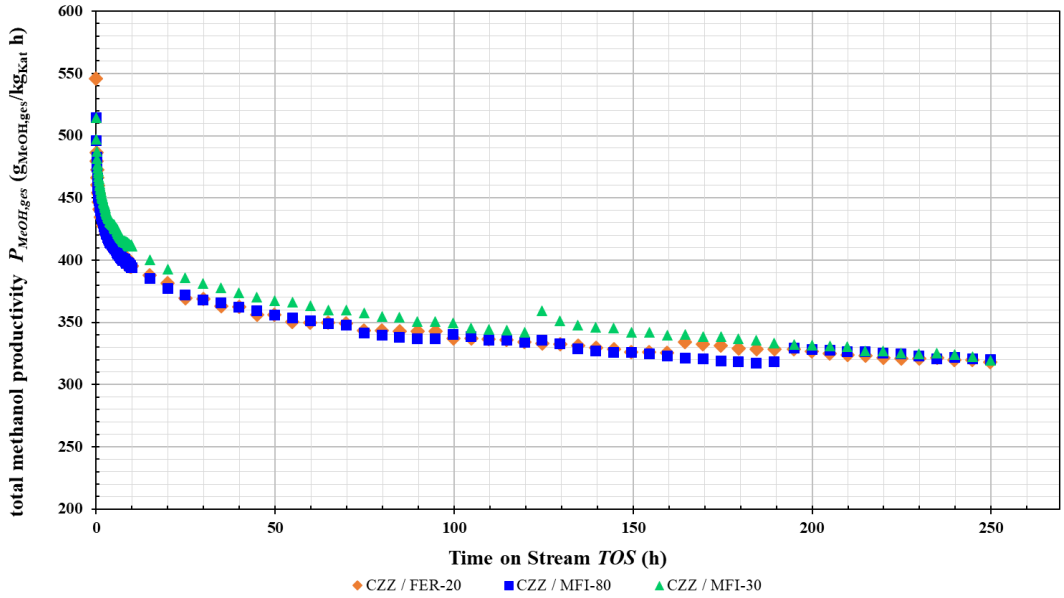

Figure 9: Curves of the total methanol productivity $P_{MeOH,ges}$ of the three investigated catalyst systems CZZ/FER-20, CZZ/MFI-80 and CZZ/MFI-30 over a reaction time of TOS = 250 h

Figure 9 shows the plots of the total methanol productivity of the three different catalyst systems over 250 h TOS. It can be seen that the reproducibility of the CZZ catalysts was the same for all catalyst systems. A characteristic curve emerges over the entire process, starting with a strong deactivation during the first 10 h and flattening out as the process continues until 250 h. The total methanol productivity at the beginning of the reaction is used as the reference value for the relative percent deactivation ($\Delta P_{MeOH,ges}$). The relative percent deactivation of the CZZ catalyst is $\Delta P_{MeOH,ges}$ = 18.7-20.6 % for a period of t = 0-10 h, $\Delta P_{MeOH,ges}$ = 30.7-32.1 % for t = 0-100 h, and $\Delta P_{MeOH,ges}$ = 34.5-37.9 % for t = 0-250 h.
The absolute percentage deviation of the deactivation between the experimental series is in the range of 1.4 % to 3.4 %.

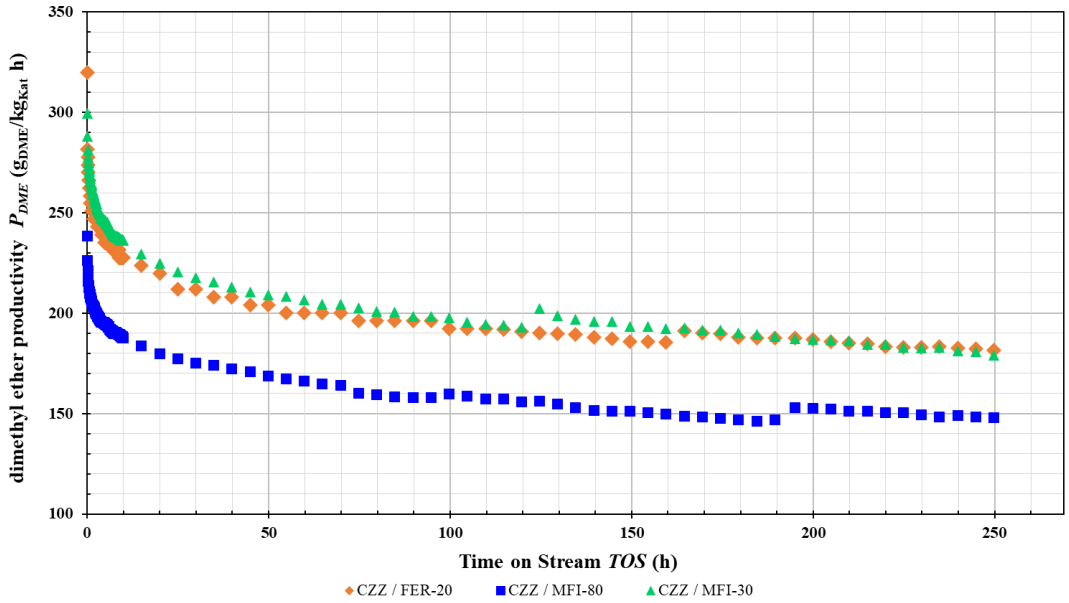

Figure 10: Curves of the total DME productivity P_{DME} of the three investigated catalyst systems CZZ/FER-20, CZZ/MFI-80 and CZZ/MFI-30 over a reaction time of t = 250 h.

Figure 10 shows the different DME productivity curves for the selected catalyst systems over the reaction time of 250 h. The curves with respect to the activity decrease of the three catalyst systems are similar to the curves in Figure 9. It can be seen that the catalyst systems with the MFI-30 and the FER-20 show significantly higher DME productivities than the one with MFI-80.
Comparing all catalysts, it can be observed that the initial DME productivity ($P_{DME,0}$) of the zeolite MFI-80 (238.47 g_{DME}/(kg_{cat} h)) is significantly lower than for FER-20 (319.86 g_{DME}/(kg_{cat} h)) and the zeolite MFI-30 (299.60 g_{DME}/(kg_{cat} h)). The FER-20- and MFI-30 zeolites exhibit similar and much higher DME productivity over the entire reaction time compared to MFI-80.

Table 2 shows the relative decrease in DME productivity for all three catalytic systems as function of TOS. As a result, the strongest deactivation of the catalyst takes place at the beginning of the reaction (TOS= 0-10 h), especially for CZZ/FER-20. Between 10-250 h, the hourly deactivation rate is higher for the CZZ/MFI-30 system than to the other two systems.
Over the entire experimental period (TOS= 0-250 h) the CZZ/MFI-80 catalyst system presented the lowest deactivation and CZZ/FER-20 the highest.

Table 2: Relative percentage decrease in DME productivity P_{DME} of the catalyst systems with respect to the maximum DME productivity P_{DME} at the start of the reaction over the reaction time TOS

TOS	CZZ/FER-20 ΔP_{DME}	CZZ/MFI-80 ΔP_{DME}	CZZ/MFI-30 ΔP_{DME}
0- 10 h	- 28.9 %	- 21.4 %	- 21.2 %
0 - 100 h	- 39.8 %	- 33.0 %	- 34.0 %
0 - 250 h	- 43.3 %	- 38.0 %	- 40.2 %

The slight deviations between the curves of the total methanol productivity (Figure 9) presumably result from purging the system with nitrogen, which took place at different times (e.g. for the CZZ/FER-20 catalyst system approx. at t = 160 h, for CZZ/MFI-80 approx. at t = 190 h and for CZZ / MFI-30 approx. at t = 120 h). Due to the purging process, a catalyst system can be regenerated to a small extent, since water is flushed out of the pores of the catalysts with the nitrogen stream. Another reason for the small differences between total methanol production could be due to the CZZ catalyst deactivation as result to water formation. In the publication by Li et al. [34] and Wild et al. [35] a temporary deactivation of the active sites of the Cu-based catalyst by water is described, resulting in a suppression of methanol formation. The zeolites of structure MFI produce significantly more water than FER, which can explain small deviations between the test series.

The steep drop in DME productivity (Figure 10) at the beginning of the reaction indicates strong deactivation in all catalyst systems. Since the course of the deactivation shows the same characteristic when looking at the total methanol productivity (Figure 9), it can be assumed that the deactivation is mainly due to the loss of activity of the CZZ catalyst and only a small fraction is due to a deactivation of the zeolites. In the literature, the deactivation of Cu/ZnO-based catalysts is attributed to sintering processes at the onset of the reaction. [35, 36]

Nevertheless, as shown in Figure 11, a decrease in DME selectivity is observed with increasing reaction time, this indicates a decrease in the activity of the zeolite catalyst. One possible reason for the decrease in selectivity is coke formation on the dehydration component. [37, 38, 39] To verify this, IR images of the MFI 30 zeolite catalyst were taken in the calcined state and in the used state after the series of experiments were performed. However, no coke formation was detected. Based on the amount of unreacted methanol, it can be concluded that the zeolite component was under-supply in terms of quantity.
As a next step in our investigations, we will perform new experiments increasing the amount of the zeolite component in the CZZ/FER-20 CZZ/MFI-80 and CZZ/MFI-30 systems, as well as studying other zeolites in combination with our CZZ catalyst. This in order to find the best catalyst combination, which will be used to carry out detailed kinetic experiments for the model-based optimization of the experimental conditions and thus obtain the maximum productivity.

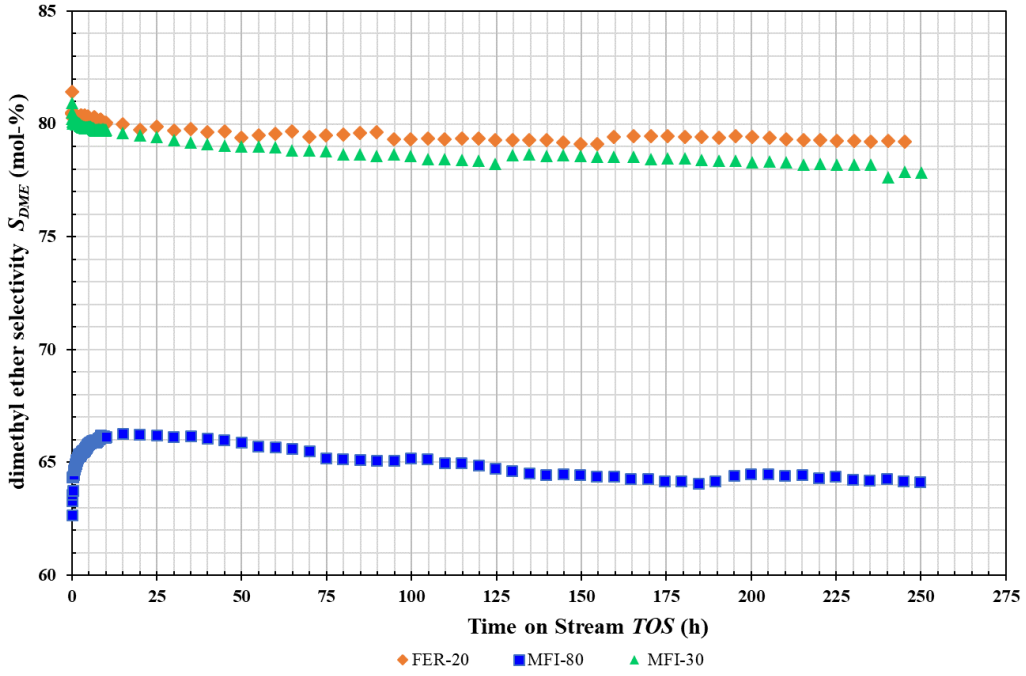

Figure 11: Curves of the dimethyl ether selectivity of the CZZ catalyst systems with investigated zeolite catalysts FER-20, MFI-80 and MFI-30

5. Conclusions

Our recent studies showed that CO_2 can be (co-)fed in methanol synthesis by using Cu/Zn/Zr-based catalysts. These catalysts can be produced in a scalable process, called continuous coprecipitation, ensuring the supply for high quality catalysts with high productivity for the methanol synthesis, which can be also used in combination with a dehydration catalyst (e.g. zeolites) for the direct DME synthesis.

A vast array of experimental data for kinetic studies have been gathered at different reaction conditions (i.e. temperature, pressure, GHSV and CO_2/CO_x) using one of ours CZZ catalyst in combination with H-FER-20 for direct DME synthesis. With these results, a new kinetic model for direct DME synthesis was developed and applied in a model-based optimization to determine the optimal acid catalyst share (i.e. H-FER-20) with respect to DME productivity under variation of process conditions.

When looking at the total methanol productivity in the long-term experiments, it was concluded that a strong deactivation take place in the first 10 h TOS for all catalytic systems. As the TOS increased, the deactivation approached a steady-state point. When comparing the different catalyst systems, the MFI dehydration catalysts showed lower deactivation in terms of DME productivity than the FER-20 catalyst system. However, the FER-20 showed a slightly increased in DME productivity than the MFI-30.

Our investigations will be further extended by using new combinations of our self-developed CZZ catalysts that are constantly under optimization with other zeolites types. This in order to extent our kinetic models and thus optimized the reactor and process efficiency.

References

[1] Doleski OD, Kaiser T, Metzger M, Niessen S, Thiem S (2021) Digitale Dekarbonisierung. Springer Fachmedien Wiesbaden, Wiesbaden

[2] ES. Sanz-Pérez, CR. Murdock, SA. Didas, CW. Jones Chem Rev, Vol. 116(19) pp.11840, (2016).

[3] Core Writing Team, R.K. Pachauri and L.A. Meyer (eds.), IPCC,: Climate Change 2014: Synthesis Report. Contribution of Working Groups I, II and III to the Fifth Assessment Report of the Intergovernmental Panel on Climate Change, . IPCC, Geneva, Switzerland, 151 pp, (2014)

[4] M.L. Parry, O.F. Canziani, J.P. Palutikof, P.J. van der Linden and C.E. Hanson, IPCC: Climate Change 2007: Impacts, Adaptation and Vulnerability. Contribution of Working Group II to the Fourth Assessment Report of the Intergovernmental Panel on Climate Change, , Eds., Cambridge University Press, Cambridge, UK, (2007)

[5] IPCC, Summary for Policymakers. In: Climate Change 2021: The Physical Science Basis. Contribution of Working Group I to the Sixth Assessment Report of the Intergovernmental Panel on Climate Change, (2021)

[6] B. Niethammer, S. Wodarz, M. Betz, P. Haltenort, D. Oestreich, K. Hackbarth, U. Arnold, T. Otto, J. Sauer, Chemie Ingenieur Technik, Vol. 90(1-2): p. 99, (2018)

[7] S. Drünert, U. Neuling, S. Timmerberg, M. Kaltschmitt, Zur Energiewirtschaft Vol. 43(3), p. 173, (2019)

[8] AK. Agarwal, H. Valera, Greener and Scalable E-fuels for Decarbonization of Transport. Springer Singapore, Singapore, (2022)

[9] V. Dieterich, A. Buttler, A. Hanel, H. Spliethoff, S. Fendt, Energy Environ. Sci., Vol. 13 (10), p. 3207, (2020)

[10] S. Banivaheb, S. Pitter, K. Herrera Delgado, M. Rubin, J. Sauer and R. Dittmeyer, Chem. Ing. Tech., Vol. 94, No. 3, p, 240, (2022)

[11] Jie Ren, Jing-Pei Cao, Xiao-Yan Zhao, Fei-Long Yang, Xian-Yong Wei, Renewable and Sustainable Energy Reviews, Vol. 116, (2019)

[12] J. R. Rostrup-Nielsen, Catalysis Today, Vol. 63, Issues 2-4, p. 159, (2020)

[13] SR. Foit, IC. Vinke, LGJ. de Haart, R-A. Eichel, Angew. Chem., Vol. 129(20), p. 5488, (2017)

[14] I. Kiendl, H. Schmaderer, N. Schödel, H. Klein (2020) Chem. Ing. Tech., Vol. 92(6), p.:736, (2020)

[15] A. Álvarez, A. Bansode, A. Urakawa, AV. Bavykina, TA. Wezendonk, M. Makkee, J. Gascon, F. Kapteijn, (Chem Rev, Vol. 117(14), p.9804, (2017)

[16] A. Behr, T. Seidensticker, Chemistry of Renewables. Springer Berlin Heidelberg, Berlin, Heidelberg, (2020)

[17] O. Machhammer, A. Bode, W. Hormuth, Chem. Ing. Tech., Vol. 87(4), p.409, (2015)

[18] ES. Sanz-Pérez, CR. Murdock, SA. Didas, CW. Jones, Chem Rev, Vol. 116(19), p11840, (2016)

[19] SD. Ebbesen, M. Mogensen, Journal of Power Sources, Vol. 193(1), p.349, (2009)

[20] SD. Ebbesen, R. Knibbe, M. Mogensen, (J. Electrochem. Soc., Vol. 159(8), p.F482, (2012)

[21] Flaticon Icons, Freepik, https://www.flaticon.com/authors/freepik, (accessed May/2022)

[22] L. Zwiener, F. Girgsdies, D. Brennecke, D. Teschner, A. G. Machoke, R. Schlögl, E. Frei, Appl. Catal. B-Environ. Vol.249, p. 218; (2019) b) M. Behrens, F. Girgsdies, Z. Anorg. Allg. Chem. , Vol. 636, p. 919, (2010)

[23] F. Schüth, M. Hesse, K. K. Unger in Handbook of heterogeneous catalysis. 8 volumes (Hrsg.: G. Ertl), WILEY-VCH, Weinheim, p.. 100, (2008)

[24] D. Guse, S. Polierer, S. Wild, S. Pitter, M. Kind, CIT, (2022)

[25] S. Polierer, D. Guse, S. Wild, K. Herrera Delgado, T. N. Otto, T. A. Zevaco, M. Kind, J. Sauer, F. Studt, S. Pitter, Catalysts, Vol. 10, p. 816, (2020)

[26] S. Wild, B. Lacerda de Oliveira Campos, T. A. Zevaco, D. Guse, M. Kind, S. Pitter, K. Herrera Delgado and J. Sauer, React. Chem. Eng., Vol. 7, p. 943, (2022)

[27] B. Lacerda de Oliveira Campos, K. Herrera Delgado, S. Wild, F. Studt, S. Pitter, J. Sauer, *Reaction Chemistry and Engineering*, Vol. 6, p. 868, (2021)

[28] F. Studt, M. Behrens, F. Abild-Pedersen, *Catalysis Letters*, Vol. 144, p. 1973, (2014)

[29] F. Studt, M. Behrens, E. L. Kunkes, N. Thomas, S. Zander, A. Tarasov, J. Schumann, E. Frei, J. B. Varley, F. Abild-Pedersen, J. K. Nørskov, R. Schlögl, *ChemCatChem*, Vol. 7, p. 1105, (2015)

[30] B. Lacerda de Oliveira Campos, K. Herrera Delgado, S. Pitter, J. Sauer, *Industrial & Engineering Chemistry Research*, Vol. 60 (42), p. 15074, (2021)

[31] L. Meng, Y. Y. Duan, *Fluid Phase Equilibria*, Vol. 238, p. 229, (2005)

[32] L. Meng, Y. Y. Duan, X. D. Wang, *Fluid Phase Equilibria*, Vol. 260, p. 354, (2007)

[33] A. A. Arvidsson, P. N. Plessow, F. Studt, A. Hellman, *Journal of Physical Chemistry C*, Vol. 124, p. 14658, (2020)

[34] C. Li, X. Yuan, K. Fujimoto, Applied Catalysis A, General, Vol. 469, p.306, (2014)

[35] S. Wild, S. Polierer, TA. Zevaco, D. Guse, M. Kind, S. Pitter, K. Herrera Delgado, J. Sauer , RSC Adv, Vol. 11(5), p. 2556, (2021).

[36] MV. Twigg, MS. Spencer, Applied Catalysis A, General, Vol.212(1-2), p. 161, (2001)

[37] K. Saravanan, H. Ham, N. Tsubaki, JW. Bae, Applied Catalysis B: Environmental, Vol. 217, p.494, (2017)

[38] F. Yaripour, F. Baghaei, I. Schmidt, J. Perregaard, Catalysis Communications , Vol. 6(2), p.147, (2005)

[39] H. Bateni, C. Able, Catal. Ind., Vol. 11(1), p.7, (2019)

Preparation of Cu/Zn Based Catalyst Precursors – Importance of Thermodynamics and Seeding

D. Guse[1], L. Warmuth[2], F. Kreißig[1], S. Pitter[2], M. Kind[1]
[1]Karlsruhe Institute of Technology, Institute of Thermal Process Engineering
[2]Karlsruhe Institute of Technology, Institute of Catalysis Research and Technology

Abstract

Aging is one of the key steps in the preparation of Cu/Zn based catalysts. An initially amorphous intermediate transforms, depending on the exact process parameters, into the wanted crystalline precursor phase zincian malachite which is characterized by a periodic arrangement of Cu and Zn atoms and proved to be advantageous for the qualities of the final catalyst. Our approach to better understand and thus control aging is twofold. For one thing, by applying a thermodynamic model based on solubility products of naturally occurring minerals and a hybrid activity coefficient model we could show that aging can be understood as a process driven by the thermodynamic equilibrium. We were able to predict the qualitative predominance of zincian malachite for the pH and temperature ranges investigated. The model also predicted the phase composition of the aged precursor as a function of the Cu/Zn ratio in the reactant solution and the Zn fraction in zincian malachite. For another thing, we could show that aging can be significantly accelerated by seeding: the aging time necessary to induce the phase transformation was reduced by 43 to 50 % for seeding mass fractions of 3 w% and from 96 min to only 8 min for 42 w%. No negative influence of seeding on the phase composition, specific surface area, molar metal ratios and the morphology of the aged precursor could be detected. Thus, we conclude that understanding aging as a thermodynamic equilibrium process will be fruitful for the further process optimization in terms of phase composition and that seeding is a potent tool to accelerate aging, presumably also on an industrial scale.

1 Introduction

Fossil resources as raw materials for the chemical and the energy industry are becoming increasingly scarce due to geological limitations and political issues. Thus, efficient chemical processes, ideally using sustainable sources, are both essential to address climate change and from an economic point of view. Methanol (MeOH), as a key material of the chemical industry [1] and a raw material for synthetic fuels [2,3], is mainly produced from non-renewable syngas (CO, H_2) [4]. Current research shows a great potential for the synthesis from CO_2 which may be won from industrial waste streams or the atmosphere and from green H_2 obtained from electrolysis by solar or wind power [5,6].

Using syngas rich in CO_2 instead of CO requires adaptation of the process parameters as well as the Cu/Zn based catalyst used to facilitate the reaction [5]. Important catalyst properties are the specific surface, the copper surface, the arrangement of Cu and Zn atoms as well as their contact and the pore size which all result from the preparation conditions [7-10]. For syngas rich in CO_2, more H_2O is formed as a by-product and the presence of ZrO_2 as a promoter seems to become more important [5,11,12]. In general, Cu/Zn based catalysts are manufactured in a process chain with the following three key steps which determine the properties of the later catalyst:

I. co-precipitation, where an amorphous precursor precipitates by mixing two aqueous reactant solutions [13-15]
II. aging, where, by keeping a temperature between typically 60 °C and 70 °C [16] in the mother liquor, the precipitate transforms into zincian malachite ($Cu_{(2-x)}Zn_x(OH)_2CO_3$), a salt containing both Cu and Zn atoms in its lattice
III. calcination, where the aged precursor decomposes into CuO and ZnO while maintaining the arrangement of Cu and Zn atoms on the nanoscale [17].

The periodic arrangement on the atomic scale is vital for the activity [8,9,17,18] and stability [19] of the catalyst. The material is then shaped, filled into the reactor and reduced to Cu/ZnO to obtain the operational catalyst. Co-precipitation pre-determines the nanostructure of the

later catalyst [20-22], but does not ensure a defined periodic arrangement of Cu and Zn atoms [13]. Only by obtaining the intermediate zincian malachite by aging, high activities, CO_x conversions and MeOH yields are achieved [23].

However, depending on the applied recipe and aging conditions, other intermediate phases may be produced which are detrimental to the catalyst properties like the mass specific surface area or the copper surface area due to different spatial atomic arrangements [23], metal ratios [24] or substances, e.g. Na^+ [25] or NO_3^- [14,26], showing an inhibiting effect during catalysis.

Therefore, a method to predict the phase composition of the aged precursor as a function of temperature, pH and reactant composition would be a desirable tool to adapt the preparation of Cu/Zn catalysts, e.g. to the changed syngas composition. Based on previous results [13], we propose that aging may be understood as a thermodynamic equilibrium process. Thus, a thermodynamic model should be able to predict the phase composition of the aged precursor.

Furthermore, these results coincide with studies showing that co-precipitation is completed in milliseconds to seconds [13,22,27]. In contrast, aging, in general, takes 30 min or several hours [10,28,29] before the phase transformation to zincian malachite is completed. According to recent studies by Güldenpfennig et al. at milliliter scale [30], this phase transformation seems to consist of a long induction period, which may be shortened by seeding, and a short transformation time. Seeding is a widespread tool in industrial crystallization processes to control processes in the metastable zone limit of primary nucleation and better control particle morphology and size distribution of the product. We aim to transfer the results by Güldenpfennig et al. to the liter scale and analyse the influence of seeding on the properties of the aged precursor and the precatalyst. Thus, the potential to optimize aging regarding the process time required and in terms of process control is to be evaluated.

2 Theoretical Basis

2.1 State of the art of precursor aging and its description

Cu/ZnO based catalysts show a high MeOH selectivity [31], stability [32] and activity [7,8,18] if the Cu and Zn atoms in the catalyst material are finely und homogeneously distributed on the nanoscale. Therefore, the goal of catalyst preparation is to produce such a material, e.g. by flame-spray pyrolysis [10,33,34] or by forming zincian malachite as the intermediate after aging in the aforementioned multi-step process [16]. If co-precipitation is conducted under high mixing intensities, a co-precipitate is formed which is already homogeneous on the nanoscale [13,17,23]. However, if aging is skipped, this material does not result in a good catalyst [17,23] emphasizing the role of aging in general and the importance of zincian malachite as an intermediate in particular.

The crystal lattice of zincian malachite is based on the mineral malachite ($Cu_2(OH)_2CO_3$).When malachite is formed from a solution containing Zn^{2+} or is in contact with such a solution, Zn^{2+} ions may substitute up to 27 mol% [35] or 31 mol% [36] of the Cu^{2+} ions, thus creating zincian malachite [37,38]. The naturally occurring variant with Zn fractions of approx. 42 mol% is called rosasite and shows small differences in the space group symmetry operators [38], but, according to Behrens et al., a discrimination between both forms is nearly impossible [35]. Additionally, Parádsasvárite, another mineral in the malachite-rosasite group with the chemical formula $(Zn_{1.91}Cu_{0.06}Mg_{0.02})(CO_3)(OH)_2$ was discovered in 2008 [39-41]. However, it was not yet found in any synthetic material. Accordingly, only zincian malachite with a variable Zn fraction is considered in this study.

Studies showed the resulting catalyst improves its properties if the Zn fraction of zincian malachite is as close as possible to this maximum [36,37]. When Zn^{2+} ions are incorporated into the lattice, its parameters change accordingly. On basis of data by Behrens et al. [35] the following linear correlations (Eqs. (2) to (5)) can be found for the lattice parameters a_{zM}, b_{zM}, c_{zM} and β_{zM} as a function of the Zn fraction in zincian malachite as defined in Eq. (1), each

with a coefficient of determination of $R^2 > 0.99$. These four correlations can then be used in a Rietveld refinement to determine a mean Zn fraction in zincian malachite $\tilde{x}_{\mathrm{Zn,zM}} \pm \sigma$ from the XRD diffractogram. Zwiener et al. determined similar correlations up to 31 mol% Zn [36]. However, these functions led to higher deviations in our evaluation than Eqs. (2) – (5). Furthermore, small amounts of aurichalcite were detected for the process parameters applied in Sect. 4.2 in samples with total Zn fractions of 30 – 35 mol%. Therefore, we exclusively used the data by Behrens et al. and assumed an upper boundary of $\tilde{x}_{\mathrm{Zn,zM}} = 27\ \mathrm{mol\%}$.

$$\tilde{x}_{\mathrm{Zn,zM}} = \frac{n_{\mathrm{Zn^{2+},zM}}}{n_{\mathrm{Zn^{2+},zM}} + n_{\mathrm{Cu^{2+},zM}}} \qquad (1)$$

$$a_{\mathrm{zM}} \cdot \mathrm{Å}^{-1} = -0.0045\ \tilde{x}_{\mathrm{Zn,zM}} + 9.4938 \qquad (2)$$

$$b_{\mathrm{zM}} \cdot \mathrm{Å}^{-1} = 0.0056\ \tilde{x}_{\mathrm{Zn,zM}} + 11.9131 \qquad (3)$$

$$c_{\mathrm{zM}} \cdot \mathrm{Å}^{-1} = -0.0024\ \tilde{x}_{\mathrm{Zn,zM}} + 3.2451 \qquad (4)$$

$$\beta_{\mathrm{zM}} \cdot (°)^{-1} = -0.0924\ \tilde{x}_{\mathrm{Zn,zM}} + 98.7179 \qquad (5)$$

Experimental studies determined the process parameter ranges in which zincian malachite with $\tilde{x}_{\mathrm{Zn,zM}}$ close to maximum forms predominantly. For Cu/ZnO/Al_2O_3 catalysts, the most widespread variant, 60 - 70 °C and pH = 6 - 7 should be chosen to obtain high amounts of zincian malachite [16]. In addition to pH and temperature, the ratio of Cu and Zn ions in the liquid phase is a dominant factor. If too few Zn^{2+} ions are available or not enough can be incorporated, the Zn fraction in zincian malachite is too low. If more than 27 % Zn^{2+} ions are present in the solids, by-product such as aurichalcite ($Zn_{(5-x)}Cu_x(OH)_6(CO_3)_2$) or hydrozincite ($Zn_5(OH)_6(CO_3)_2$) form. Although aurichalcite also consists of Cu and Zn, it results in a worse catalyst, probably due to too high Zn fractions of at least 60 mol% [37].

There are some studies using a kinetic crystallization model on the basis of population balance equations and thermodynamic data to describe und understand the co-precipitation step in the multi-step catalyst preparation [42-44]. However, there is no focus on aging. Yet, parts of the thermodynamic description and solubility data used can also be applied to aging.

Güldenpfennig et al. showed that the metal ratio, temperature and pH influence aging kinetics [30]. However, these parameters cannot be chosen freely since they also determine the physicochemical properties of the intermediate and thus catalyst properties. Therefore, they can only be varied to a limited extent. Guse et al. showed that the specific surface of the co-precipitate can almost be quadrupled by applying higher energy dissipation rates in the mixing of the two reactant solutions. Higher mass-specific surface areas appear to reduce improve aging kinetics significantly [13]. Yet, the most promising approach to improve aging kinetics respectively reduce aging times is apparently seeding. Güldenpfennig et al. could reduce the aging time by approx. 47 % by adding 4 % of the total solids mass as seeds: $x_{\mathrm{Seeds}} = 0.04$, cp. Eq. (6) [30]. The higher the seed fraction, the shorter the indution time seemed to be. Currently, though, these results are limited to small volumes at the milliliter scale.

$$x_{\mathrm{Seeds}} = \frac{m_{\mathrm{Seeds}}}{m_{\mathrm{Solids,total}}} \qquad (6)$$

Seeding is a standard procedure in many crystallization processes, e.g. to control the crystal morphology and the particle size distribution as they determine the filterability and flow properties of the particles in the downstream processes. They may also be crucial for the application, e.g. due to the resulting dissolution properties of proteins [45] or the surface and microstructure properties of the catalyst [13,20,21]. Seeding is likewise applied to improve control and the reproducibility of processes especially if small particles are involved or the

process is conducted in the range of the metastable zone limit of primary nucleation [46,47]. This way, it is also possible to enable secondary nucleation instead of uncontrolled primary nucleation and to control polymorphism [45,48-50]. In general, a minimum weight fraction of 0.1 – 1.0 w% is necessary to enable secondary nucleation below the metastable zone limit [51].

2.2 Thermodynamic modeling

The solubility product $K_{\mathrm{SP},j}$ according to Eq. (7) describes the equilibrium between the solids-forming ions i in the liquid phase and each solid phase j and is a function of the individual activities of each ion i of the solid j at thermodynamic equilibrium $a_{i,j}^{*}$ and its stoichiometric coefficient $\nu_{i,j}$.

$$K_{\mathrm{SP},j} = \prod {a_{i,j}^{*}}^{\nu_{i,j}} \qquad (7)$$

The driving force for solids formation during co-precipitation and aging is the phase-specific supersaturation S_j according to Eq. (8). It is described in terms of the actual activities of solids-forming ions a_i in the solution, the solubility product $K_{\mathrm{SP},j}(T)$ of the solid phase j and the stoichiometric coefficients ν_i and $\nu_{\pm}$. The activity a_i of an ion i can be calculated from its molality b_i, the reference value $b^0 = 1\ \mathrm{mol \cdot kg^{-1}}$ and its activity coefficient γ_i according to Eq. (9). Thus, non-ideal ion interactions are considered.

$$S_j = \left(\frac{\prod a_{i,j}^{\nu_{i,j}}}{K_{\mathrm{SP},j}(T)} \right)^{1/\nu_{\pm}} \qquad (8)$$

$$a_i = \gamma_i \cdot \frac{b_i}{b^0} \qquad (9)$$

The amount of available solids-forming ions (free ions) is further reduced by speciation reactions or complex formation. The respective equilibrium is described with the ion association constant according to Eq. (10).

$$K_{\mathrm{IA},k} = \frac{a_k}{\prod a_{i,k}^{\nu_{i,k}}} \qquad (10)$$

Activity coefficient models for the calculation of γ_i vary in their number of ion- or ion-pair-specific parameters and accordingly in their range of validity. In general, activity coefficient models only consider ion interactions, but no ion associations. Hybrid models consider both. The reaction schemes for all solids forming ions (Cu^{2+}, Zn^{2+}, Zr^{4+}, Na^{+}, CO_3^{-}, NO_3^{-}) involve interactions with OH^{-} respectively H_3O^{+} and, thus, influence the pH of the electrolyte [13]. Therefore, the pH of the electrolyte or aging suspension is an easily accessible measurand to observe the aging progress, but also to understand the underlying chemistry.

Four activity coefficient models are compared in Fig. 1a and 1b with regard to their applicability for Cu/Zn based catalyst precursors:

I. the Davies extended Debye–Hückel model (CHEAQS Next (64 bits, Version 0.2.1.3)) [42,52] without ion specific parameters ($I_{\mathrm{Davies}} \leq 0.5\ \mathrm{mol \cdot (kg\ H_2O)^{-1}}$)
II. the WATEQ model (WATEQ_minteq.v4) [53] with ion specific parameters ($I_{\mathrm{WATEQ}} \leq 1.0\ \mathrm{mol \cdot (kg\ H_2O)^{-1}}$)
III. the Pitzer model with ion-pair specific parameters. Ion association reactions are only considered if the respective interaction parameters are unavailable ($I_{\mathrm{Pitzer}} \leq 6\ \mathrm{mol/l}$ [54]) [13]
IV. a modified hybrid Pitzer model where both Pitzer parameters and $K_{\mathrm{IA},k}$ are considered for the same ion pairing (cp. [13] but with re-activated ion association reactions)

First, pure reactant solutions without solid formation are considered in order to exclude a possible influence by solubility products.

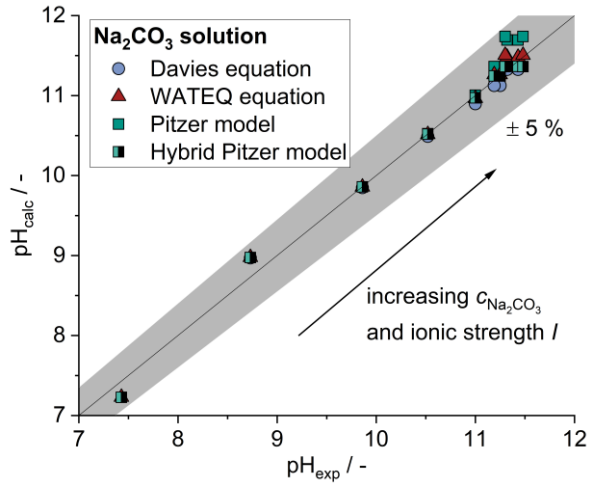

Figure 1a. Parity plots for calculated and experimentally determined pH for three different activity coefficient models for 8 different molalities of an aqueous Na_2CO_3 solution between $10^{-5}\ mol/kg\ H_2O < b_{Na_2CO_3} < 2\ mol/kg\ H_2O$ at 298 K.

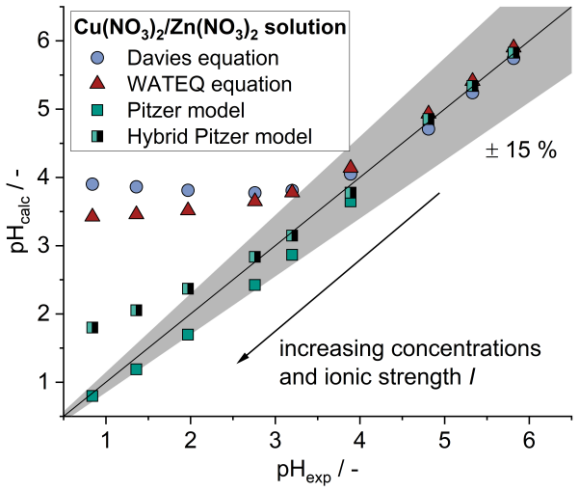

Figure 1b. Parity plots for calculated and experimentally determined pH for three different activity coefficient models for 9 different molalities of an aqueous $Cu(NO_3)_2/Zn(NO_3)_2$ solution at 298 K between $10^{-4}\ mol/kg\ H_2O < b_{metal\ nitrates} < 4\ mol/kg\ H_2O$. $n_{Cu(NO_3)_2}/n_{Zn(NO_3)_2} = 1$.

In Fig. 1a, the calculated pH of Na_2CO_3 solutions with varying molalitites between 10^{-5} mol·(kg H_2O)$^{-1}$ and 2 mol·(kg H_2O)$^{-1}$ at 298 K is plotted against the measured pH. All four models show a good fit with deviations of less than 5 % across the entire range up to $I = 6\ \mathrm{mol} \cdot (\mathrm{kg\ H_2O})^{-1}$. Thus, all four models seem to correctly represent the complex formation and non-ideal interaction of Na^+ and $CO3^{2-}$ ions and accordingly calculate accurate activities for these species. A direct comparison of both Pitzer model variants shows that the hybrid approach is favorable for $I \geq 0.3\ \mathrm{mol} \cdot (\mathrm{kg\ H_2O})^{-1}$. In Fig. 1b, the same procedure is repeated for the other reactant solution, an aqueous mixture of $Cu(NO_3)_2$ and $Zn(NO_3)_2$ with $10^{-4}\ \mathrm{mol} \cdot (\mathrm{kg\ H_2O})^{-1} < m_{\mathrm{metal\ nitrates}} < 4\ \mathrm{mol} \cdot (\mathrm{kg\ H_2O})^{-1}$. Here, all models show deviations of less than 6 % when compared to the measured data for $pH_{\mathrm{exp}} > 3.9$, thus $I \leq 0.6\ \mathrm{mol} \cdot (\mathrm{kg\ H_2O})^{-1}$, which is in agreement with known ranges of validity. For higher molalities up to $I = 12\ \mathrm{mol} \cdot (\mathrm{kg\ H_2O})^{-1}$, the Davies and WATEQ models show deviations of 18 % to more than 300 %. The hybrid Pitzer model also shows deviations of more than 15 % for $I \geq 6\ \mathrm{mol} \cdot (\mathrm{kg\ H_2O})^{-1}$. In contrast, deviations for the Pitzer model remain below 15 %. Yet, in the range of $0.6\ \mathrm{mol} \cdot (\mathrm{kg\ H_2O})^{-1} < I < 3\ \mathrm{mol} \cdot (\mathrm{kg\ H_2O})^{-1}$ $(2.8 < pH < 3.9)$, the hybrid variant is more accurate which has been predicted by Pitzer et al. by talking about "maxima of association" in certain concentration ranges depending on the stoichiometry of ion pairings [55].

Even relatively simple activity coefficient models like the Davies approach are suited to describe Na^+ and CO_3^{2-} based electrolytes. However, for the more complex behavior of $Cu(NO_3)_2$ and $Zn(NO_3)_2$ solutions, a more sophisticated approach becomes necessary, e.g. the use of a Pitzer model variant. Since the reactant solutions show an opposite trend comparing both Pitzer approaches, ion association reactions have to be considered only if proven necessary as suggested in general by Lassin et al. [56]. Thus, the applicability of solubility products of minerals for the thermodynamic description of aging will be discussed separately in Sect. 4.1 using a Pitzer model modified accordingly.

3 Materials and Methods

3.1 Materials and Model

A ternary Cu/Zn/Zr based catalyst precursor produced according to Sect. 3.2 is used in this

study to evaluate the predictability of the phase composition in the aged precursor using a thermodynamic model and to characterize the influence of seeding on both aging kinetics and properties of the aged precursor. The reactant solutions were prepared from $Cu(NO_3)_2{\cdot}3H_2O$ (purity ≥ 99.5 %, Merck), $Zn(NO_3)_2{\cdot}6H_2O$ (purity ≥ 99 %, Alfa Aesar), $ZrO(NO_3)_2{\cdot}6H_2O$ (purity > 99 %, Sigma-Aldrich), $NaHCO_3$ (purity ≥99 %, Carl Roth) and demineralized water. In some studies a HNO_3 solution (65%, Carl Roth) and NaOH (purity ≥99 %, Carl Roth)) were used to adjust the initial pH after co-precipitation. For the study on the influence of the metal ratio discussed in Fig. 3 Na_2CO_3 (purity ≥99 %, Carl Roth) and a binary Cu/Zn based catalyst precursor were used instead.

We consider four kinds of intermediates: 1) the co-precipitate directly after co-precipitation is completed ($t_{\mathrm{age}} = 0\ \mathrm{min}$), 2) samples taken at defined moments (t_{age}) during aging, 3) the aged precursor after aging is completed and 4) the precatalyst consisting of CuO, ZnO and ZrO_2 and obtained by calcination.

The software PHREEQC (iphreeqc Version 3.7.1) is used to calculate the thermodynamic state of equilibrium for aging. A modified database on the basis of PITZER.DAT [13] containing information on the activity coefficient model as well as literature data for $K_{\mathrm{IA},k}$ and $K_{\mathrm{SP},j}$ is applied. The following solids were relevant at the considered parameter ranges: rosasite (zincian malachite) [44], malachite [57], aurichalcite [58], hydrozincite [59] and ZrO_2 [60]. PHREEQC solves mass and substance balance equations and calculates speciation of ions in the liquid phase. By iteration, these calculations are repeated until all phases considered are saturated or undersaturated. An ideally mixed and isotherm system as well as no interaction with any gas phase are assumed. Any CO_2 formed is dissolved in the liquid phase as a separate species so that no interaction with the ambient air is considered.

3.2 Experimental Set-up and Procedure

Based on results on the influence of mixing in co-precipitation [13], continuous co-precipitation and batch aging were strictly separated according to Fig. 2. A $NaHCO_3$ solution (feed 1) and a metal nitrate solution (feed 2) with equal volume flows were continuously mixed by an impinging micro jet mixer. Co-precipitation then takes place. The dimensions of the mixer are given in Fig. 2 in mm. Two gear pumps (MCP-Z Standard, Ismatec with GJ-N23 pump heads, Micropump) in combination with magnetic-inductive flow meters (IFC90, Krohne) were used at constant total volume flows of 600 ± 40 mL·min^{-1}. Deviations results from the collision of the two reactant streams and the associated highly sensitive control system. Regarding all experiments at $pH(t_{\mathrm{age}} = 0\ \mathrm{min}) = 7.1$, $T = 55\ °\mathrm{C}$, $b_{\mathrm{NaHCO_3,Feed1}} = 1.018\ \mathrm{mol} \cdot (\mathrm{kg\ H_2O})^{-1}$, $b_{\mathrm{Cu(NO_3)_2,Feed2}} = 0.162\ \mathrm{mol} \cdot (\mathrm{kg\ H_2O})^{-1}$, $b_{\mathrm{Zn(NO_3)_2,Feed2}} = 0.081\ \mathrm{mol} \cdot (\mathrm{kg\ H_2O})^{-1}$ and $b_{\mathrm{ZrO(NO_3)_2,Feed2}} = 0.027\ \mathrm{mol} \cdot (\mathrm{kg\ H_2O})^{-1}$ were used. The temperature of co-precipitation and aging was adjusted for the temperature study in Fig. 4. The experiments with $pH(t_{\mathrm{age}} = 0\ \mathrm{min}) = 6.7$ were conducted using the same molalities but by additionally adding a 65% HNO3 solution to feed 2: $X_{\mathrm{HNO_3,Feed2}} = 22\ \mathrm{mL} \cdot (\mathrm{kg\ H_2O})^{-1}$. The pH for the pH study in Fig. 5 was adjusted by additionally adding HNO_3 or NaOH to the reactant solutions while maintaining constant concentrations of $NaHCO_3$ and the metal reactants. For the binary Cu/Zn based precursor discussed in Fig. 3 $b_{\mathrm{Na_2CO_3,Feed1}} = 0.6\ \mathrm{mol} \cdot (\mathrm{kg\ H_2O})^{-1}$, $b_{\mathrm{Cu(NO_3)_2,Feed2}} + b_{\mathrm{Zn(NO_3)_2,Feed2}} = 0.5\ \mathrm{mol} \cdot (\mathrm{kg\ H_2O})^{-1}$ and $T = 65\ °\mathrm{C}$, were applied.

The co-precipitate suspension was fed directly into one of two double-jacketed 4000 mL glass tank reactor ($d_{\mathrm{tank}} = 120\ \mathrm{mm}$) with four baffles according to DIN 28131, where aging took place under stirring with a two-staged three-blade propeller agitator ($d_{\mathrm{stirrer,1}} = 40\ \mathrm{mm}$; $d_{\mathrm{stirrer,2}} = 50\ \mathrm{mm}$, 30° pitch) at 1000 rpm. The pH was measured with a HI1190T electrode (Hanna). The pH electrode was calibrated daily with two reference solutions (HI 70004 and HI 70007 for $4 < pH < 7$ or HI 70007 & HI 70010 for $7 < pH < 10$, respectively by Hanna). Temperature was controlled with ±1 K accuracy. Samples during aging were obtained

by withdrawing 30 mL – 50 mL suspension near the stirrer. These samples were processed identically to the co-precipitate suspension, as described in Sect. 3.3. In general, aging was completed 30 min after a pH minimum has occurred.

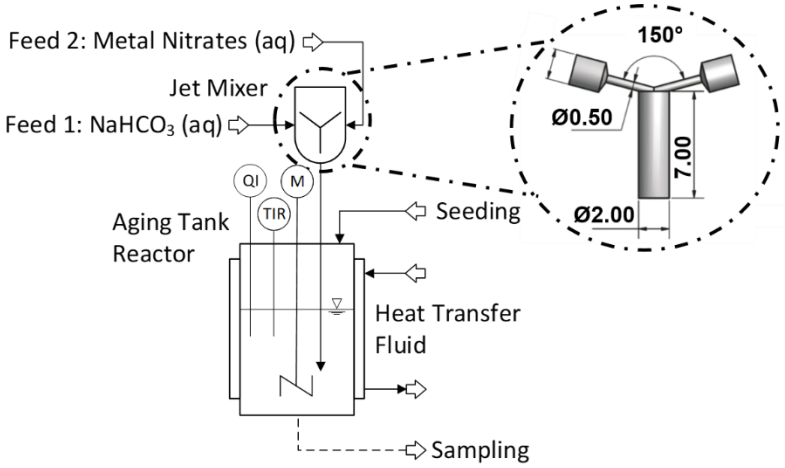

Figure 2. Experimental setup for a continuous co-precipitation followed by batch aging. M: motor, TCR: temperature control and recording, QR: pH recording. Based on [13].

The suspension of both the time samples and the aged precursor was collected without dilution for the analytics described in Sect. 3.3. It was then filtered (MN85/70, Macherey-Nagel or similar) using a water aspirator. The filter cake was suspended and washed with demineralized water until an electrical conductivity of < 50 µS·cm-1 was achieved and no nitrate could be detected by nitrate test strips (< 10 mg·L-1, VWR Chemicals). The moist sample was then dried at the aging temperature for at least 15 h. Some samples were then calcined as described elsewhere [10] and ground in a mortar until no more lumps can be visually detected.

Dried seeding material was obtained by completing an aging at the same process conditions as the intended seeding experiment and then washing, drying and grinding the solids as described above. Seeding suspensions were obtained by conducting aging until the pH minimum is reached and then withdrawing the desired amount of suspension. For certain studies the seeding suspension was concentrated by filtration and resuspension of the filter cake in a suspension with the original solids content. Dried seeding material and seeding suspensions were added by syringe or funnel from the top of the reactor directly after co-precipitation was finished. Seeding was completed within a maximum of 2 min. Inverse seeding was realized by aging a small volume until aging is completed and then adding fresh co-precipitate suspension to the aged suspension.

3.3 Analytics

Fourier-transform infrared spectroscopy (FT-IR) and X-ray diffraction (XRD) measurements of the dried and ground samples were used to determine the phase composition of the solids. The FT-IR spectra in the range of 4000 cm-1 < $\tilde{\nu}$ < 230 cm^{-1} with a resolution of 2 cm^{-1} were measured using a Varian 660-IR spectrometer (Agilent) in combination with the software Resolution Pro and the KBr disc technique [29]. X-ray diractograms in the range of 5° < 2θ < 80° were measured using a Panalytical X'Pert Pro X-ray diffractometer (Malvern Panalytical) with Bragg-Brentano geometry and Cu K-α radiation with a Ni filter over a period of 120 min. Some samples were measured with a STOE STADI MP instead. A Rietveld refinement was used to determine mass fractions of solids phases from the diffractogram. For this purpose the software Profex Version 4.3.5 was used [61]. The following reference data were used: malachite (BGMN [61]), modified according to Eqs. (2) – (5), hydrozincite (BGMN), aurichalcite (RRUFF ID R060426.1), $Na_2Zn_3(CO_3)_4{\cdot}3H_2O$ (ICSD 81305), ZrO_2 (ICSD 83862 and 18190), β-$Zr(OH)_2(NO_3)_2{\cdot}5(H_2O)$ (ICSD 84658), $Zr(OH)_3NO_3$ (ICSD 80062), CuO (04-007-1375, Ceramics, Profex) and Zincite (BGMN).

XRF measurements to determine metal ratios of the samples were conducted using a Bruker Pioneer S4 [10]. Elemental analysis was performed with a vario EL cube (Elementar). A 725 ICP-OES spectrometer (Agilent) was used for complementary ICP-OES measurements. Solid samples for ICP-OES measurements were digested beforehand using a Multiwave 3000 (Anton Paar) with an added acid for 2 h at a maximum of 60 bar and 240 °C. The specific particle surface areas (S_{BET}) of the precatalysts were determined by N_2 physisorption measurements using a Quantachrome NOVA 2000e device (Anton Paar) at 77 K. Samples were degassed for 12 h at 120 °C. Isotherms were evaluated with the Brunnauer-Emmett-Teller model (BET) in the range of 0.01 – 0.5 p/p_0. The particle morphology was analyzed by scanning electron microscopy (SEM) with a Zeiss GeminiSEM 500 with a Schottky field emission cathode. The particles of the dried sample were fixated on adhesive carbon pads. In order to complement the metal composition determined by ICP-OES and XRF measurement, additional EDXS measurements using an Oxford X-Max^N system were conducted.

4 Results and Discussion

As discussed in Sect. 1 and 2.1 aging is crucial for the aforementioned product qualities of the final catalyst. The studies here aim to help improving the aging process on two levels. First, in Sect. 4.1 phase compositions calculated with a thermodynamic model are compared to experimental data to resolve if the phase composition after aging can be predicted. Then, in Sect. 4.2 the influence of seeding with different techniques and mass fractions will be discussed to quantify how far seeding can accelerate the aging process at liter scale.

4.1 Model Based Prediction of the Phase Composition

Three main factors that significantly influence the aged intermediate have been established in the experimental studies discussed previously: the Cu/Zn ratio, pH and temperature [7,16]. Therefore, the applicability of the thermodynamic model to predict phase composition after aging shall be discussed on basis of these parameters.

In Fig. 3a the mass fractions of the solids phases of the aged intermediate are plotted as a function of the total Zn fraction $\tilde{x}_{\mathrm{Zn,Feed2}}$ in the metal reactant solution as defined in Eq. (11) for a simplified binary Cu/Zn based catalyst precursor. The mass fractions of the experimental samples (dots) were determined by XRD and a Rietveld refinement as described in Sect. 3.3. Therefore, only crystalline portions of the solid can be registered. Process conditions corresponding to the experimental conditions were applied for the calculated data (lines). In Fig. 3b the corresponding molar fraction of Zn in zincian malachite $\tilde{x}_{\mathrm{Zn,zM}}$ is plotted as a function of $\tilde{x}_{\mathrm{Zn,Feed2}}$.

$$\tilde{x}_{\mathrm{Zn,Feed2}} = \frac{b_{\mathrm{Zn,Feed2}}}{b_{\mathrm{Cu,Feed2}} + b_{\mathrm{Zn,Feed2}}} = \frac{b_{\mathrm{Zn(NO_3)_2,Feed2}}}{b_{\mathrm{Cu(NO_3)_2„Feed2}} + b_{\mathrm{Zn(NO_3)_2„Feed2}}} \qquad (11)$$

For $\tilde{x}_{\mathrm{Zn,Feed2}} = 0\ \mathrm{mol\%}$, Cu is present as the only metallic reactant. Accordingly, only pure malachite (equal to zincian malachite with $\tilde{x}_{\mathrm{Zn,zM}} = 0$) is formed as shown by the thermodynamic model and confirmed experimentally in Fig. 3a and 3b. Only zincian malachite continues to be formed for increasing Zn fractions in the feed of up to $\tilde{x}_{\mathrm{Zn,Feed2}} = 20\ \mathrm{mol\%}$. Concurrently, the Zn fraction in zincian malachite increases in both the model and the experiments. While the model shows zincian malachite as the only product up to $\tilde{x}_{\mathrm{Zn,Feed2}} = 30\ \mathrm{mol\%}$, the Rietveld refinement indicates, contrary to expectations, small amounts of aurichalcite. For higher $\tilde{x}_{\mathrm{Zn,Feed2}}$, aurichalcite is increasingly formed as an additional phase. The XRD evaluation also shows the existence of hydrozincite which is only present in the model above $\tilde{x}_{\mathrm{Zn,Feed2}} = 50\ \mathrm{mol\%}$. For $\tilde{x}_{\mathrm{Zn,Feed2}} = 1$ aurichalcite with $\tilde{x}_{\mathrm{Cu,Aur}} = 0$ is formed exclusively both in the model and experimentally. Discrepancies between predicted fractions and the values determined by Rietveld refinement can be seen in particular for $0.3 < \tilde{x}_{\mathrm{Zn,Feed2}} < 0.6$ when the predominance swaps between zincian malachite and aurichalcite.

Probable reasons for these deviations are on the one hand the scarcity of thermodynamic data for the synthetic phases. For this reason, $K_{\mathrm{SP},j}$ of mineral phases with fixed stoichiometries deviating from the experimentally determined metal ratios in the solids had to be used. The difference in the maximum of $\tilde{x}_{\mathrm{Zn,zM}}$ between model and XRD evaluation can also be explained with differences in the maximum Zn fraction of zincian malachite between the thermodynamic data used in the model and the boundaries applied in the Rietveld refinement. On the other hand, the use of the two distinct mineral phases aurichalcite and hydrozincite with fixed Zn and Cu fractions and thus relatively fixated lattice parameters may also result in uncertainties in the Rietveld refinement. Yet, the general trends for the phase composition after aging and the Zn fraction in zincian malachite are predicted correctly by the thermodynamic model.

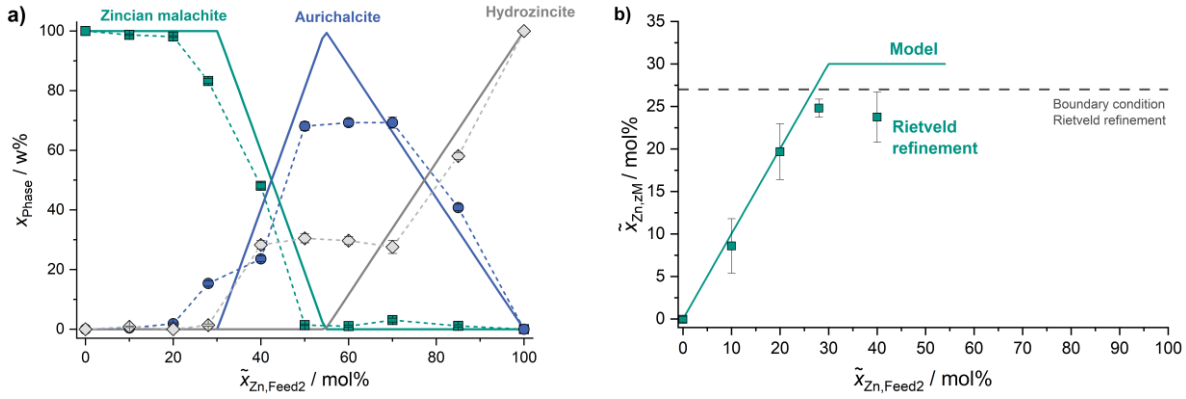

Figure 3. Mass fraction of solids phases in the aged intermediate (a) and the zinc fraction in zincian malachite $\tilde{x}_{\mathrm{Zn,zM}}$ (b) as a function of the Zn fraction in the metal reactant solution $\tilde{x}_{\mathrm{Zn,Feed2}}$ at 65 °C.

In Fig. 4a the mass fractions of the solids phases after aging are plotted as a function of temperature for $\tilde{x}_{\mathrm{Zn,Feed2}} = 0.33$. In Fig. 4b $\tilde{x}_{\mathrm{Zn,zM}}$ is plotted accordingly.

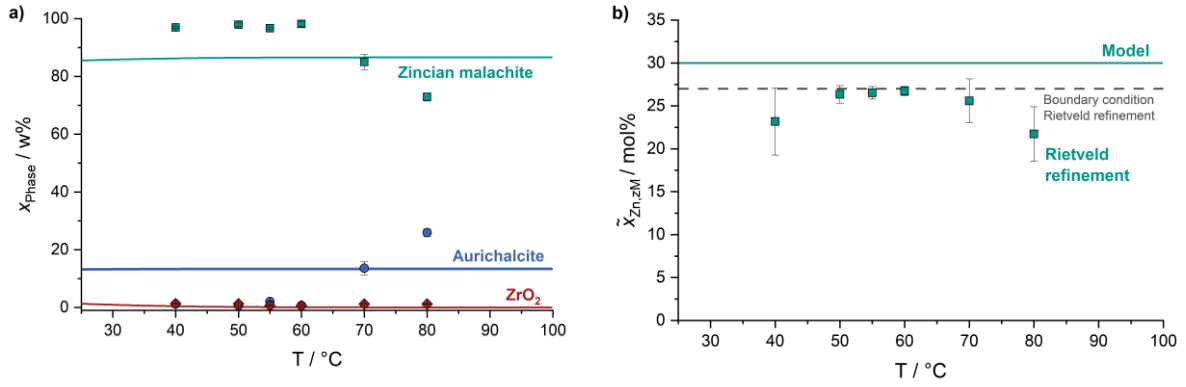

Figure 4. Mass fraction of solids phases in the aged intermediate (a) and the zinc fraction in zincian malachite $\tilde{x}_{\mathrm{Zn,zM}}$ (b) as a function of temperature for $\tilde{x}_{\mathrm{Zn,Feed2}} = 0.33$.

Both model and experiments show a predominance of zincian malachite for $T \leq 60\,°\mathrm{C}$ with a ratio of approx. 9 to 1. Deviations can be explained with differences in the Cu and Zn fractions between the literature data used in the thermodynamic model and the Rietveld refinement for both zincian malachite (30 vs. 27 mol% Zn) and aurichalcite (45.4 vs. 37.5 mol% Cu). These differences also explain the deviations in the determined $\tilde{x}_{\mathrm{Zn,zM}}$. For higher temperatures, the experiments show an increasing fraction of aurichalcite of up to 26 mol% and decreasing Zn fractions in zincian malachite. Since no temperature-dependent $K_{\mathrm{SP},j}$ are available, the model does not show any temperature dependency. Using reaction enthalpies calculated from standard formation enthalpies and the simplified van't Hoff equation according to Eq. (12) with the reaction enthalpy at T_0 $\Delta_r H^0$ and the gas constant R instead to depict temperature effects does not show significant differences. Therefore, only the latter variant is shown.

$$K_{\mathrm{SP},j}(T) = K_{\mathrm{SP},j}(T_0) \cdot \exp\left(-\frac{\Delta_r H^0}{R\,T} + \frac{\Delta_r H^0}{R\,T_0}\right) \qquad (12)$$

In Fig. 5a, the experimentally determined mass fractions of the solids phases of the aged precursor are plotted as a function of the initial pH directly after co-precipitation took place ($t_{\mathrm{Age}} = 0\ \mathrm{min}$) for $\tilde{x}_{\mathrm{Zn,Feed2}} = 0.33$. The model data shows the phase fractions as a function of the pH at thermodynamic equilibrium. In Fig. 5b $\tilde{x}_{\mathrm{Zn,zM}}$ is plotted accordingly.

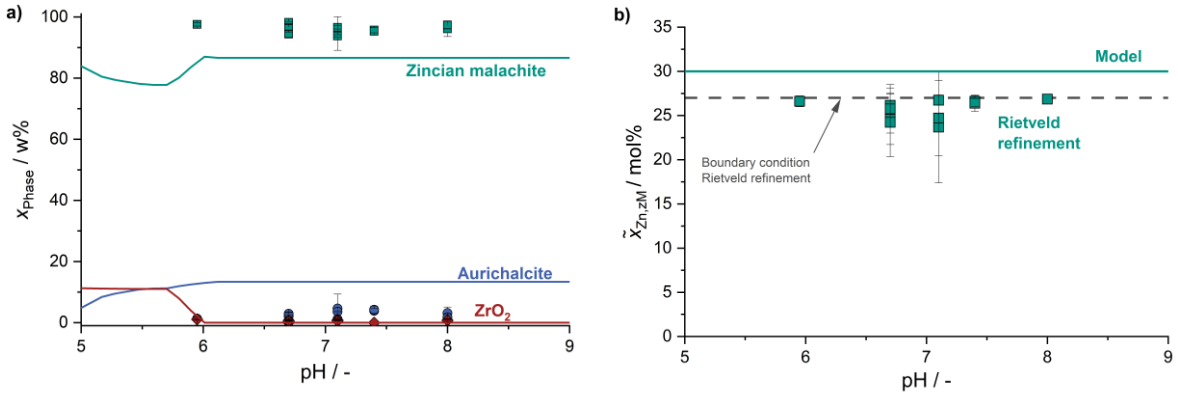

Figure 5. Mass fraction of solids phases in the aged intermediate (a) and the zinc fraction in zincian malachite $\tilde{x}_{\mathrm{Zn,zM}}$ (b) as a function of pH for $\tilde{x}_{\mathrm{Zn,Feed2}} = 0.33$.

The Rietveld refinement reveals the same phase composition for each sample independent from the initial pH. The model shows the same trend, but lower mass fractions for zincian malachite. Similar deviations also result for $\tilde{x}_{\mathrm{Zn,zM}}$ in Fig. 5b. Again, this can be explained with differences in the stoichiometries of zincian malachite and aurichalcite between the thermodynamic model and the reference data used in the Rietveld refinement.

In general, the thermodynamic model was able to predict the predominance of zincian malachite after aging for the pH and temperature ranges investigated. For varying reactant compositions, the model was able to correctly determine the change between an aged precursor rich in zincian malachite and rich in aurichalcite and the increasing Zn fraction in zincian malachite. Quantitative deviations for the phase composition and $\tilde{x}_{\mathrm{Zn,zM}}$ between the model and the results of the Rietveld refinement can be explained with inconsistent molecular formula for the solid phases considered and missing thermodynamic data for synthetic phases.

4.2 Accelerating Aging by Seeding

Aging takes much longer than co-precipitation, presumably mainly due to the induction time described by Güldenpfennig et al. [30]. A method to reduce this induction period while maintaining the properties of the aged intermediate and thus those of the final catalyst material would help to optimize aging economically and to better control the process. First, it will be discussed if seeding does have a significant impact on aging kinetics at liter scale and how this influence may be increased by varying the seed mass fraction or the seeding method. Then, the influence of seeding on the phase and metallic composition as well as the surface properties of the aged precursor and the precatalyst, known to correlate with the quality of the final catalyst, will be quantified. Finally, the transferability to other process conditions will be analysed and the significance of seeding will be assessed on this basis.

In Fig. 6a, the pH profile is plotted as a function of the aging time for seven independent experiments. The general progression over time will be discussed exemplarily using one curve (red line). The other curves are intended to show the reproducibility. In Fig. 6b, the same aging conditions were applied but seeds were added directly after co-precipitation is completed.

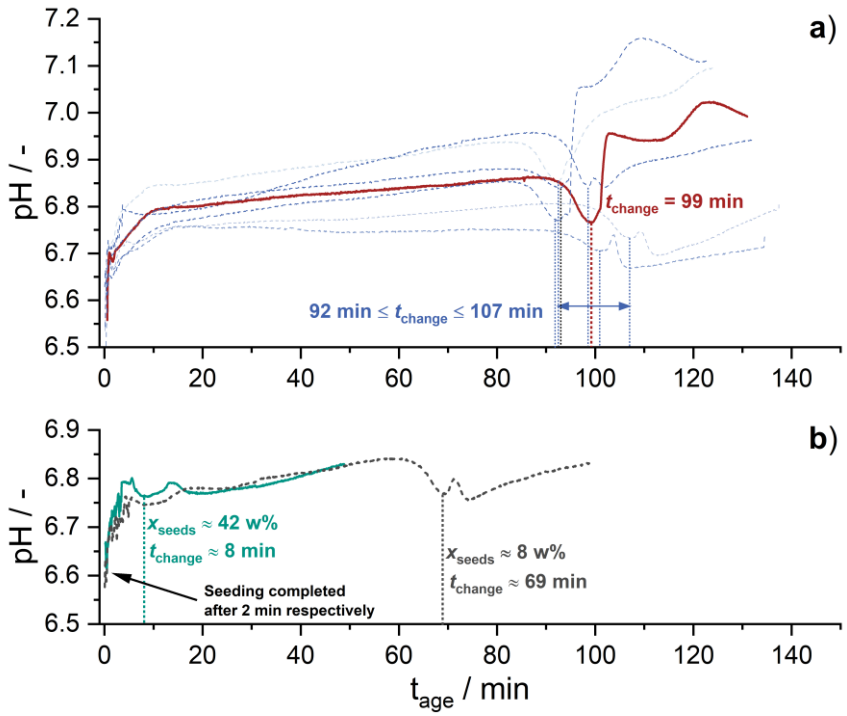

Figure 6. pH profiles as a function of aging time for (a) seven independent unseeded experiments with one progress marked exemplary for discussion and (b) two seeded experiments with different seed weight fractions.

The curves in Fig. 6a all show a similar trend. First, during wetting of the pH electrode, the pH rises rapidly up to the intended start value of $pH(t_{\mathrm{age}} = 0\ \mathrm{min}) = 6.7$. It then quickly continues to rise to $pH \approx 6.75 - 6.8$ in the first approx. 10 min from where the pH is almost stable or rises only slightly. After a total aging time of 92 to 107 min a pH minimum is passed which coincides with a change in color, s. Fig. 7, and indicates that the phase change to zincian malachite happens [16,28,62].

Figure 7. Color change during aging: the reactors in the background and on the left respectively show a blue color before the phase change begins ($t_{\mathrm{age}} \ll t_{\mathrm{change}}$). The reactors in the front and on the right respectively are greenish after zincian malachite was formed ($t_{\mathrm{age}} \gg t_{\mathrm{change}}$).

Furthermore, the formation of zincian malachite results in a change in crystallinity which will be discussed in Fig. 9ff. To ensure that the phase change is completed, aging is continued for additional 30 min. In some cases, a second pH minimum could be observed but not correlated to any events or altered properties. The three stages of rapid pH increase, slow increase and pH minimum can also be identified in both seeded experiments in Fig. 6b. However, depending

on the seed mass fraction chosen, the minimum already occurs at 69 min for $x_{\mathrm{Seeds}} = 8$ w% or after just 8 min for $x_{\mathrm{Seeds}} = 42$ w%. Thus, an influence of x_{Seeds} on the necessary aging time is present and will be quantified.

In Fig. 8 the turnover point indicating the phase change to zincian malachite is shown as a function of the seeding mass fraction x_{Seeds}. Both the quantitative method following the pH minimum and a simple optical method based on a change in color are shown. Each point is an individual experiment.

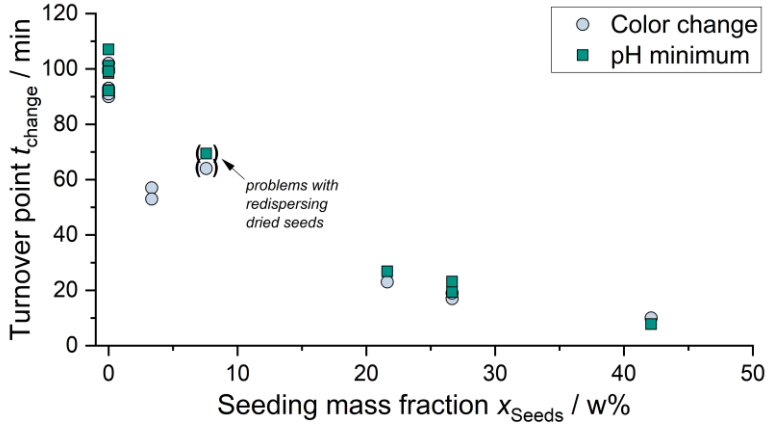

Figure 8. Time of the phase change as a function of seeding mass fraction. Both the quantitative method following the pH minimum and a simple optical method based on a change in color are shown.

Without seeding the phase change occurs after an average of $\bar{t}_{\mathrm{change}} = 96 \pm 5$ min and a minimum of $t_{\mathrm{change,min}} = 90$ min. The higher the seeding mass fraction, the faster the turnover point is reached. Already for $x_{\mathrm{Seeds}} = 3$ w%, the necessary time is reduced by 43 % to only $\bar{t}_{\mathrm{change}} = 55 \pm 3$ min. Higher x_{Seeds} lead to increasingly short turnover times resulting in $t_{\mathrm{change}} = 8$ min for the highest seeding mass fraction considered. Güldenpfennig et al. found a similar trend at milliliter scale by varying x_{Seeds} between 4 % and 20 % [30]. A runaway is observed for $x_{\mathrm{Seeds}} = 8$ w% where dried seeding material was used instead of a suspension with freshly aged seeds. The unexpected late turnover point is probably due to the poor wettability and aggregation of the dry particles reducing the mass-specific surface area. For $x_{\mathrm{Seeds}} = 27$ w% inverse seeding as described in Sect. 3.2 was additionally tested (points not specially marked), but no significant differences to the standard method are evident. The total yield of dried aged intermediate $Y_{\mathrm{aged\ precursor,total}}$ is defined according to Eq. (13) and increases with increasing x_{Seeds} from $11.2 \pm 1.4\ \mathrm{g \cdot L^{-1}}$ for the unseeded experiments to $19.0\ \mathrm{g \cdot L^{-1}}$ for $x_{\mathrm{Seeds}} = 42$ w%. The yield of new solid $\Delta Y_{\mathrm{aged\ precursor}}$ where the added seeding mass is substracted is defined by Eq. (14) with $\Delta Y_{\mathrm{aged\ precursor}} = Y_{\mathrm{aged\ precursor,total}}$ for unseeded experiments. A mean value of $\Delta \bar{Y}_{\mathrm{aged\ precursor,seeded}} = 11.6 \pm 1.2\ \mathrm{g \cdot L^{-1}}$ for all seeded experiments indicate that seeding does not influence the yield as expected for a reaction which is dominated by the thermodynamic equilibrium. A higher mass fraction of seeds leads to a larger specific surface area of the solids during aging when assuming constant particle size distributions. According to Zander et al. the phase transformation occurs via the liquid phase [63]. Thus, the larger surface area when more seeds are present may explain the increasingly rapid transformation.

$$Y_{\mathrm{aged\ precursor,total}} = \frac{m_{\mathrm{dried\ aged\ precursor,total}}}{V_{\mathrm{Suspension,total}}} \qquad (13)$$

$$\Delta Y_{\mathrm{aged\ precursor}} = \frac{m_{\mathrm{dried\ aged\ precursor,total-m_{Seeds}}}}{V_{\mathrm{Suspension,total}}} \qquad (14)$$

The aging process was also observed by means of XRD samples taken every 20 min. A Rietveld refinement with the references and parameters listed in Sect. 3.3 and 2.1 was used to evaluate the solids phase composition. In Fig. 9 the general procedure is shown for an aged precursor and a precatalyst both prepared with $x_{\mathrm{Seeds}} = 0\ \mathrm{w\%}$.

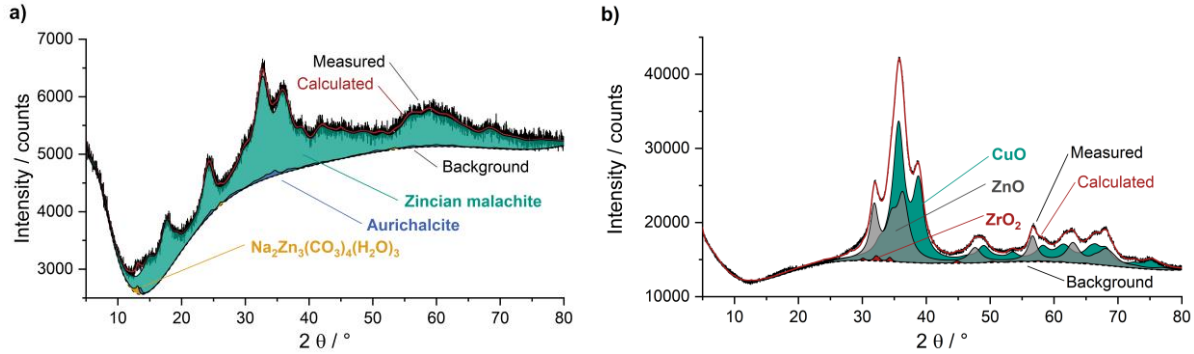

Figure 9. Exemplary Rietveld refinement of an aged precursor and a precatalyst (respectively: $x_{\mathrm{Seeds}} = 0\ \mathrm{w\%}$).

This procedure is then used in Fig. 10 a) to d) to observe the solids phase composition evolution during aging for x_{Seeds} between 0 w% and 42 w%. The range of turnover points determined by color change and pH minimum is marked as a hatched area. In Fig. 10 e) to h) the respective corresponding molar Zn fraction in zincian malachite $\tilde{x}_{\mathrm{Zn,zM}}$ determined according to Sect. 2.1 is plotted. For $x_{\mathrm{Seeds}} = 0\ \mathrm{w\%}$ the total Zn fraction in the solids was additionally quantified by means of ICP-OES and XRF.

For $x_{\mathrm{Seeds}} = 0\ \mathrm{w\%}$ (Fig. 10a) the first three samples show an amorphous diffractogram. At the same time, the XRF measurements in Fig. 10e indicate a constant Zn fraction in the solids over the entire aging process with only small fluctuations without a visible trend. This implies the existence of one common amorphous Cu/Zn predecessor phase (zincian georgeite) or multiple amorphous phases in the initial stage of aging what is consistent with the literature [15,63,64]. The first crystalline structures are present in the 80 min sample. However, the evaluation of $\tilde{x}_{\mathrm{Zn,zM}}$ shows high uncertainties up to 100 min indicating a change in crystal structure is taking place. Only after the phase change, as indicated by the pH minimum and color change, is completed, consistently high Zn fractions in the expected range of $\tilde{x}_{\mathrm{Zn,zM}} \approx 0.27$ prevail. In general, the total Zn fractions determined with ICP-OES and XRF are in the range of 0.277 to 0.321 and thus slightly higher than expected. A possible explanation is the existence of small amounts of Zn rich aurichalcite or hydrozincite which was confirmed by the Rietveld refinement: $0.3\ \mathrm{w\%} < x_{\mathrm{Aur,End}} < 2.6\ \mathrm{w\%}$.

If seeds are added, a crystalline structure can be detected accordingly in the first time sample. For low x_{Seeds} only a small amount of crystalline material is present in the sample, thus only weakly pronounced peaks exist and result in high deviations. As well as for the unseeded experiments, some deviations for x_{zM} from $x_{\mathrm{zM}} > 95\ \%$ (Fig. 10b to d) and for $\tilde{x}_{\mathrm{Zn,zM}}$ from $\tilde{x}_{\mathrm{Zn,zM}} \approx 0.27$ (Fig. 10f to h) exist for $x_{\mathrm{Seeds}} > 0\ \mathrm{w\%}$ for aging times below the turnover points determined by pH minimum and color change. After the apparent phase change is completed, $x_{\mathrm{zM}} > 95\ \%$ and $\tilde{x}_{\mathrm{Zn,zM}} \approx 0.27$ result for all seeded experiments. This confirms the acceleration of aging by seeding also at the scale of the crystal lattice.

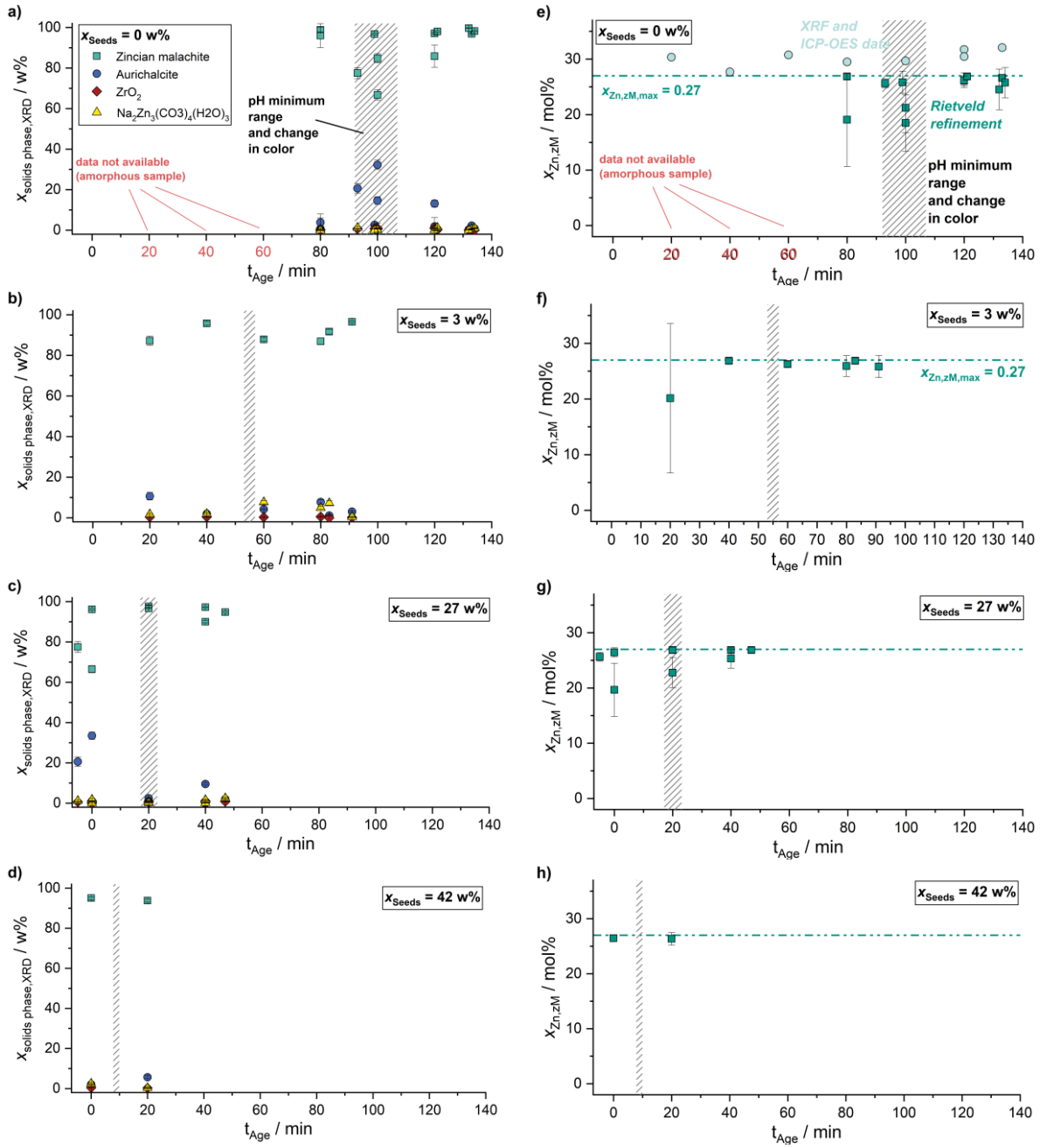

Figure 10. Solids phase composition as a function of aging time for four different seeding mass fractions (a to d) and Zn fraction in the zincian malachite phase determined by Rietveld refinement (e to h).

Fig. 11a shows the final solids phase composition of the aged precursor as a function of x_{Seeds}. For all x_{Seeds} except two outliers the fraction of zincian malachite is between 92 % and 100 %. No significant correlation between x_{zM} and x_{Seeds} is evident. Thus, the thermodynamic model discussed in Sect. 4.1 can be used for both seeded and unseeded aging. In Fig. 11b, the solids phase composition of the resulting precatalysts is plotted as a function of x_{Seeds}. The mass fractions of CuO x_{CuO} are between 48 % and 65 %, $33\,\% < x_{\mathrm{ZnO}} < 46\,\%$ and $1\,\% < x_{\mathrm{ZrO_2}} < 7\,\%$ if the data for $x_{\mathrm{Seeds}} = 8$ w%, the only set showing high deviations, is excluded. The measured metal fractions discussed in Table 1 indicate much more consistent results in between experiments. Thus, the deviations in Fig. 11b are attributed to differences in crystallinity as well as inaccuracies in the Rietveld refinement where in some cases the relative error between measured and calculated curve were in the range of $2 < X^2 < 3$ and thus above the target value of $X^2 = 1.5$. Within the scope of these inaccuracies no correlation between the

solids phase composition of the precatalyst and the mass fraction of seeding material is evident. More fixated boundary conditions, e.g. a fixed metal composition based on ICP-OES or XRF analysis of the sample, should improve the accuracy of the Rietveld refinement in the future.

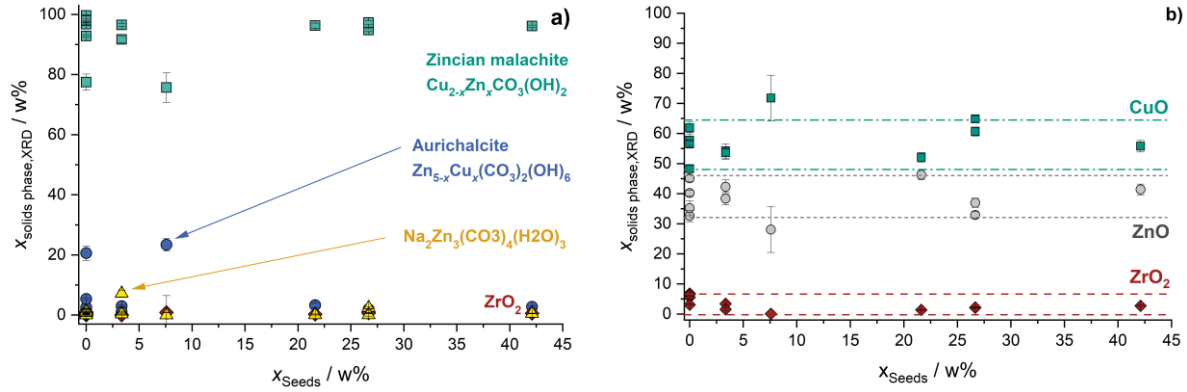

Figure 11. Solids phase composition of (a) the aged precursor and (b) the precatalyst as a function of the seeding mass fraction.

In Fig. 12 excerpts of complementary FT-IR measurements for respectively two experiments for $x_{\mathrm{Seeds}} = 0\ \mathrm{w\%}$ and $x_{\mathrm{Seeds}} = 3\ \mathrm{w\%}$ are shown. The spectra for both operating modes are congruent except for the two marked areas. The peak in the area 1163 cm^{-1} is most similar to the reference spectrum for rosasite analyzed by Stoilova et al. [65]. According to the authors, a peak in the range 960 – 971 cm^{-1} can be attributed to hydrozincite or aurichalcite. This may indicate a low level of aurichalcite or hydrozincite accumulation in the use of seeding. However, the XRD data shown in Fig. 11 show no significant influence. Therefore, future studies should characterize the impact of repeated use of the same seeding material on the hydrozincite and aurichalcite fractions in the aged precursor.

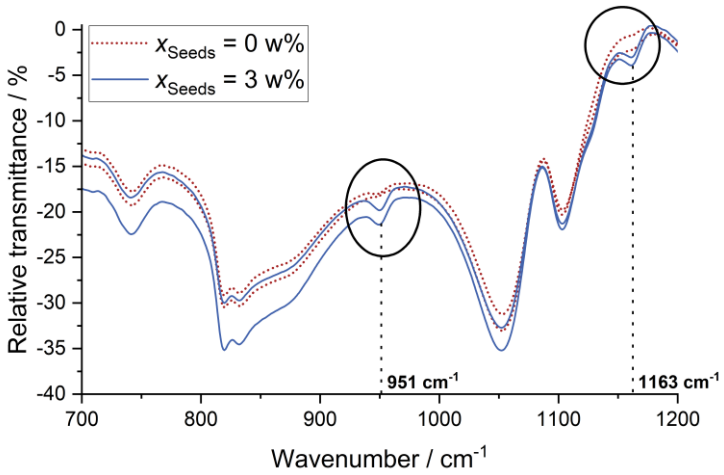

Figure 12. FTIR spectra of, respectively, two aged precursors prepared by unseeded ($x_{\mathrm{Seeds}} = 0\ \mathrm{w\%}$) and seeded aging ($x_{\mathrm{Seeds}} = 3\ \mathrm{w\%}$). Complete measuring range: 0 – 4000 cm^{-1}.

Fig. 13 shows SEM images of two aged precursors from an unseeded (left) and seeded ($x_{\mathrm{Seeds}} = 3\ \mathrm{w\%}$, right) aging at two different magnifications. Both the overview image and the detail shot show a very similar morphology in either case. This implies that the reduced aging time resulting from seeding does not influence the morphology and in particular the microstructure. Table 1 provides an overview on how seeding may influence properties of the resulting precatalyst. Additionally to the experiments at $pH(0\ \mathrm{min}) = 6.7$, data for $pH(0\ \mathrm{min}) = 7.1$ is specified. For $pH(0\ \mathrm{min}) = 7.1$ aging could also be accelerated by approx. 50 % reducing the necessary aging time from an average of 76 min to 38 min by adding a seeding mass fraction of $x_{\mathrm{Seeds}} = 3\ \mathrm{w\%}$.

$x_{\mathrm{Seeds}} = 0$ w%: $x_{\mathrm{Seeds}} = 3$ w%:

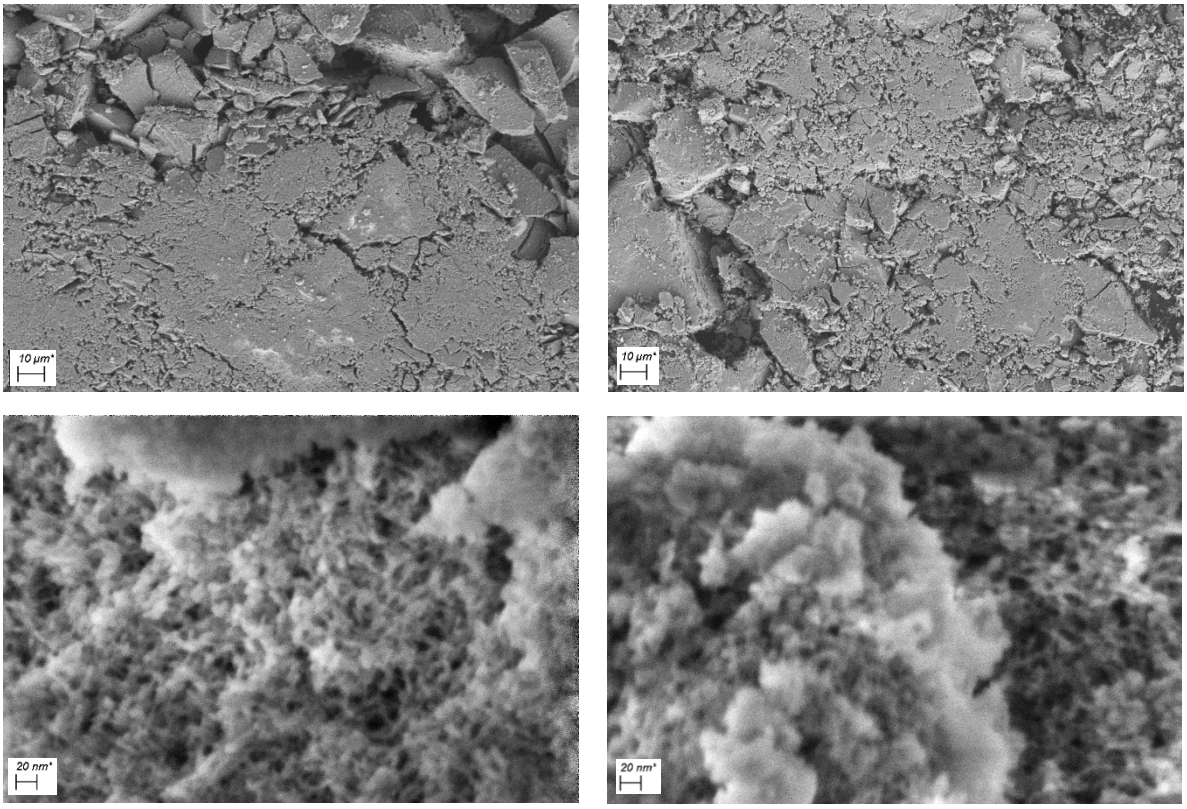

Figure 13. SEM images of two aged precursor from an unseeded (left) and seeded (right) aging, respectively, at two magnifications.

Table 1. Selected $t_{\mathrm{change,pH}}$ and physicochemical properties of the aged precursors and precatalysts from unseeded and seeded experiments for two initial pH. Values missing due to limited resources are indicated by 'n.a.'.

Precatalyst	$t_{\mathrm{change,pH}}$ [min]	$\tilde{x}_{\mathrm{Cu,metals}}$ [mol%]	$\tilde{x}_{\mathrm{Zn,metals}}$ [mol%]	$\tilde{x}_{\mathrm{Zr,metals}}$ [mol%]	S_{BET} [$\mathrm{m^2 \cdot g^{-1}}$]	$\bar{d}_{\mathrm{Pore,BJH}}$ [nm]	$d_{\mathrm{CuO,XRD}}$ [nm]
$pH(0\ \mathrm{min}) = 6.7$ $x_{\mathrm{Seeds}} = 0$ w%	96 ± 5	59.1; 60.2; 61.9; 64.1	32.4; 31.8; 29.2; 28.1	8.5; 8.0; 7.1; 7.7	117; 120; 125	9.2; 9.2; 11.2	2.9 ± 0.8
$pH(0\ \mathrm{min}) = 6.7$ $x_{\mathrm{Seeds}} = 3$ w%	53; 57	59.1	32.1	8.7	122; 124	9.2; 9.2	3.0; 3.7
$pH(0\ \mathrm{min}) = 6.7$ $x_{\mathrm{Seeds}} = 8$ w%	(69.4)	63.7	28.0	8.1	n.a.	n.a.	1.7
$pH(0\ \mathrm{min}) = 6.7$ $x_{\mathrm{Seeds}} = 27$ w%	12.5; 14.7	64.3	28.4	7.2	n.a.	n.a.	1.7; 2.0
$pH(0\ \mathrm{min}) = 7.1$ $x_{\mathrm{Seeds}} = 0$ w%	72.4; 79.9	60.2	31.8	8.0	104; 107	9.2; 11.2	4.1; 4.3
$pH(0\ \mathrm{min}) = 7.1$ $x_{\mathrm{Seeds}} = 3$ w%	36.0; 40.1	n.a.	n.a.	n.a.	94; 103	9.2; 9.2	4.0; 4.6

The molar fractions of Cu, Zn and Zr, analyzed on the aged precursor, are consistent in between samples with different x_{Seeds} as are the mass specific surface areas and the pore sizes which were respectively characterized by N_2 physisorption on the precatalyst. Compared to S_{BET} and $\bar{d}_{\mathrm{Pore,BJH}}$ of other Cu/Zn/Zr based precatalysts in literature [10,13], the values are

well within the expected range. This confirms the assumption from the SEM images that seeding does not affect the microstructure. For both initial pH no influence of x_{Seeds} on the CuO crystallite size determined by Rietveld refinement is evident.

Overall, the results show that aging time at liter scale can be reduced significantly by seeding without altering the considered properties of the aged precursor and the precatalyst. Thus, the nanostructure seems to remain unchanged. Higher x_{Seeds} lead to increasingly short turnover times in aging. In general, the activitiy, selectivity and longevity of a Cu/Zn based catalyst are correlated to the fraction of zincian malachite after aging as well as S_{BET}, the metal fractions and the pore size of its precatalyst [10,16,23]. Thus, if these properties remain unchanged, the catalyst quality should accordingly remain unchanged. Nevertheless, a comparison of catalysts from an unseeded and a seeded aging in a MeOH synthesis is strongly recommended to confirm that both methods deliver equivalent catalysts.

5 Conclusions

The focus of this study was on the aging step in the preparation of Cu/Zn based catalysts for the MeOH synthesis with a twofold objective. For one thing, it was to be resolved if aging can be understood as a thermodynamic equilibrium process and thus the solids phase composition after aging could be predicted using a thermodynamic model which might be useful when adapting the preparation to new requirements on the catalyst. On the other hand, seeding as a potential method to accelerate aging and thus enhancing process control and reducing energy consumption while maintaining the same product qualities was to be evaluated.

The thermodynamic model consists of two components: an activity coefficient model, which may consider ion association by complex formation in addition to ion interaction, and a compilation of solubility products of the solids phases relevant for aging $K_{\mathrm{SP},j}$. A comparison of four activity coefficient models comparing measured and calculated pH values of the reactants revealed that the ion interaction in the $NaHCO_3$ reactant solution up to $I = 6\ \mathrm{mol} \cdot (\mathrm{kg\ H_2O})^{-1}$ can be described with deviations of less than 5 % even by more simple models, e.g. the Davies extended Debye-Hückel equation. In contrast, only a more complex model, here the Pitzer model, allowed to correctly depict the speciation of the $Cu(NO_3)_2/Zn(NO_3)_2$ solution up to $I = 12\ \mathrm{mol} \cdot (\mathrm{kg\ H_2O})^{-1}$, however with errors of up to 15 %. Values for $K_{\mathrm{SP},j}$ were taken from mineral phases in the literature. The thermodynamic model was able to depict the general influence of the Cu/Zn ratio as well as the pH on the solids phase composition and the molar Zn fraction in zincian malachite after aging. However, a quantitative comparison does show significant deviations between model and measurement in the transition area between zincian malachite predominance and aurichalcite predominance. Also, the temperature dependency cannot be accurately modelled using only literature data. It is strongly recommended to fit existing data to the shown properties of the synthetic phases or to experimentally determine $K_{\mathrm{SP},j}$ for these phases in the future to improve the model quality. For future Rietveld refinements the use of a single aurichalcite phase with a variable Cu fraction between 0 and approx. 40 mol% and corresponding variable lattice parameters similar to the procedure chosen for zincian malachite may prove beneficial for even more precise phase compositions.

A study by Güldenpfennig et al. [30] showed that seeding does influence the aging kinetics at microliter scale. Based on that study, we quantitatively examined the influence of seeding on aging kinetics at liter scale for more process conditions, higher concentrations and in regard to the influence on the physicochemical properties of the aged precursor and the precatalyst. Comparative studies for two different initial pH showed that necessary aging times can be reduced by 43 % to 50 % by adding a seeding mass fraction of just $x_{\mathrm{Seeds}} = 3\ \mathrm{w\%}$. pH minima, color changes and phase compositions determined by XRD measurements were used and compared as indicators to show a completed phase transformation during aging. A further increase of x_{Seeds} leads to progressively shorter process times necessary to complete phase

change down to a minimum of 8 min for $x_{\mathrm{Seeds}} = 42\ \mathrm{w\%}$ instead of 96 min.

A comparison of the metallic and phase composition as well as the morphology of the aged precursors from unseeded and seeded experiments showed no differences. Furthermore, the mass specific surface area S_{BET}, the mean pore size $\bar{d}_{\mathrm{Pore,BJH}}$, the CuO crystallite size $d_{\mathrm{CuO,XRD}}$ and the phase composition of the precatalysts also seem to be independent from the seeding mass fraction used in aging. Only a comparison of FT-IR spectra of unseeded and seeded samples hints at a possible accumulation of aurichalcite in the aged precursor when using seeds. In total, the almost unchanged properties of the aged precursor and the precatalyst for different x_{Seeds} indicate that seeding accelerates aging significantly without altering the qualities of the final catalyst which correlate with the analyzed physicochemical properties.

Our next step is to compare catalysts from an unseeded and a seeded aging in a MeOH synthesis to confirm that seeding does not influence the catalyst properties negatively. If the catalyst prepared by seeded aging proves adequately operational, seeding experiments at the industrial scale are advisable to ensure the applicability of the findings of this work on the necessary scale. Complementary studies at lab scale on the influence of total solids weight fraction in the aging suspension, even higher seeding mass fractions and repeated seeding on the aging kinetics and resulting physicochemical properties of the aged precursor should be performed to conclusively evaluate the great potential of seeding for process control and economic optimization of aging.

Acknowledgements

The authors thank their students and colleagues at IKFT and TVT, especially Diana Deutsch and Sabrina Polierer, for their work in the lab and workshop.

Symbols used

a	[-]	activity
a_{zM}	[Å]	lattice parameter of zincian malachite
b	[mol· (kg H_2O)$^{-1}$]	molality
b^0	[mol· (kg H_2O)$^{-1}$]	reference molality; $1\ \mathrm{mol \cdot kg^{-1}}$
b_{zM}	[Å]	lattice parameter of zincian malachite
c_{zM}	[Å]	lattice parameter of zincian malachite
d	[nm]	particle/ pore size
d_{stirrer}	[mm]	diameter
I	[mol· (kg H_2O)$^{-1}$]	ionic strength
K_{IA}	[-]	ion association product
K_{SP}	[-]	solubility product
m	[kg]	mass
n	[mol]	amount of substance
pH	[-]	pH value
R	[J·K^{-1}·mol^{-1}]	gas constant
R^2	[-]	coefficient of determination
S	[-]	supersaturation
S_{BET}	[m^2·g^{-1}]	mass-specific surface area
T	[°C]	temperature
t_{Age}	[min]	aging time
V	[m^3]	volume
X	[mL·L^{-1}]	volumetric load

x	[w%]	mass fraction
$\tilde{x}$	[mol%]	molar fraction
Y	[kg·L^{-1}]	yield

Greek letters

β_{zM}	[°]	lattice parameter of zincian malachite
$\Delta_r H^0$	[J·mol^{-1}]	standard reaction enthalpy
ΔY	[kg·L^{-1}]	corrected yield (deducting the seeding mass)
γ	[-]	activity coefficient
ν	[-]	stoichiometric coefficient
$\tilde{\nu}$	[cm^{-1}]	wavenumber
σ	[mol%]	standard deviation
θ	[°]	scattering angle
χ^2	[-]	Error in Rietveld refinement

Sub- and Superscripts

±	all ions of a salt
*	at thermodynamic equilibrium
0	standard conditions
age	aging time; starting when co-precipitation is completed
Aur	aurichalcite
BET	determined by the Brunnauer-Emmett-Teller model
BJH	determined by the Barett-Joyner-Halenda method
change	turnover point in aging indicating a phase change
End	Final state
i	solids-forming ion
j	solid phase
k	complex/ ion associate
metals	in relation to the total metal content
pH	determined by local pH minimum
phase	solid phase
XRD	determined by XRD/ Rietveld refinement
zM	zincian malachite

Abbreviations

BET	Brunnauer-Emmett-Teller model
BJH	Barett-Joyner-Halenda method
EDXS	energy-dispersive X-ray spectroscopy
ICP-OES	inductively coupled plasma optical emission spectrometry
FT-IR	Fourier-transform infrared spectroscopy
MeOH	methanol
SEM	scanning electron microscopy
XRD	X-ray diffraction
XRF	X-ray fluorescence spectroscopy

References

[1] D. E. Brown, T. Edmonds, R. W. Joyner, J. J. McCarroll, S. R. Tennison, *Catal Lett (4)*, *144*, 545ff, (2014).
[2] G. A. Olah, *Angewandte Chemie (International ed. in English) (18)*, *44*, 2636ff, (2005).
[3] M. Bjørgen, F. Joensen, M. Spangsberg Holm, U. Olsbye, K.-P. Lillerud, S. Svelle, *Applied Catalysis A: General (1)*, *345*, 43ff, (2008).
[4] M. Behrens, F. Studt, I. Kasatkin, S. Kühl, M. Hävecker, F. Abild-Pedersen, S. Zander, F. Girgsdies, P. Kurr, B.-L. Kniep, M. Tovar, R. W. Fischer, J. K. Nørskov, R. Schlögl, *Science (New York, N.Y.) (6083)*, *336*, 893ff, (2012).
[5] F. Arena, K. Barbera, G. Italiano, G. Bonura, L. Spadaro, F. Frusteri, *Journal of Catalysis (2)*, *249*, 185ff, (2007).
[6] A. Sternberg, A. Bardow, *ACS Sustainable Chem. Eng. (8)*, *4*, 4156ff, (2016).
[7] C. Baltes, S. Vukojevic, F. Schuth, *Journal of Catalysis (2)*, *258*, 334ff, (2008).
[8] Y. Choi, K. Futagami, T. Fujitani, J. Nakamura, *Applied Catalysis A: General (1-2)*, *208*, 163ff, (2001).
[9] S. Kuld, M. Thorhauge, H. Falsig, C. F. Elkjær, S. Helveg, I. Chorkendorff, J. Sehested, *Science (New York, N.Y.) (6288)*, *352*, 969ff, (2016).
[10] S. Polierer, D. Guse, S. Wild, K. Herrera Delgado, T. N. Otto, T. A. Zevaco, M. Kind, J. Sauer, F. Studt, S. Pitter, *Catalysts (8)*, *10*, 816ff, (2020).
[11] F. Arena, G. Italiano, K. Barbera, S. Bordiga, G. Bonura, L. Spadaro, F. Frusteri, *Applied Catalysis A: General (1)*, *350*, 16ff, (2008).
[12] S. Wild, S. Polierer, T. A. Zevaco, D. Guse, M. Kind, S. Pitter, K. Herrera Delgado, J. Sauer, *RSC Adv. (5)*, *11*, 2556ff, (2021).
[13] D. Guse, S. Polierer, S. Wild, S. Pitter, M. Kind, *Chemie Ingenieur Technik 94, 3*, 314ff, (2022).
[14] B. Bems, M. Schur, A. Dassenoy, H. Junkes, D. Herein, R. Schlögl, *Chemistry*, *9*, 2039ff, (2003).
[15] A. M. Pollard, M. S. Spencer, R. G. Thomas, P. A. Williams, J. Holt, J. R. Jennings, *Applied Catalysis A: General (1)*, *85*, 1ff, (1992).
[16] M. Behrens, R. Schlögl, *Z. anorg. allg. Chem. (15)*, *639*, 2683ff, (2013).
[17] D. M. Whittle, A. A. Mirzaei, J. S. J. Hargreaves, R. W. Joyner, C. J. Kiely, S. H. Taylor, G. J. Hutchings, *Phys. Chem. Chem. Phys. (23)*, *4*, 5915ff, (2002).
[18] T. Fujitani, J. Nakamura, *Applied Catalysis A: General*, *191*, 111ff, (2000).
[19] M. S. Spencer, *Topics in Catalysis*, *8*, 259ff, (1999).
[20] X. Jiang, L. Zheng, Z. Wang, J. Lu, *Journal of Molecular Catalysis A: Chemical*, *423*, 457ff, (2016).
[21] X. Jiang, X. Qin, C. Ling, Z. Wang, J. Lu, *AIChE J. (2-3)*, *124*, 123ff, (2018).
[22] Q.-C. Zhang, K.-P. Cheng, L.-X. Wen, K. Guo, J.-F. Chen, *RSC Adv. (40)*, *6*, 33611ff, (2016).
[23] N. Mota, R. Guil-Lopez, B. G. Pawelec, J. L. G. Fierro, R. M. Navarro, *RSC Adv. (37)*, *8*, 20619ff, (2018).
[24] T. Fujitani, J. Nakamura, *Catal Lett (2/3)*, *56*, 119ff, (1998).
[25] P. J. Smith, S. A. Kondrat, P. A. Chater, B. R. Yeo, G. M. Shaw, L. Lu, J. K. Bartley, S. H. Taylor, M. S. Spencer, C. J. Kiely, G. J. Kelly, C. W. Park, G. J. Hutchings, *Chemical science (3)*, *8*, 2436ff, (2017).
[26] G. Sengupta, D. P. Das, M. L. Kundu, S. Dutta, S. K. Roy, R. N. Sahay, K. K. Mishra, S. V. Ketchik, *Applied Catalysis (1)*, *55*, 165ff, (1989).
[27] S. Kaluza, M. Behrens, N. Schiefenhövel, B. Kniep, R. Fischer, R. Schlögl, M. Muhler, *ChemCatChem (1)*, *3*, 189ff, (2011).
[28] M. Behrens, *Journal of Catalysis (1)*, *267*, 24ff, (2009).
[29] J. Schumann, T. Lunkenbein, A. Tarasov, N. Thomas, R. Schlögl, M. Behrens, *ChemCatChem (10)*, *6*, 2889ff, (2014).
[30] A. Güldenpfennig, M. Distaso, W. Peukert, *Chemical Engineering Journal*, *369*, 996ff, (2019).
[31] F. Liao, Y. Huang, J. Ge, W. Zheng, K. Tedsree, P. Collier, X. Hong, S. C. Tsang, *Angewandte Chemie (9)*, *50*, 2162ff, (2011).
[32] D. R. Palo, R. A. Dagle, J. D. Holladay, *Chem. Rev. (10)*, *107*, 3992ff, (2007).
[33] S. Tada, K. Larmier, R. Büchel, C. Copéret, *Catal. Sci. Technol. (8)*, *8*, 2056ff, (2018).
[34] R. Ahmad, M. Hellinger, M. Buchholz, H. Sezen, L. Gharnati, C. Wöll, J. Sauer, M. Döring, J.-D. Grunwaldt, U. Arnold, *Catalysis Communications*, *43*, 52ff, (2014).
[35] M. Behrens, F. Girgsdies, *Z. anorg. allg. Chem. (6)*, *636*, 919ff, (2010).
[36] L. Zwiener, F. Girgsdies, D. Brennecke, D. Teschner, A. G. Machoke, R. Schlögl, E. Frei, *Applied Catalysis B: Environmental*, *249*, 218ff, (2019).
[37] M. Behrens, F. Girgsdies, A. Trunschke, R. Schlögl, *Eur. J. Inorg. Chem. (10)*, *2009*, 1347ff, (2009).
[38] N. Perchiazzi, *Z. Kristallogr. Suppl. 23*, 505ff, (2006).
[39] B. Fehér, S. Szakáll, S. Bigi, *2nd Central-European Mineralogical Conference. Mineralogia - Special Papers 32*, (2008).
[40] B. Fehér, S. Szakáll, N. Zajzon, J. Mihály, *Miner Petrol (4)*, *109*, 405ff, (2015).

[41] N. Perchiazzi, N. Demitri, B. Fehér, P. Vignola, *Can Mineral (6)*, *55*, 1027ff, (2017).
[42] M. A. Hartig, N. Jacobsen, W. Peukert, *Chemical Engineering Science*, *109*, 158ff, (2014).
[43] M. A. J. Hartig, W. Peukert, N. Jacobsen, A. Leuthold, *AIChE J. (7)*, *61*, 2104ff, (2015).
[44] M. Haderlein, A. Güldenpfennig, D. Segets, W. Peukert, *Computers & Chemical Engineering*, *98*, 197ff, (2017).
[45] A. S. Myerson, *Handbook of industrial crystallization*, 2nd edn, (2002).
[46] J.W. Mullin, *Crystallization*, 4th edn, (2001).
[47] J. Manuel García-Ruiz, *Journal of structural biology (1)*, *142*, 22ff, (2003).
[48] W. Beckmann, *Crystallization: Basic concepts and industrial applications,* (2013).
[49] T. L. Threlfall, R. W. De’Ath, S. J. Coles, *Org. Process Res. Dev. (3)*, *17*, 578ff, (2013).
[50] T. L. Threlfall, S. J. Coles, *CrystEngComm (3)*, *18*, 369ff, (2016).
[51] M. Barros Groß, M. Kind, Crystal Growth & Design (6), 17, 3491ff, (2017).
[52] F.M.M. Morel, J. G. Hering, *Principles and applications of aquatic chemistry*, (1993).
[53] A. H. Truesdell, B. F. Jones, *Journal of Research of the U.S. Geological Survey (2)*, *2*, 233ff, (1974).
[54] K. S. Pitzer, G. Mayorga, *J. Phys. Chem. (19)*, *77*, 2300ff, (1973).
[55] K. S. Pitzer, G. Mayorga, *J Solution Chem (7)*, *3*, 539ff, (1974).
[56] A. Lassin, C. Christov, L. Andre, M. Azaroual, *American Journal of Science (3)*, *315*, 204ff, (2015).
[57] K. J. Powell, P. L. Brown, R. H. Byrne, T. Gajda, G. Hefter, S. Sjöberg, H. Wanner, *Pure and Applied Chemistry (5)*, *79*, 895ff, (2007).
[58] A. K. Alwan, J. H. Thomas, P. A. Williams, *Transition Metal Chemistry (1)*, *5*, 3ff, (1980).
[59] W. Preis, H. Gamsjäger, *The Journal of Chemical Thermodynamics (7)*, *33*, 803ff, (2001).
[60] E. Giffaut, M. Grivé, P. Blanc, P. Vieillard, E. Colàs, H. Gailhanou, S. Gaboreau, N. Marty, B. Madé, L. Duro, *Applied Geochemistry*, *49*, 225ff, (2014).
[61] N. Doebelin, R. Kleeberg, *J Appl Crystallogr (Pt 5)*, *48*, 1573ff, (2015).
[62] S. Klokishner, M. Behrens, O. Reu, G. Tzolova-Müller, F. Girgsdies, A. Trunschke, R. Schlögl, *The journal of physical chemistry. A (35)*, *115*, 9954ff, (2011).
[63] S. Zander, B. Seidlhofer, M. Behrens, *Dalton transactions (43)*, *41*, 13413ff, (2012).
[64] S. A. Kondrat, P. J. Smith, P. P. Wells, P. A. Chater, J. H. Carter, D. J. Morgan, E. M. Fiordaliso, J. B. Wagner, T. E. Davies, L. Lu, J. K. Bartley, S. H. Taylor, M. S. Spencer, C. J. Kiely, G. J. Kelly, C. W. Park, M. J. Rosseinsky, G. J. Hutchings, *Nature (7592)*, *531*, 83ff, (2016).
[65] D. Stoilova, V. Koleva, V. Vassileva, *Spectrochimica Acta Part A: Molecular and Biomolecular Spectroscopy (9)*, *58*, 2051ff, (2002).

Advanced Recycling in the Petrochemical Industry

A. Goehrt
INEOS Manufacturing Deutschland GmbH (INEOS in Köln)

Abstract

INEOS is a global manufacturing company making raw materials and energy used for everyday life. Its products make indispensable contributions to society by providing the most sustainable options for many societal needs. INEOS is driving the transition to a net zero economy by 2050. As part of its greenhouse gas emission reduction strategy, it aims to move to a more circular economy, re-using materials to their maximum extent. INEOS operates 36 individual business units and 194 sites across 29 countries with huge variety of products relating to and used in oil & gas, chemicals and polymers. It generates $61 billion annually and employs over 26,000 people. We are committed to delivering a circular plastics economy in which products are re-used and recycled to the maximum level, and no plastic waste is disposed to the environment. Our strategy: **Advanced Recycling (Chemical Recycling)**

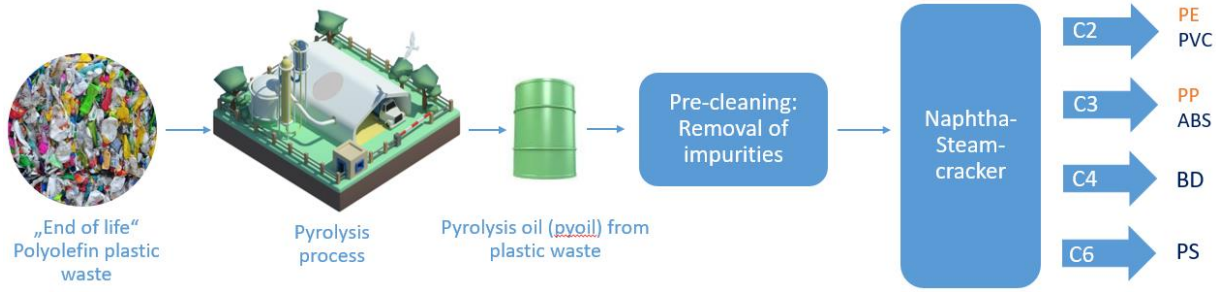

Pyrolysis of Mixed Plastic Waste

In this method, mixed plastic waste is converted to an oil via a thermal cracking process. The resulting oil is further purified and processed, then used as feedstock in steam crackers to produce the base molecules (ethylene, propylene, butadiene, benzene) for polymer production. This recycling method is developing rapidly and INEOS is at its forefront. The advantage is that it can process a wide range of post-consumer mixed plastic waste that could not otherwise be recycled and would be disposed in landfill or burnt. We recently demonstrated the technology at commercial scale by feeding oils derived from mixed plastic waste to our large olefin unit in Cologne. The process and resulting products have been certified by an independent accreditation body. Our intention is to build now several new pyrolysis recycling plants in partnership with the technology developer Plastic Energy.

Investigating the Opposing Catalyst Compositions Required for Gas and Liquid Phase Selective Alkyne Hydrogenation

J. Williams[1], K. Kley[2], N. Dummer[1], F. Schüth[2], G. Hutchings[1]
[1] Max Planck–Cardiff Centre on the Fundamentals of Heterogeneous Catalysis FUNCAT, Cardiff Catalysis Institute, School of Chemistry, Cardiff University, Cardiff, UK
[2] Max-Planck-Institut für Kohlenforschung, Mülheim an der Ruhr

Abstract

Selective alkyne hydrogenation is an industrially important reaction typically used to remove alkynes in monomeric alkene streams. Alkynes are known to poison the catalysts used to polymerise the alkenes. Therefore, the gas stream is passed over, primarily, palladium-based catalysts beforehand to lower the alkyne concentration to below 10 ppm. Ideally this can be achieved without converting the alkene to the alkane and without producing oligomers known as green oil in the case of acetylene removal in ethylene feeds.

Selective hydrogenation reactions of acetylene and phenylacetylene have been undertaken using catalysts comprising of palladium-silver nanoparticles supported on various metal oxides. Using both a combination of palladium and silver affords a balance of the high selectivity of silver and the high activity of palladium resulting in a more efficient catalyst. This synergy is seen with other bimetallic catalysts across a range of applications. The catalysts in this work were prepared by sol immobilisation, where the dissolved metal salts were reduced in situ with sodium borohydride whilst being stabilised by a polymeric agent. It is known that this method produces small, uniform nanoparticles, which has been shown in the field to give better selectivity and hence a better catalyst. We found that selective hydrogenation of gas-phase acetylene and liquid-phase phenylacetylene required opposite catalyst compositions. That is low Pd content for acetylene hydrogenation and high Pd content for phenylacetylene hydrogenation. We will be presenting EM images, XPS and TPR as well as the catalytic reaction data to rationalise our observations.

Opportunities and Challenges in Industrial Selective Oxidation Processes

K. Amakawa
BASF SE, Ludwigshafen, Germany

Abstract

Selective oxidation processes belong to the energy-intensive chemical segment with large product volume accompanied by significant CO_2 emissions. The CO_2 emission of a product comprises direct emissions during the production (Scope 1 emission), indirect emissions from the generation of energy (Scope 2 emission) and CO_2 footprints of raw materials (Scope 3 upstream emission). Options for reduction of CO_2 emissions include (1) efficiency measures and process innovations to reduce consumption of raw material and energy, (2) use of green electricity and process electrification, (3) use of low carbon feedstock, (4) carbon capture use and storage. All the options are of relevance to reach the zero-emission target. The options exhibit a broad spectrum of technological and economic feasibility. This contribution discusses some examples how industrial catalytic oxidation processes tackle the challenge to reduce CO_2 emission. As a unique opportunity for the oxidation processes in mid- to long-term future, enhanced utilization of by-product oxygen from green water electrolysis for hydrogen production in today's air oxidation technologies (*oxygenization*) is highlighted.

1. Introduction

This contribution discusses some examples how industrial catalytic oxidation processes tackle the challenge to reduce CO_2 emission.

First, we examine the position of the catalytic oxidation processes as well as the chemical sector in the entire human activity in terms of the energy transition challenge.

1.1. CO_2 emission of chemical sector

Chemical products are ubiquitous in modern society. The chemical sector is the largest industrial energy consumer and the third largest emitter of carbon dioxide behind cement and steel industries,[1] accounting for 11 % of final energy consumption and 4.4 % of CO_2 emission in 2019 (**Table 1**). Among the chemical sector, the primary chemicals comprising ammonia, methanol, ethylene, propylene and BTX (benzene, toluene, xylenes) account for more than 60% of energy consumption and CO_2 emission (**Table 1**).

Table 1 World energy consumption and CO_2 emission in 2019

Scope	Final energy consumption (TWh)	CO_2 emission (Gt/a)
World total [2]	116,000	34
Chemical sector total [1]	13,350	1.5
Primary chemicals (=ammonia, methanol, ethylene, propylene, BTX)	8,900[1, a]	0.94 [3]
Rest of the chemical sector [b]	4,450	0.56

[a] estimation based on the 2/3 of chemical sector total,[1] [b] difference between chemical sector total and primary chemicals

1.2. Mitigation pathways for chemical sector

Studies on the climate change mitigation have indicated that a set of CO_2 reduction measures are required to reach the zero-emission target within the next decades ─ independent of the assumed scenario details. **Figure 1** presents the CO_2 emission reduction pathways of the chemical sector in a recent study by IEA.[1] The sustainable development scenario (SDS) assumes continuous implementation of various measures including efficiency, electrification, renewable hydrogen, bioenergy and carbon capture use and storage (CCUS). It is not sufficient for the chemical sector to tackle on primary chemicals with the largest volume only. It is responsibility of the chemical industry to address CO_2 emissions of downstream chemical processes with (lower than primary chemicals but still) significant volumes.

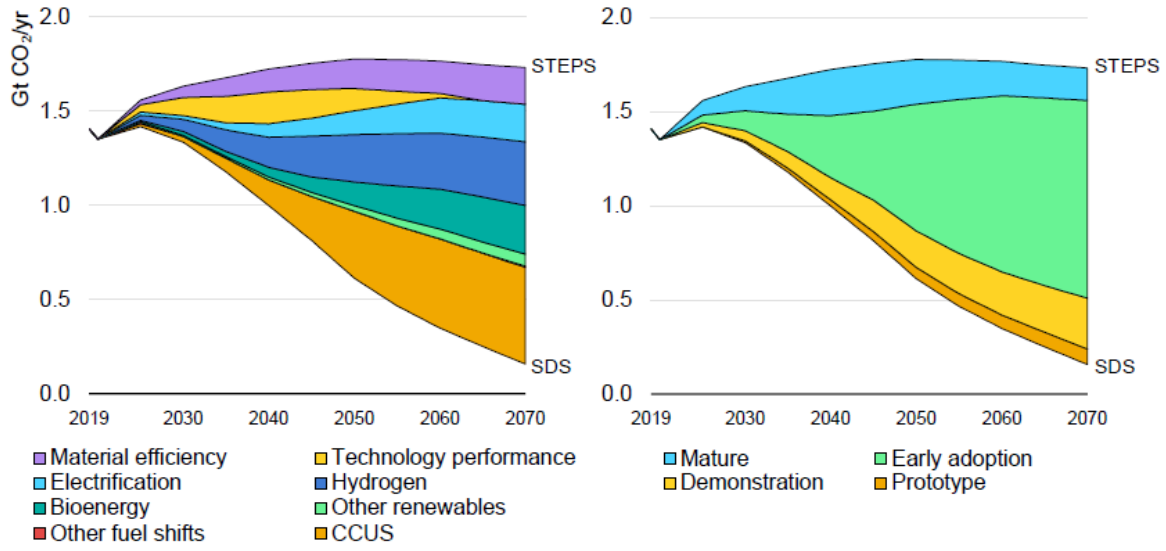

Notes: STEPS = Stated Policies Scenario; SDS = Sustainable Development Scenario. CCUS = carbon capture, utilisation and storage. Electrification here includes only direct electrification, primarily via conventional technologies. See Box 2.6 in Chapter 2 for the definition of the maturity categories: large prototype, demonstration, early adoption and mature.

CCUS and electrolytic hydrogen routes play the largest role in cumulative chemicals sector emissions reductions in the Sustainable Development Scenario. Electrification and the use of bioenergy for low- to medium-temperature process heat play an important role downstream.

Figure 1 Global CO_2 emissions reductions in the chemical sector by mitigation strategy and current technology maturity category, 2019-70. Image source: reprinted from IEA (2020) Energy Technologies Perspectives[1] with permission.

1.3. Selective oxidation processes in chemical sector

Selective oxidation processes are entry steps to the downstream chemicals in many chemical value chains. The selective oxidation segment is characterized by large product volumes and direct CO_2 emission caused by yield loss. **Table 2** lists the capacity, yield, and theoretical CO_2 emission by yield loss of some representative products by oxidation. The sum of the theoretical direct CO_2 emissions by the yield loss in **Table 2** alone (without including energy-related CO_2 emission for the production) gives ca. 40 Mt/a CO_2 emission, accounting for 7% of the CO_2 emission by the non-primary chemicals.

Table 2 Estimation of the CO_2 emission by yield loss in some selective oxidation products [a]

Feedstock	Product	world capacity 2018 [a] (Mt/a)	process yield [a] (mol%)	**CO_2 emission by yield loss** (Mio. t-CO_2/a)
p-xylene	terephthalic acid	80	95	**8.9**
ethylene	ethylene dichloride	25	90	**2.5**
ethylene	ethylene oxide	26	85	**9.2**
methanol	formaldehyde	20	90	**3.3**
propylene	acrylic acid	9	83	**3.4**
propylene	acrylonitrile	7	80	**4.4**
o-xylene	phthalic anhydride	6	80	**3.6**
n-butane	maleic anhydride	3	55	**4.4**
Sum		205		**39.5**

[a] Entire yield loss is assumed to end up with CO_2. The world capacities and process yields are estimation based on publicly available information.

2. Options for reduction of CO_2 emissions

2.1. Structure of CO_2 emissions and mitigation strategies

Figure 2 presents general structure of CO_2 emissions in chemical production processes and mitigation options. The CO_2 emissions comprise direct emissions during the production (Scope 1 emission), indirect emissions from the generation of utility energies such as electricity and steam (Scope 2 emission), and CO_2 footprints of raw materials (Scope 3 upstream emission).

Options for reduction of CO_2 emissions include:

- Efficiency measures to reduce consumption of raw material and energy,
- Process innovations to reduce consumption of raw material and energy,
- Replacement of fossil-electricity to renewable electricity (grey-to-green)
- Electrification of fossil-powered heating (steam and firing) and drives (steam turbine etc.)
- Replacement of fossil feedstock to low carbon feedstock (biomass, recycled chemicals, green hydrogen-based chemicals)
- Carbon capture utilization and storage (CCUS).

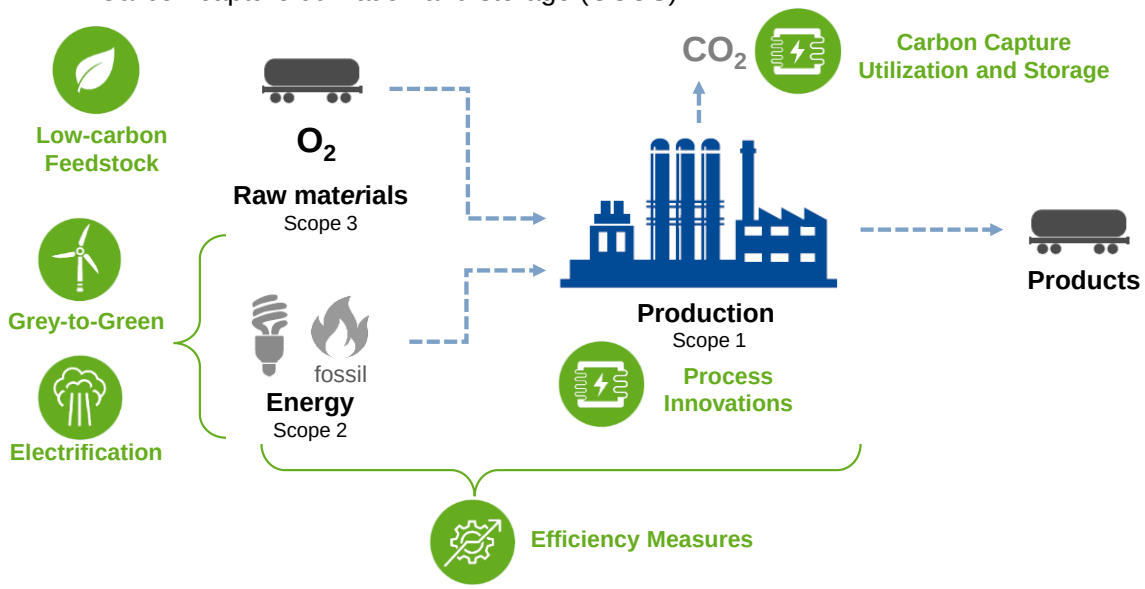

Figure 2 General structure of CO_2 emissions in chemical production processes and mitigation options. Image source: BASF

2.2 Efficiency measures

Reduction of CO_2 emission is an additional driver for efficiency measures that aim to reduce consumption of feedstock and energy.

(1) Yield improvement

Figure 3 illustrates an estimation of the impact of a 1 % reactor yield improvement in acrylic acid production by propylene oxidation on the economic and the CO_2 emission aspects.

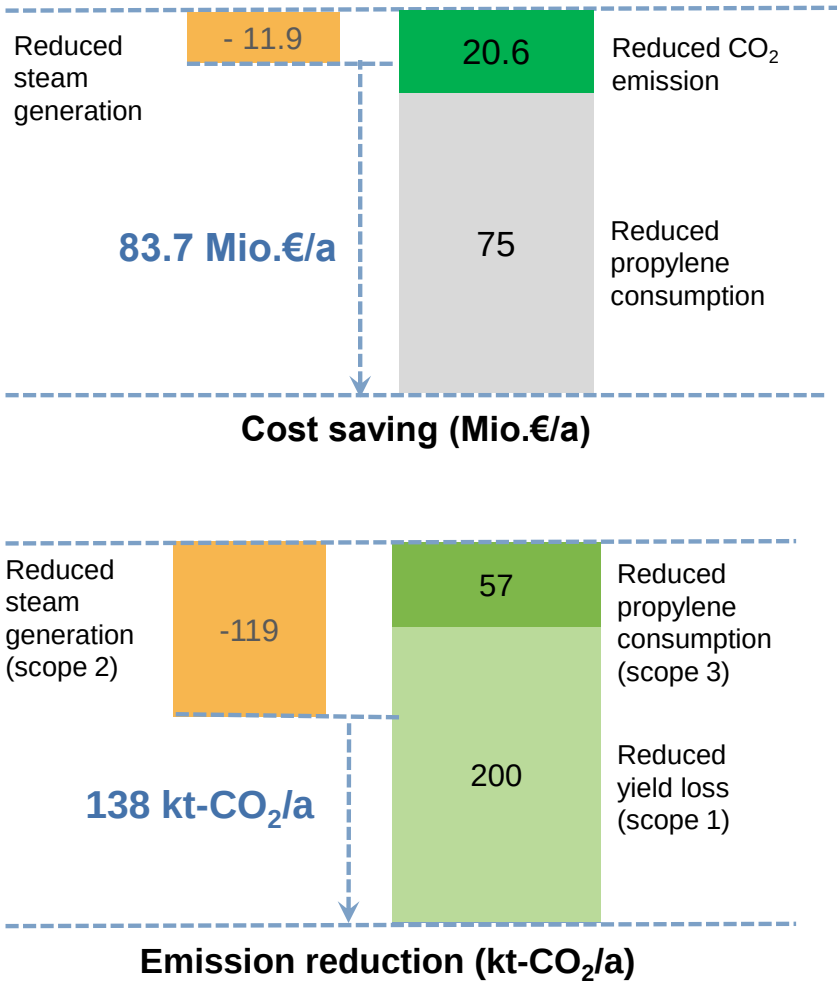

Figure 3 Estimated impact of a 1% reactor yield improvement in acrylic acid production from propylene: cost saving by reduction of propylene consumption and CO_2 emission (upper panel), reduction of CO_2 emission due to reduced yield loss and reduced propylene consumption (lower panel). The estimation is based on the following assumptions: Yield 83 → 84 mol%, production capacity 9 Mio. t/a, entire yield loss ends up with CO_2, propylene price 1000 €/t, CO_2 emission price 80 €/t, carbon footprint of propylene 0.76 t-CO_2/t, carbon footprint of steam 0.15 t-CO_2/t, reduction of the steam generation by the yield gain 0.088 t-steam/t-acrylic acid.

In this assumption, the reactor gives a 1 % higher acrylic acid and 1 % lower CO_2 yield. The saving in the propylene consumption reduces not only the propylene cost, but also the reduction of the indirect CO_2 emission assigned to the production of propylene which is typically done by energy intensive cracking chemistry. The yield improvement results in a reduction the direct CO_2 emission and the associated CO_2 emission cost. The reduction of the yield loss however reduces the steam generation at the reactor due to the reduced heat generation by total combustion to CO_2 in the reactor. This reduced steam amount should be

compensated by a fossil steam generation that partly compensate the benefit in the CO_2 mitigation as well as the cost saving. Despite this partial compensation which is particular for selective oxidation processes with the reaction heat recovery, yield improvements of catalysts and process (where no "steam compensation" occurs) have become even more important with the CO_2 challenge.

(2) Energy saving by pressure drop reduction

Saving electricity energy contributes to reduce CO_2 emission especially when the electricity is generated by fossil resources. The world average carbon intensity for electricity generation was 475 kg CO_2/MWh in 2018.[4] Though the carbon intensity of electricity is expected to decline by increase of the renewable sources in future, the transition would be gradual over next decades.

An energy saving measure concerning heterogeneous catalysts is the reduction of reactor pressure drops by optimizing catalyst shapes. The pressure drop reduction decreases the energy consumption of gas compressors. There has been continuous development of catalyst shapes in the field of gas phase selective oxidation reactions since last decades (**Figure 4**). Optimization efforts are still ongoing to find optimum reconciling of the conflicting performance criteria including the pressure drop, catalyst mass density upon reactor filling, mass transport properties that impacts catalyst activity and selectivity, mechanical stability, and ease of shaping relevant for the cost and scalability.

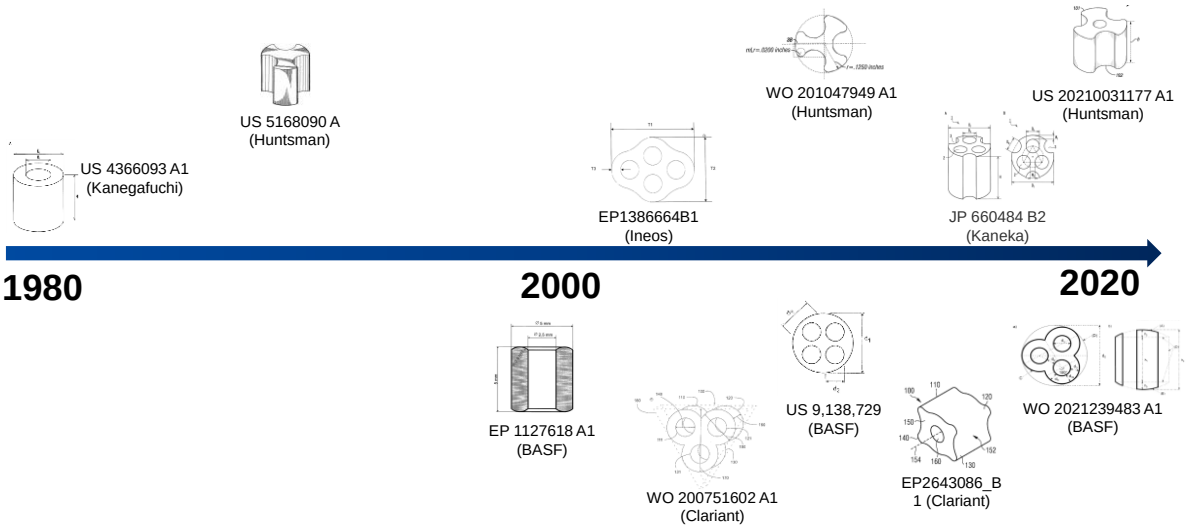

Figure 4 Shapes of catalysts for gas-phase oxidation reactions found in patent literature. Image source: BASF with use of public patent documents

2.2 Electrification with renewable electricity

Electricity, steam, and cooling water are ubiquitous utilities in chemical industry. Large chemical complexes ("Verbund" in German) are often equipped with gas-powered cogeneration systems to supply electricity and steam because of its high energy efficiencies. The use of electricity in Verbund ranges from driving motors of pumps and, heating and cooling, and electrochemistry represented by chlorine production. Steam is the standard heating medium and to some extent driver for pump and compressors. The heat generated in oxidation reactors with high temperatures (>200°C) can be readily recovered as steam for utilization within the site (Verbund). In contrast, heat with low temperature has narrower possibilities for use and often wasted in environment.

Utilization of renewable electricity is the ultimate lever for decarbonization of energy supply in chemical processes (**Figure 5).** Most renewable energies are generated as electricity. Direct use of (green) electricity is preferred for the efficiency reason over renewable fuels derived from renewable electricity via Power to X strategies that involve large energy loss.[5] Hence, electrification of gas-based energy instruments is of crucial importance. Steam generation by electricity (E-boilers), heat pumps especially for upgrading low temperature heat, replacement of steam-driven turbines to modern energy-efficient electrical drives represent important measures.

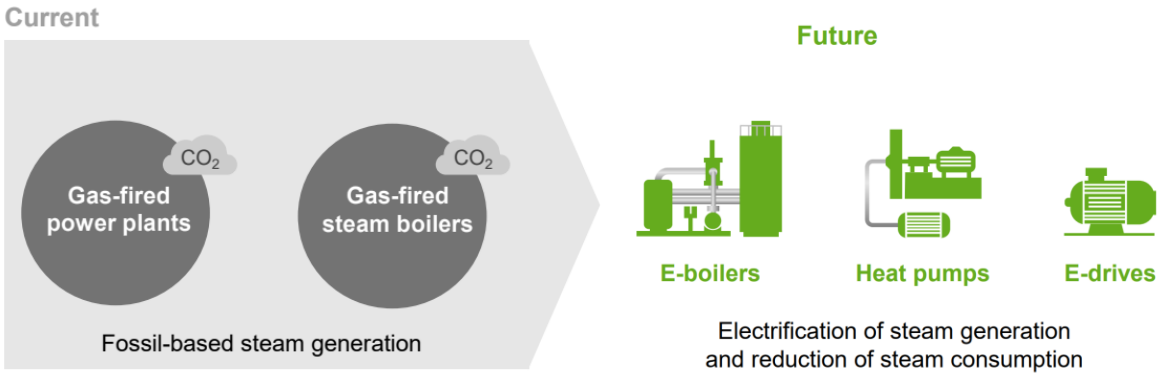

Figure 5 Suggested strategy of energy transition in chemical industry. Image source: BASF

2.3 *Oxygenization*: use of by-product oxygen from green water electrolysis

Hydrogen generation by water electrolysis powered by renewable electricity is considered an indispensable element for low-emission chemical industry, though its major implementation would be not in near future but gradual over a few decades. While the demand of hydrogen is large as it may ultimately replace today's hydrogen production by steam- and autothermal-reforming of natural gas for ammonia and methanol, utilization of the huge amount of co-produced oxygen (8 ton per 1 ton hydrogen) have attracted little attention. By-product oxygen is often assumed in literature as valueless being wasted in the atmosphere.

Integration of water electrolysis in a Verbund dealing with oxidation reactions offers the opportunity to utilize by-product oxygen (**Figure 6**). Some selective oxidation processes including the production of ethylene oxide, autothermal methane reforming, vinyl acetate and acetaldehyde use pure oxygen from cryogenic air separation that costs electricity with carbon footprint. The oxygen source of these processes can be replaced by the by-product "green" oxygen.

Moreover, large volume of cheap by-product oxygen could motivate air oxidation processes to use pure oxygen instead of air, which may be called *oxygenization*. The use of pure oxygen in chemical processes (e.g., terephthalic acid (PTA), KA-oil by cyclohexane oxidation, cumene hydroperoxide), combustion processes (Oxy-fuel), and in wastewater treatment can be

advantageous in consumption of raw materials and in energy efficiency.[6] Furthermore, flue gas streams from oxygenized processes will be rich in carbon with significant less volume compared to the situation using air, thus more suitable for carbon (CO_2) capture for use or storage.

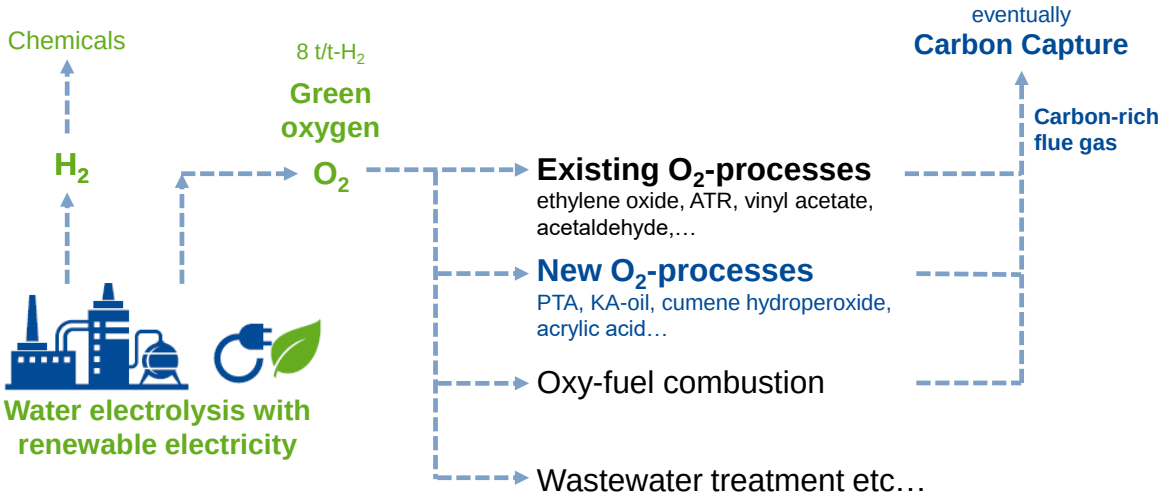

Figure 6 Proposed ox*ygenization* concept utilizing oxygen occurring as by-product of hydrogen production by water electrolysis with renewable energy. Image source: BASF

BASF has recently developed an oxygenization concept for the acrylic acid production from propylene by two-step catalytic oxidation (**Figure 7**).[7] The standard air oxidation process is accompanied by a significant yield loss through the purge of unreacted propylene. Replacing air to oxygen reduced the volumetric flow of the purge significantly while maintaining the propylene concentration in the purge gas (meaning that the single pass propylene conversion over the catalytic reactor is unchanged), reducing the loss of the unreacted propylene down to negligible levels that in turn increases the acrylic acid yield. The replacement from air to oxygen could be done on existing plants as no essential process flow change in the reactor section is involved. The purge gas contains large concentrations of CO_x (from reaction) and propane (originated from impurity in propylene feedstock, accumulated by recycling due to its inertness) with some heat value, that could be used as feedstock for reformer for syngas production.

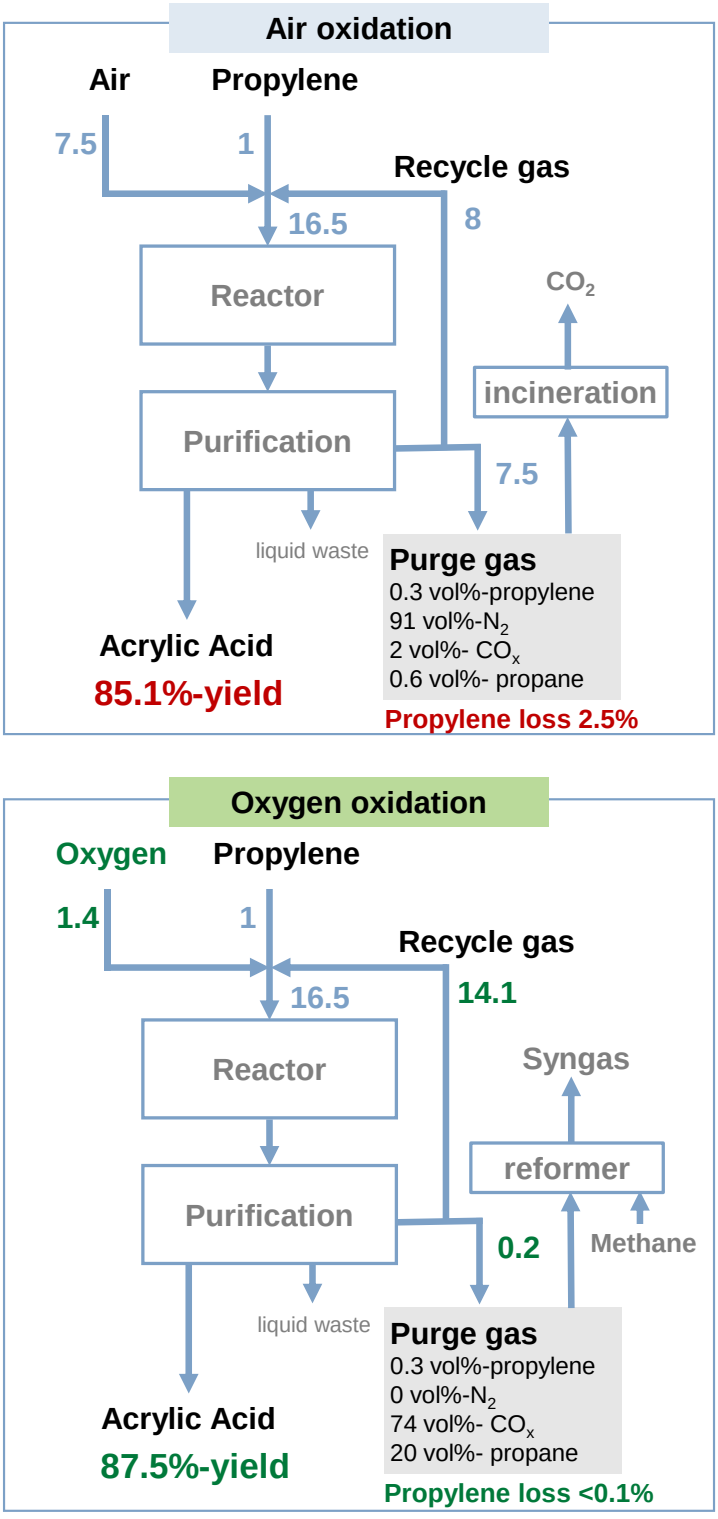

Figure 7 Process scheme and mass balance of acrylic acid production from propylene by standard process using air as oxidant with purge gas treatment by incineration (upper panel), and proposed process using oxygen as oxidant with purge gas export to reformer as feedstock for syngas (lower panel).[7] Image source: BASF

2.4 Low carbon feedstock

Low carbon feedstocks include biomass, recycled waste plastic, and primary chemicals obtained from low carbon hydrogen generated by renewable energy.

Among these options, bioethanol is to date one of the most prominent low carbon feedstocks due to its high availability (**Figure 8**). Production of ethylene and propylene from ethanol is possible by existing technologies. The current production volume of bioethanol appears large enough for ex-bioethanol C2-C3 olefin feedstocks to take part in selective oxidation processes (refer **Table 2**).

Table 3 compares carbon footprints of ethylene and propylene produced by fossil and bioethanol. [8] The ex-bioethanol olefins exhibit negative carbon footprints due to the sequestered biogenic carbon that overcompensating the energy demand necessary for the bioethanol production and the upgrading of ethanol to olefin. Production of C2 and C3 value chains oxidation products (e.g., ethylene oxide, vinyl chloride, acrylonitrile, acrylic acid) with low carbon ex-bioethanol olefins is possible from availability and technology aspects.

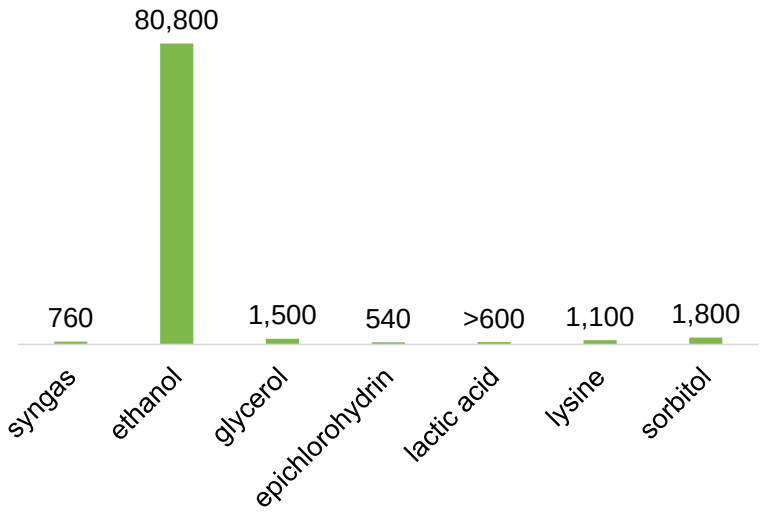

Figure 8 Global bio-based production capacity (kt/a) of products with a capacity higher than 500 kt/a. Data source: reference [9] Image source: BASF

Table 3 Estimation of carbon footprint of ethylene and propylene produced by fossil and bioethanol-based routes. Data source: reference [9]

Product	Carbon footprint (t-CO_2/t-product)		
	ex-fossil	ex -bioethanol	difference
Ethylene	1.15	-1.9	3.05
Propylene	0.76	-0.44 [a]	1.2

[a] via ethylene dimerization to n-butene and subsequent cross metathesis

3. Summary and conclusion

This contribution discusses some examples how industrial catalytic oxidation processes tackle the challenge to reduce CO_2 emissions. Mitigation of the CO_2 emission requires a broad technology portfolio (**Figure 9).** The wide range of options can provide large potential but demands from us the challenging task to identify a right mix of measures. This task is not easy because it is highly dependent on technical, geographic, social, and political circumstances that are partly dynamic and uncertain along the time scale of the challenge. Nevertheless, having a set of strategies with an overview of available options (as exemplified in Figure 9) can provide a starting point for the challenge.

As a unique opportunity for the oxidation processes in mid- to long-term future, enhanced utilization of by-product oxygen from green water electrolysis for hydrogen production in today's air oxidation technologies (*oxygenization*) is highlighted.

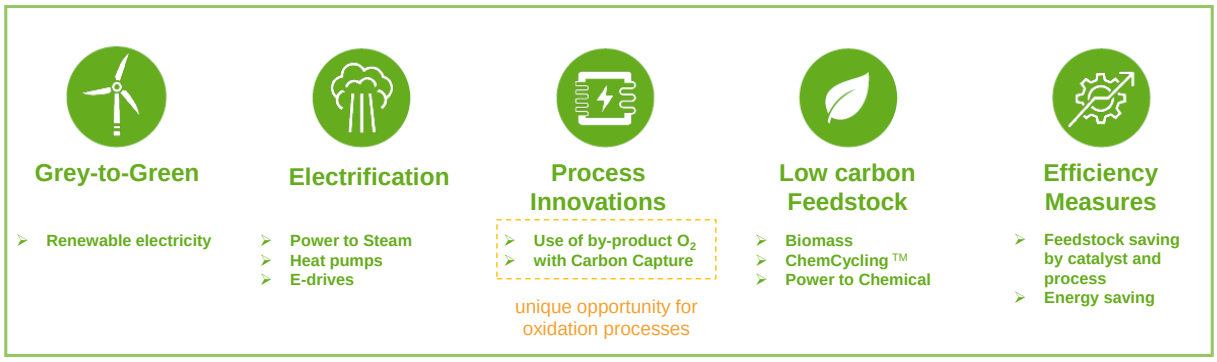

Figure 9 Strategies to reduce CO_2 emission in selective oxidation processes. Image source: BASF

References

[1] International Energy Agency, *Energy Technologies Perspectives* (2020)
[2] International Energy Agency, *Energy Statistics Data Browser*, Paris, https://www.iea.org/data-and-statistics/data-tools/energy-statistics-data-browser (2022)
[3] International Energy Agency, *Chemicals*, Paris https://www.iea.org/reports/chemicals (2021)
[4] International Energy Agency, *Global Energy & CO_2 Status Report 2019* https://www.iea.org/reports/global-energy-co2-status-report-2019 (2019)
[5] F. Ueckerdt, C. Bauer, A. Dirnaichner et al. *Nat. Clim. Chang.,* 11, 384 (2021)
[6] H.J. Reinhardt, H.D. Obermeyer, B. Schreiner, S. Wolf (Air Liquid), *Oxygen enrichment for intensification of air oxidation reactions*, ISBN 978-3-00-051546-0 (2015)
[7] K. Amakawa, L. Schulz, M. Bender, K.J. Müller-Engel, C. Walsdorff (BASF), WO202113640A1 (2021)
[8] DECHEMA, Technology Study*: Low carbon energy and feedstock for the European chemical industry* (2017)
[9] International Energy Agency Bioenergy, *Bio-Based Chemicals - A 2020 Update* (2020)

Production of Sustainable Transportation Fuels and Chemicals via Catalytic Cracking

L. Dorazio[1], J. Shi[1], J. Fu[1], CP Kelkar[1], M. J. Castaldi[2], S. S. Ail[2], G. Chowdhury[2]
[1] BASF Corporation, 25 Middlesex Essex Turnpike, Iselin, NJ, USA
[2] The City College of New York, 140th Street Convent Ave, New York City, NY, USA

Abstract

The refining industry has played a vital role supplying much of the world's transportation fuels and commodity chemicals, yet new regulations are forcing them to transition to more sustainable processes. The transition will require fossil-based feedstocks be partially or entirely replaced with more sustainable feedstocks derived from renewable & recycled materials. Compared to conventional fossil-based feedstocks, these materials will present new challenges such as additional metal and mineral components and differences in feedstock chemistry. Catalytic cracking has proven to be a cost effective, flexible process for the conversion of crude oil into transportation fuels and chemicals for more than 80 years. The ability of catalytic cracking to manage metal contaminants and tolerate a wide variety of feedstocks will likely prove to be valuable again.

One challenge refiners will face is choosing from a wide variety of distinctive feedstocks prepared using different processes. Those variations will yield oils with diverse properties that will ultimately influence their upgradability. In this work, we have conducted a broad survey of potential feedstocks spanning vegetable oils, plastic pyrolysis oils, and oils derived from biogenic wastes that were produced from commercial scale processes and a model laboratory process. Each oil was characterized using a several techniques to gain a deeper understanding of its chemistry and the implications on upgrading to final products. The catalytic cracking performance was assessed using lab-scale ACE® units with different commercial FCC catalyst technologies.

In this presentation, we will discuss the broad spectrum of upgradability associated with different feedstocks and catalyst technologies. On one end of the upgradability spectrum will be pyrolysis oils derived from recycled polyethylene and polypropylene where random scission of these polymers during pyrolysis results in a broad distribution of hydrocarbons that will be well behaved during catalytic cracking. The findings to date indicate that catalytic cracking of these oils is clearly suitable, yet how to most optimally apply it in the conversion to final products needs to be understood. On the other end of the spectrum will be oils produced from the pyrolysis of biogenic wastes that are significantly more complex and more problematic in any process, not just during catalytic cracking. For these feedstocks, the combination of the high content of oxygen, lack of hydrogen, and nature of the molecules inherent to biomass will tend to result in higher yields of coke and gas. Opportunities and challenges for catalyst design for all feedstocks will also be discussed.

Introduction

Historically, transportation fuels and the chemical value chain have been based on fossil carbon derived from the refining of crude oil. However, this linear manufacturing process results in much of the fossil carbon extracted from the ground being converted to atmospheric carbon contributing to climate change. It is recognized that this linear approach should be replaced with more sustainable processes where the fossil carbon is either recycled or replaced with renewable carbon. Synthesis of chemicals from waste materials such as plastics, tires, or the organic fraction of municipal solid waste will need to become more common to incorporate fossil carbon in a more circular manufacturing process. Greater introduction of renewable carbon into the chemical value chain through renewable feedstocks such as lipid-based oils or those derived from biomass wastes will be needed. Ultimately, it is likely that a combination of the two approaches will be required. From a sustainability perspective, it would be ideal to switch completely to renewable carbon-based fuels and chemicals. Currently, this is not economically feasible and significant technology challenges remain. However, combining carbon recycling with the introduction of renewable carbon, wherever feasible, offers a pathway to increasing the renewable carbon content in the chemical value chain over time.

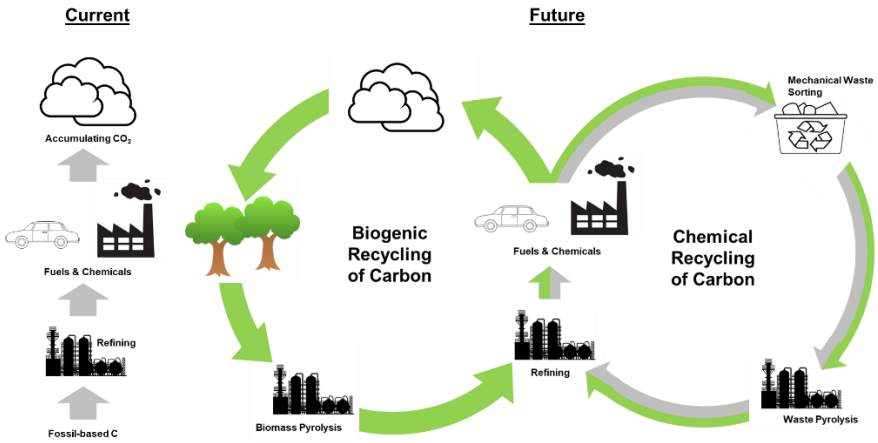

Figure 1: Illustration of linear use of fossil carbon currently compared to a more circular use of fossil and renewable carbon in the future.

Whichever approach is pursued, using existing refining technologies and assets would be preferred to accelerate implementation and reduce the CO_2 footprint associated with added infrastructure. The existing refinery process that is most suitable will vary between applications for a variety of reasons, one of which being the diversity of these new feedstocks and the varying challenges associated with each. Refiners will have the task of choosing from a broad selection of different recyclable or renewable feedstocks, requiring the need to weigh the potential economic benefits against the challenges that each will present. Some feedstocks will be easier to upgrade than others. On one end of the spectrum will be oils derived from mixed polyolefin wastes that are well behaved in all existing refining processes. However, the issue with these fossil carbon-derived oils is that chemical recycling is not fully circular. Production of gas phase hydrocarbons during the depolymerization of plastic to produce pyrolysis oil, the production of additional gaseous hydrocarbons during the upgrading of this oil, and even the transportation fuel by-products will all contribute to an increase in atmospheric carbon. On the other end of the spectrum of sustainable feedstocks will be oils derived from biomass wastes such as forest and agricultural residues that will be challenging to upgrade using any traditional refining process. However, the advantage these materials offer is carbon neutrality since the CO_2 yielded from the conversion process, and even as the result of the combustion of fuels derived from these oils, will not add to the inventory of atmospheric carbon. Refiners and chemical manufacturers will need to weigh the advantages and disadvantages of different feedstocks processed through different existing processes as they find their optimal

path towards more sustainable manufacturing.

For over 80 years, catalytic cracking has been used to convert low-value heavy fractions of crude oil into higher-value transportation fuels and chemical feedstock. For upgrading challenging sustainable feedstocks, the flexibility and low cost of catalytic cracking may again offer advantages. Catalysts used for catalytic cracking involve a system of active components where an acidic mesoporous silica-alumina, for primary cracking of large hydrocarbons, is combined with the strongly acidic Zeolite Y for secondary cracking to yield transportation fuels and chemical feedstock. To increase the yield of light olefins, the catalyst formulation can also include secondary zeolite frameworks such as ZSM5 and Zeolite Beta. Due to the contaminant metals commonly found in conventional crude oils, significant experience already exists to incorporate reactive adsorbents into the catalyst design for metals passivation and trapping that could be applied to managing metals contained in renewable and recycled feedstocks.

Catalytic cracking of heavy hydrocarbons involves the rejection of carbon as coke accumulating on the catalyst and resulting in nearly immediate deactivation. As a result, the refinery process for catalytic cracking has been engineered around a short contact time fluidized catalytic cracking (FCC) reaction combined with continuous catalyst regeneration where the catalyst constantly circulates between the tubular riser reactor and a fluidized bed regenerator. Additionally, to manage irreversible hydrothermal catalyst deactivation and accumulation of metals from the gasoil, the modern FCC process is designed around the daily withdrawal of aged catalyst (Equilibrium Catalyst, ECat) that is replaced with the fresh catalyst to maintain constant activity and desired yields. It is this combination of flexible catalyst design, continuous regeneration, and routine catalyst replacement that could make the present-day FCC process perfect for the processing of problematic renewable and recyclable feedstocks that are not suitable for other refinery processes.

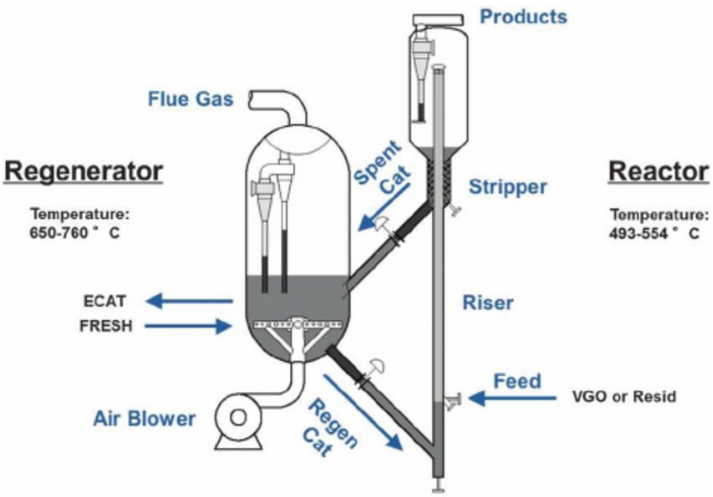

Figure 2: Process flow illustration of the modern FCC process

BASF is committed to supporting refiners in achieving their sustainability targets as they explore their options for incorporating renewable and recycled feedstocks into their processes. The feedstock that is most economically viable will vary from refinery to refinery based on several factors such as local environmental policies, accessibility to different feedstocks, and the availability of different processes within a particular refinery. We have embarked on a program of exploring an ever-expanding collection of feedstocks to understand their chemistry, the implications it has on the operation of the FCC unit, and how the catalysts can be designed to address the new challenges.

The potential sources of renewable and recycled feedstocks are numerous; yet they should not be thought of as discrete unrelated materials. While the source can be quite varied, what

ultimately dictates the outcome of catalytic cracking is the chemistry of the oil, which can be defined by (1) the nature of the organic molecules comprising the oil, (2) the quantity and chemistry of heteroatoms incorporated into these molecules, and (3) the quantity and chemistry of contaminant minerals and metals contained in the oil. It is possible to group the various sources of sustainable feedstocks into categories of similar chemistry, which can be used to draw connections and make predictions about how various materials will behave. We discuss how the nature of various recycled and renewable materials influences the chemistry of the resulting feed oil and the impact this chemistry will have on the upgradability of the oil using catalytic cracking. Furthermore, we highlight how we can use this information to gain insights about other materials without necessarily needing to experimentally evaluate them.

Chemistry of Sustainable Feedstocks

Renewable and recycled feedstocks can be derived from any organic-based waste. The feedstock that is most commercially viable is a complex topic varying by geographic location and even from one refiner to the other within a given geographic location. The technical viability of different starting materials is perhaps a more straightforward question since it's ultimately dictated by chemistry. As a first comparison of different materials, the ultimate analysis of different feedstocks provides valuable insights into the ease at which a particular material can be upgraded to fuels and chemicals. All potential materials will be comprised of an organic fraction containing carbon, hydrogen, possibly heteroatoms, and usually, an inorganic fraction collectively called ash. To produce fuels and chemicals, carbon and hydrogen are the most important. The heteroatoms and ash can be expressed as the cost of working with renewable and recycled materials. In biogenic wastes and oils, the ash represents the minerals and metals incorporated into the structure of the plant. For plastics, the ash can be the performance additives within the plastic or contaminants not removed during mechanical sorting processes. The higher the ash fraction, the more metals are likely to be carried over, as the solid waste feedstock is converted into the produced oil.

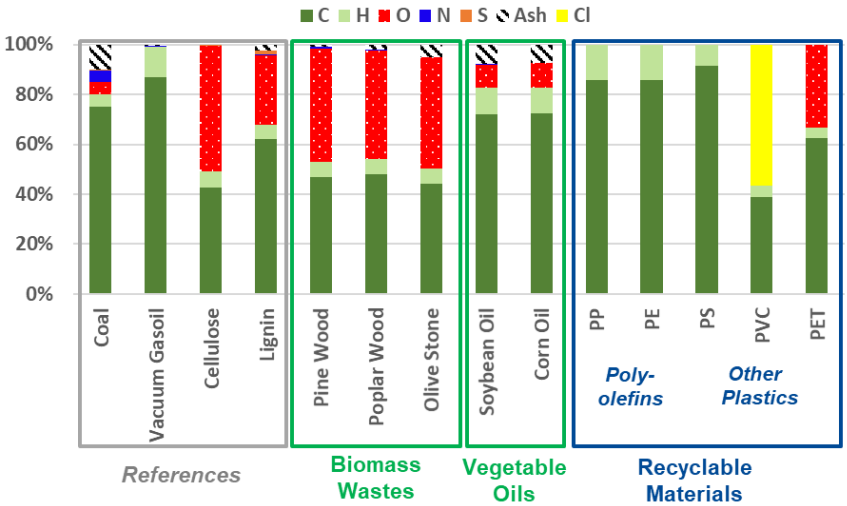

Figure 3: Ultimate analysis of select sources of renewable and recycled wastes compared to relevant reference materials

The relative amount of hydrogen to carbon ratio provides insight into how easily a particular source can be upgraded into fuels and chemicals. Transportation fuels have a hydrogen to carbon ratio of approximately 2.0. The lower the hydrogen to carbon ratio is below 2.0, the more external hydrogen must be added or the more carbon that must be rejected to produce transportation fuels. The presence of heteroatoms will reduce the effective hydrogen content as hydrogen will likely be consumed as the heteroatoms are removed during the conversion

to oil or as the oil is further upgraded to fuels and chemicals. For example, oxygen can undergo dehydration to water, consuming two hydrogen atoms and nitrogen can form ammonia by consuming three hydrogen atoms. Nearly three decades ago, Chen *et al.* [1] introduced using the effective hydrocarbon content using the equation below to characterize upgradability and suggested a threshold for effective hydrogen to carbon of 1.0 be satisfied for further upgrading. Below this threshold, upgrading to fuels becomes increasingly more challenging. More recently, many others have applied this parameter to characterize the suitability of different renewable feedstocks for producing fuels [2-3].

$$\left[\frac{H}{C}\right]_{eff} = \frac{H - 2O - 3N - 2S - 1Cl}{C}$$

Hydrogen rich polyolefins have an effective hydrogen to carbon of 2.0 making these materials more easily upgradable. Vegetable oils contain oxygen (~12% O) in the glycerol backbone of the triglyceride but otherwise are rich in hydrogen along the fatty acid hydrocarbon chain yielding an overall effective hydrogen to carbon ratio of ~1.6 depending on the specific oil being considered. Conversely, biomass wastes contain the lowest effective hydrogen content where values are typically less than 0.5. As a result, during pyrolysis and catalytic cracking, significant carbon rejection should occur yielding char and coke respectively. Therefore, these feedstocks must be co-processed with conventional oils that can donate hydrogen to improve the conversion of the renewable carbon into fuels and chemicals.

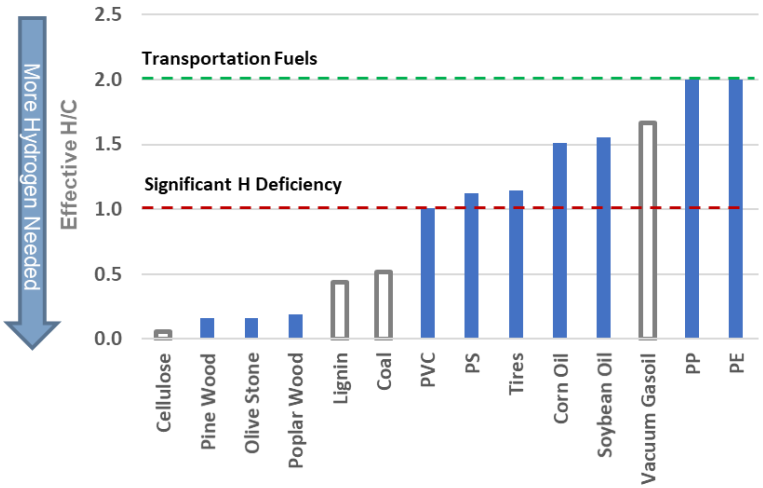

Figure 4: Effective Hydrogen to Carbon for various renewable and recycled wastes compared to relevant reference materials

Commensurate with the ultimate content of carbon, hydrogen, and heteroatoms is how these atoms are structured in the molecules that form when the waste is converted into an oil. The chemistry of the oil will dictate its behavior during catalytic cracking and what products are produced. The impact that varying chemistry of conventional oils has on the products produced during catalytic cracking has long been known and well documented in the literature. The impact of differences in feedstock chemistry will be particularly important for upgrading renewable and recycled oils since the variations in chemistry will be even more significant. Of particular interest will be the tendency of the oil to yield coke, which will divert carbon from valuable products, could disrupt the autothermal operation of the FCC unit, and in general is an indicator of the oil chemistry. To gain insight into the tendency of the feedstock to form coke we can measure the Conradson Carbon Residue (Concarbon) content. Concarbon is determined using the ASTM D4530 laboratory method that measures the amount of carbonaceous residue remaining after the pyrolysis and evaporation of an oil. This test has a long history in the refining industry to characterize different conventional feedstocks where

higher concarbon is an indication of a feedstock that will be more difficult to crack. Conventional FCC feedstocks are typically classified as either "vacuum gasoil (VGO)" or "vacuum resid (Resid)", where vacuum resid represents the heavier fraction from crude oil distillation. For reference, the concarbon for VGO is typically less than 1% and Resid typically less than 5%. Concarbon content higher than 5% is considered very high and an indicator of a potentially problematic feedstock.

To gain a more complete picture of the upgradability of different feedstocks, we can combine effective hydrogen content with the concarbon content in a single plot using a Van Krevelen diagram. More easily upgradable feedstocks will be those with higher effective hydrogen and lower concarbon content. Higher effective hydrogen to carbon will indicate more hydrogen is available to produce valuable products and fewer heteroatoms are present to consume hydrogen (or potentially carbon in the case of oxygen). Lower concarbon content is an indication that the molecules comprising the oil can be readily cracked and less likely to undergo condensation reactions to yield coke. Figure 5 compares commonly used renewable and recycled oils based on their effective hydrogen and concarbon contents. On one end of the spectrum are plant oils and oils derived from mixed polyolefins which both exist near conventional feedstocks indicating they will be more easily upgradable in existing refinery processes. On the other end of the spectrum are oils derived from biomass pyrolysis that are characterized by low effective hydrogen content and extremely high concarbon content. The concarbon for biomass pyrolysis oils will be several times higher than typical concarbon of conventional Resid. In Figure 5, a large area is noted for oils derived from municipal solid wastes (MSW), which highlights the fact that MSW will be mixture of varying materials that could be rich in hydrogen deficient biomass or cellulosic wastes, or contain more hydrogen rich plastic wastes. Depending on the composition of the MSW, the effective hydrogen and concarbon content could vary significantly. In Figure 5, the MSW derived oil marked "Urban Waste" was evaluated and will be discussed below.

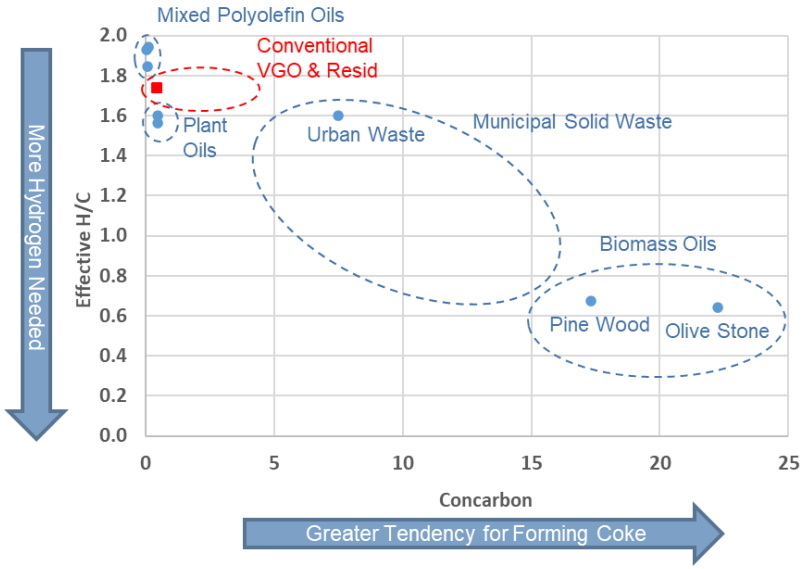

Figure 5: Effective Hydrogen to Carbon versus Concarbon for various pyrolysis oils and plant oils illustrating varying upgradability

Understanding why the characteristics of different feedstocks will vary so significantly requires a closer examination of the molecular makeup of the oils. In addition to the physical and chemical analysis, for each oil, we also performed a more detailed analysis of the hydrocarbons comprising the oil using Agilent 7890B gas chromatograph equipped with the Agilent 5977A mass spectroscopy. For the results described below, the pyrolysis oil were dissolved in cyclohexane solvent in the ratio of 1:100 and the hydrocarbon spectrum were characterized using a slightly polar SHRX5LB column.

Polyolefin Pyrolysis Oils

Polyolefins are a class of polymers derived from simple olefins where polypropylene and polyethylene are the most commercially dominant examples representing roughly 45% of commercial plastic production. Both polyethylene and polypropylene are rich in hydrogen with a hydrogen to carbon content of 2.0. During pyrolysis, the large polyolefin molecules undergo random scission resulting in a broad distribution of hydrocarbons ranging in carbon chain length from C_1 to C_{34} that are similar in structure and behavior to hydrocarbons found in cracked conventional oil (Figure 6). The severity of pyrolysis (residence time and temperature) will dictate the extent of thermal cracking that occurs and the average molecular weight of the products. It is the condensable fraction of hydrocarbons that ultimately becomes the feedstock for further upgrading, while the non-condensable gases are typically burned to generate the heat required for the pyrolysis process. The resulting oil is a mixture of olefinic and paraffinic aliphatic hydrocarbons that will behave similarly to hydrocarbons found in conventional oils (Figure 7). Much of the hydrogen contained in the polyolefin is retained in the products yielding an oil with an effective hydrogen content approaching 2. The molecules themselves will readily crack and the oil is characterized by a very low concarbon content typically below 0.2.

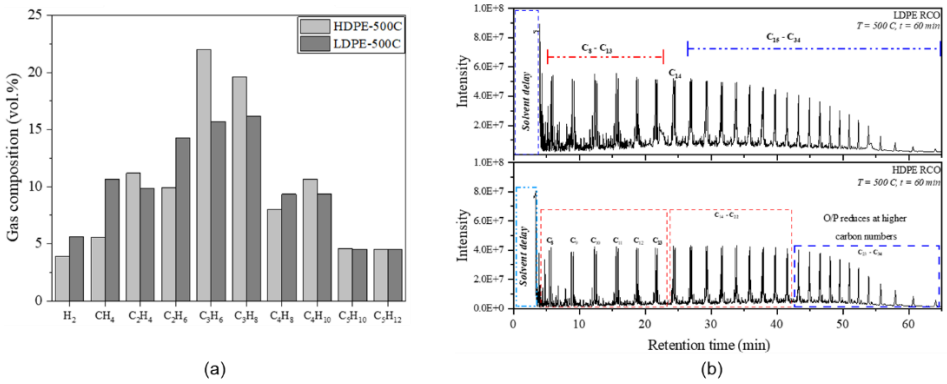

Figure 6: Composition of PE derived pyrolysis products for (a) non-condensable gases measured using gas GC, and (b) condensable products measured using GCMS

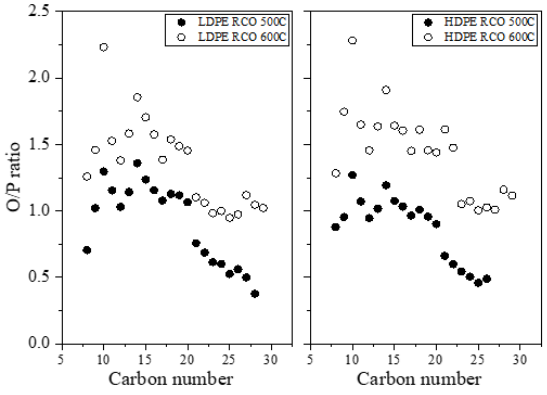

Figure 7: Olefin to Paraffin on a mass-weighted basis for the condensable liquids resulting from LDPE and HDPE pyrolysis

Non-polyolefin Polymer Pyrolysis Oils

Beyond polyolefins, the remaining 55% of commercial plastics are comprised of a variety of polymers where polystyrene (~7% commercial production) and polyethylene terephthalate

(~10% commercial production) are notable examples. Compared to polyolefins, these polymers will be more challenging to chemically recycle due to the combination of the polymer structure and the presence of heteroatoms. For example, the repeating aromatic structure of polystyrene will result in non-random scission within the repeating ethyl group resulting in an oil largely comprised of monoaromatics including mainly styrene, but also toluene, ethylbenzene, and methylbenzene (Figure 8). There will also be smaller concentrations of other mult-ring aromatics such as diphenylpropane and tetrahydro-phenylnaphthalene. During catalytic cracking, the aromatics will be relatively inert and will not crack into smaller fragments. However, Puente *et al.* [4] have shown that oligomerization is possible, ultimately leading to the significant formation of coke. Polyethylene terephthalate undergoes a similar fate during pyrolysis where the benzene ring contained in the polymer structure will remain intact yielding largely benzoic acid [5] resulting in an acidic pyrolysis oil.

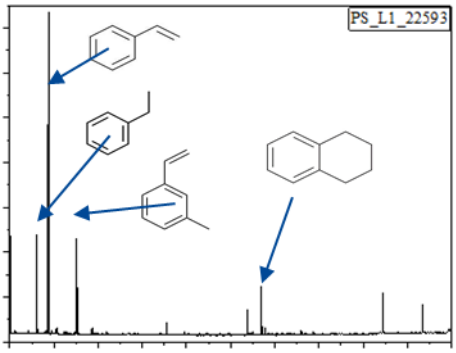

Figure 8: Composition of pyrolysis oil derived from polystyrene as measured using GCMS

Plant Oils

Oils extracted from plants are comprised of a relatively narrow distribution of triglycerides. Triglycerides are comprised of glycerol combined with three fatty acid molecules. Different plant oils will differ in the specific fatty acids incorporated into the glycerol. However, all plant oils are generally comprised of combinations of linoleic ($C_{18}H_{32}O_2$), oleic ($C_{18}H_{34}O_2$), palmitic ($C_{16}H_{32}O_2$), and steric ($C_{18}H_{36}O_2$) acids. There are numerous plant oils being explored as potential feedstocks, but they will all have a similar effective hydrogen content since the fatty acids comprising the triglyceride are all structurally similar. Further, the structure of all possible fatty acids is a similar highly saturated straight chain hydrocarbon. Thus, during catalytic cracking, they will all behave similarly. Given the similar fatty acid structures for varying plant oils, the oxygen content will also be similar (~12wt%). As a result, all plant oils will have an effective hydrogen content of ~1.6. Due to the relatively saturated linear structure of the fatty acids, vegetable oils are also characterized by a concarbon content similar to conventional VGO. The combination of higher hydrogen and low concarbon content should make the upgradability of plant oils similar to conventional oils.

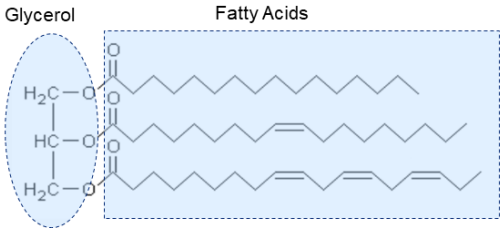

Figure 9: Example of typical structure of triglyceride found in plant oils

Biomass Pyrolysis Oils

Oils derived from biomass wastes will be the most challenging feedstocks to upgrade regardless of what process is applied. Beyond it being hydrogen deficient and rich in oxygen, the molecular structure of biomass is also problematic. While there are many possible sources of biomass wastes, they are all comprised of three basic structural components: cellulose, hemicellulose, and lignin. What will vary between sources of biomass is the relative amounts of each component where the range in the composition is typically 40-50 wt% cellulose, 20-40 wt% hemicellulose, and 10-40 wt% lignin. In general, woody biomass will contain higher lignin content than non-woody biomass such as grasses. The composition of the oil resulting from the pyrolysis of biomass will be the result of the pyrolysis of these three structure components that will yield a molecularly diverse oil containing hundreds of oxygenated compounds. The example shown below is the result of the fast pyrolysis of olive stone, which is an abundant biogenic waste product in Spain originating from olive oil production (oil prepared and provided by Neoliquid).

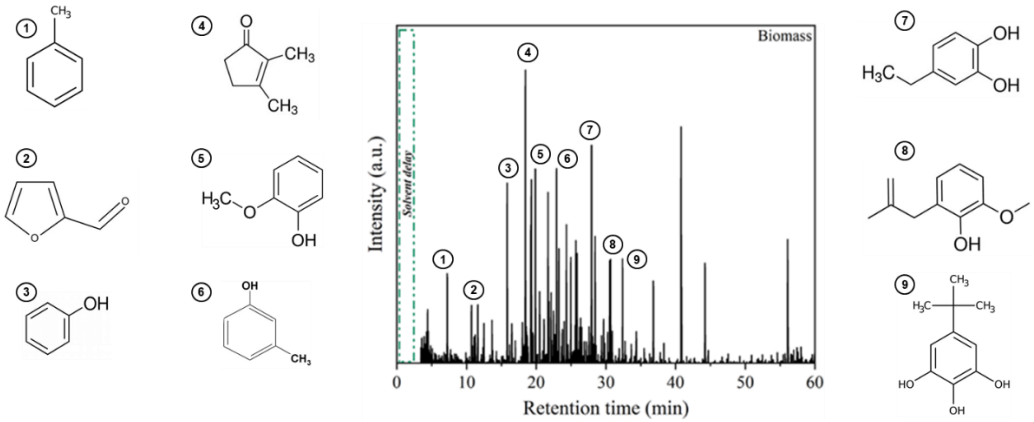

Figure 10: Composition of pyrolysis oil derived from olive processing waste as measured using GCMS

Cellulose and hemicellulose are similar in that both are polysaccharides containing significant oxygen content (~50%), but they differ in their specific structures. Cellulose consists of an organized linear structure of repeating glucose units, while hemicellulose consists of various randomly organized mixtures of sugars consisting of a more amorphous structure. During pyrolysis, cellulose and hemicellulose will yield two classes of oxygenated hydrocarbons: (i) small carbonyl compounds such as acetic acid, acetaldehyde, acetone, and carboxylic acids, and (ii) sugar-derived compounds such as furfural, levoglucosan, and furan/pyran ring compounds [6-7]. The structure of lignin is quite different from cellulose and hemicellulose consisting of a complex organic polymer made by cross-linking phenolic precursors. Therefore, the make-up of lignin is rich in aromatic structures. During pyrolysis, lignin will decompose into a mixture of phenols and guaiacols. In addition to the deconstruction reactions occurring during pyrolysis, deoxygenation reactions leading to CO, CO_2, and H_2O will begin to occur where the extent of deoxygenation will be a function of the pyrolysis conditions. Higher severity pyrolysis will result in a greater extent of deoxygenation, however at the added cost of higher char formation and lower liquid yield.

Regardless of the source, all biomass will be rich in oxygen and yield a diverse mixture of oxygenates. As a result, the effective hydrogen content of the biomass pyrolysis oil will be very low and typically less than 0.5. Additionally, all lignocellulosic biomass will yield a pyrolysis oil rich in aromatic and phenolic structures that will readily undergo condensation to produce coke. As a result, all biomass pyrolysis oils will be characterized by a relatively high concarbon content several times larger than conventional Resid oils. The combination of low hydrogen content and the high tendency to yield coke will make upgrading these oils into fuels

and chemicals challenging using existing refinery processes.

Municipal Solid Waste Pyrolysis Oils

Municipal solid waste (MSW) is not necessary a new category of waste, rather a collection of different materials. MSW can contain a wide variety of different materials that will vary from region to region and even over time within a given region. As collected, MSW will contain a mixture of inorganic materials (glass, metals, minerals) and organic materials (plastics, biomass, paper, cardboard). Generally, the inorganic and organic components are mechanically separated prior to pyrolysis. It is also possible to further mechanically segregate the organic components to control the amounts of each being pyrolyzed. The variability in the incoming waste components and the ability to sort the waste will result in a wide spectrum of pyrolysis oil composition, which is indicated by the large region assigned in Figure 5. We evaluated an oil derived from MSW that was prepared using fast pyrolysis of sorted urban waste collected and processed in a facility in Spain (oil prepared and provided by Neoliquid). Detailed analysis of this oil showed the presence of both aliphatic and aromatic hydrocarbons, including the presence of polyaromatic hydrocarbons. The oil was characterized by an effective hydrogen to carbon of 1.6 and concarbon of 7.5, which is in line with a heavy conventional resid feedstock. This is just one example of the diversity of oils possible from municipal waste streams.

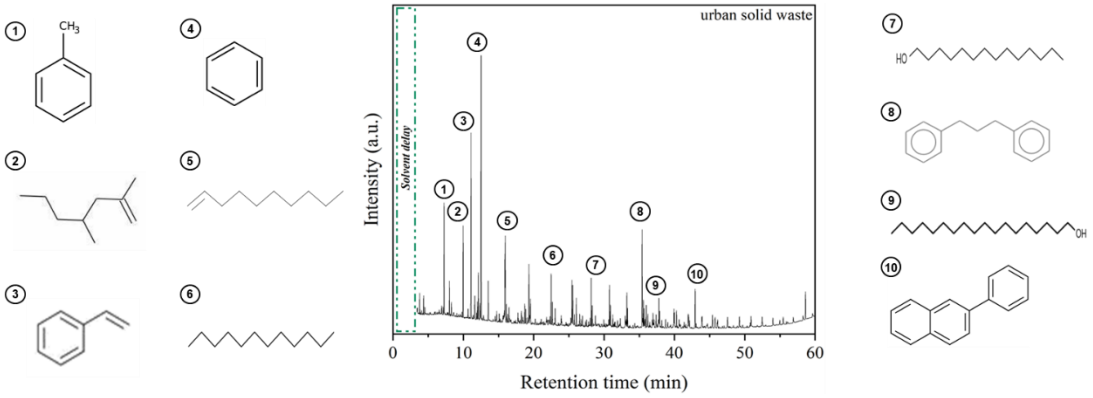

Figure 11: Composition of pyrolysis oil derived from municipal solid waste as measured using GCMS

Renewable Feedstocks during Catalytic Cracking

The behavior of different feedstocks during catalytic cracking was evaluated using a lab-scale ACE® test. This method and apparatus were developed over 20 years ago and have become the industry standard test for lab-scale catalytic cracking evaluations. In this test, a small amount of catalyst is injected into an isothermal fixed fluidized bed reactor while oil is continuously injected for a defined period that typically lasts between 30-60 seconds. While this arrangement is different than the tubular fluidized bed riser reactor, it is still useful to provide insight into the chemistry occurring during catalytic cracking and how this will translate into a commercial scale unit. As will be discussed, the nature of some feedstocks prevents upgrading undiluted without forming significant quantities of coke and gases. For these oils, the feedstock was "co-processed" with a conventional vacuum gasoil (VGO), which is an approach currently practiced commercially. For co-processing oils in the lab-scale ACE® test, the oils were heated separately to form a homogeneous mixture, then physically blended together at the appropriate ratio, then the oil mixture was used as the feed for the ACE® test. Two commercial BASF FCC catalysts were used in these studies: (A) catalyst designed for maximum naphtha yield, and (B) catalyst designed for maximum LPG olefin yield. During catalytic cracking there will be numerous simultaneously occurring reactions yielding hundreds

of different products. As a result, it is common to lump products into categories: (1) *Dry Gas*- H_2, CO, CO_2, CH_4, C_2H_6, C_2H_4 (2) *LPG*- C_3H_8, C_3H_6, C_4H_{10}, C_4H_8, (3) *Naphtha*- C_5 hydrocarbons to boiling point < 450°F, (4) *Light Cycle Oil (LCO)*- hydrocarbons boiling point between 450°F and 680°F, (5) *Heavy Cycle Oil (HCO)*- hydrocarbons boiling above 680°F, and (6) *Coke*. For feedstocks containing oxygen, the water produced during the cracking reaction was recovered as part of the condensable oil fraction, measured using Karl Fischer Titration, and reported as a separate product yield. For hydrocarbons C_5 and smaller, as well as the permanent gases including CO and CO_2, analysis was performed using an online gas chromatograph. The yields of heavier products were determined by simulated distillation using a gas chromatograph. Coke yield measures the mass of hydrocarbons bound to the catalyst surface after the cracking reaction and nitrogen stripping process is complete, as measured as CO/CO_2 oxidized during a regeneration cycle.

Polymer-based Pyrolysis Oils

The largely aliphatic hydrocarbons present in pyrolysis oils derived from polyolefins will crack similar to conventional oils during the FCC process. These oils could be co-processed with conventional gasoil, but its not required and is possible to feed these oils neat (100% py-oil feed). This approach was demonstrated in ACE® using the pyrolysis oil derived from LDPE and HDPE described in Figure 6 using both catalyst designs: Catalyst-A (max naphtha design) and Catalyst-B (max LPG design). The plots in Figure 12 illustrate product yields for the two different pyrolysis oils compared to yields from conventional vacuum gasoil (VGO) at a constant catalyst to oil of 7.0.

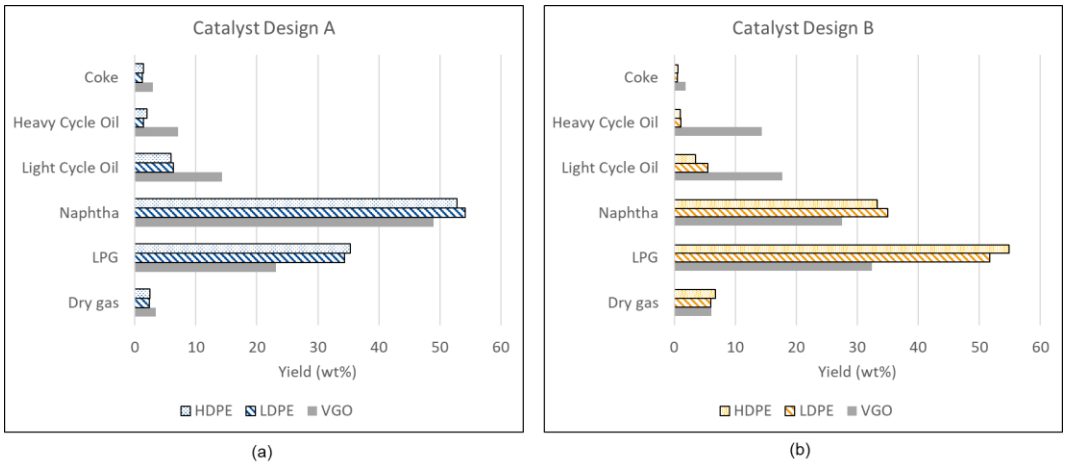

Figure 12: Product yields from catalytic cracking compared at a constant catalyst to oil ratio of 7.0 using (a) Catalyst A- max naphtha design, and (b) Catalyst B- max LPG olefin design.

The oils derived from plastic are considerably lighter than conventional VGO and contain higher natural fractions of naphtha and light cycle oil. Thus, the conversion to naphtha and lighter hydrocarbons is higher for the plastic-derived oils. The concarbon for the PE-based pyrolysis oils is less than 50% of the VGO concarbon (~0.5 compared to ~0.25). Consistent with the lower concarbon, the coke yield was roughly 50% lower for the PE-derived oils compared to the conventional VGO. Perhaps most interesting is the relatively high yield of olefins illustrated in Figure 13. The LPG fraction produced from the PE-based oil contains a high fraction of the highly valuable olefins and the design of the catalyst can be used to further increase yields of light olefins.

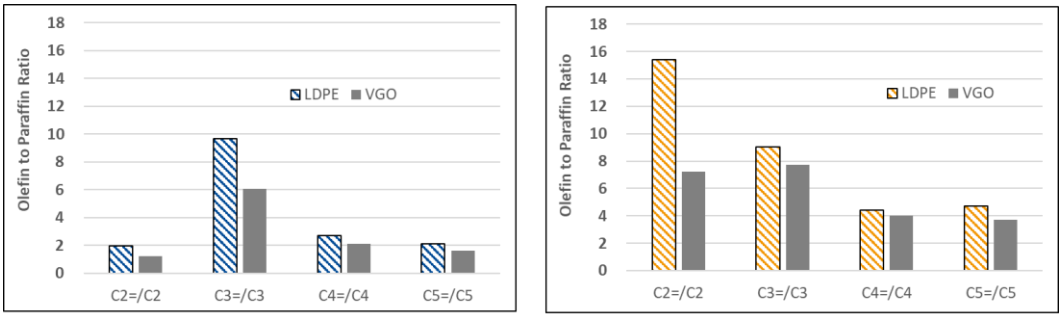

Figure 13: Olefin to paraffin yields for C_2-C_5 hydrocarbons from catalytic cracking compared at a constant catalyst to oil ratio of 7.0 using (a) Catalyst A- max naphtha design, and (b) Catalyst B- max LPG olefin design.

Plant-based oils

During catalytic cracking, the glycerol backbone of the triglyceride is likely cleaved producing propane/propene and the hydrocarbon portion of the fatty acids associated with the triglyceride. The oxygen contained in the triglyceride undergoes deoxygenation through different pathways to yield a mixture of CO, CO_2, and H_2O. The fatty acids associated with the triglyceride are all relatively saturated straight chain hydrocarbons with a boiling point in the range of light cycle oil (LCO). Similar to polyolefin pyrolysis oils, plant oils do not require co-processing with conventional VGO. While lower than polyolefin-based oils, the effective hydrogen content is still relatively high at 1.6 and the concarbon content is similar to conventional VGO.

Experiments were conducted to compare product yields from cracking 100% conventional VGO versus 100% soybean oil using Catalyst-A (max naphtha design). Figure 16 summarizes the yields from these two cases where the conversion is held constant. In the case of gasoil, the Heavy Cycle Oil (HCO) represents feed that cracks into Light Cycle Oil (LCO) and ultimately further cracks to naphtha and LPG. However, in the case of the soybean oil, the fatty acids contained in the triglyceride are already LCO sized hydrocarbons that then undergo cracking into naphtha and LPG. That results in the yield of HCO to be significantly less for the soybean oil and any HCO observed in the cracked products may be the result of oligomerization of fatty acids. Although the soybean oil is effectively already LCO, the yields of naphtha and LPG are lower. This could partially be the result of the more saturated fatty acid remnants being less reactive than VGO. This would also be partially the result of the soybean oil undergoing deoxygenation to CO, CO_2, and H_2O that diverts feedstock mass away from naphtha and LPG. The preferential pathway for deoxygenation was dehydration with nearly 80% of the oxygen contained in the soybean oil being converted into H_2O. The production of water consumes roughly 20% of the hydrogen contained in the soybean oil, which may explain the increase in light olefins. Despite the consumption of hydrogen, the yield of coke between the two cases was similar, which is consistent with the concarbon content being similar between the two feedstocks.

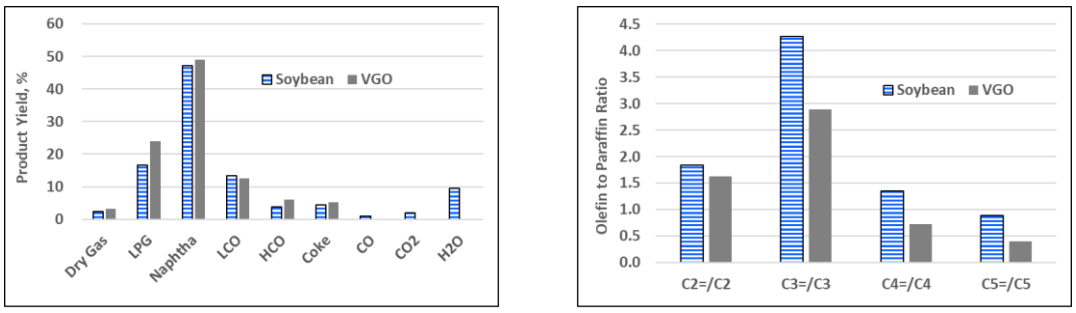

(a) (b)

Figure 15: Product yields comparison at constant conversion for soybean oil versus conventional VGO feed using Catalyst A- max naphtha design

Biomass-based & MSW-based pyrolysis oils

The pyrolysis oil derived from olive processing waste (composition illustrated in Figure 10) and the pyrolysis oil derived from municipal solid waste (composition illustrated in Figure 11) were evaluated in the same ACE® test. Compared to conventional oils, the concarbon content of both pyrolysis oils were high at 7.5% for the MSW-based oil and nearly 25% for the olive waste pyrolysis oil. To manage coke formation, it is common practice to dilute the pyrolysis oil in conventional gasoil, where the more hydrogen rich conventional oil can act as a hydrogen donor for the hydrogen deficient pyrolysis oil. For these experiments, both pyrolysis oils were diluted into conventional gasoil to a composition of 10% pyrolysis oil and 90% conventional VGO. Directionally, diluting in conventional gasoil will increase the effective hydrogen content and decrease concarbon content of the blend.

While the addition of pyrolysis oil had virtually no observable impact on overall conversion, the product yields were impacted as illustrated in Figure 14 showing the difference in product yield between the case where the pyrolysis oil was added and the case for pure VGO feed. Given the relatively small amount of pyrolysis oil added, the yields of deoxygenation products are relatively small and are excluded from Figure 14 for clarity. For the case of adding the olive waste pyrolysis oil, the yield of coke increases by roughly 10%. Even diluted with conventional gasoil, the concarbon for the blend would still be similar that of a typical Resid feedstock and the increase in coke yield is consistent with that typically observed between VGO and Resid feedstocks. For the case of the MSW pyrolysis oil, the coke yield is similar. While the concarbon of the MSW pyrolysis oil is higher than conventional oils, it is still significantly lower than the olive waste pyrolysis oil. This result suggests a higher blending ratio of MSW pyrolysis oil would be needed before a significant impact on coke yield would be observed. In commercial practice, this might suggest the MSW pyrolysis oil could be successfully co-processed at a higher percentage than the olive waste pyrolysis oil Both pyrolysis oils showed a shift in selectivity from LPG to naphtha was observed. Referring back to the composition of the two pyrolysis oils illustrated in Figures 10 and 11, both were found to have a significant content of aromatics or phenolics. During FCC, aromatics will not undergo cracking, they will either condense to form coke or be collected as part of the naphtha fraction. We suspect the higher naphtha yield is the result of the higher aromatic content of the pyrolysis oil. For both pyrolysis oils, there was also a shift from HCO to LCO, which is consistent with the higher natural fraction of LCO sized hydrocarbons contained in the pyrolysis oil.

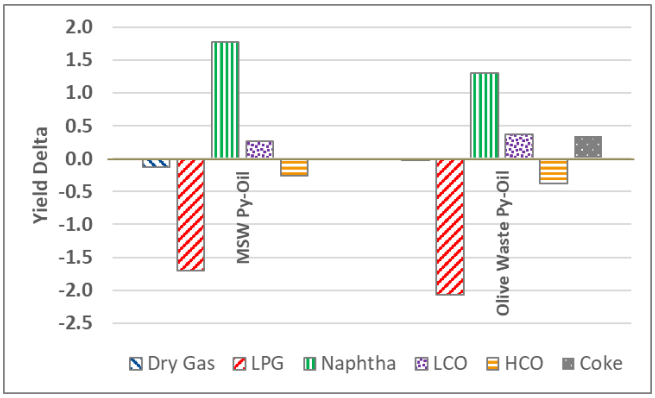

Figure 14: Yield difference at constant conversion of 80% from catalytic cracking of pyrolysis oils derived from olive waste and municipal waste compared to conventional VGO using Catalyst A- max naphtha design. "Yield Delta" defined as difference between yield with pyrolysis oil added and pure conventional VGO.

Conclusions

We have studied a broad collection of different feedstocks to understand their chemistry and the implications this chemistry will have on the operation of the FCC unit. While there will be numerous possibilities for refiners to consider as they transition to more sustainable feedstocks, the technical assessment can be simplified by focusing on the chemistry of the various oils. Effective hydrogen content and concarbon residue content are two well-known feed characteristics that can be used to characterize the upgradability of different oils. On one end of the spectrum will be plant oils and pyrolysis oils derived from polyolefins, where the combination of higher hydrogen content and low tendency to form coke makes the carbon contained in these oils easier to convert into fuels and chemicals. It's possible to upgrade these feedstocks without dilution with conventional oils and still maintain high yields of valuable products where the design of the FCC catalyst can be used to tune product yields between maximizing fuels or maximizing chemical feedstocks. On the other end of the spectrum will be pyrolysis oils derived from biomass where the combination of severe hydrogen deficiency and a high tendency for the formation of coke makes converting these feedstocks into fuels and chemicals very challenging. For these oils, significant dilution in conventional oil is required to manage the formation of coke and low value gaseous products. Moving forward, upgrading of biomass-based pyrolysis oils offers perhaps the most opportunity for new catalyst and process designs to improve the upgradability of these materials.

References

1. Chen, N. Y. Degnan, J. T. F, Koenig, L. R., ChemTech, 16, 506, [1986]
2. Naik, D. V. et al., Chemical Engineering Research & Design, 92, 1579, [2014]
3. Zhang, H. et al., Energy & Environmental Science, 4, 2297, [2011]
4. Puente, G., Arandes, J. M., Sedran, U. A., Industrial & Engineering Chemistry Research, 36, 4530, [1997]
5. Sharuddin, S. D., Abnisa, F. , Daud, W. M., Aroua, M. K., Energy Conversion & Management, 115, 308, [2016]
6. Huber, G. W., Iborra, S., Corma, A., Chemical Reviews, 106, 4044, [2006]
7. Liu, C., et al., Chemical Society Reviews, 43, 7457, [2014]

Some Aspects for Methanol and CO_2

M. Vicari, E. Frei, S. Reining, S. Britzius, L. Karrer
BASF SE Ludwigshafen

Abstract

In general, there are 2 possibilities to convert CO_2 in Methanol plants One is, together with Syngas preferentially to increase capacity or second, convert CO_2 directly with Hydrogen to Methanol. For the first case as an example, the CO_2-emission free Methanol process is presented. The basis for this process and the CO_2 only based process is a deep knowledge about the kinetics. A kinetic model and the application ASPEN+ process calculation is the next bullet point of the presentation. The CO_2 for the Methanol-synthesis may come from very different sources. A source for CO_2 to green Methanol is CO_2 coming as an off - gas from fermentation. The specification and the needs for purification and process to make it usable for MeOH synthesis are presented. For the CO_2 to Methanol process, the lack of heat of reaction, makes it necessary to generate additional steam for the distillation to pure Methanol. A concept to provide to generate this additional steam is presented. This steam generation is included in the thermosyphon system of the Methanol synthesis reactor. The presentation ends with an overview of the energy consumption of a CO_2 based Methanol plant with Hydrogen from electrolyzer.

Methanol Steam Reforming at low Temperatures Using Supported Homogeneous Catalysts – Catalyst Development and Reactor Design

H. Junge[1], A. Agapova[1], C. H. Schwarz[2], A. Rehman[2], D. Neu[2], M. Haumann[2]
[1]Leibniz-Institut für Katalyse, e. V.
[2]Friedrich-Alexander-Universität Erlangen-Nürnberg (FAU), Lehrstuhl für Chemische Reaktionstechnik (CRT)

Abstract

Today, hydrogen storage materials range from simple NH3 to more complex structures like dibenzyltoluene. A promising approach to hydrogen storage is the generation of methanol by hydrogenation of CO2. In a decentralized scenario, even for mobile applications in transport, the hydrogen can be released again by methanol steam reforming. The resulting reformate has a hydrogen to carbon dioxide product ratio of 3:1. From a thermodynamic point of view, high equilibrium conversions can be obtained at higher temperatures since the reaction is endothermic. However, in case the reaction temperatures exceed approx. 200 °C, the stronger endothermic methanol decomposition will result in high CO levels >1%, which would render the gas mixture not suitable for most fuel cell applications.

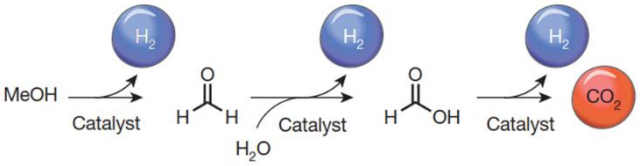

Noble-metal and base-metal transition metal complexes have been successfully employed for the homogeneously catalyzed dehydrogenation of methanol at temperatures below 160 °C.[1] In order to design potential processes based on such attractive catalysts, continuous operation must be ensured. Here, the purely liquid-phase reaction would be problematic, e.g. as high base concentrations would lead to corrosion of reactor materials.
Supported liquid phase (SLP) materials consist of a high boiling liquid, dispersed as a thin film on the inner surface of a highly porous solid material. By dissolving homogeneous transition metal complexes in the liquid film (here: aqueous KOH), the SLP concept allows tailor making of solid materials with definite properties and a controlled chemical reactivity. Since the liquid is dispersed on the inner surface of the support, a dry solid material is obtained. These materials can be handled like classical heterogeneous catalysts in continuous fixed-bed reactors.
In this work, we present results from immobilization studies using commercially available Ru-Pincer catalysts in standard SLP gas-phase scenarios.[2,3] The catalysts have been optimized by variation of the type of liquid used for coating the support surface. Kinetic data were used to model possible reactor designs in AspenPlus.

References

[1] M. Nielsen, et al., Nature, 201, 495(7439), 85.
[2] C.H. Schwarz et al. Catal. Today, 2020, 342, 178.
[3] C.H. Schwarz et al., Eur. J. Inorg. Chem. 2021, 1745.

Engineering of Highly Active Indium-based Catalysts for the Hydrogenation of CO_2 to Methanol

R. Baumgarten[1], H. Ahi[2], E. Frei[2], E. Fako[2], S. De[2], R. Naumann d'Alnoncourt[1], C. Boscagli[3], S. Schunk[3], F. Rosowski[1,2]
[1]BasCat – UniCat BASF JointLab, Technische Universität Berlin, Berlin, Germany
[2]BASF SE, Ludwigshafen, Germany
[3]hte GmbH, Heidelberg, Germany

Abstract

The utilization of CO_2 as feedstock for the chemical industry is a highly appreciated measure to control inevitable emissions. CO_2 generated as byproduct along the chemical value chain could be re-introduced by subsequent valorization processes to facilitate a circular economy. Of particular interest is the direct hydrogenation to hydrocarbons or methanol due to the rising strive for a hydrogen-based industry. Ideally, the CO_2 is captured from the earth atmosphere and combined with hydrogen from sustainable power sources. Methanol is a crucial building block for the chemical industry, especially as intermediate for the fabrication of formaldehyde or acidic acid. Furthermore, it is employed in methanol fuel cells and serves as propellant in combustion engines.

Nowadays, methanol is industrially synthesized from mixed syngas (CO, CO_2, H_2) over a copper-zinc catalyst at 50-100 bars and 200-300°C. Typically, the CO_2 content is minimized as the selectivity for the reversed water gas shift reaction (RWGS) intensifies with a rising partial pressure of CO_2. The resulting water leads to hydrothermal conditions causing severe changes of the copper-zinc interface and reduction of the hydrogenation activity.[1,2] Yet, in order to utilize CO_2 as a feedstock, its fraction in the applied syngas has to be increased and new catalyst systems have to be developed. One promising alternative are indium oxide catalysts as they have a higher long-term stability and methanol selectivity under CO_2-rich conditions.[3]

In this study, we enhanced the CO_2-hydrogenation activity of supported indium oxide catalysts by the promotion with different metals. The most potent promotor was identified while the yield of methanol could be increased by over 60% compared to the un-promoted catalyst. Additionally, the loss of hydrogenation activity was decreased by over 50% under CO_2-rich conditions. Furthermore, a recently developed method for the atomic layer deposition on particles was utilized to increase the dispersion and utilization of In_2O_3.[4] Consequently, the yield of methanol per mass of indium was improved compared to samples prepared by impregnation. Moreover, an experimental fingerprint method was developed to quantify active sites on the indium oxide surface. The resulting trend could be correlated with the hydrogenation performance of the indium-based samples.

References

[1] T. Lunkenbein, F. Girgsdies, T. Kandemir, N. Thomas, M. Behrens, R. Schlögl, E. Frei, *Angewandte Chemie* **2016**, *55*, 12708.
[2] M. B. Fichtl, O. Hinrichsen *et al.*, *Applied Catalysis A: General* **2015**, *502*, 262.
[3] O. Martin, J. Pérez-Ramírez *et al.*, *Angewandte Chemie* **2016**, *55*, 6261.
[4] R. Baumgarten, P. Ingale, K. Knemeyer, R. Naumann d'Alnoncourt, M. Driess, F. Rosowski, *Nanomaterials* **2022**, *12*, 1458.

Insights to the NH3 Reforming Process beyond Catalyst Design

E. Frei[1], N. Bottke[1], L. Karwacki[2], M. Schwab[2], M. Felischak[3]
[1]BASF SE, RCC/PP, Ludwigshafen
[2]BASF SE, G-CCP/MD, Ludwigshafen
[3]BASF SE, RCP/CD, Ludwigshafen

Abstract
Ammonia (NH_3) is seen as an energy vector of the future, able to chemically store significant amounts of H_2 and be produced on a large scale from regenerative energy sources. The reforming of NH_3 (equation 1) on site, where the H2 is needed, might be the last step in closing a H2 value chain based on renewable electricity.

(1) $2\ NH_3 \rightleftharpoons N_2 + 3\ H_2 \quad \Delta Hr = +91.2\ kJ/mol$

For the endothermic reforming of ammonia, significant amounts of energy are needed. So, the reaction temperature is an important measure from the process perspective. Since the thermodynamic limitation at lower temperatures are huge, it is a clear trade-off between kinetics and thermodynamics. The same holds for the reaction pressure, at lower pressures the thermodynamic limitation is also lower, but the hydrogen is produced on a lower pressure level. This means, dependent on the down-stream application, a lot of energy for compressor work is needed.

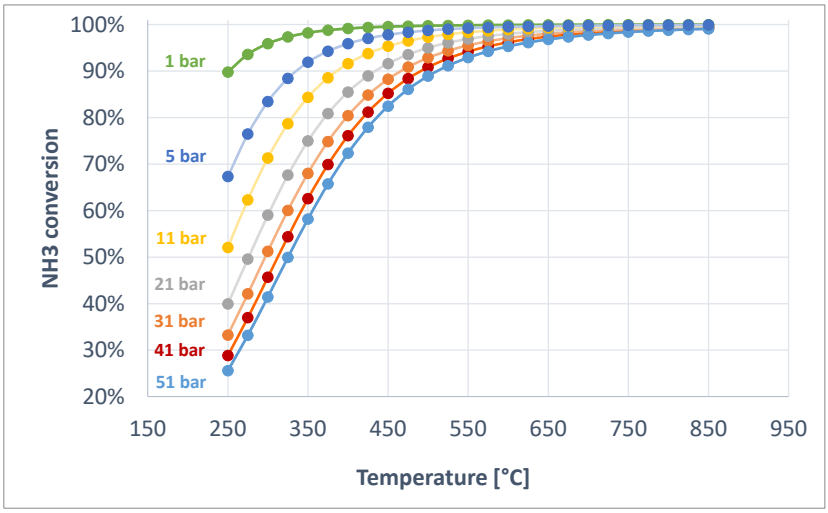

Within our contribution, we want to show possible catalytic and process solutions for the entire pressure and temperature range. Based on our catalytic solutions we developed kinetic models, allowing us to simulate the ammonia reforming process itself and optimizing the CapEx and OpeEx of a plant. The process simulations will be discussed within the thermodynamic frame and certain applications.

rWGS as a Key-step to Transform CO_2 into Valuable Products - Accelerated R&D Applying Advanced High Throughput Technology

B. Mutz, C. Hauber, P. Kolb, M. Weber
hte GmbH – the high throughput experimentation company, Heidelberg, Germany

Abstract

Carbon management is a major challenge that is attracting growing interest for transforming the chemical industry and transportation sector toward greater sustainability with lower carbon dioxide emissions. The production of sustainable syngas from CO_2 and the integration of the process into existing refineries for chemicals and fuels production is an important step on the road from CO_2-to-value, *e.g.* sustainable aviation fuel from power-to-liquid plants.
This article describes the CO_2-to-value path with the focus on CO production *via* reverse water-gas shift (rWGS) reaction supported by performance results from high throughput experimentation. Our internal rWGS study includes the testing of Cu and Ni catalysts to investigate the influence of temperature, pressure, space velocity, and the H_2/CO_2 ratio on the catalytic performance. The Cu catalysts produce methanol as a by-product, whereas the Ni catalysts only produce methane besides the CO. In the course of parameter optimization, the selectivity of the catalysts could be improved, and the reaction conditions could be found where the catalysts are active and selective.
Within this article, we are describing the most advanced high throughput approach for accelerated catalyst screening and parameter optimization for the rWGS process. hte's flexible 16-fold setup is equipped with high-temperature reactor technology operated at elevated pressures, high-precision online GC analytics as well as tailor-made software solutions for big data handling. Operating rWGS at elevated pressures allows coupling with the established FT processes. In this context, hte outlines its experience in FT as well as hydrocracking to cover the full process chain toward CO_2 neutral fuels and chemicals.

Introduction

The reduction of CO_2 emissions can be realized via a) enhancing process efficiency and the implementation of renewable energies or b) capture and storage of waste CO_2 or c) utilization of CO_2 as feedstock in chemical production processes. In terms of option c) "CO_2 utilization", making use of the existing assets from the petrochemical refinery and the smart integration of CO_2 as well as renewable H_2 production into the industrial value chain are key strategies for a fast transition. [1]
The reverse water-gas shift (rWGS) reaction (1) can serve as a key process utilizing CO_2 from industrial exhaust streams, biogas plants, or direct air capture to generate CO for syngas of greater sustainability. CO-rich feedstocks produced from CO_2 via rWGS can be fed into existing Fischer-Tropsch (FT) units followed by product upgrading toward fuels and chemicals (Figure 1). Operating the rWGS process at pressures around 30 bar allows direct coupling with Fischer-Tropsch reactors to avoid intermediate cooling/heating and compression steps. [2]

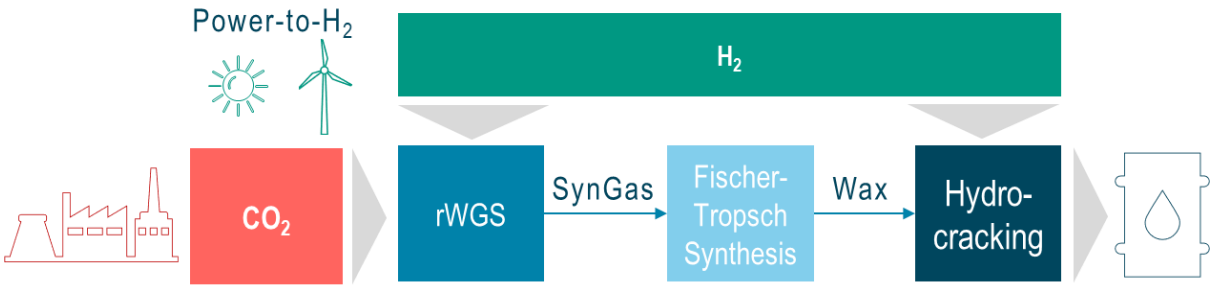

Figure 1: Scheme of the CO_2-to-value track starting from captured CO_2 followed by an integrated reverse water-gas shift reaction coupled with Fischer-Tropsch plants. The obtained wax is upgraded via hydrocracking and isomerization toward fuels and chemicals. Renewable H_2 is added to the rWGS process as well as during wax upgrading.

As an alternative route, CO from rWGS can serve as a valuable intermediate for methanol synthesis followed by the Methanol-to-olefins process [3] and olefins oligomerization to produce sustainable aviation fuels (SAF). In both cases, rWGS represents a new challenge for process and energy integration where high temperature, endothermic as well as low temperature, exothermic reactions need to be coupled.
The containerized design of coupled rWGS and FT reactors on a pilot-scale is currently being developed *e.g.* by Ineratec and VTT, producing white oils and high molecular aliphatic waxes. CO_2 can be taken from a biogas upgrading plant and H_2 is supplied by a chloro-alkali electrolyzer plant. [4] The rWGS process is currently carried out using an Ni-based catalyst by Clariant. [5] A rWGS technology called HyCOgen™ was launched by Johnson Matthey to produce sustainable aviation fuel from captured CO_2 and green H_2. The rWGS process integration is realized with FT synthesis that was developed together with BP. [6] The rWGS technology is an essential building block within the G2L™ collaboration by Topsoe and Sasol to license and develop sustainable liquid fuels and chemicals *via* FT synthesis. FT tail gas is recycled to the rWGS section, where it is converted to syngas *via* steam reforming. Hence, carbon efficiency can be improved and the H_2/CO ratio can be tuned for FT. [7]

rWGS is an endothermic reaction (1) and, therefore, requires elevated temperatures for a high CO yield. The exothermic CO_2 hydrogenation to methane (2) is favored in the lower temperature regime. According to the thermodynamic equilibrium composition of the product gas reported by Kaiser *et al.* [8] for 1 bar and a molar H_2/CO_2 inlet ratio of 3, CO formation occurs at around 500°C and increases with temperature, while hydrogenation toward methane is suppressed. Operating rWGS at elevated pressures relevant for coupling with FT reactors, the undesired CH_4 formation curve shifts toward higher temperatures, thereby making even higher temperatures necessary to produce CO as the main product.
Considering the stoichiometry of the reactions, the CO selectivity could be tuned by decreasing the H_2/CO_2 feed ratio, however, applying an inlet ratio of 3 should result in a suitable H_2/CO product ratio for FT of 2-2.5. [2] On the other hand, high H_2/CO_2 feed ratios enhance the conversion of CO_2.

(1) $CO_2 + H_2 \rightleftharpoons CO + H_2O$, $\Delta H_r = 41$ kJ/mol
(2) $CO_2 + 4H_2 \rightleftharpoons CH_4 + 2H_2O$ $\Delta H_r = -165$ kJ/mol
(3) $CO_2 + 3H_2 \rightleftharpoons CH_3OH + H_2O$ $\Delta H_r = -50$ kJ/mol

To achieve a high yield of CO, the rWGS process requires operation at high temperatures according to thermodynamics. Since CO is assumed to be the intermediate for CO_2 methanation, the quick removal of CO from the reactor before the hydrogenation of the carbon atom toward methane occurs can be beneficial when operating at increased gas hourly space velocity (GHSV).
High CO selectivity at low operating temperature could be achieved utilizing catalysts that are active in CO_2 reduction to CO but feature low hydrogenation activity. Various active metals, metal/support combinations, and promotors for the rWGS reaction have been reported in the literature and are summarized in recent review articles. [9-11] Next to noble metal catalysts, Ni and Cu based materials but also metal-free catalysts feature high relevance for rWGS due to their reduced cost. [10] Enhanced CO selectivity for an Ni catalyst after the *in situ* formation of a highly active NiC phase has been reported by Galhardo *et al.* [12] The catalyst was tested in a first temperature ramp of 200-800°C at atm pressure, resulting in a peak in methanation activity at around 400°C, as expected from thermodynamics. In a second cycle, no CH_4 was formed, leaving CO as the main product and indicating that an active NiC phase was formed at high temperatures that suppresses CH_4 formation. Only a few reports address rWGS at elevated pressures, which is relevant for rWGS-FT coupling. Juneau *et al.* [10] tested rWGS in pilot-scale at 450°C, 21 bar, and an H_2/CO_2 ratio of 3 achieving 44% CO_2 conversion and >98% CO selectivity.

The scope of this study was to validate hte's 16-fold high throughput test units equipped with high-temperature reactor systems and to demonstrate its fitness for rWGS operated at vast GHSV and elevated pressures, that are relevant for coupling with FT reactors. Benchmark, commercially available Cu- and Ni-based catalysts, typically producing MeOH and CH_4, respectively, should be applied in order to gradually tune the process parameter toward high CO selectivity.

High throughput testing technology

Within this study, the most advanced 16-fold high throughput system designed for CO_2 conversion has been utilized for accelerated catalyst screening and parameter optimization for the rWGS process. A simplified scheme of the high throughput testing equipment is shown in Figure 2. The concept of a high throughput testing setup at hte has already been described for FT synthesis, syngas to MeOH, and hydroprocessing studies and presented during earlier DGMK conferences. [13-15] However, the latest technology developments include the implementation of individual high-temperature heaters up to 900°C as well as high-temperature metal alloy reactors equipped with ceramic inlay tubes that feature inertness under these conditions and can be set under pressure. Making use of small reactor inner diameters of 3-5 mm allowed performing rWGS at vast GHSV.
The current developments at hte address novel heater concepts to realize reactor temperatures up to 1200°C within the parallel high throughput testing units.

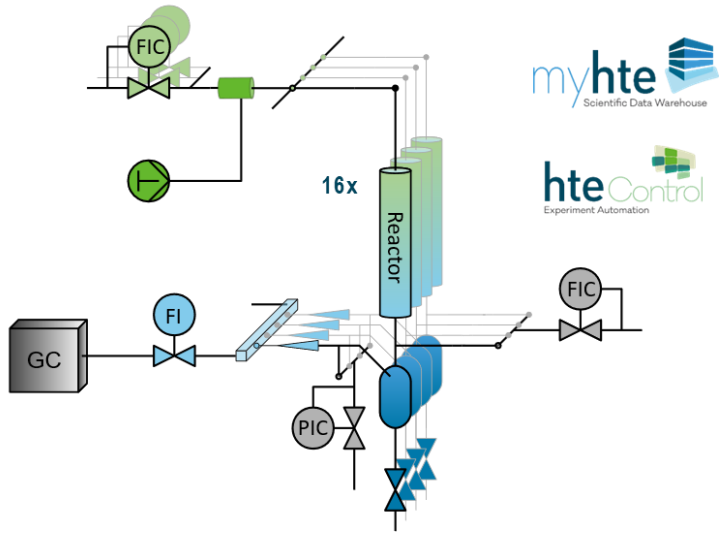

Figure 2: Simplified scheme of the 16-fold parallel high throughput testing unit by hte.

The feed gases were dosed using individual mass flow controllers, which allows for applying a wide range of feed rates and gas compositions. CO_2 was dosed as a liquid using a high-precision syringe pump. The feed was mixed in a common feed line and distributed equally over the 16 parallel reactors. The catalysts were tested as powder in a size fraction of 120-160 µm and diluted in SiC of a similar size to avoid temperature gradients in the catalyst bed. The catalysts were loaded with a different amount into the parallel reactors to realize GHSV variation at a fixed common feed rate. The catalysts were activated in H_2 at 10 barg as the pressure of the first experiment and a final temperature of 200°C and 750°C for the Cu and Ni catalysts, respectively. Ar was used as the internal standard and to track the feed distribution over the 16 parallel reactors. Despite Ar, no further inert gas dilution of the feed was applied.
Reactor pressure was controlled downstream feeding additional N_2. The analysis of the reactor outlet gas was performed using an in-house configured multi-detector gas chromatograph equipped with different TCD for permanent gas and water analysis plus FID/Jetanizer combinations for hydrocarbon, oxygenates, and CO_X detection. hte process

control software enabled the fully automated and continuous operation and monitoring of the high throughput system. Data evaluation was performed by the myhte software solution, which was especially developed for the treatment of large amounts of data produced by a high throughput setup. [16]

rWGS results

Commercial Cu- and Ni-based catalysts, which are known to be active for methanation (2) and methanol (3) synthesis, respectively, were used for the internal rWGS study, while tuning the process conditions toward high CO productivity. The same catalyst was loaded in a different amount into each of the parallel reactors to realize the fast screening of GHSV between 10,000-50,000 h^{-1} for the Cu catalyst and 100,000–500,000 h^{-1} for the Ni catalyst within every single experiment. Each loading was duplicated for the internal validation purposes of the unit and to investigate its reproducibility. Even higher GHSV would have been possible when loading less catalyst and increasing the flow rate, but this was beyond the scope of this short study.

During the first set of experiments, the process was operated in the low temperature regime (250/500°C) for MeOH or CH_4 production, respectively. The H_2/CO_2 feed ratio was set to 3 to produce a suitable syngas mixture for FT and to support CO_2 conversion. As a starting pressure, 10 bar was applied, which was then increased stepwise to the target pressure level of 30 bar. The results of the Cu catalysts during pressure screening are shown in Figure 3 a). It is observed that high CO selectivity was reached already at 10 bar, whereby the best results were achieved at the lowest GHSV ($X(CO_2)$ = 16%, S(CO) = 88%). With increasing pressure, more MeOH is formed at the cost of CO selectivity. Only minor CH_4 formation was observed on the Cu catalyst at any condition.

The results for the Ni catalyst are presented in Figure 3 b). The main product is CH_4, and only minor CO formation was observed. Higher shares of CO were observed at the highest GHSV, most prominent at 10 bar reaching 15%. This observation already supports the thesis mentioned hereinabove that removing the CO as the intermediate in CO_2 methanation quickly from the reaction zone applying high GHSV should avoid deep hydrogenation and increase its selectivity. Performing rWGS at further increased GHSV requires further investigation but was not part of the described experiments. With increasing pressure, the product selectivity shifted even more toward CH_4, and CO_2 conversion increased especially under high GHSV operation. The results at low GHSV operation remained similar at around 70% CO_2 conversion during pressure increase, indicating a limitation from thermodynamic equilibrium.

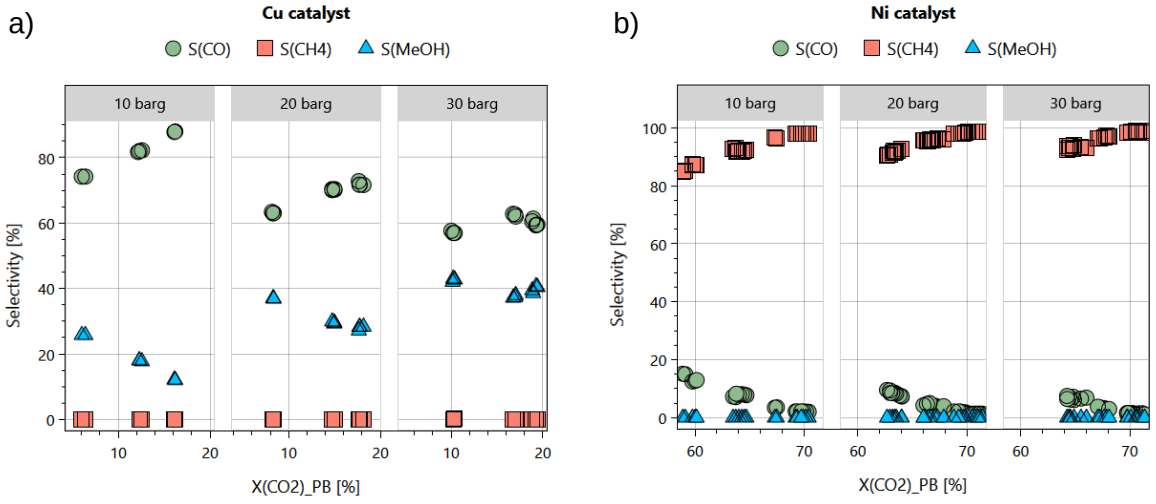

Figure 3: a) Pressure screening during rWGS using a commercial Cu catalyst (250°C, H_2/CO_2 = 3, 10,000-50,000 h^{-1}) and b) Ni catalyst (500°C, H_2/CO_2 = 3, 100,000-500,000 h^{-1}).

To follow the thermodynamics toward CO as the main product, the reactor temperature was increased, while maintaining 30 bar as the target pressure for potential coupling with FT reactors. Figure 4 a) shows the performance of the Cu catalyst, which especially improved at the high GHSV operation. The selectivity to CO increased to 90% at a CO_2 conversion of 22%. The catalytic performance at 300°C was observed to be independent of the residence time and resulting in an H_2/CO outlet ratio of 13. MeOH formation declined with temperature, which could be due to the exothermic nature of the reaction. However, a detailed investigation of that was beyond the scope of this study. The formation of dimethyl ether or higher hydrocarbons was not observed.
A similar behavior was observed for the Ni catalyst (Figure 4 b), but operated at higher temperatures. At 750°C, a 67% conversion of CO_2 was achieved, independent of the residence time. The selectivity to CO increased to 38%, resulting in an H_2/CO outlet ratio of 4.5 as well as a CO productivity 68 kg(CO)/kg(cat)/h for the reactor loaded with the lowest amount of catalyst. By increasing the temperature, it was possible to reduce the selectivity to CH_4 for an Ni catalyst significantly from close to 100% toward 63%. Achieving similar results in a wide range of applied space velocities implies that even higher GHSV and, therefore, higher CO space time yield would have been possible. From the technological viewpoint, it was possible to realize a large temperature difference of 450°C between the individual reactors containing Cu or Ni catalysts using the smart distribution of the reactors in the 16-fold parallel reactor setup.

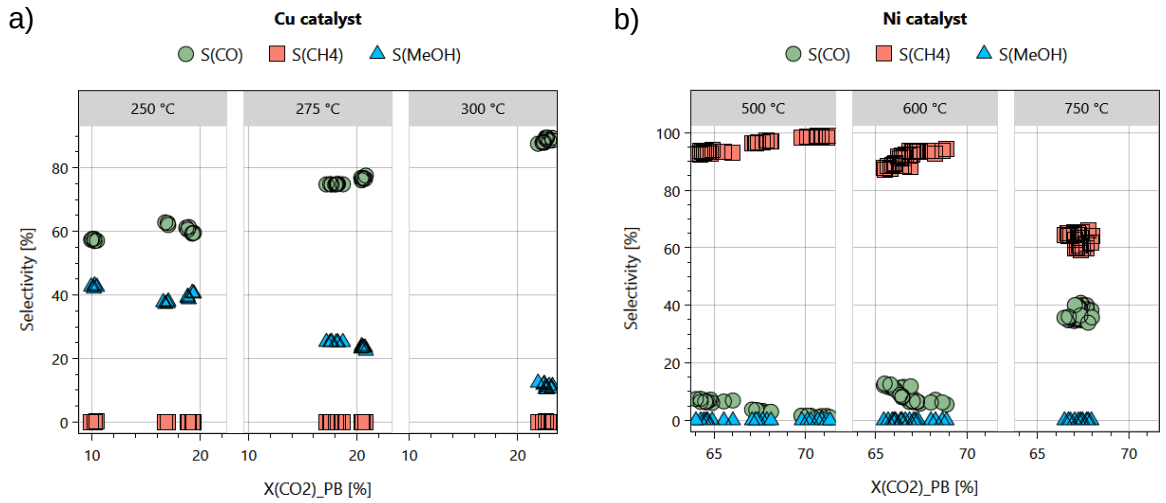

Figure 4: a) Temperature screening during rWGS using a commercial Cu catalyst (30 barg, H_2/CO_2 = 3, 10,000-50,000 h^{-1}) and b) Ni catalyst (30 barg, H_2/CO_2 = 3, 100,000-500,000 h^{-1}).

After the rWGS run at 750°C, a check-back condition at 500°C was set to investigate the effect of an active NiC phase that was potentially formed at high temperatures as reported by Galhardo *et al.* [12] Comparing the first cycle at 500°C with the second cycle after the temperature ramp to 750°C (Figure 5), it was indeed observed that the CO selectivity significantly increased while less CH_4 is formed. However, the overall conversion deceased as well, which is not in line with the report by Galhardo *et al*. [12], who observed a similar conversion from the sum of the individual yields but applied different process conditions. Clearly, structural changes of the catalyst occurred at 750°C, but a detailed characterization was beyond the scope of this study. Nevertheless, the results of this quick check into the proposed active NiC phase formation under high temperature rWGS conditions indicate that it is worthwhile for deeper investigation.

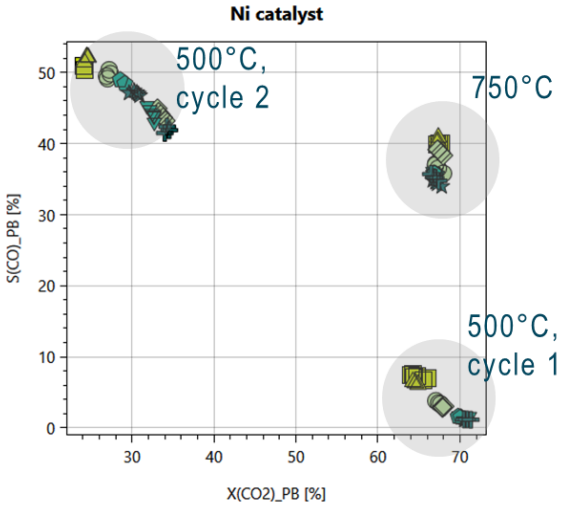

Figure 5: Values for CO selectivity as a function of CO_2 conversion in rWGS during the initial conditions at 500°C and 30 barg (cycle 1) compared to the check-back condition (cycle 2) with a temperature step at 750°C in between.

To further boost the selectivity to CO in accordance with thermodynamics, the reactor pressure was lowered again at the highest temperature levels tested and identified as the most promising. However, this meant leaving the suitable operating conditions for FT reactor coupling. Figure 6 shows the effect of reactor pressure on the CO selectivity, achieving 98% for the Cu catalyst and around 60% for the Ni catalyst, while maintaining the conversion level for each material group, respectively. H_2/CO product ratios of 13-15 for the Cu catalysts and 4.3 for the Ni catalyst were reached.

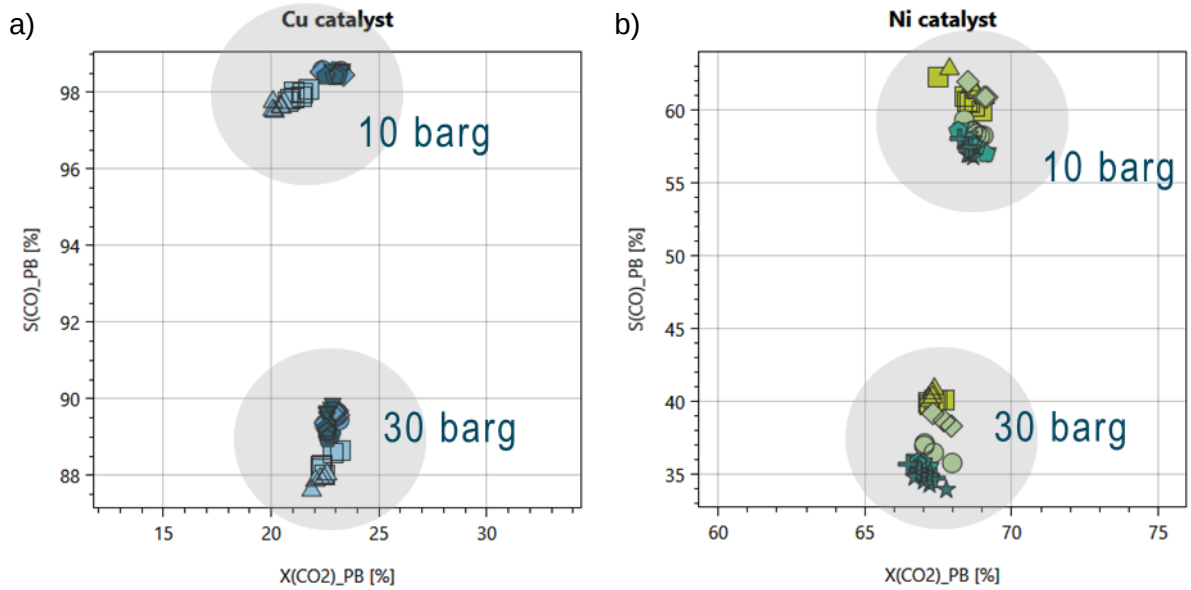

Figure 6: a) Pressure reduction during rWGS using a commercial Cu catalyst (250°C, H_2/CO_2 = 3, 10,000-50,000 h^{-1}) and b) Ni catalyst (750°C, H_2/CO_2 = 3, 100,000-500,000 h^{-1}).

The H_2/CO_2 feed ratio was varied as the final parameter within our study, which was kept constant to 3 during the experiments so far in order to realize high CO_2 conversion. However, lower H_2 partial pressure should result in a lower formation of hydrogenated by-products according to the stoichiometry of the occurring reactions methanation (2) or methanol synthesis (3), respectively. As shown in Figure 7 and expected from theory, decreasing the

H_2/CO_2 inlet ratio led to a lower CO_2 conversion for both material groups. The Cu catalyst already showed high CO selectivity around 98% at the 3:1 ratio. However, decreasing the inlet ratio further improved the selectivity, especially at ratios of 1:1 and lower. At the lowest H_2 partial pressure in the feed, an H_2/CO product ratio of 4.5 was reached during low space velocity operation. It is also observed that the catalyst activity reacted more sensibly on the applied GHSV since the decline in CO_2 conversion is more pronounced at a higher GHSV range. It is due to the precise data quality that enables distinguishing the results of the Cu catalysts within the different conditions at this narrow conversion and selectivity levels.
The effect on the results when lowering the H_2 partial pressure is more significant for the Ni catalyst, achieving 98% CO selectivity at 30% CO_2 conversion. A suitable H_2/CO product ratio for the Fischer-Tropsch synthesis of ca 2.5 was reached using a 2:1 feed ratio. At lower H_2/CO feed ratios, the product composition became more CO-rich.

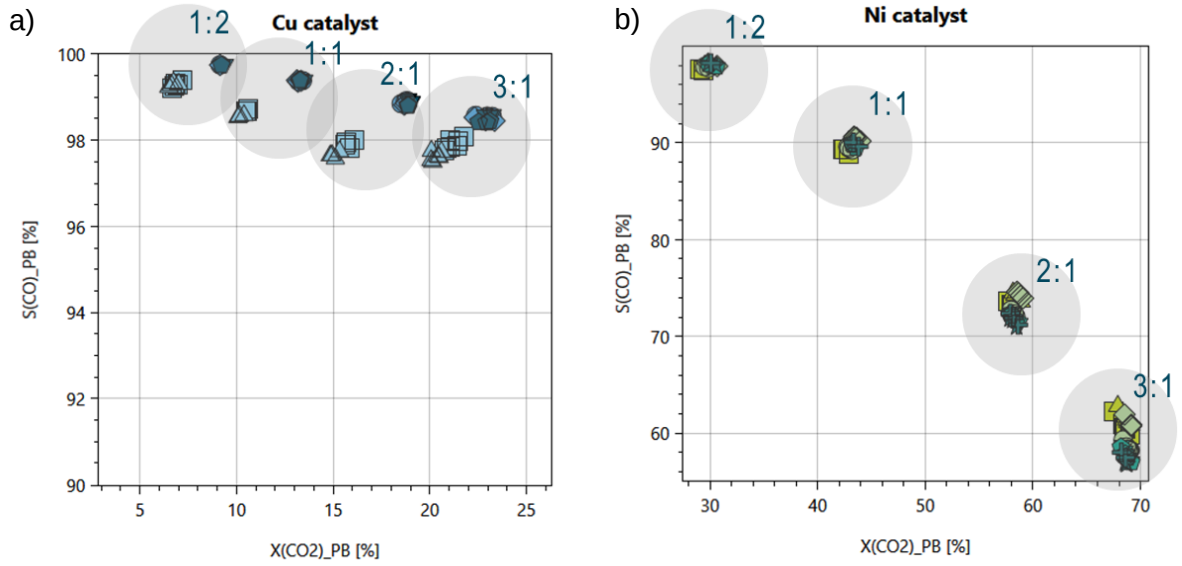

Figure 7: a) Variation of the H_2/CO_2 feed ratio during rWGS using a commercial Cu catalyst (250°C, 10 barg, 10,000-50,000 h^{-1}) and b) Ni catalyst (750°C, 10 barg, 100,000-500,000 h^{-1}).

The overall CO productivity of the catalysts could be increased significantly during the parameter optimization, reaching values of 2.4 kg(CO)/kg(cat)/h for the Cu catalyst and 129 kg(CO)/kg(cat)/h for the Ni catalyst, exceeding values from state-of-the-art literature reports. [10] The key for achieving such high productivities was the vast GHSV applied during the experiments. Furthermore, since similar results were achieved for the catalysts operated at different GHSV, even higher productivities should be possible when further increasing the GHSV, at least for the Ni catalyst.
Within this study, GHSV, reactor pressure, temperature, and the H_2/CO_2 feed ratio were screened for two different catalysts (Figure 8) in only 13 days using high throughput experimentation. As reported in recent review articles [9-11], more than 100 catalyst materials including various metal/promotor/support combinations, can be relevant for rWGS. For the material screening within rWGS catalyst development, high-throughput testing is crucial to ensure best comparability of the catalysts and to accelerate catalyst R&D as well as process optimization toward commercialization.

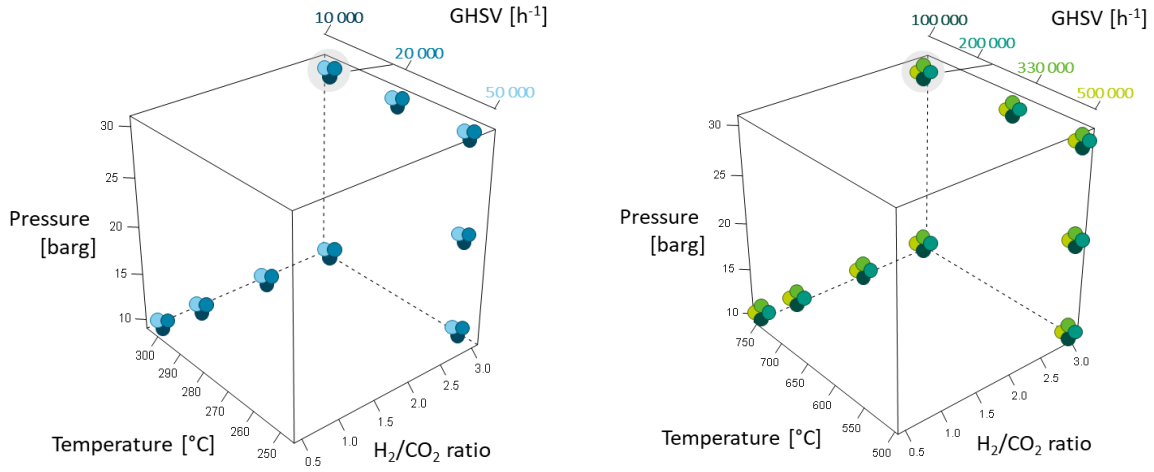

Figure 8: Parameter space varied during the rWGS case study using a Cu- and Ni-based catalysts.

CO_2-to-value

Integrating rWGS into the syngas conversion value chain is a promising concept for CO_2 utilization as well as the production of *e.g.* sustainable aviation fuel. Startups and research institutes as well as global leaders for Fischer-Tropsch synthesis are currently developing strategies and technology for coupling the rWGS step with a syngas consuming reaction, *e.g.* FT synthesis. Despite being thermodynamically less favored, it is beneficial to operate rWGS within a pressure range of the downstream Fischer-Tropsch reactor for direct coupling in order to avoid cooling, water removal, compression, and re-heating steps in between. [2] Heat management is crucial since, according to the current state of the art, rWGS is operated at much higher temperatures compared to the exothermic Fischer-Tropsch process. As shown in this study, rWGS can be operated under tremendous GHSV of 500,000 h^{-1} and higher in case of an Ni catalyst, whereas FT reactors are operated in an approx. range of 1,000–10,000 h^{-1}. Therefore, the reactor size and catalyst amount for an upstream rWGS reactor can be designed significantly smaller than the FT reactor. This can be beneficial for the rWGS process integration into the existing FT assets, since electrically heated rWGS microreactors could be an option.

Further catalyst and process optimization is required for rWGS to achieve higher CO selectivity and low CH_4 formation at high CO_2 conversion. Operating rWGS at a reduced temperature could be beneficial for overall heat integration within the CO_2-to-value process. Therefore, catalysts featuring low methanation activity need to be developed and applied. Furthermore, performance stability at FT-relevant pressures needs to be investigated. Moreover, FT synthesis requires further investigation, since the process will face differing feed compositions compared to conventional FT processes from upstream rWGS including *e.g.* CO_2, H_2O, and by-products. Wax upgrading is probably less affected but requires additional (green) H_2. The coupling of FT and hydrocracking as well as integration of hydrocracking into the FT process using bifunctional catalysts is part of the current research activities. [17, 18]

Each of the process steps related to the CO_2-to-value path can be covered individually by hte's technology to support FT plant operators or technology providers on their way toward CO_2 integration. Test systems and workflows for rWGS as a first step within the process chain was demonstrated in this article, which was crucial for the current R&D activities regarding catalyst development and process optimization. hte's flexible parallel GtL testing units available in different scales (demonstrated during earlier DGMK conference [13] as well as within a recently published study together with Venator [19]) can be used to investigate and optimize the process in consideration of the new feedstock composition provided from rWGS reactors.

The fast screening of bifunctional catalysts addressing rWGS/FT as well as FT/hydrocracking can already be supported applying existing units and workflows. Current technology developments at the hte address coupling of the individual steps using separate reactors in series for the detailed investigation of the process integration. Fischer-Tropsch wax upgrading completes the CO_2-to-value chain toward production of sustainable fuels, once again supported by hte, as recently published together with BP. [20]

Summary and Conclusion

Commercial Cu- and Ni-based catalysts were used to gain insights into the rWGS process and to demonstrate the feasibility of hte's high-temperature parallel testing setup for fast material screening and parameter optimization. Within the starting conditions of the experiment, MeOH and CH_4 were observed as major products, which built the baseline for further process optimization toward a high CO production. Using high throughput experimentation, a wide range of parameters of 250-750°C, 10-30 bar 10,000-500,000 h^{-1} and H_2/CO_2 feed ratios of 0.5-3 was screened within only 13 days of testing. Large temperature differences of 450°C can be realized without thermal pollution between the 16 parallel reactors. It was possible to significantly reduce the selectivity to CH_4, even for an Ni catalyst only by tuning the process parameters, resulting in >98% selectivity to CO for the Cu as well as the Ni material (Figure 9). CO productivities reached 2.4 and 129 kg(CO)/kg(cat)/h over the respective materials. Further improvement of the CO productivity is expected when applying even higher GHSV, which is still feasible for hte units.

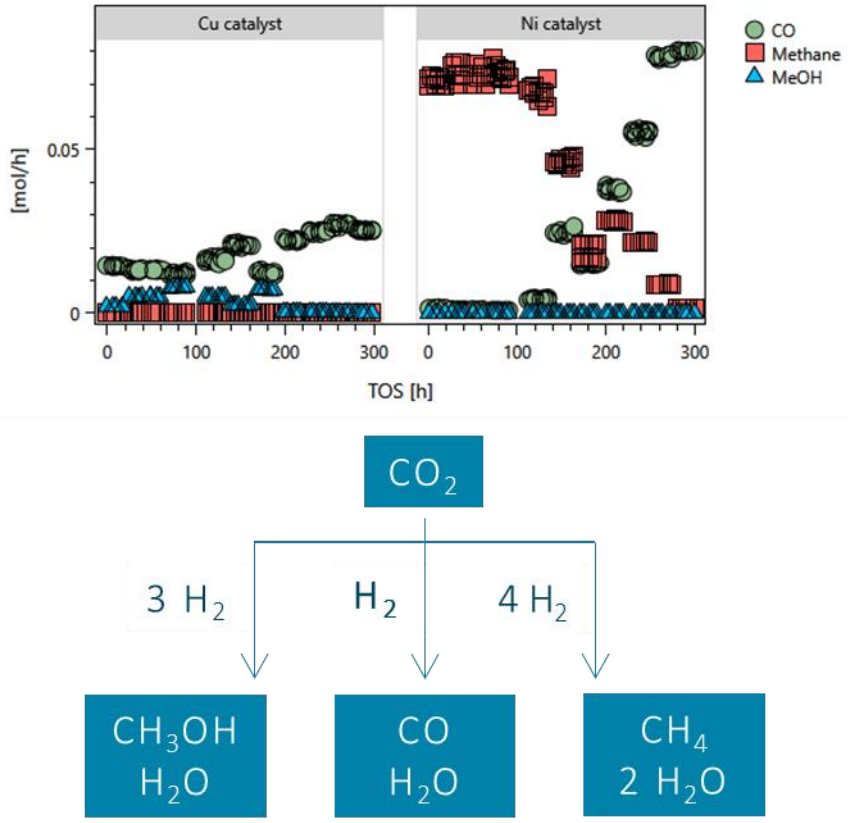

Figure 9: Summary of parameter tuning toward high the CO production of commercial Cu and Ni catalysts.

The present paper demonstrates the benefits and feasibility of high throughput testing for applications at elevated temperatures. Material screening and process optimization toward high selectivity to CO can be significantly accelerated, outperforming single-fold testing units, and enabling rapid, cost-effective innovations to allow our customers to stay ahead of the competition.

References

[1] F. Huber, P. Kolb, B. Mutz, C. Schulz, R. Henkel, M. Weber, J. Stalica, C. Traut, *"Carbon management - 7 Opportunities for improving the carbon footprint through CO_2 utilization"*, White paper, http://www.hte-company.com/en/industries/co2sday/white-paper-carbon-management

[2] F.V. Vázquez, P. Pfeifer, J. Lehtonen, P. Piermartini, P. Simell, V. Alopaeus, Industrial & Engineering Chemistry Research, 56, 13262, (2017).

[3] A. Haas, C. Hauber, M. Kirchmann, ACS Catalysis, 9, 5679, (2019).

[4] https://ineratec.de/ico2chem-press-release/

[5] https://ineratec.de/en/ineratec-and-clariant-joined-forces-for-a-cleaner-future/

[6] https://matthey.com/en/news/2022/hycogen

[7] T.S. Christensen, K. Aasberg-Pedersen, P.M. Mortensen, *"eFuels technology for converting CO_2 and renewable electricity to renewable synthetic fuels"*, White paper, www.topseo.com/g2l

[8] P. Kaiser, R.B. Unde, C. Kern, A. Jess, Chemie Ingenieur Technik, 85 (4), 489, (2013).

[9] Y.A. Daza, J.N. Kuhn, RSC Advances, 6, 49675, (2016).

[10] M. Juneau, M. Vonglis, J. Hartvigsen, L. Frost, D Bayerl, M. Dixit, G. Mpourmpakis, J.R. Morse, J.W. Baldwin, H.D. Willauer, M.D. Porosoff , Energy & Environmental Science, 13, 2524, (2020).

[11] M. Zhu, Q. Ge, X. Zhu, Transactions of Tianjin University, 26, 172, (2020)

[12] T.S. Galhardo, A.H. Braga, B.H. Arpini, J. Szanyi, R.V. Gonçalves, B.F. Zornio, C.R. Miranda, L.M. Rossi, Journal of American Chemical Society, 143, 4268, (2021).

[13] C. Knobloch, A. Haas, T. Kaltschmitt, *"Accelerated Catalyst Testing for Synthesis Gas Based Reactions"*, DGMK Tagungsbericht (2015).

[14] J. Berg, A. Haas, F. Huber, M. Kirchmann, C. Liebold, *"High Throughput Testing of Resid Hydroprocessing & Naphtha Reforming Catalysts"*, DGMK Tagungsbericht (2016).

[15] P. Kolb, T. Kaltschmitt, *"Methanol Synthesis in a Fixed Bed Recycle-reactor System: Effect of once-Through and Recycle Operation on Activity and Productivity"*, DGMK Tagungsbericht (2017).

[16] C. Hauber, T. Sauer, *"Big data in catalysis"*, Hydrocarbon Engineering, August (2022).

[17] T.J. Stadler, B. Bertin-Mente, R. Dittmeyer, L.T. Brübach, T. Böltken, P. Pfeifer, Chemie Ingenieur Technik, 94(3), 289, (2022).

[18] R.E. Yakovenko, A.P. Savost'yanov, G.B. Narochniy, V.N. Soromotin, I.N. Zubkov, O.P. Papeta, R.D. Svetogorov, S.A. Mitchenko, Catalysis Science & Technology, 10(22), 7613, (2020).

[19] C. Schulz, P. Kolb, D. Krupp, L. Ritter, A. Haas, M. Soorholtz, T. Emmerich Maldonado, T.B. Thiede, C. Knobloch, Catalysts, 11, 352, (2021).

[20] T. Roberts, K. Dannenbauer, F. Huber, *"Test for success - enhanced laboratory testing supports Fischer-Tropsch wax upgrading technology development for sustainable fuels"*, Hydrocarbon Engineering, September (2020).

High Throughput Catalyst Evaluation of Commercial Hydrogenation Catalysts for Processes with High Hydrogen to Feed Ratios

E. Lorenz[1], T. Zimmermann[1], M. Dahlinger[1], J. Haertle[1], A. Higelin[1], N. S. Govender[2], S. Teli[2], A. A. Almathami[3]
[1] hte GmbH, Heidelberg, Germany [2] Sipchem, Al Khobar, Saudi Arabia, [3] Prince Mohammed Bin Fahd University, Al Khobar, Saudi Arabia

Abstract

Butanediol is an important intermediate for the production of polymers and agricultural products. It can be manufactured starting from different feedstocks. The fastest growing process is the gaseous reaction starting from butane via maleic anhydride and dimethyl maleate to form butanediol with high selectivity. Sipchem, which is a globally recognized manufacturer of base chemicals, intermediates, and polymers, requested a catalyst performance test to assist the catalyst selection for the next turnaround. hte supported this task by performing an accelerated catalyst aging study on a 16-fold high throughput catalyst screening system.

The herein investigated reaction is a multi-step selective hydrogenation that is operated under high hydrogen to substrate ratios on an industrial scale. Such conditions are routinely practiced for vapor phase hydrogenations, e.g. butanediol from dimethyl maleate, fatty acid methyl esters to fatty alcohols, or nitroaromatics to aromatic amines.

Herein, we describe how the process was successfully transferred to the laboratory scale. The entire parameter space relevant for commercial application was screened at a closed mass balance. The high severity protocol for accelerated aging included a variation of the reaction temperature, total pressure, and feed concentration for 16 different spatial catalyst arrangements in parallel. The tested catalyst showed very high activity with a product yield close to thermodynamic equilibrium, suppressing the formation of side products to a minimum. We observed excellent stability within 500 hours-time-on-stream at 24/7 operation.

Sipchem was impressed by the data quality and reproducibility. hte's proprietary solutions for advanced big data handling provided a fast and convenient way to evaluate the results by selective clustering. These results facilitated the further decision process for the next catalyst change out.

The content of this article refers to the publication in [5].

Introduction

1,4-Butanediol (BDO) is an important intermediate for the manufacture of polymers as well as agricultural and nutrition products. From a commercial perspective, BDO can be produced starting from different feedstocks. The most prominent examples are the REPPE, MITSUBISHI-KASEI, and DAVY process, as shown in Figure 1. The former two, especially REPPE, are well established and were optimized over decades. However, they start from acetylene and butadiene, which are hazardous feedstocks and difficult to handle, thereby resulting in larger and more complex unit operations with a lack in process efficiency.

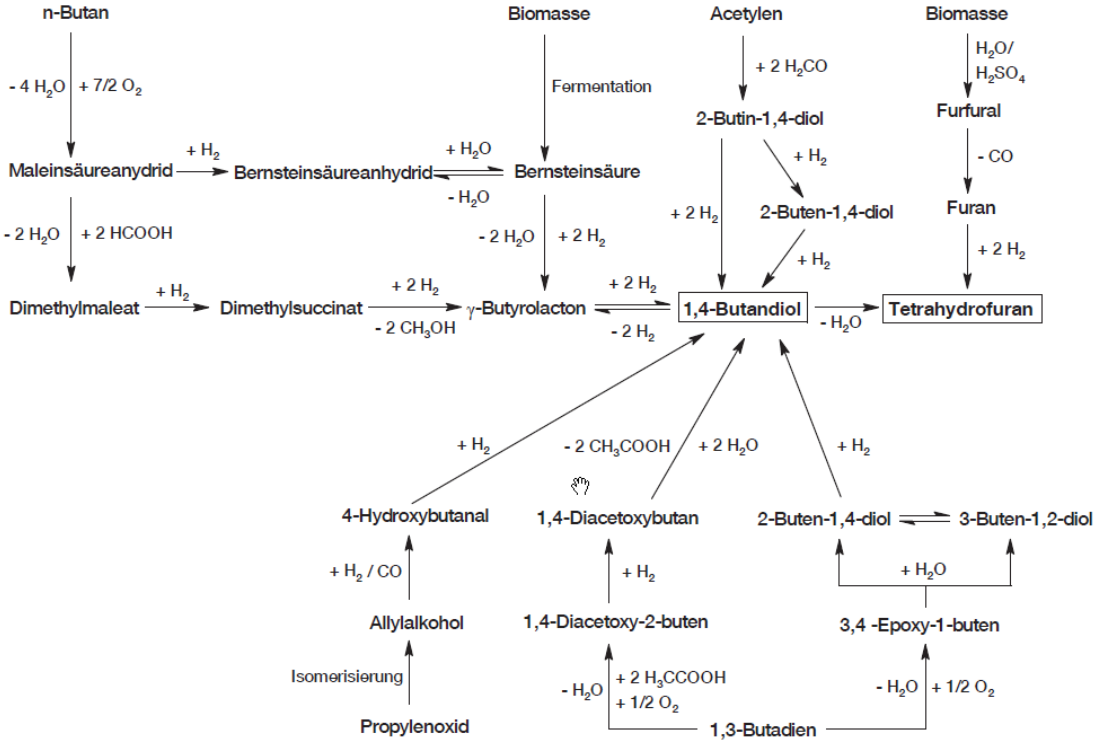

Figure 1: Commercial production routes of 1,4-Butanediol, including the REPPE-process (starting from acetylene), MITSUBISHI-KASEI-process (starting from butadiene and acetic acid), and DAVY-process (starting from n-butane) [1].

The industrial DAVY-Process considers the BDO synthesis by the selective hydrogenation of dimethyl maleate (DMM) in the gaseous phase via γ-Butyrolactone (GBL) as an intermediate. This route starts upstream from n-butane, which provides low costs and easy handling. By the choice of the reaction conditions, the produced BDO can be shifted to the consecutive product Tetrahydrofuran (THF), which is also a valuable feedstock for polymer synthesis. It is in this way that the DAVY-process competes with the conventional routes by gaining in product flexibility, milder process conditions, and driving down the overall investment. Sipchem, a global manufacturer of base chemicals, intermediates, and monomers, requested hte to carry out a benchmarking study to assist the catalyst selection process for the next turnaround of the commercial unit. The evaluation and selection of the right catalyst that meets the technical and commercial requirements was accelerated together with our customer using high throughput technology. A 16-fold unit has been used to test different catalysts and spatial arrangements in parallel at various temperatures, pressures, and feed concentrations. The major challenge was to cope with the complex oxygenate analytics as well as the enormous hydrogen flow rates.

Experimental

Davy type selective hydrogenations require moderate temperatures and elevated pressures. The major challenge, however, is to provide an enormous excess of hydrogen and to control the H2:DMM molar feed ratio. A 16-fold high throughput setup has been used for the screening. Figure 2 shows the filling scheme of all 16 reactors, and the experiments for which they were filled are described in the boxes underneath. Two commercial shaped catalysts have been tested, both comprising a typical composition to be active for selective hydrogenation reactions. The physical and chemical properties of the materials will not be specified in more detail within this report. The basic structure of the reactor filling was similar for all 16 positions. Stainless steel reactors with an inner diameter of 5 mm and 400 mm length have been mounted to the unit. On the top of each reactor, an inlet zone of silicon carbide (SiC, F46) provided a uniform heat transfer to the inlet flow. Furthermore, a plug flow pattern was ensured by the selection of the appropriate particle size in this section. Both catalysts were crushed and sieved to meet the requested particle size distribution. A stacked bed of both materials was placed in the catalyst zone wherein catalyst one (yellow) was acting as a guard bed layer and catalyst two (green) represents the main conversion layer. They were separated by a thin glass wool layer to avoid mixing. Both catalysts have been diluted with SiC (F100) in the same ratio to distribute the reaction heat across the catalyst bed and to enhance the overall heat withdrawal. An outlet zone, filled with silicon carbide (F46), closed the packing, sealed on the top with a second glass wool layer protecting the catalyst from getting carried downwards.
A high throughput unit served to carry out the catalyst testing, allowing for a fast screening of up to 16 catalysts in parallel. Hydrogen, Argon, and Nitrogen (Air Liquide N5.0) were dosed by mass flow controllers, dimethyl maleate (Sigma Aldrich, purity 96%, 4% DMF) was fed by a syringe pump for a precise control of the inlet rate. Subsequently, it was evaporated at 180°C within a hydrogen flow running H2:substrate ratios far beyond 50:1. The gaseous feed flow was equally distributed to the 16 reactors. Each reactor could be heated individually to the desired temperature by electrical resistance heaters. The isothermal conditions (+/- 1K) in every reactor could be processed on a length of 140 mm and were ensured by validation experiments upfront to the screening. The control of the reactor pressure was carried out by using a backpressure regulation with downstream inert gas dilution.
The analytics section comprised a hot gas flow meter to close the flow balance across the reactors and, furthermore, two gas chromatographs (GC7890). The GC were equipped with TCD and FID detectors in order to analyze the permanent gases, such as H2, N2, and Argon, and the hydrocarbons. The detection of oxygenates is the most demanding among all the component species in the reactor effluent since some of them have a poor signal response, and especially heavier molecules are difficult to calibrate. To solve this problem, the FID detector has been upgraded by a Polyarc. Using this technology, the effluent in the FID sample loop undergoes a sequence of total combustions and methanation after passing the GC column. It is in this way that only methane will enter the FID and supply a clear response for every component and, furthermore, an easy calibration of the GC setup. Figure 3 shows a sample of a FID-Polyarc chromatogram with the hydrocarbon spectrum. The design of the entire downstream section was optimized to cope with the pressure drop in consequence of the high hydrogen feed rates. The offgas-treatment comprised a condensation vessel to remove heavy hazardous substances like THF from the effluent, and the resulting gas flow was emitted to the environment. Different spatial catalyst arrangements have been tested with varying reactor temperature, total pressure, and H2:DMM molar feed ratio to describe the activity, selectivity, and decay. The mass ratio between both stack layers has been varied (positions 2 to 5), and different residence times were realized by filling different catalyst masses (positions 6 to 9) at an equal layer mass ratio. Single layer arrangements (positions 10 to 12) as well as duplicates for the purpose of reactor-to-reactor reproducibility (positions 14 to 16) were also investigated.

A fully integrated digital workflow supported the screening and data evaluation. Each parameter, e.g. filling heights, bulk densities, surface areas, etc., could be uploaded to a central database for structure performance correlation.

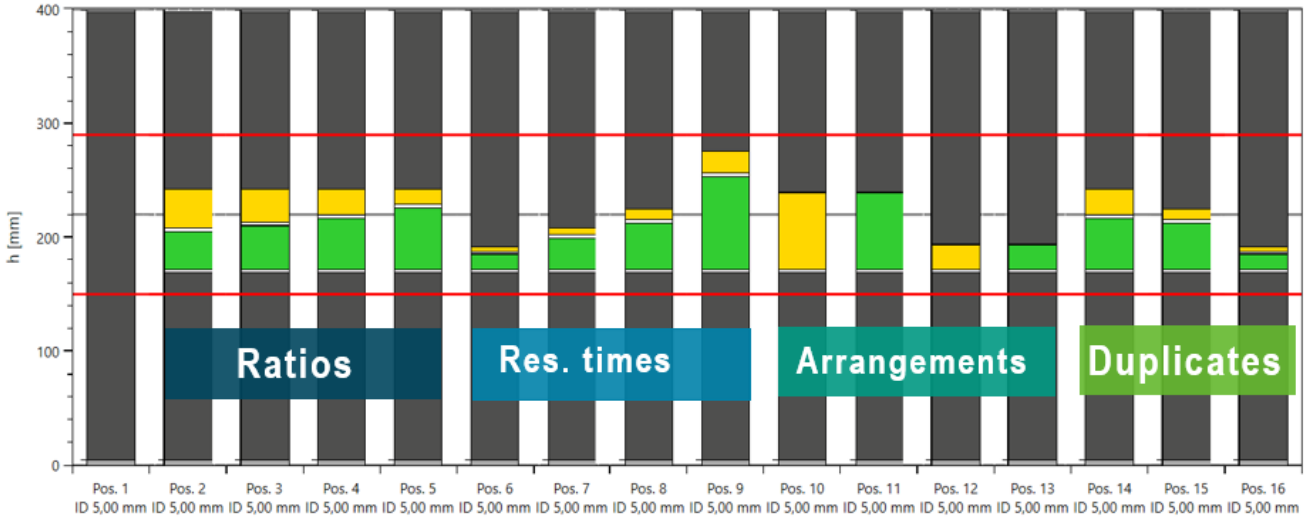

Figure 2: Reactor filling design of the 16-fold high throughput setup with a stacked bed fillings guard bed (yellow) and conversion bed (green) [4].

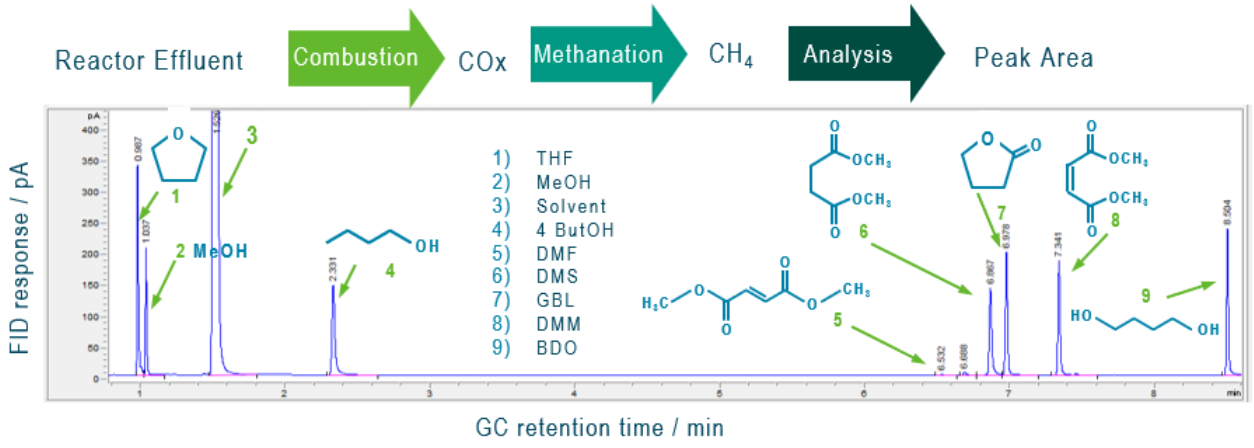

Figure 3: Chromatogram of the FID-Polyarc including the main components of the reaction, [4].

The data has been evaluated using equations (1) modified residence time, (2) conversion, and (3) carbon-based selectivity.

$$\tau_{mod} = \frac{m_{Cat}}{\dot{V}_{inlet}} \quad (1)$$

$$X = \frac{\dot{n}^0_{Ester} - \dot{n}_{Ester}}{\dot{n}^0_{Ester}} \quad (2)$$

$$S_{i,C} = \frac{\dot{n}_{Product,i} \cdot C_{number}}{(\dot{n}^0_{Ester} - \dot{n}_{Ester}) \cdot C_{number}} \quad (3)$$

Results

The 16 reactor fillings were exposed to 16 experimental conditions resulting in 256 experiments. More than 1,280 data points have been screened within two weeks of runtime, thereby giving detailed insights into the catalyst performance and product rates. A scheme of the reaction network is shown in Figure 4.

The initial hydrogenation of the DMM carbon-carbon double bond is a very fast reaction. Even at low residence time, only small amounts of DMM left could be observed in the effluent. The signal of the dimethyl fumarate isomer (DMF) was neglectable for all the experiments. This observation is in agreement with the literature [2]. Since this first step was measured to be non-rate determining, all ester components (DMM, DMF, DMS) have been considered as one lumped component to simplify the data evaluation. The subsequent hydrogenation of dimethyl succinate (DMS) is yielding GBL and MeOH as a co-product that is not considered to react further. The final conversion of the GBL to form BDO is limited by thermodynamic equilibrium.

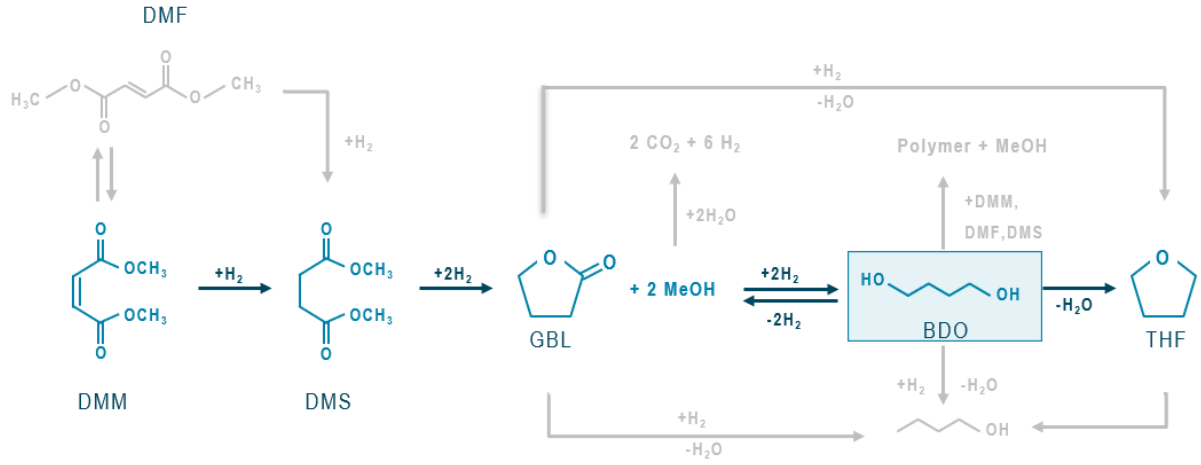

Figure 4: Reaction scheme for the synthesis of 1,4-Butanediol, main reaction pathway (blue), and side-reactions (gray) [4].

Figure 5 shows the calculated GBL equilibrium conversion with dependence on the total pressure, temperature, and H2:DMM molar feed ratio. From a thermodynamic point of view, running high total pressure and low temperature favors the BDO formation. The hydrogen partial pressure has no influence under the given conditions since it is dosed far in excess for all the feed compositions considered. If the catalyst provides acidic sites, BDO can be converted in a consecutive dehydration reaction to THF, especially when processing beyond

200°C at very long residence times. Another BDO consuming side reaction is the formation of n-butanol or heavies. The latter ones are of polymeric nature and they are reported to be formed from both BDO and/esters and are strongly dependent on the hydrogen dilution [2,3].

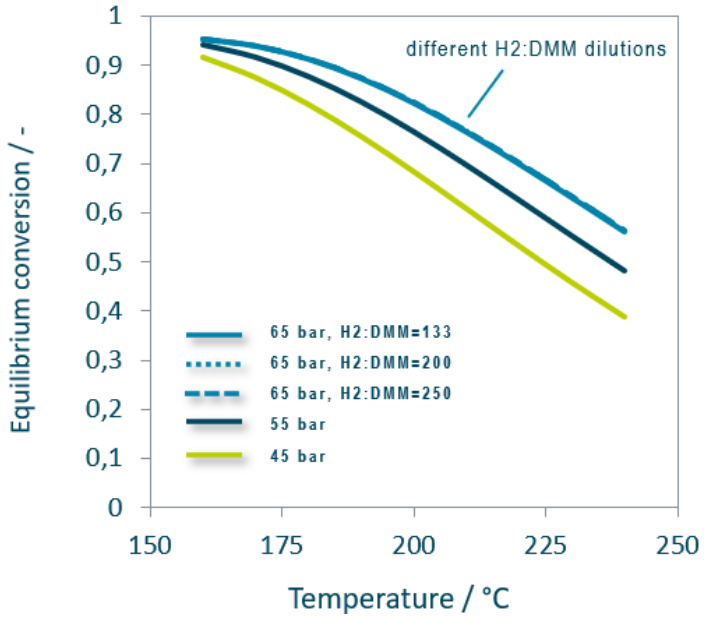

Figure 5: Equilibrium conversion for GBL to BDO reaction for different temperatures, total pressures, and H2:substrate dilution ratios, [4].

The carbon balance has been closed for all of the experiments; an abstract is shown in Figure 6. Since all of the substances, especially the main product BDO, are prone to condense, the mass balance reacts very sensitively to changes in the temperature or feed dilution and requires precise unit control. Figure 6 shows two examples that compare the dew point curve of BDO with the calculated partial pressure of BDO for a given Ester conversion at different H2:DMM feed dilutions (upper charts) and reactor temperatures (lower charts) in relation to the carbon balance. Ester conversion has been close to 100% for the shown experiments. The product consisted almost exclusively of BDO and MeOH. Investigating high BDO product concentrations at low temperature and elevated pressure means in turn to approach the dew point line (blue dots, green dots). If the temperature or substrate dilution fall below a certain level (dashed lines), condensation was observed, which was represented by a sudden gap in the carbon balance (red dots). For these conditions, the calculated BDO product partial pressure exceeds the dew point curve which is in good agreement with the experimental results. By increasing the feed dilution or temperature again above this critical level after a condensation incident, the carbon balance could be restored. All 16 reactors run with a precise process control as highlighted by this example.

hte's proprietary software allows for optimized big data handling by providing a facile clustering and filtering of the bulk data for enhanced performance correlation.
Figure 7 (left chart) shows the ester conversion versus the modified residence time of reactor positions 5 to 9 at different reaction temperatures. The commercial catalyst system is characterized by high activity, and a very short residence time needs to be approached to run differential ester conversion. Higher temperatures lead to higher ester conversion, while the maximum temperature investigated was far from endangering the sintering of active metals on the catalyst surface.

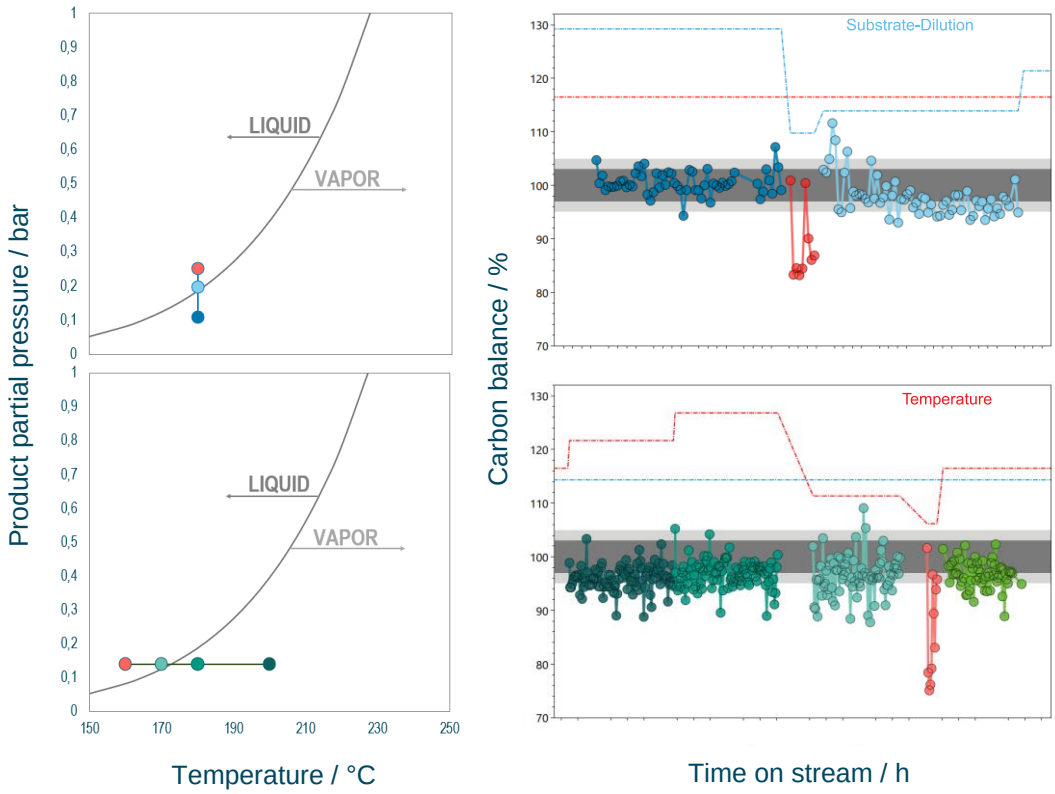

Figure 6: Carbon balance during variation of H2:DMM dilution (upper right chart) and reactor temperature (lower right chart) in comparison with the corresponding BDO product partial pressure (Left charts), [5].

This conclusion was affirmed by run-to-run reproducibility experiments that ensured stable conversion (crosses) and selectivity (not shown) over the entire runtime. Increasing the partial pressure of the substrate also leads to elevated conversion.
The selectivity vs. ester conversion pattern reflects the reaction scheme from Figure 4. GBL (blue squares) is potentially observed as the initial product from the ester hydrogenation. This is assumed by extrapolating the selectivity curve approaching zero ester conversion.
MeOH was co-produced with GBL at stable selectivity with increasing ester conversion.
The results do not suggest a secondary reaction that consumes MeOH. No alkylated products were found, and the temperature was always below the typical decomposition temperatures.

With proceeding ester conversion the GBL selectivity is almost dropping to zero while the BDO concentration climbs up (yellow circles). When processing very long residence times and high temperatures, selectivity can be shifted to the consecutive product THF (blue tringles) at the expense of the diol, thereby indicating that the catalyst provides acidic sites that are active for the dehydration at higher temperatures.

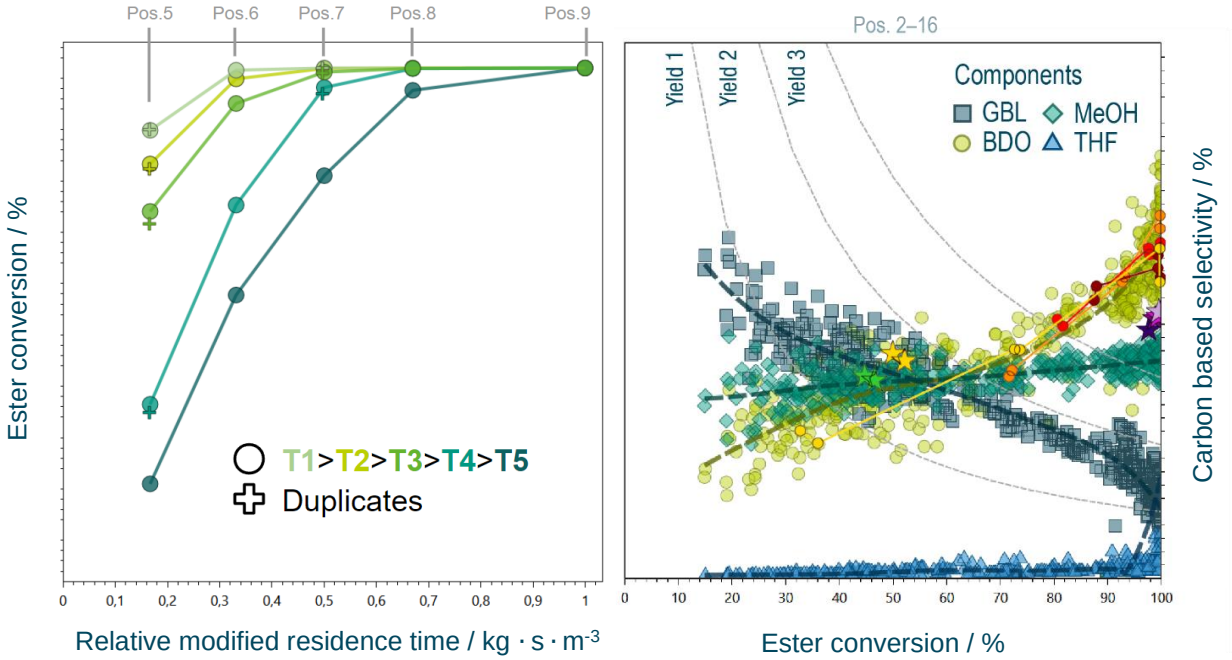

Figure 7: Conversion vs. modified residence time of selected catalyst positions for different temperatures at a constant total pressure H2:DMM feed dilution ratio and catalyst layer ratio (left chart), Carbon based selectivity vs. ester conversion of main products GBL (squares), MeOH (diamonds), BDO (circles), and THF (triangles) (right chart), [5].

Between 0% and 100% ester conversion, the temperature has no measurable effect on the selectivity, as shown in Figure 7 with red, orange, and yellow circles, representing the different temperature levels.
The purpose of the guard bed layer is to protect the catalyst against impurities and side products and, therefore, serves as stable commercial production without interruption. Reactors 10 to 13 carry single layer filings to compare the performance of both materials.

Yellow (pos. 12) and green stars (pos. 13) show conversion and selectivity of both single loadings at equal reaction conditions. The main conversion layer as well as the guard bed layer run at a similar conversion and product selectivity and, therefore, the data show no significant difference in performance between the two materials. A variation of guard to conversion bed mass ratio (purple stars) reveals that the same BDO yield can be achieved even with a reduced top layer thickness. This would enable lower efforts in the top layer skimming, which is carried out frequently for commercial DAVY type units.

The catalyst operated at very low side product selectivity. The major component found was n-butanol with selectivity of one order of magnitude lower than for THF in the entire ester conversion range. Heavy polymeric substances, as reported in the literature, have been found to a minor extent. After two weeks of runtime, a few grams of solid deposits were caught in the safety condensers underneath the reactors.

Activity and selectivity have been successfully described by the high throughput study, enabling an initial mathematical description of the hydrogenation reaction with respect to the following assumptions. Due to their similar performance, the stacked bed system has been considered as a single catalyst for the modeling task. The model includes all of the rate determining steps that have been observed in the experiments, comprising all the blue highlighted pathways shown in Figure 4 extended the butanol formation step from BDO.

Based on the design of the reactor equipment and the choice of an appropriate reactor packing, the plug flow behavior can be assumed for all 16 tubular reactors. Dispersion has been theoretically characterized, calculating the Bodenstein and Mears criteria. Due to the enormous excess of hydrogen dilution, the volume contraction of the hydrogenation reaction can be neglected. Furthermore, the limitation of bulk diffusion as well as pore diffusion could be excluded experimentally, and isothermal conditions have been ensured upfront to the screening. The overall material balance could be simplified to equation (4).

The power law model was chosen as a formal kinetic approach, according to equation (5). Hydrogen was far in excess within all the experiments and was, therefore, not considered to influence the reaction rates, which was mathematically expressed as a zero-order reaction for this component. DMM, DMS, and DMF have been lumped as a single component, as described above. The rate coefficient was described by the Arrhenius equation (6). Matlab © was used to calculate the model for every single pathway simultaneously.

$$\frac{dc_i}{d\tau} = r_i \tag{4}$$

$$r_i = k_i \cdot C_y^{n1} \cdot C_{H2}^{0} \tag{5}$$

$$k_i = k_{\infty,i} \cdot \left(\frac{-E_{A,i}}{RT}\right) \tag{6}$$

Figure 8 shows the comparison of the measured data points and model curves that are in good agreement. The kinetic model that describes the major reaction pathways is supposed to be upgraded in more detail in future screenings in order to describe side product formation and potentially deactivation. A process simulation has been set up using ChemCAD © to show the process optimization with high throughput based kinetic models.

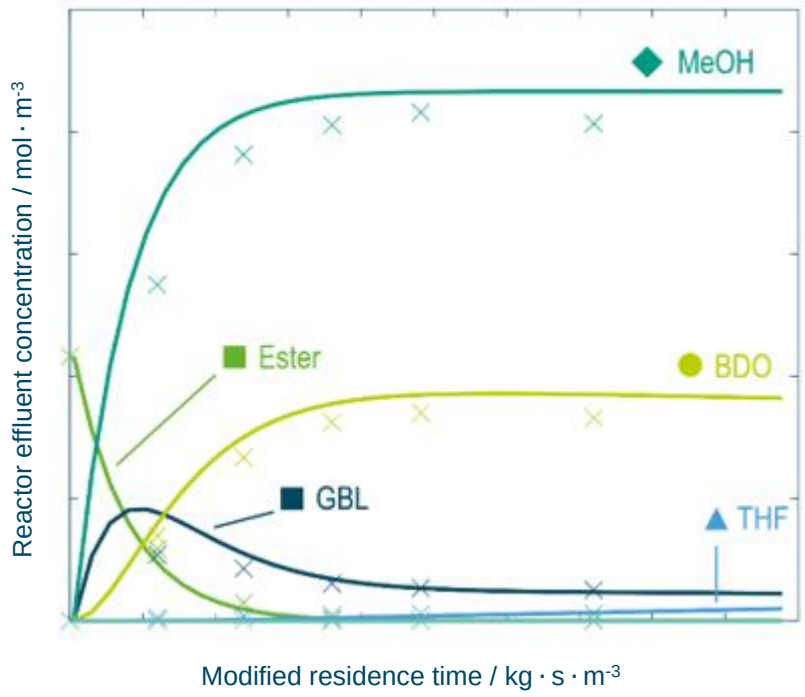

Figure 8: Reactor effluent concentration vs. modified residence time of the main components at a constant pressure temperature and H2:DMM molar feed ratio with the measured data points (crosses) and model data (solid lines), [5].

Conclusions

With this contribution, we show the successful transfer of Davy-type selective hydrogenation from a commercial unit to a high throughput lab scale environment. A commercial stacked bed catalyst system consisting of a guard bed top layer and a main conversion bottom layer was screened using a 16-fold high throughput unit, exposing the catalyst to various conditions.

The catalyst provided high activity and selectivity to the target product BDO at low byproduct formation rates. The catalyst was qualified for commercial use based on the outstanding performance revealed by the high throughput screening.

A basic kinetic model has been created based on the data of the catalyst benchmarking describing the main reaction pathways. The activation energy, frequency factor, and reaction order have been disclosed for every single pathway. This contribution shows how high throughput data can provide the data for the mathematical description of reactions and, in this way, foster kinetic modeling by high throughput experimentation.

Literature

[1] S. Marz, Dissertation, Karlsruhe Institute of Technology (2013)

[2] J. H. Schlander, T. Turek, Ind. Eng. Chem. Res. 38 p. 1264-1270 (1999)

[3] C. Ohlinger, B. Kraushaar-Czarnetzki, Chem. Eng. Sci. 58 p. 1453 (2003)

[4] E. Lorenz, ME-TECH 12th Middle East Technology Forum for Refining & Petrochemicals, Dubai (2022)

[5] E. Lorenz, T. Zimmermann, M. Dahlinger, J. Haertle, A. Higelin, N.S. Govender, S. Teli, A.A. Almathami, Chemical Processing, Issue 11 (2021)

Homogeneous Catalysis for Feedstock Diversification: From Laboratory to Miniplant Scale

F. Lehmann, N. Herrmann, J. Bianga, J. Vondran, T. Roth, T. Riemer, D. Vogt, T. Seidensticker*
Laboratory for Industrial Chemistry, TU Dortmund University, Dortmund/Germany

Abstract

Unsaturated renewables, such as terpenes, oleochemicals, etc. have shown to be promising feedstocks in the synthesis of biobased chemical intermediates in the production of, e.g. polymers, lubricants and surfactants. Homogeneous transition metal catalysis certainly possesses great potential in this regard, considering selectivity, atom economy and mild reaction conditions by selectively attaching various functional groups to C=C double bonds.
In a nutshell: Homogeneously catalysed reactions may contribute to the success of the necessary transformation process of the chemical industry towards feedstock diversification and thus sustainability.
However, for such transformations to become competitive to existing synthesis routes and attractive to be run on a continuous and larger scale, different major challenges remain in the downstream process beyond chemistry: efficient product separation considering sufficient purity, recovery of the precious homogeneous catalyst including recycling, etc., only to name a few. Established concepts already operated in the chemical industry addressing these points are not applicable one-to-one to the conversion of renewables due to their generally higher boiling points, polarity, and the usually very sensitive nature of the applied transition metal catalytic system.
Hence, for all the numerous homogeneously catalysed transformations of renewables towards the synthesis of biobased platform intermediates, novel solutions for sustainable processes must be developed to allow a successful and economically viable transfer on a larger scale.
Some of these concepts developed at TU Dortmund will be highlighted in the present contribution and discussed critically. Among these are thermomorphic solvent (TMS) systems, membrane-assisted separation processes, aqueous biphasic systems and the innovative approach of selective product crystallisation. Additionally, these concepts will be discussed concerning their implementation into continuous miniplant processes.
This contribution aims to highlight the importance of efficient recycling of homogeneous catalysts, to compile the criteria necessary to evaluate those approaches and to stimulate the discussion and further research in this exciting field.

Introduction

Shaping the transformation process in the chemical industry, as a necessarily carbon-based branch of industry, towards greenhouse gas neutrality and sustainability is challenging. Two aspects are of central importance on this path: the so-called defossilisation, which can be achieved e.g. through raw material diversification. Secondly, the development of energy-efficient processes while avoiding waste streams is essential. In the necessary defossilisation away from fossil raw materials and basic chemicals towards renewable raw materials, new and effective ways to synthesise the chemicals and products we know are extremely important. This is because the previously industrially established synthesis routes and process steps cannot be transferred one-to-one to these hitherto industrially underrepresented raw materials. It is therefore important to take an integrated view of the overall process in terms of energy efficiency and avoidance of waste streams at an early stage in the development of conversion processes for these sustainable feedstocks. Only in this way can this transformation process succeed in the medium term.

Innovative processes for manufacturing products based on renewable raw materials can make an important contribution to making the chemical industry more sustainable and thus more future-proof. The main challenge for these bio-based products, such as plastics, surfactants, lubricants, plasticisers, etc., is to make them available in a similar quantity, but also in the same quality as in the petrochemical-based chemical industry.

Renewable raw materials often have complex molecular structures that can be used to direct chemical advantage for certain purposes without the need for complex build-up steps as in petrochemistry. However, the general challenge of renewable raw materials also lies in their molecular structure and elemental composition, because petrochemical base chemicals usually consist only of carbon and hydrogen. In renewable raw materials, on the other hand, oxygen is often present in larger quantities, e.g. in the form of carboxylic acid, aldehyde, ketone and/or alcohol groups. Therefore, it is often necessary to defunctionalise the molecules. In this context, fats and oils occupy a special position among the renewable raw materials, because they are still the most similar to petroleum, which also explains their leading position in consumption in the chemical industry (45 % of all renewable raw materials in the chemical industry in Germany in 2020 were fats and oils). Moreover, they are available in larger quantities as primary ingredients. However, fats and oils always consist of a mixture of various esterified or free fatty acids, which can only be separated into individual components with relatively high effort. For the selective execution of reactions, however, substrates that are as pure as possible are important, which motivates new breeds such as sunflower oil, which contains high oleic acid.

Global production of fats and oils has increased enormously in recent years and decades. In the 2021/22 season, about 212 million tonnes of the major vegetable oils alone have been produced, with palm oil leading the way, followed by soybean, rapeseed and sunflower oils. Median oil prices in 2020/21 in Rotterdam were $1,266 per tonne for soybean oil, $1,350 per tonne for sunflower oil and $1,306 per tonne for rapeseed oil.

Worldwide, about 25 % of oils were used industrially in 2019, for example for the production of biodiesel and oleochemicals or as animal feed. The remaining 75 % was used for human nutrition. This means that the share of industrially used oils increased by about three percentage points compared to the previous decade. Particularly in the last ten years, renewable raw materials have also increasingly been used for energy purposes, such as biodiesel or bioethanol. There is a danger here that without a decoupling of the markets, the industrial and energetic applications will lead to a shortage of staple foods and thus to an increase in food prices.

Oleochemistry is in a state of upheaval: until the 1990s, it was mainly run by large companies from Europe, the USA and Japan, including for example Henkel, Procter and Gamble, Unilever, Akzo Nobel or Kao. This has changed significantly in recent decades for various reasons: Nowadays, continuously operated large-scale plants are necessary for the economic production of oleo basic chemicals. The high investments of 80-100 million US dollars in a complete fatty acid plant with a capacity of 100,000 tonnes per year (including splitting, fractionation and glycerine processing) are only made by companies if they can open up new markets with their products locally if possible. Due to strong competition from Asian companies and the ever-increasing cultivation of oil palms in the Asian region and the associated overcapacities, the profitability of oleochemical basic chemicals has fallen sharply. Due to the rather low profit combined with high capital costs, many traditional oleochemical companies have withdrawn from the market and partly left it to Asian companies. In the long term, a takeover of a large part of the oleochemical production plants in Europe and the USA by Asian companies cannot be ruled out. Opening up new markets and concentrating on special products can counteract this development.

Oleochemistry

In oleochemistry, as in petrochemistry, little chemistry is performed directly with the fats and oils. Instead, a platform of basic chemicals is often produced from feedstocks like in petrochemistry. For example, petroleum contains hydrocarbons that are petrochemically processed into many intermediate and final chemical products. In oleochemistry, the triglycerides are split into glycerol and fatty acids or their derivatives to produce the "basic oleochemicals" fatty acids, fatty esters, soaps, fatty alcohols and the co-product glycerol (Figure 1).

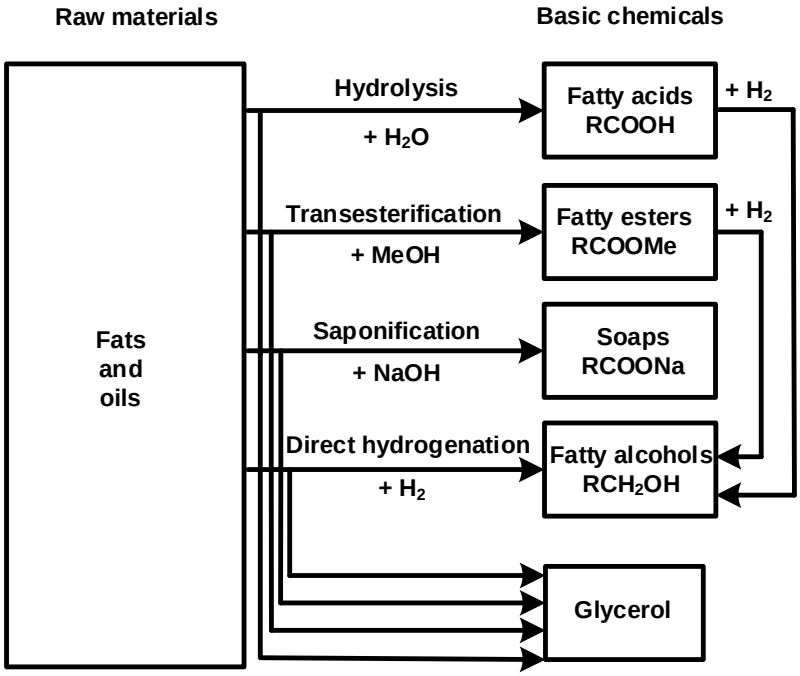

Figure 1: Overview of basic oleochemicals and their production routes

Fatty acids are produced from fats and oil via hydrolysis, whereas fatty acid methyl esters (FAME) are produced via transesterification with methanol. Glycerol is formed as a co-product in ca. 10w% depending on the used raw material. Fatty alcohols, however, are produced from fatty acids or FAME via hydrogenation rather than direct hydrogenation of the raw materials. Particularly fatty alcohols and FAME find several uses as basic chemicals in the chemical industry for the production of detergents, lubricants, etc. Fatty acids and their salts (soaps) are rather being used directly without substantial downstream chemistry.

Fatty alcohols and FAME feature several structural characteristics (Figure 2) that can be utilized for installing new functional groups via functionalization reactions. Thus, platform chemicals for a variety of applications are accessible.

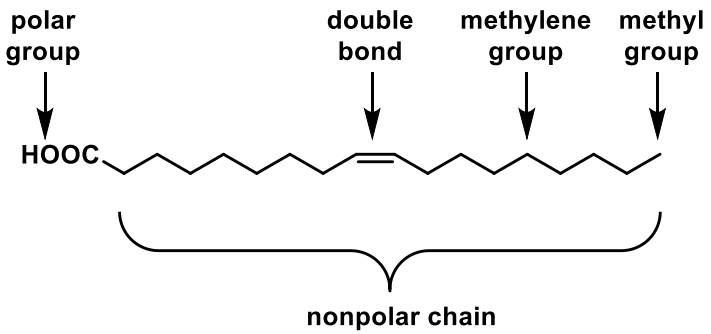

Figure 2: Potential reactive groups of oleochemicals on the example of oleic acid.

Reactions on the unsaturated alkyl chain of oleochemicals

In particular, unsaturated oleochemicals, are very promising for the generation of sustainable products. Their structural properties can be exploited in a targeted manner to generate highly selective e.g., bifunctional molecules as precursors for, for instance, bioplastics. To illustrate the enormous potential of fats and oils in this context, the current statistics of the European plastics market is shared: of 71 million tons of plastics in the EU, only just under 1.1 million tons, and thus less than 2%, are bio-based. With reference to the goal proclaimed by the EU of increasing the share of biobased or renewable raw materials in the chemical industry as a whole to 25% by 2030, there is a very great deal of leverage here. The production of polymer precursors is the most important area of application in the chemical industry.

The functionalization of the C=C double bond of unsaturated oleochemicals (Figure 2), which is necessary for the production of polymer precursors, is achieved particularly efficiently with the help of homogeneous transition metal catalysis. A broad spectrum of possible functional groups can thus be introduced into the molecule, making new platform chemicals available for a bio-based product range.

The advantages of homogeneous transition metal catalysis, such as the high selectivities and mild reaction conditions in the homogeneous liquid phase, coupled with renewable oleochemicals, potentially lead to sustainable manufacturing processes of bio-based products. This approach has been described several times in the academic literature and found to be viable and sustainable. However, so far only very few of the developed homogeneous catalytic functionalization reactions have made it into an industrial application. This is due to the fact that the initial focus of reaction development is of course always on the reaction itself. As a result, process steps for commercial use are rarely taken into account and only very few technically relevant substrates have been used. Homogeneous catalytic functionalization reactions of unsaturated oleochemicals have so far typically been developed and tested using single model starting materials

These challenges, which have not yet been solved, have so far hampered a broad application of homogeneous catalytic functionalization reactions for a bio-based chemical industry. Their great potential can thus not or only insufficiently be exploited. Expanding the research focus to include market-relevant basic oleochemicals and the subsequent separation operation is imperative for the successful implementation of homogeneous catalytic functionalization reactions in the biobased value chain.

In the research at the laboratory for industrial chemistry of the TU Dortmund University, final separation steps are integrated at an early stage of the development of efficient and sustainable homogeneously catalyzed functionalization reactions of oleochemicals. In this research approach, a holistic concept, and its practical implementation in continuously operated laboratory plants (so-called miniplants) is being developed, which allows the selective conversion of oleochemicals, which are not in competition with food production, into

bifunctional, biobased molecules. On the one hand, these can be integrated into the existing structure of the chemical industry as drop-in solutions and, on the other hand, new material properties can be generated for novel applications.

In the following, two exemplary reactions are presented, that are currently under investigation at our laboratory, name oxidative cleavage reactions (Figure 3) and carbonylations (Figure 4 and Figure 5).

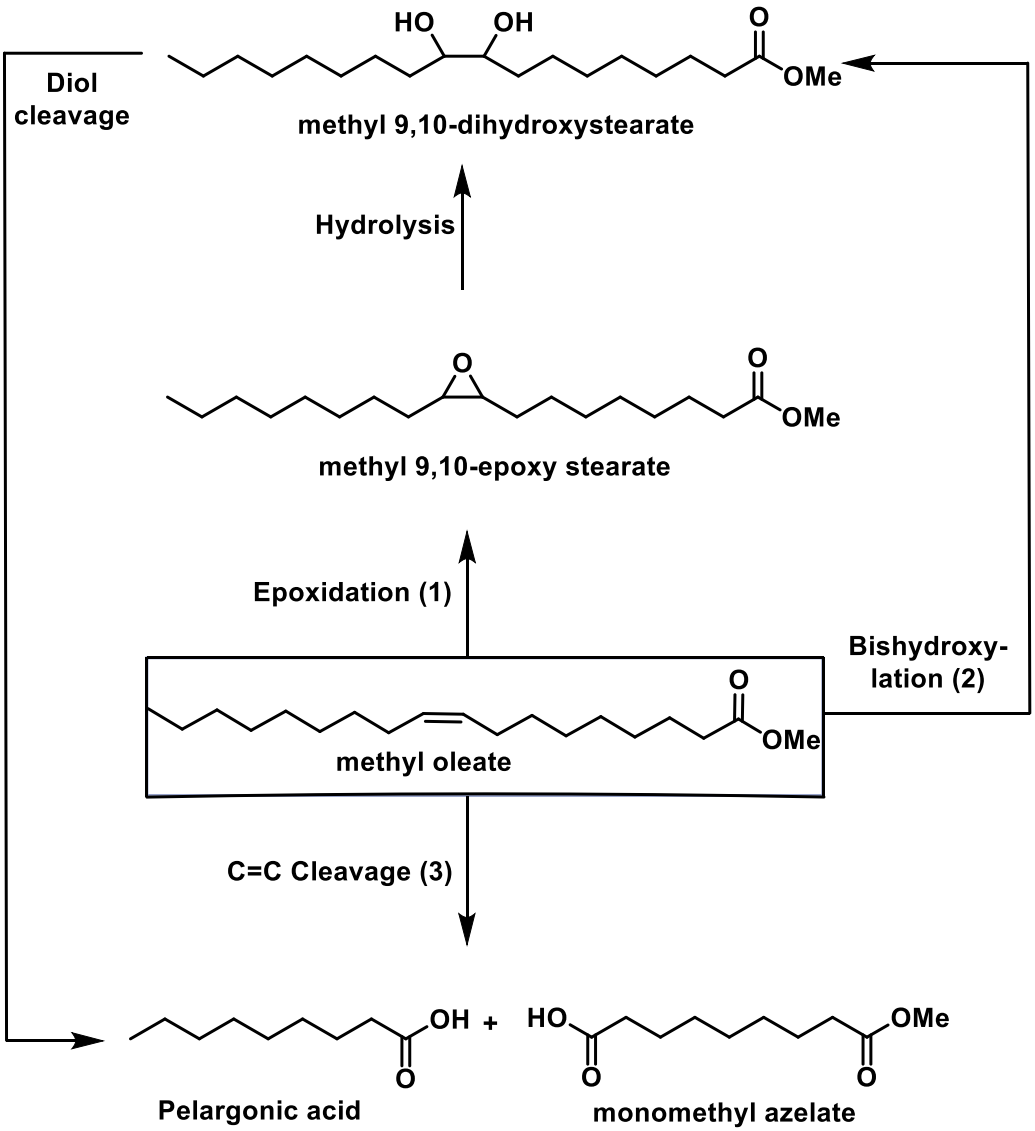

Figure 3: Reactions pathways for methyl oleate under oxidative conditions

Epoxidation products of oleochemicals (such as epoxy stearate, Fig. 3) have many uses, especially in the plastics sector. They make excellent plasticizers and are used as flame retardants, antioxidants as well as light stabilizers. Soy epoxides, in particular, are used extensively in polyvinyl chloride and related polymers because they scavenge the hydrogen chloride in a chlorine-containing plastic that is split off by the influence of heat or light, thus protecting it from further autocatalytic, i.e. self-accelerating, degradation of the polymer.

The epoxide group can also enter numerous catalyzed subsequent reactions, probably the most important of which is ring opening by hydrolysis with water, producing a vicinal diol. In addition, further reactions to polyols for polyurethane foams or products with pharmacological properties are possible due to a nitrogen atom introduced into the triple ring.

Based on the homogeneously catalyzed reaction systems using a Ru-catalyst already developed for the catalytic, oxidative cleavage of methyl oleate with the sustainable and benign oxidant hydrogen peroxide, work on the development of an associated recycling concept based on the use of multiphase systems is targeted in our work.

The oxidative cleavage consists of three sequential partial reactions: Epoxidation of methyl oleate, hydrolysis of the resulting epoxide and oxidative cleavage of the diol (Fig. 3). The Ru-based catalyst system known from the literature was first used in the epoxidation.[1] The reaction was carried out in homogeneous solution. However, a multiphase system was shown to be successful in catalyst recycling: by adding an extractant, the formed epoxide could be removed from the reaction mixture. Using GC-FID and determination of the epoxide number as complementary analytics, the yields of epoxide were determined. The catalyst remains in the aqueous reaction solution, which is recycled after extraction. Since hydrogen peroxide is used as an aqueous solution (50wt%), water emerges as a co-product from epoxidation with hydrogen peroxide and excess hydrogen peroxide decomposes to oxygen and water, however, the influence of the increasing water content must be investigated in the context of catalyst recycling and checked for possibilities of water separation. It was already evident from targeted interference tests that an increase in the water content leads to poorer catalyst productivity. Therefore, water removal was first investigated by means of distillation, whereby the catalyst was recycled 13 times. The catalyst productivity, measured as TON, was thereby increased from originally 200 to almost 1200 within seven recycling runs. Further catalyst recycling hardly leads to an increase in productivity. Through a cooperation with the Chair of Fluid Process Engineering at the TU Dortmund University, pervaporation was finally investigated as an alternative and elegant method for water separation in the homogeneous, Ru-catalysed epoxidation of oleic acid methyl ester. The catalyst was efficiently retained by the membrane used and still showed excellent activity in a further recycling run. The decisive advantage of pervaporation is the selective separation of water from the reaction mixture, whereas in distillation water can only be removed as part of an azeotrope with the solvent acetonitrile.

The oxidative cleavage of methyl oleate was also investigated with a W catalyst, tungstophosphoric acid.[2] This offers the advantage of a very high molar mass (2880 g/mol), which makes retention by means of a membrane appear promising. The catalyst is known from the literature mainly in two-phase reaction systems in the presence of a phase transfer reagent. Here, selectivity is often a challenge due to undesirable, and largely unexplained, side reactions. In this project, the W-catalyst system will first be investigated in a homogeneous reaction system. The aim is to achieve at least a comparable selectivity as in the examples known from the literature, since it is assumed that the selectivity can be improved in a homogeneously catalyzed reaction system. The analysis is carried out by means of GC-FID. The most important influences on the selectivity are to be identified so that optimization can take place. Finally, the retention of the catalyst will be checked by means of organophilic nanofiltration in the continuous operation of a membrane system already available at the chair.

After the Ru-catalyzed epoxidation of methyl oleate was investigated in batch operation, the hydrolysis of the epoxide is added as a second sub-step.[3] This also takes place in a homogeneous reaction solution. The sequence of epoxidation and hydrolysis is transferred directly to a tubular reactor and optimized to enable the continuous production of the diol. However, the modular design of the tubular reactor also enables the simple, continuous synthesis of the epoxide. Further functionalization of the epoxide and diol in continuous operation are conceivable through specific extensions. By choosing the solvent, the different solubility properties of the substrate, epoxide and diol can be used: The diol has a relatively high melting point and is poorly soluble in the chosen acetonitrile/water system. By collecting the reaction solution and coolingit, the diol can therefore subsequently be crystallized out of the reaction solution without the need for further organic solvents.

Hydroformylation is probably one of the best-known reactions that has been carried out

industrially with petrochemical substrates for a long time. In this process, suitable unsaturated substrates are reacted with synthesis gas, a 1:1 mixture of carbon monoxide and hydrogen, on homogeneous transition metal catalysts to form aldehydes. These can then react with further hydrogen to form primary alcohols. Worldwide, this reaction with petrochemical substrates is already carried out in technical plants with capacities of about 12 million tonnes per year. The hydroformylation of oleochemicals has also been known since the beginnings of hydroformylation in 1938. The reaction is shown in Figure 4 for methyl oleate: The formyl group can be added at both the C9 and C10 positions. Depending on the catalyst used, an isomerisation of the C=C double bond can also take place in advance, so that the formyl group can be found at many different C atoms. Such isomerising hydroformylation is particularly interesting if the terminal carbon atom is selectively hydroformylated. ω-Functionalised oleochemicals are then formed, which can be used for the synthesis of unbranched polymers. An undesirable side reaction during hydroformylation is the hydrogenation of methyl oleate with hydrogen from the syngas to the fully saturated methyl stearate.

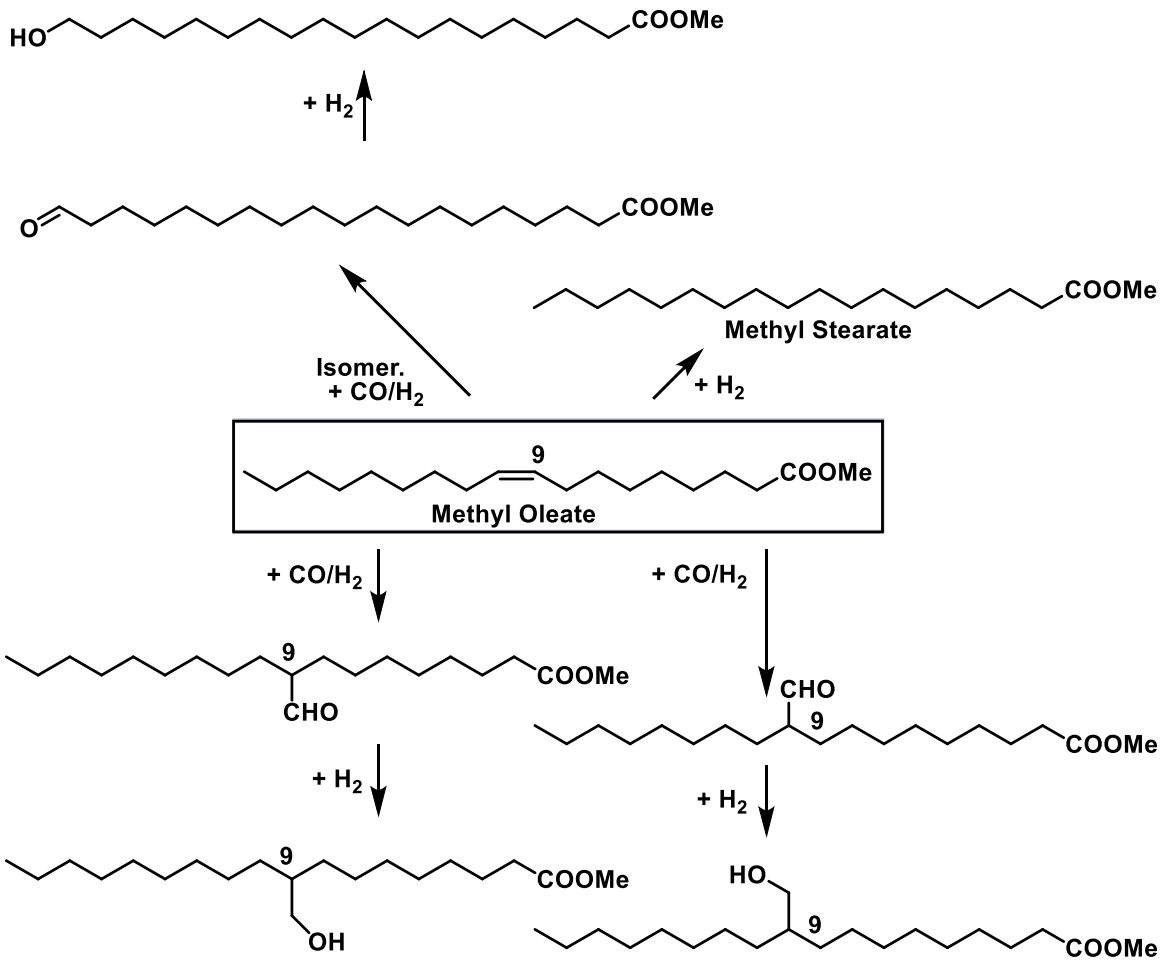

Figure 4: Hydroformylation of methyl oleate as an example of carbonylation reactions of unsaturated oleochemicals (including corresponding reaction network)

At the laboratory for industrial chemistry at TU Dortmund University, we are working on efficient recycling techniques for the precious and thus expensive Rh catalyst. One means of realizing an efficient separation of the nonpolar product phase as a prerequisite for catalyst recycling is the use of so-called multiphase system. In our particularly green approach, we use water as the catalyst containing polar phase to ensure efficient separation after reaction. Activity is, however, affected since mass transport between the two liquid phases is limited. To overcome this issue, we are working on different approaches: One is the use of mediating co-solvents such as isopropanol.[4] In that system, the homogeneous Rh catalyst was successfully reused in several runs, always forming a pure organic product phase, which facilitates down-stream

operation. Current investigations are performed to transfer this reaction system into continuous operation. We assembled a miniplant consisting of a continuously stirred tank reactor (CSTR) and a decanter for phase separation. First runs look very promising and the corresponding results will be presented soon. Another means of overcoming mass transport limitations in liquid-liquid biphasic systems is the use of intensified reactor concepts. We have shown that the use of a Jet-Loop Reactor is beneficial for creating large interfacial areas to increase mass transport and thus performance of the overall system.[5] For two different substrates, namely methyl oleate and methyl 10-undecenoate (from cracking castor oil) this approach was successfully demonstrated. We are now working on the continuous operation of that Jet-Loop reactor in combination with a decanter for phase separation. The status of these investigations will also be presented soon.

Another carbonylation reaction which is very promising for upgrading unsaturated oleochemicals is methoxycarbonylation. For instance, methyl oleate is converted with carbon monoxide and methanol using a homogeneous diphosphine modified Pd catalyst to selectively yield dimethyl 1,19-nonadecanoate.

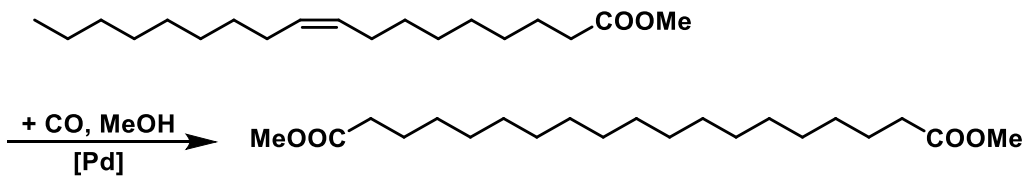

Figure 5: Isomerizing methoxycarbonylation of methyl oleate yielding a linear diester as promising polymer precursor.

This special Pd/diphosphine catalyst system is capable of isomerizing the double bond along the chain and selectively attaching the ester group only at the very end of the carbon chain. The corresponding diester is a very promising polymer precursor for polyesters, which on the one hand are biodegradable and on the other hand possess properties similar to polyethylene.

One drawback so far is the limited activity of that catalyst system. We could show that selective product crystallization is efficient for separating a pure product from the Pd-containing methanol phase.[6] The latter was successfully recycling in several batch runs and the total turnover number of the Pd catalyst thus significantly increased. Current work focusses on the optimization of crystallization conditions and the use of other oleochemicals, such as methyl 10-undecenoate.[7] This work will be presented and critically discussed in the presentation.

Alternative oleochemicals for feedstock diversification

What most of the oils used so far have in common is that they are either in direct or indirect competition with the production of food: Either they could be used as food, such as palm or soybean oil, or the cultivated land could be used to produce food. In addition, importing non-domestic oils risks dependence on only a few producers. The use of non-edible, locally grown oils as well as the use of waste materials would therefore be optimal. The following oils could meet these requirements:

Algae provide a very high oil yield per area, much higher than conventional oil crops such as soy. By using an equivalent amount of algae oil, a lot of arable land could be made available for other purposes. Industrial algae production ideally does not take place in oceans or lakes, but on land in special reactors. Since there are many different types of algae, no generally applicable oil composition can be given, but many oils have in common that they contain some short-chain, saturated fatty acids such as the laurics lauric and myristic acid as well as palmitic acid. In addition, oleic acid, which has already been well studied, is mainly contained. However, the largest proportion in algae oil is made up of the polyunsaturated omega-3 fatty acids eicosapentaenoic acid and docosahexaenoic acid (Fig. 6). In addition to direct conversion at

one of the double bonds, these could first be selectively hydrogenated and then further converted using the known methods. Furthermore, the use of algae oils as a renewable fuel is being discussed.

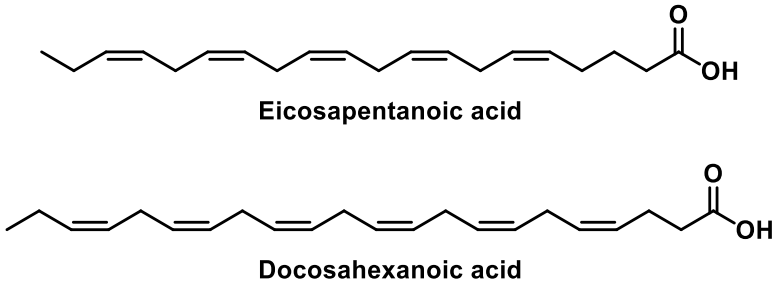

Figure 6: The omega-3 fatty acids eicosapentaenoic acid and docosahexaenoic acid contained in algae oil

Hemp oil is very similar to soybean oil in its composition. It contains a lot of polyunsaturated C18 fatty acids. This makes it suitable as a substitute for soya oil: Hemp is a productive and adaptable crop plant, which can therefore also be cultivated in Germany. In addition to the use of its oil, other parts of the plant can also be used, for example to produce fibres, which makes the degree of utilisation of the plant very high.

Tall oil is produced in a very small percentage during the production of pulp from wood using the Kraft process. In addition to free and esterified fatty acids, it contains hydrocarbons and rosin. For use as an oleochemical raw material, tall oil must first be further purified. The product containing over 90 % fatty acids is called "tall oil fatty acids". High-quality tall oil fatty acids contain over 97 % fatty acids, about half of which are oleic acid and half linoleic acid and their isomers. Already established applications are tall oil fatty acids as dimer fatty acids and as epoxides for stabilising plastics.

Tung oil or Chinese wood oil, as already evident from the name, is obtained from the tung oil tree, which grows mainly in China. It essentially contains small amounts of oleic and linoleic acid, but in particular up to almost 90 % of eleostearic acid (Figure 7), a triple unsaturated C18 acid which, unlike linolenic acid, consists of conjugated double bonds. This means that, as with linseed oil, polymerisation can start very quickly, so that similar areas of application are also possible here.

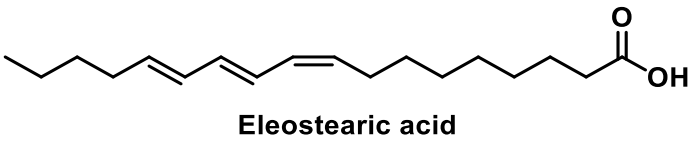

Figure 7: Chemical structure of eleostearic acid found in tung oil.

Finally, an oil is introduced that is not an oil at all according to the chemical definition of fats and oils: the oily cashew nut shell liquid. When cashew nuts are harvested for food purposes, the shell remains as a waste product. This contains a toxic oil, the cashew nutshell liquid, which is accordingly not suitable for food purposes. However, due to the production of cashew nuts, about 450,000 tonnes of liquid are produced worldwide every year. From this, the main component cardanol can be obtained during the processing, a mixture of various long-chain phenol derivatives, whereby the alkyl chain resembles fats and oils (Figure 8). Cardanol derivatives can be used in many ways, especially in the field of polymer chemistry, since not only can the double bonds of the alkyl chains undergo reactions, but conversions can also take place on the aromatic ring. Examples include dimerisation, metathesis, epoxidation and sulphonation. Further research on conversions of cardanol is being conducted worldwide.

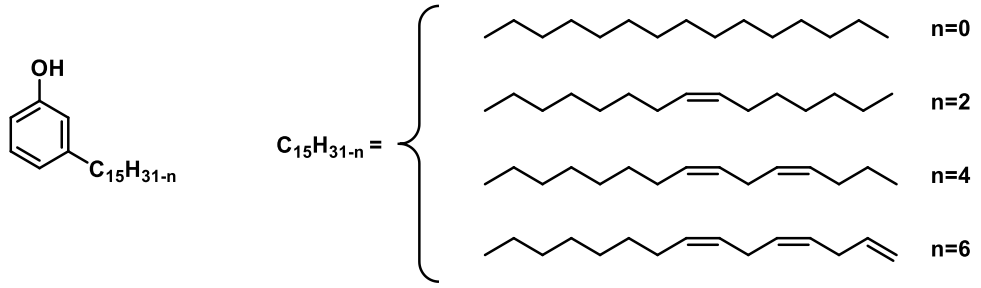

Figure 8:Chemical structure and composition of cardanol, available from cashew nutshell liquid.

References:

[1] J. Vondran, J. Pela, D. Palczewski, M. Skiborowski, T. Seidensticker, „Curse and Blessing–The Role of Water in the Homogeneously Ru-Catalyzed Epoxidation of Technical Grade Methyl Oleate", *ACS Sustainable Chem. Eng.* **2021**, 9, 34, 11469–11478.

[2] J. Vondran, M. Peters, A. Schnettger, C. Sichelschmidt, T. Seidensticker, "From tandem to catalysis – organic solvent nanofiltration for catalyst separation in the homogeneously W-catalyzed oxidative cleavage of renewable methyl 9,10-dihydroxystearate", *Catal. Sci. Techn*., **2022**, *12*, 3622-3633.

[3] J. Vondran, T. Benninghoff, A. Emminghaus, T. Seidensticker, "Catalytic Synthesis of Methyl 9,10-dihydroxystearate from Technical Feedstocks in Continuous Flow via Epoxidation and Hydrolysis", *Eur. J. Lipid Sci. Technol*., **2022**, 124, 2200041

[4] N. Herrmann, J. Bianga, T. Gaide, M. Drewing, D. Vogt, T. Seidensticker, "Aqueous biphasic hydroformylation of methyl oleate: a green solvent-only strategy for homogeneous catalyst recycling", *Green Chem.* **2019**, *21*, 6738–6745.

[5] N. Herrmann, J. Bianga, M. Palten, T. Riemer, D. Vogt, J. M. Dreimann, T. Seidensticker, "Improving Aqueous Biphasic Hydroformylation of Unsaturated Oleochemicals Using a Jet-Loop-Reactor", *Eur. J. Lipid Sci. Technol.* **2020**, *122*, 1900166 p. 1-8.

[6] N. Herrmann, K. Köhnke, T. Seidensticker, "Selective Product Crystallization for Concurrent Product Separation and Catalyst Recycling in the Isomerizing Methoxycarbonylation of Methyl Oleate", *ACS Sustainable Chem. Eng.* **2020**, *8*, 10633–10638.

[7] J. Vondran, A. I. Seifert, K. Schäfer, A. Laudanski, T. Deysenroth, K. Wohlgemuth, T. Seidensticker, "Progressing the Crystal Way to Sustainability: Strategy for Developing an Integrated Recycling Process of Homogeneous Catalysts by Selective Product Crystallization", *Ind. Eng. Chem. Res.*, **2022**, *61,* 9621–9631.

Innovative Heterogeneous Catalysts for the Reduction of Levulinic Acid Derivatives to γ-valerolactone and Consecutive Reduction Products

R. Bacchiocchi[1], T. Tabanelli [1], D. Bianchi[2], F. Cavani[1]
[1]Dipartimento di Chimica Industriale "Toso Montanari", Università di Bologna, [2]Istituto Eni Donegani, Italy

Abstract

Levulinic acid (LA) and its esters (e.g. methyl levulinate, ML) are polyfunctional molecules that can be obtained directly from lignocellulosic biomass by hydrolysis or alcoholysis respectively[1]. Regard to LA valorisation, the most investigated strategy is its hydrogenation toward valuable compounds such as fuel additives, solvents and other added-value chemicals. Most of the published manuscripts on this topic mainly focused on the conversion of LA to γ-valerolactone (GVL) using relatively high pressure of H_2. However, few studies in literature report on the production of consecutive reduction products, namely 2-methyltetrahydrofuran (2-MTHF), 1,4-pentadiol (1,4-PDO)[2], valeric acid (VA) and its ester (e.g. methyl valerate, MV)[3]. In this context, the use of noble metal catalysts supported over acid supports (e.g. zeolites) is reported as a suitable strategy in order to promote GVL over reduction to VA or its esters. **Fig.1** shows the results in terms of ML conversion, GVL yield, MV+VA yield and carbon balance (expressed as yield sum/conversion ratio, Y/C) in function of the reaction temperature, using Rh/H-ZSM-5 as catalyst. Increasing the reaction temperature caused an increase of MV+VA yield with a concomitant decrease in GVL yield. This is mainly due to the strong acidity of the support which promote the ring-opening hydrogenolysis of GVL, usually identified in literature as the rate determining step[3]. Furthermore, a different strategy has been investigated by preparing a bimetallic system supported over silica (i.e. 4wt%Rh4wt%Re/SiO_2). Interestingly, this material shows that is possible to reduce GVL, obtaining 2-MTHF as main product. In conclusion, these preliminary results demonstrate the enhanced catalytic activity of Rh/H-ZSM-5 in promoting the consecutive reduction of GVL to valeric acid and its esters. A completely different behavior was observed using Re-based catalyst, which promotes the selective hydrogenation of carboxylic group[4]. In the near future more efforts will be directed toward the synthesis of Re-based bimetallic catalysts supported on zeolites (e.g. RhRe/H-ZSM-5) with the aim of further improve the catalytic activity and the production of consecutive reduction products, like pentanol.

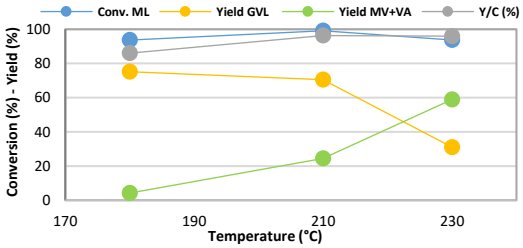

Fig. 1 Reaction conditions: *Solvent free*, P_{H2} = 40 bar; time = 4 h m_{cat} = 5wt% of **Rh/H-ZSM-5**

References:

[1] J. Baruah, B. K. Nath, R. Sharma, S. Kumar, R. C. Deka, D. C. Baruah and E. Kalita, Front. Energy Res., 2018, 6, 1–19.
[2] Y. Cen, S. Zhu, J. Guo, W. Jiao, J. Wang and W. Fan, RSC Adv., 2018, 8, 9152–9160.
[3] K. Kon, W. Onodera and K. I. Shimizu, Catal. Sci. Technol., 2014, 4, 3227–3234.
[4] T. Toyao, S. M. A. H. Siddiki, A. S. Touchy, W. Onodera, K. Kon, Y. Morita, T. Kamachi, K. Yoshizawa and K. I. Shimizu, Chem. - A Eur. J., 2017, 23, 1001–1006.

Toward an Efficient, Continuous-flow, Production of GVL through a Catalytic Transfer Hydrogenation Processes with Ethanol in the Gas Phase

T. Tabanelli[1], L. Conte[1], R. Bacchiocchi[1], E. Paone[2], N. Dimitratos[1], F. Mauriello[2], F. Cavani[1]
[1]Dipartimento di Chimica Industriale "Toso Montanari", Università di Bologna, Bologna, Italy
[2]Dipartimento DICEAM, Università Mediterranea di Reggio Calabria, Reggio Calabria, Italy

Abstract

Levulinic acid (LA) and its esters (LE) are important, polyfunctional molecules that can be obtained from lignocellulosic biomass. Nowadays, the most common strategy for their valorization is the chemical reduction (i.e. hydrogenation) in order to obtain valuable compounds such as fuel additives, solvents and intermediates. In particular, γ-valerolactone (GVL) has been proposed both as an innovative solvent (due to its low toxicity, high stability and high boiling point) and as bio-based liquid fuel.[1] GVL may be obtained from LA by catalytic transfer hydrogenation (CTH) through the Meerwein-Ponndorf-Verley (MPV) mechanism. This approach uses organic molecules (e.g. alcohols) as reducing agents for substrates which contain a carbonyl group. Most of the studies published for the CTH of LA and its esters have been performed in liquid phase using batch reactors, secondary alcohols (i.e. 2-propanol) as H-donor and ZrO_2 as heterogeneous catalyst.[2] However, very long reaction time and high autogenic pressures are needed in order to work in the liquid phase at high temperature with light alcohols. Recently, we reported on the possibility to enhance the CTH of alkyl levulinates with ethanol (and bio-ethanol) in a continuous-flow, fixed bed, gas-phase reactor using a high-surface-area tetragonal ZrO_2. In this way, by working at 250°C and atmospheric pressure with a contact time of just one second over the catalyst, methyl levulinate (ML) was completely converted promoting the formation of GVL with yield up to 70%.[3,4]
Unfortunately, ZrO_2 undergoes to a progressive deactivation during the time-on-stream, due to the deposition of heavy carbonaceous compounds over the Lewis acid sites leading to unwanted alcoholysis and transesterification reactions (i.e. formation of ethyl levulinate, EL). In addition, we proved that the deactivation rate is strongly affected by the zirconia crystalline phase, being the monoclinic one promptly promoting parasite oligomerization reactions of the intermediate angelica lactones. Nonetheless, an effective regeneration of the catalyst can be promoted in-situ, in the same reactor, by feeding air at 400°C.
Finally, new efforts have been done toward the synthesis of improved catalytic systems based on zirconia, including mixed metal oxides (e.g. Ti-doped zirconia) with the aim of promoting both the catalytic activity and the stability of the material. Interestingly, in this way we were able to obtain a much more stable and efficient continuous flow production of GVL and/or C5 esters (ethyl pentenoates and pentanoates) in the gas-phase using ethanol as H-donor.

References

[1] S. Dutta et al. Chem. Eng. J. 2019, 372, 992-1006.

[2] T. Komanoya et al. J. Phys. Chem., 2015, 119 (47), 26540-26546.

[3] T. Tabanelli et al. ACS Sust. Chem. Eng. 2019, 7, 9937-9947.

[4] P. B. Vasquez et al. ACS Sust. Chem. Eng. 2019, 7, 8317-8330.

Electrified Methane Steam Reforming via Resistive Heating of SiSiC Foams Washcoated with a Rh/Al_2O_3 Catalyst

L. Zheng, M. Ambrosetti, F. Zaio, A. Beretta, G. Groppi, E. Tronconi
Laboratory of Catalysis and Catalytic Processes, Politecnico di Milano, Italy

Abstract

Electrified methane steam reforming (eMSR), as a promising concept for low-carbon H_2 production, offers great potential to exploit excess renewable energy and mitigate CO_2 emissions.[1] In this context, we have systematically investigated a Rh/Al_2O_3 washcoated SiSiC foam-based eMSR system,[2] where the SiSiC foam serves as the coated catalyst support as well as the Joule heating element (Fig. 1(a)). We tested foams with different catalyst loadings, at different space velocities and different operative pressures. During the test, the voltage of the power generator was varied to reach a target outlet temperature, measured at the end of the catalytic bed. The results demonstrated methane conversions close to equilibrium at space velocities as high as 150.000 $Ncc/h/g_{cat}$. In these conditions the lab-scale system was operated with a power density of 8 MW/m^3, i.e., higher than in industrial reformers. The heat losses are a sole function of the internal reactor temperature; therefore, the thermal efficiency of the system increases on incrementing the space velocity and the catalyst inventory, reaching unprecedented values of 80%. Fig. 1 (b) shows that our modelling results can predict both methane conversion and thermal efficiency with reasonable accuracy. Accordingly, the model was used to design a preliminary scaled-up eMSR unit. The system is designed so that the total ΔV across the system is equal to 380 V, the catalyst inventory is equal to 100 g/l. The foam diameter was set equal to 12 cm, considering the current manufacturing limits of SiC foams. This unit is able to produce 200 Nm^3/h of hydrogen.

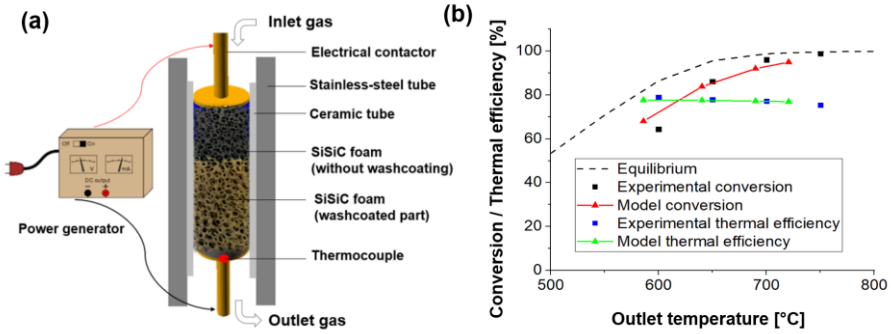

Figure 1: a) Experimental setup, b) experimental versus modelling results for a SiSiC foam with d = 3.2 cm, coated with 5.5 g of Rh/Al_2O_3 catalyst. GHSV = 150000 $Ncc/h/g_{cat}$.

Acknowledgements

This project has received funding from the European Research Council (ERC) under the European Union's Horizon 2020 research and innovation programme (GA No. 694910 -'INTENT'), and the project "PLUG-IN" funded by the MIUR Progetti di Ricerca di Rilevante Interesse Nazionale (PRIN) Bando 2020.

References

1. S.T. Wismann *et al.*, *Science*, 2019, **364**, 756-759.
2. L. Zheng *et al.*, *AIChE J.*, 2022, doi.org/10.1002/aic.17620.

High-throughput Technology in Electrochemistry

A. Müller[1], F. Schneider[1], Florian. Huber[1], M. Dejmek[1], G. Wasserschaff[1], O. Püttmann[1],
J. Fechtmann[1], D. Zahlmann[1], C. Hose[1], F. Eversheim[1], Frank. Huber [1]
B. Hecker[2], D. Dogan[2], H. Tempel[2], R.-A. Eichel[2]
C. Kröger[3], S. Haug[3], Sef Coenen[3]
P. Löb[4], C. Hofmann[4], A. Ziogas[4], H. Kost[4]
[1]hte GmbH, Heidelberg, Germany
[2]Forschungszentrum Jülich GmbH, Jülich, Germany
[3]Deutsche Metrohm GmbH, Germany
[4]Fraunhofer Institute for Microengineering and Microsystems IMM, Mainz, Germany

Abstract

In order to reach a 55% reduction in greenhouse gas by 2030 and achieve net zero by 2050 hydrogen technologies will play a vital role in the next decades in Europe. In particular, water electrolysis will become a key technology for producing green hydrogen. The first generation of electrolyzers is currently installed in large-scale industrial applications such as refineries or steel factories.
The operational experience gathered there will be the basis for further optimization. In addition, large-scale production and material use are in a continuous improvement and quality control process. All of these efforts need strong R&D support with enhanced experimentation and testing technology. At present, classical single fold test technology or short stacks are mostly used for electrochemical R&D on electrolysis or fuel cell applications.
Due to the obvious similarity between electrocatalysis and heterogeneous catalysis, combinatorial methods developed for the latter can also be applied in electrocatalysis. The objective in this common project was to build on this analogy and to introduce a new tool for combinatorial testing in electrocatalysis. The aim was to address the electrochemical synthesis of renewable feeds, for example, or the conversion of these feeds to release stored energy. Obviously, online analytic tools, applied in heterogeneous catalysis to measure gases or liquids, need to be supplemented by voltammetry and impedance spectroscopy instruments to measure electrochemical properties as well.
Therefore, electrocatalysis requires more advanced digitalization tools as the parameter space expands by numerous new electric parameters. It seems likely that the current tools will no longer suffice and must be upgraded by applying feedback loops or machine learning or both, for example.
In this presentation, we will introduce the high throughput platform for enhanced electro-chemical testing to support the ongoing effort of optimizing electrochemical conversion technology. A case study will illustrate the key features of high throughput experimentation in the electrochemical space.

Introduction

In the transition from fossil energy to renewable energy the transmitter of energy also changes. Renewable energy is based on electrons while fossil energy relies on molecules. The latter also holds true for hydrogen with the important difference that hydrogen is a molecule that is generated from electrons and abundant water and can be considered an energy storage medium like a battery which can be worldwide traded as an energy commodity. Instead of pure hydrogen better to handle carriers such as ammonia or methanol can also be traded [SMO].

The public discussion about whether hydrogen-driven or battery electric vehicles offer the most efficient technology for mobility introduced the misconception of hydrogen being preferably used for transport means. The IRENA agency indicates a different vision. In 2019 a negligible amount of hydrogen was used for public transport. Most of the hydrogen was used in industry sectors such as chemistry as well as for agricultural fertilizers.

However, the vision for 2030 and 2050 is different. In 2030 3% of the overall energy amount and up to 12% in 2050 will be replaced by hydrogen. Most of it will be used in the chemical industry, steel industry, or agriculture. Some of it will also be used in transport [IRE].

Water, as an abundant source, will be the feed, and solar or wind will be the energy source that produces hydrogen via electrolysis. Pipelines are supposed to be the backbone of the future hydrogen infrastructure, connecting producers and consumers because of their high energy density and low loss compared to conventional electric power lines [THY, SIE]. Modular and, therefore scalable electrolyzer will feed this pipeline grid with hydrogen and offer attractive "bite-sizes" for investors at the same time [SMO].

In addition to the expansion of the already industrial-scale available water electrolysis, in general further electrochemical reactions can be applied for the direct conversion of electrical energy into chemical energy carriers. This expands the possible applications for the utilization and storage of renewable electric energy. The educts and products from the water electrolysis and some additional chemical reactions as described by [ZHI] are shown in Figure 1. As indicated there the reaction processes differ in their technological readiness. Water electrolysis has been developed for more than 200 years and is now well established. The electrochemical CO_2 reduction or CO_2 electrolysis toward formic acid and carbon monoxide has already been realized with high selectivity and resulting in acceptable efficiencies. However, the situation is different for the direct CO_2 reduction to further reduced products such as ethylene. The reaction paths with multiple reaction intermediates lead to low selectivity toward the desired products and lower efficiency. Similar to this, the selectivity of the electrochemical reaction of N_2 to ammonia is also too low to reach high efficiencies for the reaction process. Nevertheless, depending on the use case, desired products, or reactants, for further application, all of these reactions have the potential to play a growing role in our future energy supply.

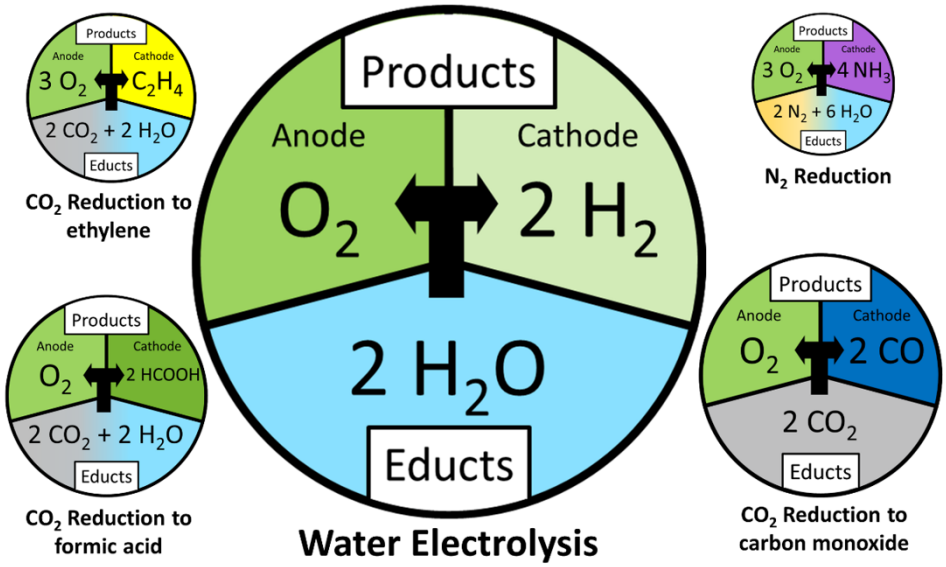

Figure 1: Educts and Products for the water electrolysis and further electrochemical reactions that can be applied storing renewable electricity. Cycle sizes represents the technological readiness of the different reaction processes.

Demand for electrochemical research

Based on the different technological readiness for the different reaction processes that have been discussed previously, there are different approaches to further improve their respective applications. In water electrolysis, for example, there are ongoing research activities searching for active, stable and low-cost catalysts [WAN]. A further example of a current research field is new materials such as anion exchange membranes with improved stability that offer new promising possibilities and challenges [LOP]. In contrast to this, the research regarding the CO_2 reduction toward ethylene or N_2 reduction toward ammonia focuses much more on the complex reaction mechanism and how to improve the selectivity toward the desired product [NIT][ZHO]. In the case of CO_2 reduction to carbon monoxide and formic acid, on the other hand, a part of the scientific community is concerned with optimizing the detailed reaction performance. In addition to selectivity and efficiency, additional performance indicators such as durability, CO_2 utilization, and purity of the products, are given special consideration [HOO][YAN].
Regardless of the concrete research focus from these and further examples, many studies are generally done by performing a small to medium number of variation experiments. In order to investigate the coherence, different experiments are carried out in which most of the test conditions are kept as constant as possible while one or more parameters are varied. Parallel, the effects of varying these parameters on the performance of the reaction were evaluated.

Figure 2 shows two examples of the effect of a high-throughput system on the time frame of such studies. Individual time frames for the Planning, Preparation, Experiments and Evaluation are estimated from different previously planned and performed studies [MUE].

The time frame for planning includes the determination of the parameters which to be varied, to be kept constant and to be observed based on literature research and theoretical estimates for the experiments. If necessary, small preliminary experiments will also be carried out here or during preparation. In the preparation time frame further, the investigated materials and further cell components are provided. The type of materials strongly depends on the aim of the study. In general, however, it is usually necessary to use technically relevant electrodes. For their preparation, the electrochemical catalyst must be applied to suitable carrier materials by well-designed coating processes. During the time frame of the experiments, the actual measurements are carried out, including reference and repeated measurements for statistical evaluation. Finally, in the last time frame, the obtained data are evaluated. For this purpose, they are converted into relevant quantities, compared with theoretical models, displayed graphically and summarized to gain the most relevant results. It is noted that these separate time frames strongly differ depending on the performed experiments and are only used as an example in this case.

As indicated, a high throughput system can increase the electrochemical (EC) laboratory (Lab) capacity a lot decreasing the overall time frame and increasing the relative time spent on planning, preparation and evaluation compared to performing the experiment. Studies with longer experiment runtimes are particularly more efficient in this respect. In the theoretical example in Figure 2, the complete study duration is reduced from over two years to about six months. The use of a high-throughput system thus makes it possible to carry out studies that were previously only possible in less practicable time frames or with particularly high personnel costs and many single experiment stations.

Not yet considered in Figure 2 is the fact that by using uniform experimental conditions and software solutions the time frames for the preparation and especially for the evaluation probably also decrease when applying a high throughput system. In particular, advanced data management and evaluation is an essential and integral part of high throughput experimentation due to the vast number of data that are produced in a relatively short time

frame. This can further improve the system performance by reducing the overall time frame. Further the usage of uniform setups and standardized experimental conditions increases the reproducibility and the comparability between different results. Thereby advanced research strategies or data evaluation techniques are enabled, which already improved the technological advancement in different fields [BIN].

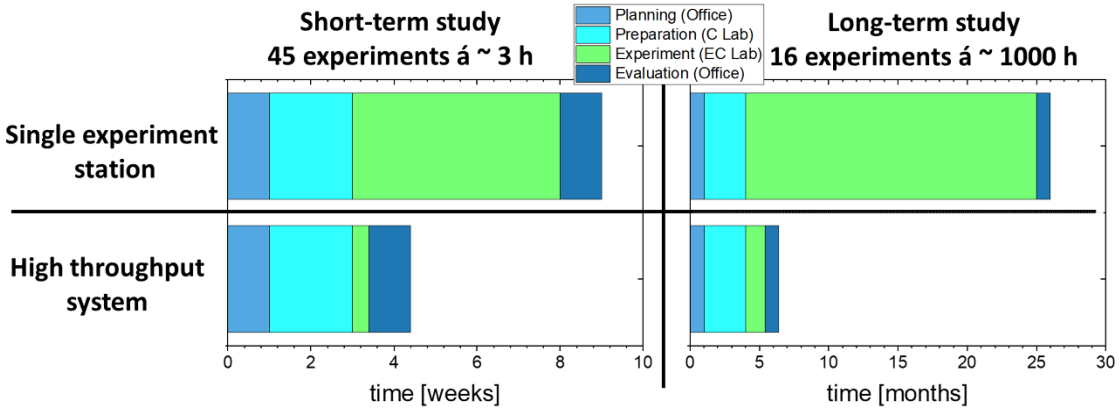

Figure 2: Estimated time frames for a short-term and a long-term study performed with a single experiment station and a high throughput system (16 parallel experiments).

Catalyst Screening

There is a common understanding among the early pioneers in catalyst screening that a proper balance between the quantity of samples and the quality of data should be met [HSV]. This led to the introduction of a multi-stage screening methodology consisting of 3 levels with increased data accuracy but a reduced sample number (Figure 3).

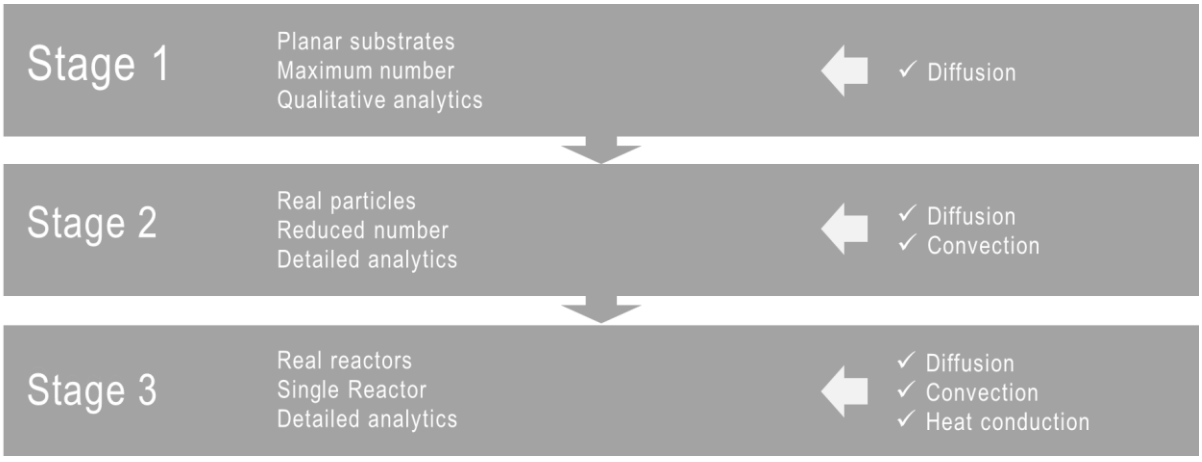

Figure 3: Multi-stage screening method as proposed by the authors in [HSV].

The aim in this chapter is to show the similarities between heterogeneous catalysis and electrocatalysis when using this screening methodology as well as to identify the possible gaps for future development.

Besides a change of quantity and quality, you can also differentiate according to the type of molecular movement. In stage 1, planar surfaces mass transport is mainly dominated by the diffusive transport of molecules into the surface. In stage 2, diffusion will be complemented by convection as particles introduce an additional three-dimensional quality into the mass transport. Stage 3 then adds thermal unbalance due to restricted heat transport to the

environment when using real reactor tube dimensions. As a reasonable general conclusion, you could state here that automation will help in all of the stages and should be applied in order to avoid a situation where a fast reactor screening method will be slowed down by manual catalyst preparation or data analysis.

In his tutorial Roduner [ROD] compares electrocatalysis to heterogeneous catalysis and shows some analogies among both. The typical reactors for heterogeneous catalysis consist in single chamber systems as tube or tank reactors. In electrocatalysis preferably double-chamber systems are applied. These systems like the modern plate-type fuel cells have the advantage of reduced internal resistance in the electrolyte which excludes bulky reactor types.

To find possible analogous solutions and to uncover the technological gaps in electrocatalysis a short survey was executed. Exemplary literature was selected that describes screening methods in different scales using both pure catalytic and electrocatalytic reactions. The comparison charts starting with Figure 4 show combinatorial methods for catalytic (left column) and electrocatalytic (right column) applications listed for synthesis, experiment, and analytics, respectively.

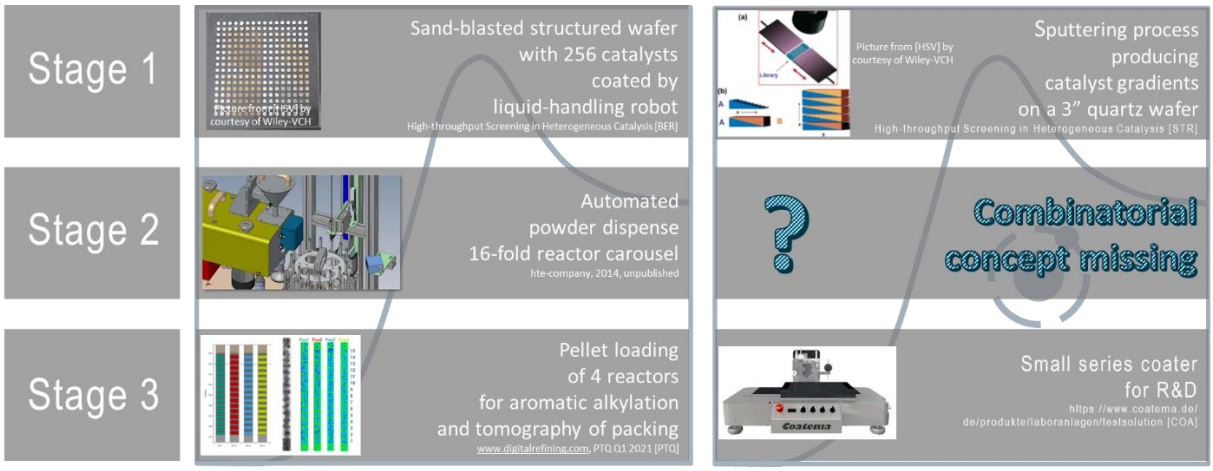

Figure 4: Type of substrate and degree of automation in *synthesis* in catalysis (l) and electrocatalysis (r).

In catalysis one early adoption of a fast combinatorial stage-1 synthesis was the wafer-based catalyst library synthesized on structured quartz wafers that were coated with liquid-handling robots and later dried and calcined [BER]. The electrocatalytic analog was published in 2003 by the same company [STR]. They used gradient sputtering onto a quartz wafer with an individually addressable 64-electrode array. Other examples can be found here showing that planar wafer-type substrate is ideal for automated stage-1 synthesis.

This situation is different in the stage-2 synthesis of catalyst powders or granules. While in powder impregnation, liquid handling robots are still applied, additional manual work is needed to load the reactor with powder sometimes using complicated stacked-bed structures. A proprietary powder dosing device with an automated rotating reactor tube carousel was designed by hte but later suspended due to its lack of adaptability to varying reactor sizes. In this limited survey no combinatorial example for electrocatalysis was found.

Stage-3 synthesis does not really require automated synthesis. The aim here is to study non-adiabatic reaction conditions of selected hits from stage-2 and process them for elongated times. An example of a reactor packing is given in [PTQ] using the so-called single-pellet-string-reactor concept which was verified using tomography. Coatema© [COA] introduced a small series coater that is offered for non-automated (or non-integrated) sequential coating of substrates in electrocatalysis being the pendant to the manual procedure of pelletizing powders as described in [PTQ].

Summarizing, electrocatalysis seems to lack an efficient automated and integrated synthesis workflow solution in stage 2. That the situation is not much better in catalysis with complex reactor loading procedures does not mean that such an attempt should not be possible in electrocatalysis. The herein used planar substrates are by nature better adapted to automated processes and that is demonstrated by sheet metal coating factories in the automotive industry.

Stage-1 screening reactors (Figure 5, left) used glass wafer substrates with adsorption pads [BER] or tubular reactors with transparent planar windows for IR thermography [KLE]. Despite of early success clearly demonstrating that the screening and characterization of many (up to 256) catalysts at the same time is possible, later reproduction during up-scaling was difficult.

Therefore, stage-2 reactors were developed that matched the industrial results better. A typical setup consists in 10 to 20 reactors combined with a shared common media supply and analytics section. [MKI] shows such a state-of-the-art configuration that enables screening 16 catalysts using steady-state GC analysis combined with a fast time-resolving FTIR analysis to follow the reaction progress of DME to olefins. An early example of stage-2 screening in electrocatalysis was presented in [HSV]. Strasser introduced 16 parallel operating rotating disc electrodes (RDE). The catalyst was deposited as a thin film on polished carbon electrodes. The results were not published, and to the authors' knowledge, this concept was not further developed. Besides the low current loads that can be applied compared to real MEA cells, a possible second reason could be that RDE results are due to their rotational symmetric flow fields difficult to compare to planar flow fields that are found in plate-type reactors, e.g., fuel cells. Therefore, one finding here could be that to simplify upscaling from stage 2 to industrial reactor sizes, the flow field quality should be of similar characteristics in the stage-2 design compared to the industrial stacked-plate cell design. Later results for single fuel cell test experiments were published in a 3 lab round robin testing [SMA], that showed the better reproducibility of RDE setups when supplemented with floating electrode measurements at higher current loads. Lazaridis et al. [LAZ] pointed out the limitations of RDE-type setups with respect to industrially relevant quantitative data and durability studies and recommended to include MEA testing already at an earlier stage of catalyst development.

In stage 3, one normally applies a larger tube diameter and reduces the number of reactors up to just one single tube reactor under steady state conditions. In [MID] the authors presented another mode of operation, a dynamic engine simulator. The catalyst consists of a core manufactured from a real size catalyst monolith. They substitute the automotive exhaust gas track by preparing gas mixtures encountered in the exhaust track and injecting the mixture applying dynamic drive protocols that change the gas composition and temperature according to a schedule. The principle of this setup was later automated by adding a catalyst exchanger carousel by hte [MKO]. A stage-3 conform single-cell setup using a planar electrode design was used for measuring ionic resistances in comparison to a modeled cell resistance under galvanostatic and potentiostatic conditions by FZ Jülich [FZJ]. [RAE] reported an electrochemical cell designed for insertion into a large nuclear magnetic resonance spectrometer. This setup enabled molecular dynamic observations that are not accessible in more complex parallel setups. They concluded that the electrochemical measurement itself can influence the reaction.

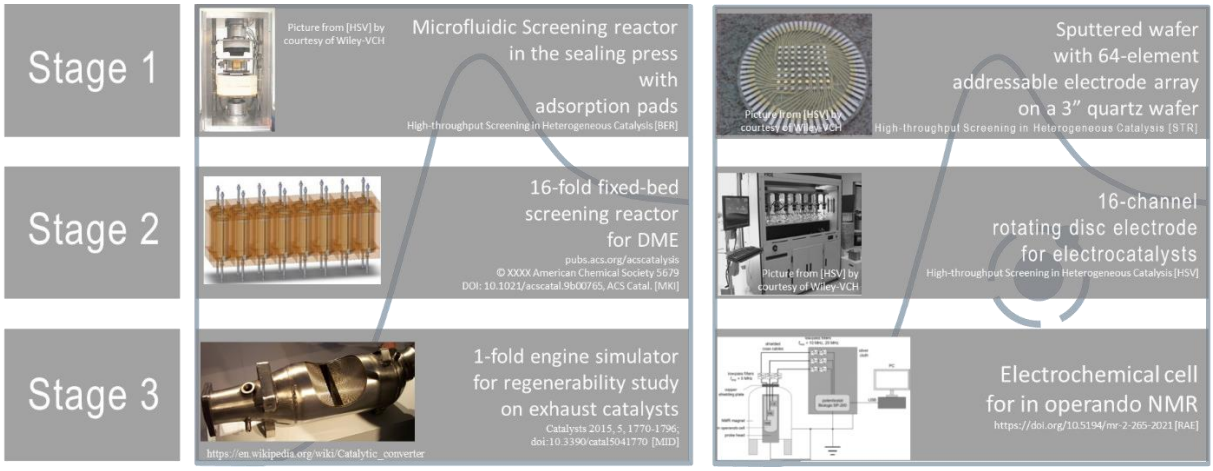

Figure 5: Sample density during the *experiment* in catalysis (l) and electrocatalysis (r).

Again summarizing from Figure 5, a stage-2 equivalent electrochemical reactor setup seems to be unavailable currently. So-called rainbow stacks [PGA] do not exactly match the required quality as they do not allow individual potential or current supply to the electrically connected cells. They also suffer from cell degradation that is dependent on the cell position in the stack. RDE setups on the other hand suffer from up-scaling issues. A setup that is equipped with individual electrochemical cells derived from high throughput catalyst testing will be presented below.

The analytical applications listed in Figure 6 are restricted to those inline connected to the reactors. Obviously there will be offline measures as well but their integration is more of an interface challenge than a plant engineering task and will not be considered here. [KLE] and [BER] demonstrate the simplicity of acquiring qualitative data from active catalysts when planar multi-well surfaces are accessible to IR measures. An electrochemical analog was reported by [CHE] in which they applied online surface scanning ICP analysis on a multi-well movable electrode substrate. A scanning flow cell was used as counter-electrode that was connected to the ICP-MS (inductively coupled plasma mass spectroscopy).

Online measurement in the stage-2 environment introduces additional complications. First, the number of detectors cannot match the number of reactors; otherwise the invest gets too high. The need for sharing one complex instrument to all reactors increases complexity. A typical solution for such requirements consists in combining a flexible instrument like a gas-chromatograph to all reactors via a multiport valve [MKI]. A stage-2 conform analog was not reported, but it could be envisioned as a matrix of electrochemical properties represented by voltammograms, Tafel plots or Nyquist plots. Single channel but also multi-channel instruments are available. Opposite to the measurement of fluid properties that requires fluid transport to the instrument and appropriate pipe and valve systems, electrochemical properties can be detected directly via simple electric connectors. A series of instruments is available from Metrohm© [MET] for parallel power supply and the testing of electrochemical cells. However, it should be noted here that these instruments still require appropriate software for parallel evaluation because, otherwise, the analysis remains a tedious manual procedure.

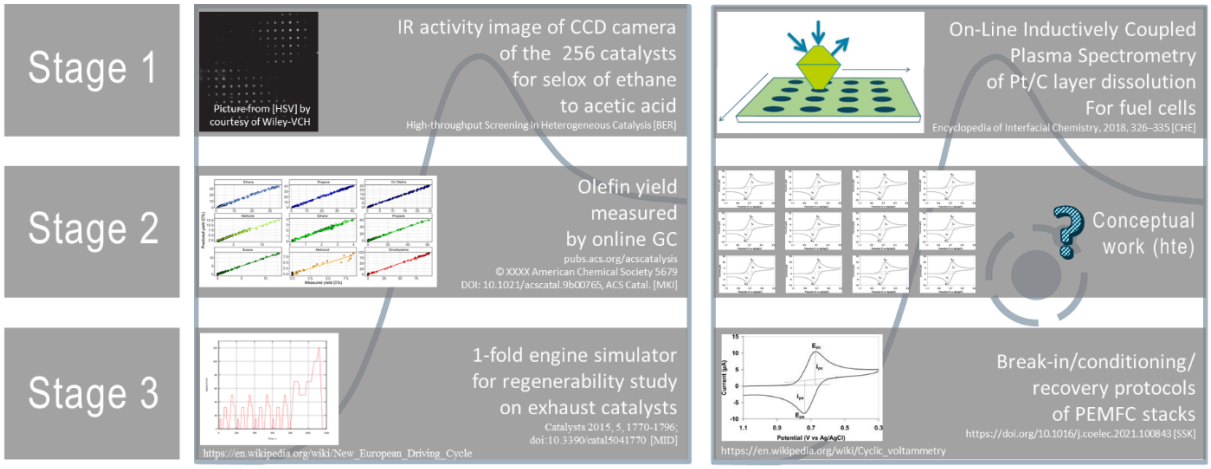

Figure 6: Degree of automation in *analytics* in catalysis (l) and electrocatalysis (r).

One additional feature of stage-3 reactor setups compared to stage 2 consists in their larger flexibility concerning reactor sizes, characterization methods or dynamic instead of steady operation, which is a consequence of a reduced number of reactors. The authors in [MID] used a dynamic engine simulator to study the fast deactivation of exhaust gas catalysts during fuel shutoff. For the study a fast micro-GC was employed that could resolve the gas composition every 3 minutes. In their review [SSK] describe the conditioning protocols found in the literature for optimizing cell stack performance of fuel cells. To reach the peak performance of a cell stack, you must follow a dynamic conditioning protocol that activates the catalyst and hydrates the membrane.

The conclusion when comparing analytical methods in all stages for white spots or synergies implies good coverage for all the stages as instruments are available. The only drawback at the moment seems to be parallel data processing as described further below.

Challenges

Before introducing the electrocatalytic testing environment, a closer look into the actual challenges of testing using potentiometric analysis should be done using the example electrocatalytic water splitting. A comparison of the contribution of energy, which is required to overcome the free energy of reaction in water splitting stresses the potential of electrocatalysis. Catalytic water splitting requires surprisingly severe reaction conditions. [ROD] states that the thermal catalysis of water would require heating above 2000K. Executed in a single-chamber reactor, the product would be an unpleasant explosive gas mixture.

The rate of reaction for thermal catalysis using Gibbs free energy is defined by:

$$k(\Delta U = 0) = k_0 \exp\left(-\frac{\Delta G^o}{RT}\right).$$

When electric potential replaces some of the splitting energy it can be formulated as

$$k(\Delta U > 0) = k_0 \exp\left(-\frac{\Delta G^{o\#}}{RT} - \frac{\Delta G_R^o}{RT}\right).$$

Electrolysis executed in a double-chamber cell reactor happens at room temperature but at the expense of an additional operational parameter, the electric potential. The total amount of energy in both systems must be the same according to Gibb´s law meaning that the thermal energy must be replaced by electric energy.

The additional term can also be expressed (simplified from [ROD]) as:

$$k(\Delta U > 0) = k_0 \exp\left(-\frac{\Delta G^{o\#}}{RT} + \frac{F \times \Delta U}{RT}\right).$$

The term $F \times \Delta U$ represents the additional electric power ideally needed to overcome the binding energy of one mol of water. The Faraday constant *F* describes the charge of a mol of electrons in the unit $A \times s$. Combined with the potential we reach at the unit $W \times s$ which is equivalent to the electric work we have to spend for splitting one mol of water.

In practice, this leads to large 10 MW electrolyzer packs consisting of several hundred parallel cells and cell surfaces on the order of square meters. These packs are containerized and connected to rectifiers that transform high-voltage DC power from renewable energy sources as shown by the example of Sunfire@ [SUN]. The hydrogen production rate in this case amounts to 2230 m^3/h.

A design rule in engineering states that dimensionless numbers should be held constant as far as possible during upscaling. In our case downscaling requires the same considerations. When using plate reactors with parallel electrodes and forced-flow flux in channels with similar dimensions all fluid dynamic dimensionless numbers can be held constant.

Due to their planar geometry electrolyzer stacks do not suffer from upscaling when compared to rotational symmetric tube reactors. In fact, upscaling should be called up-numbering with a few restrictions assuring similar pressure distribution between the cells and proper flow guidance inside of the cells. The electric analog is the potential and the current load per electrode area.

The rectifier that delivers the potential to the cells connects them all in series and the rectifier potential is, therefore, a multitude of the hydrogen evolution potential of 1.23 V. This potential is amended by the overpotential due to cell resistances and amounts to roughly 1.67 V. Reducing the number of cells when down-scaling for laboratory testing is the most obvious means to reduce the potential from 2000 V to the 1.67 V (Figure 7).

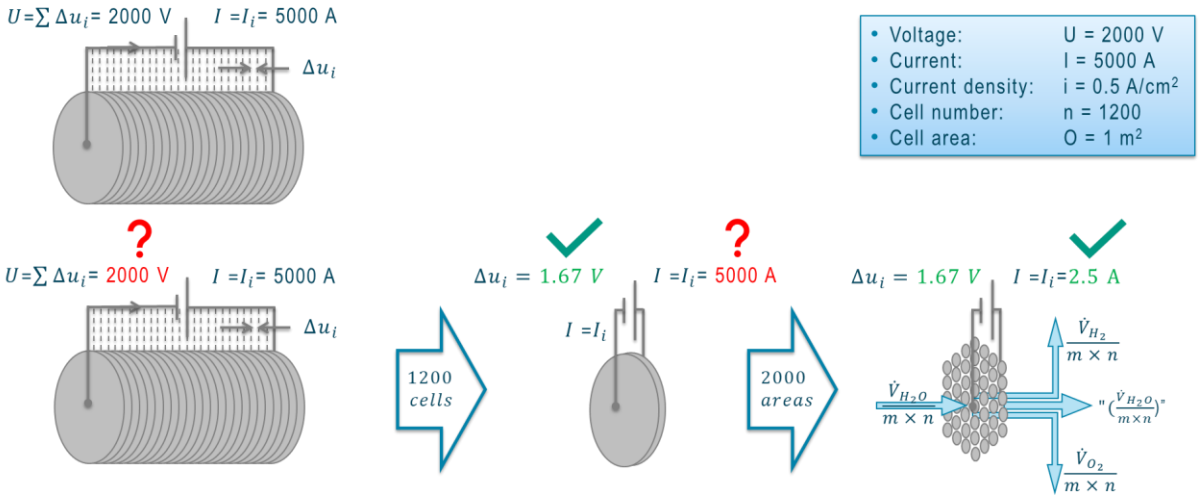

Figure 7: Down-scaling of power supply from production to laboratory scale

However, this is still not affecting the current supply. In order to further decrease the electric power, you must also reduce the cell area. A reduction from 1 m^2 to 5 cm^2 reduces the current supply in the example from 5000 A to 2.5 A.

Such a potential of 1.67 V and a current of 2.5 A are parameters that instruments from instrument manufacturers like Metrohm© are designed for. However, it should be noted that in this estimation a current load of 0.5 A/cm^2 was assumed. This is a value that is currently at the

upper end of current loads for electrodes used in alkaline electrolyzer cells and can be supplied with the actual booster generation. A further increase can be expected, and the new anion exchange membranes are supposed to be operated at even higher loads with up to 1 A/cm^2. Polymer electrolyte membranes are operated at up to 3 A/cm^2 [WEC]. Obviously, there will be a need for a new booster generation that delivers 30 A or more per cell element.

The lab infrastructure on the other hand must also be capable of handling the required and produced liquids and gases. A reduction of the cell number in combination with a shrinkage of the cell area also helps here (Figure 8).

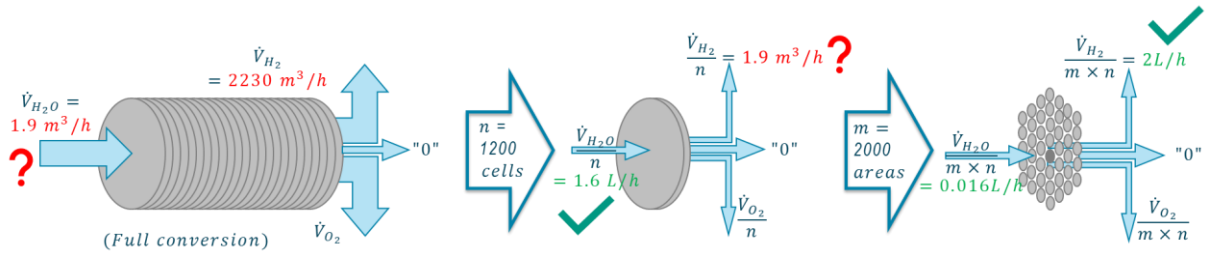

Figure 8: Down-scaling of fluidic supply from production to laboratory scale

A last consideration is the thermal similarity. Tempering the water entering the stack requires some energy. In a production plant some of the energy is recovered by looping the water and only adding as much water as was consumed during electrolysis. This looping is something that influences the thermal balance (positively) of the cell and should be considered as a fluid guiding alternative to a once-through flow in a screening unit as well. A second effect here is that small amounts of value product can agglomerate on the loop and facilitate their analysis, a feature mainly interesting in CO_2-electrolysis (Figure 9).

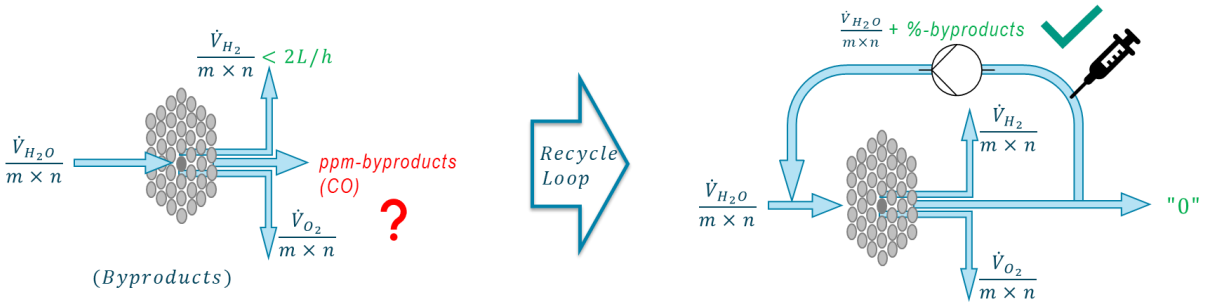

Figure 9: Agglomeration of value product in the recycle loop

As the basis design parameters are now available, the concept will be derived in the next chapter.

The Joint Project FZJ/hte

The first scouting activities back in 2019 at the DECHEMA "Infotag Elektrochemische Reaktionstechnik" led to the idea of research acceleration by introducing parallel testing into this new developing topic. The conference had a focus on batteries, fuel cells, and electrolyzer but also on electrochemical synthesis. Soon after, the first contacts were made to the Forschungszentrum Jülich (FZJ) to find out if there is enough research interest in this new community to develop a new family of screening tools to foster research in electrocatalysis. These discussions led to the idea of transferring knowledge from screening units for heterogeneous catalysis to this new topic. The general concept of the test unit was taken and modified to allow the operation of double-chamber reactors that the electrochemical cells are.

During the design, the project profited a lot from the yearlong practical experience of FZJ.

Complex systems such as research units, certainly require accurate management not only restricted to the engineering tasks but also to the appearance of the test unit as a product to the users of the unit. This is where product management plays a crucial role and has a need to apply common principles often applied in the engineering of such complex systems. One of these principles consists in the replicated usage of common building blocks. Another principle is the easy operability of such systems and the reduction of sometimes-complicated diverse process tasks into a manageable user interface that allows the experiment execution of parallel tasks using easy-access graphical surfaces.

Fortunately, the former aspect is by nature addressed when deriving a new technology from an existing modular system that has qualified itself as a reliable differentiator of heterogenous catalysis in the past. Figure 10 (left) shows a standardized screening unit that is normally equipped with 16 reactors. Recipe driven software controls all of the processes once the test system is loaded with reactor tubes containing the catalyst samples.

The key feature of such a screening system is a one-to-many-to-one approach meaning that one common feed infrastructure (gases, liquids, energy) supplies many reactors with all they need to be operable and connects them all to one common analytic instrument or a set of instruments. This approach reduces the unit invest but (and more importantly) assures the comparability of all the catalyst samples as they were supplied with the same substances and characterized with the same instrument at the same time. Therefore, small errors always present in a complex system will not affect the comparability negatively.

Having such a system with all of their (modular) supply and characterization structure now allows you to simply change its core element which is of course the reactor. Figure 10 (right) shows the different configurations that are meant to replace the core element. The first, the flow reactor is existing technology in a large variety of setups. The second configuration is topic of this publication. Configuration 3 is a derivative from the electrochemical stacked-plate reactor of configuration 2 as they both share the geometric concept but configuration 3 does not have electrodes. The screening topic here will be problems in material science, e.g. the optimization of membrane properties or corrosion studies. Configuration 4 represents a parallel 16-fold tank reactor unit for homogeneous or heterogeneous catalysis using the above-described common infrastructure principle and will not be discussed here.

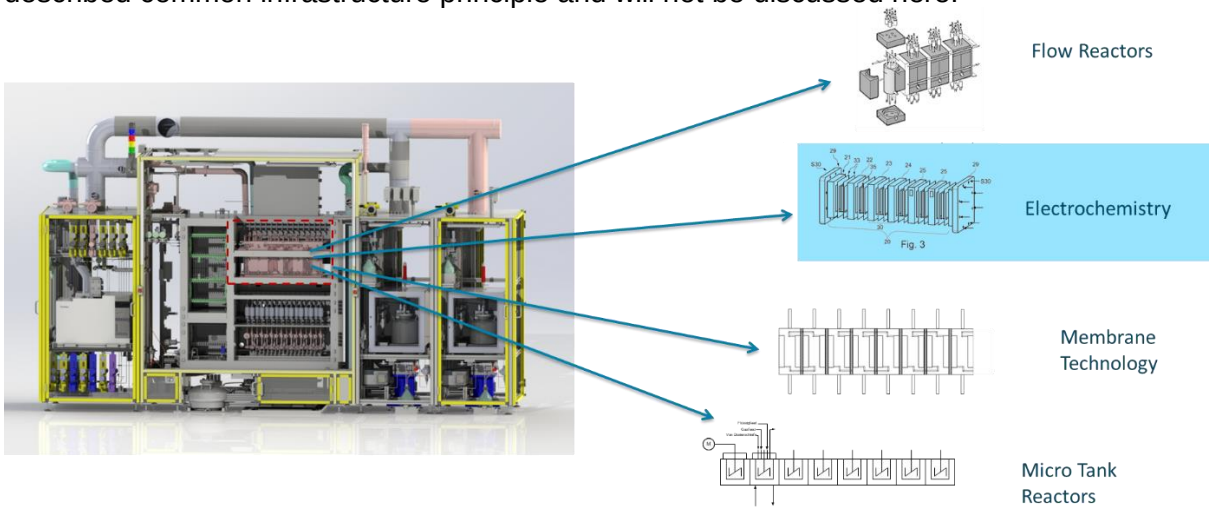

Figure 10: Modular experimental screening plant and reactor configurations

We had deducted above that by using the appropriate partitioning a stacked-plate approach allows down-scaling to laboratory infrastructure using "down-numbering" as the main scaling principle and a mild geometrical down scaling. For a number of reasons, as mentioned above,

loop processing of the electrolyte should also be possible. Such a flow circulation through the cells enables applications also beyond hydrogen, for example redox flow battery development or CO_2-electrolysis. A sketchy flow diagram (Figure 11) shows some characteristics of the patented setup [PA1].

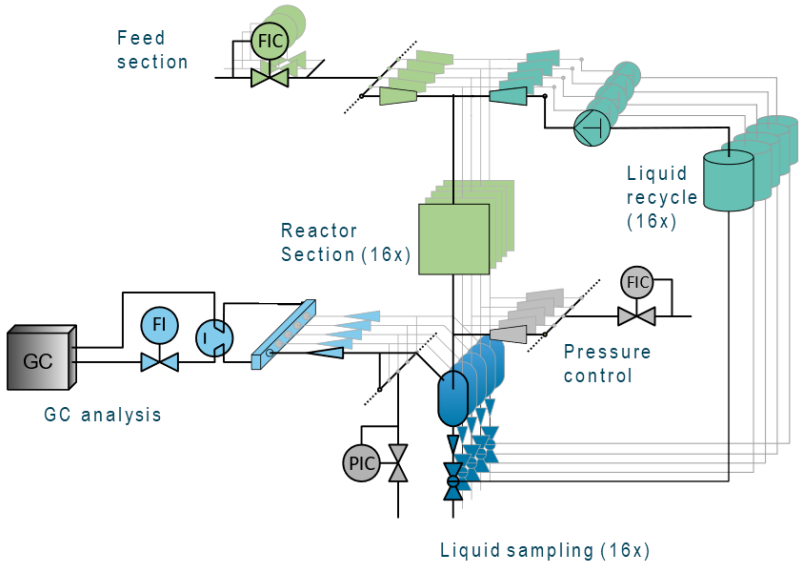

Figure 11: Simplified process flow diagram of a parallel plant for the screening of electrocatalysts

A common liquid supply combined with a common gas supply (used for the CO_2-electrolysis of gases) feeds a parallel stacked-plate reactor. An individual liquid loop allows the individual recirculation of liquid for all channels. Individual feed tanks for the liquid enables the independent characterization of different electrolytes. The one-to-many principle is considered here; the conveying means is a multi-tube peristaltic pump with a single drive. A latch of separators with common pressure control gives access to individual liquid sampling with an autosampler. The gaseous product streams are individually connected to one characterization instrument usually a gas chromatograph. The sketch shows only one set of half-cell and their process elements. The second half cell set mirrors the first set. Both half-cell sides are held completely separate throughout the process. So, there is no possibility of producing dangerous gas mixtures.

A side aspect of product management consists in portfolio development. Applied to research tools for electrochemistry, this means offering a technology to a broader clientele or adding it to the existing processes. Electric potential can in principle be applied in many chemical processes. However, there are limitations. [ROD] states that reactants must be capable of exchanging electrons with solid surfaces, and they need to have separate oxidation and reduction mechanism that then makes them suitable for a double-chamber reactor.

Broadening the scope could mean to introduce sophisticated stage-3 research systems with a reduced number of reactors but more flexibility in their operation. Such a conceptual design enables the individual exchange of reactors during operation or additional individual measure methods as, for instance integrated load cells for detecting membrane thickness variations [PA2].

The technology can also be supplemented to existing technology for the electrochemical synthesis of organic molecules, for example. The approach from above can be transferred to pressurized tank reactors or atmospheric tank reactors. Such a stage-2 setup consists of a number of parallel tank reactors equipped with additional electrode sets while otherwise the

reactor technology is that of commercial tank reactors. Tank reactors can be considered as one-chamber reactors. A tank reactor with accurately designed electrode surfaces can be operated as an (internal) loop reactor if also the internal circulation allows to set a fixed flow rate per electrode area meaning sufficient and reproducible wetting of the electrode surfaces. This goes hand in hand with a reproducible current load per electrode area. Both requirements can be satisfied when using modified baskets as known from heterogeneous slurry processing in autoclaves. On the other hand, they can also be uncoated pure electrodes in which case homogeneous catalysis will be the application [PA3].

The new high-throughput electrochemical cell

Short catalyst loading and unloading times for a screening unit indicates good usability. Screening systems usually use reactor tubes prefilled with catalyst that are inserted in the reactor heaters and then connected to feed and product pipes using two screw type fittings. Following this principle in electrocatalysis requires some new design considerations. Planar reactors need the proper sealing of the plates usually by screwing a large number of bolts into the housing. Apart from a lot of manual screwing activity, the screws positioned close to the edges of plates always introduce the bending of the plates and that has the consequence of non-contact areas inside the plates that, in the case of electrodes, is something that has to be avoided. Instead it was decided to use compression force executed onto the planar outer cell surface for sealing.

The double-chamber design and the additional electric power supply requires many cell connections to the cell supply. The fluidic connections can sum up to 12 pipe connections per cell (2 heat exchanger in- and outlets, 2 electrolyte in- and outlets, 2 gas in- and outlets), but there are also electric power connectors to both electrodes and connection to at least one reference electrode. All of these connections sum up to 12 fluidic connections and 3 electric connectors compared to only 2 for a tube reactor. Obviously, you must apply quick connectors for all the pipe connections, preferably with a self-locking feature when opened.

The reactor also exhibits a far more complex interior design compared to tube reactor, which prohibits assembly in the plant. Instead it was decided to construct a housing that exhibits only one final seal interface that can be pre-assembled in a fume hood or in a glovebox if needed and later be slipped into a compartment in the plant. To enable such fast charging, all connections and connectors had to be positioned on the slim sides of the cells and not on the wide side. Convenient cells normally do not disclose such a design that makes it impossible to use them for the space-constraint fast charging of screening units. Such a positioning has the additional advantage that the wide sides can be used for transferring the seal force when stacked in a compression device as discussed above.

Such a design was first elaborated by the Fraunhofer Institute for Microtechnology and Microsystems IMM taking into account former own experience [IMM] during early discussions of the project. Later, a modular construction set was developed on this basis in intensive discussions including the Forschungszentrum Jülich classifying many of their applications with respect to cell design used in these applications. The versatile modular cell kit designed according to this study now allows you to choose from up to 23 different configurations of the cell that presumably enables most two-chamber applications found in the literature of low-temperature electrolysis and fuel cells.

Figure 12 shows a cell configured for electrolysis applications designed by IMM. It also shows a clamping mechanism that enables you to pre-seal the cell after assembly for gas-tight transport to the plant. On the other hand, the mechanical seal mechanism also enables you to send the cell after testing for further "post-mortem" offline analysis. The seal clamp avoids contamination but also keeps the moisture of the membrane constant.

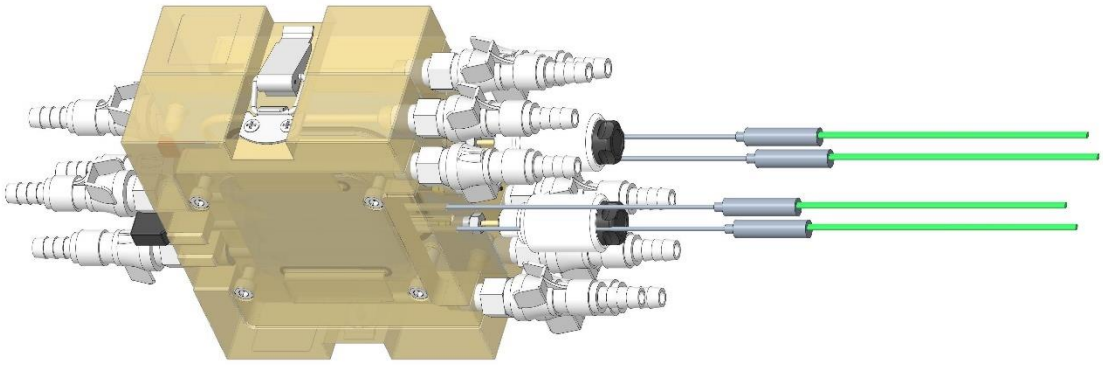

Figure 12: CAD image of the modular cell showing fluidic and electric connections.

The new Software & Analytic interface

Parallel testing produces enormous data sets. The complex operation of the testing plants excludes manual operation. Both aspects are considered in the layer structure of the software architecture explained in Figure 13. The top layer receives all the data collected in the SCADA layer. This layer acts as the brain that concentrates the knowledge obtained from all the connected instruments in visual matrices but also by calculating the derived values from distributed data. This can be simple recovery calculations but also new advice to the testing unit when the measured results indicate uncovered interesting areas in the multi-parameter screening space.

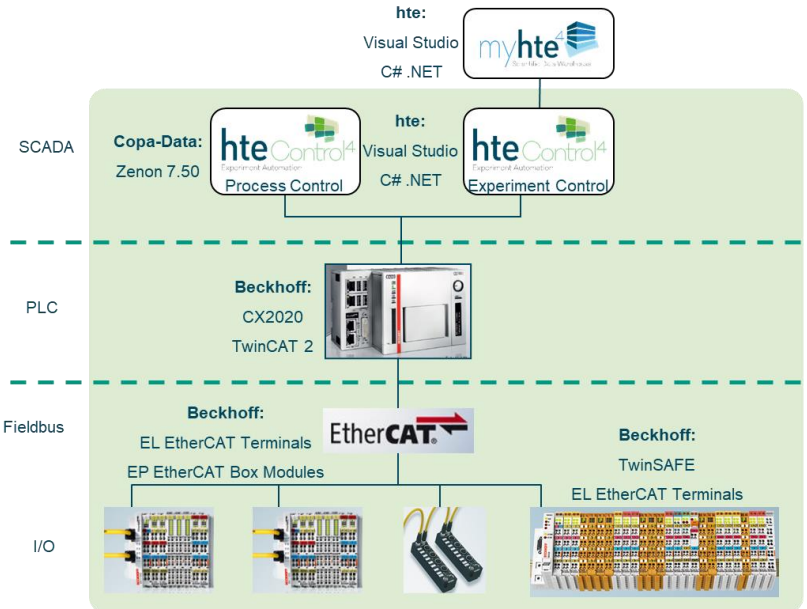

Figure 13: Layer structure of software architecture.

As mentioned, the SCADA layer collects all the electronically available data from the test unit. New instruments need to have an interface that enables you to exchange data bidirectionally. This means that the export of data from the instrument is possible but also sending trigger commands from the central control software to the instrument must be available in order to start measurements in a sequence of experiments.

Further details of such a command structure are shown in Figure 14. The recipe controller sits at the core of the experiment control. Its user interface enables you to pick and place so-called

activities and to arrange them in a series of process steps. Examples for such activities are the heating of reactors, dosing of gases or liquids and collecting data from instruments. After editing, these work sequences are then executed automatically for all of the reactors specified. The new programmed interface to NOVA© now enables you to execute their commands by adding them to the list of activities (left column). The Metrohm© "activities" can be parametrized using a parameter window (right column). Programming of these interface has largely progressed and is expected to be operational by the end of 2022.

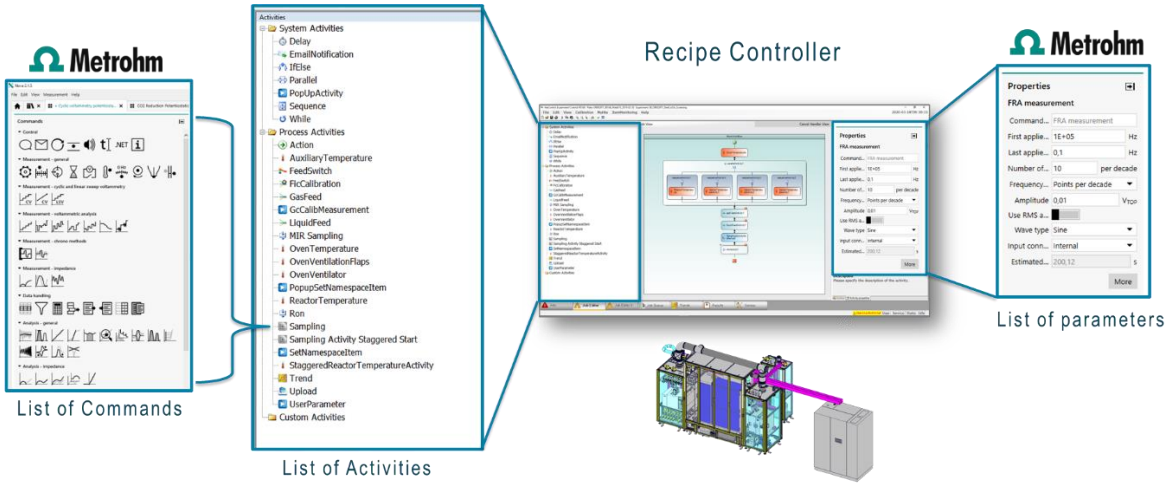

Figure 14: Programmable recipe controller with access to the Metrohm© command level.

Figure 15 shows a vision of the diagrams often used in electrochemical analysis arranged in a matrix pattern for the fast first comparison of the results. The diagrams will be exported automatically from Metrohm´s proprietary NOVA software suite and imported into myhte© (Figure 13) for visualization and the combination with process data obtained via hteControl© in the SCADA layer during the measurement of these diagrams.

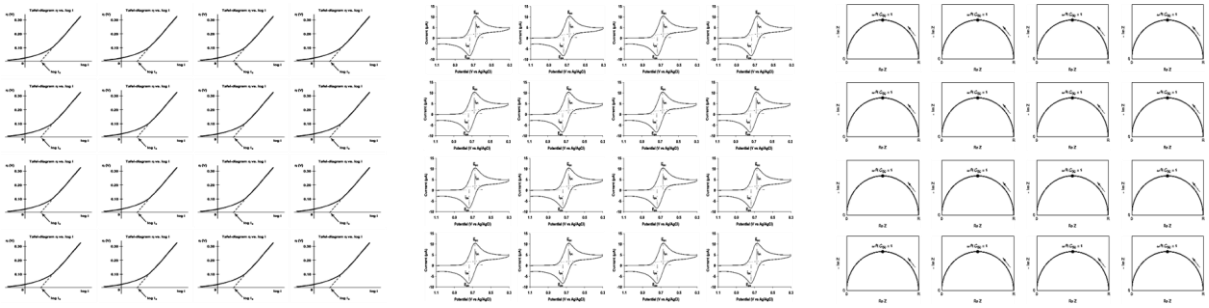

Figure 15: Quick-survey Matrices of Tafel plots, Voltammograms and Nyquist diagrams (arranged from [WI1, WI2, WI3])

Outlook

The parallelization of laboratory-scale electrolysis experiments under industry-relevant reaction conditions by the high-throughput system published in this paper will significantly accelerate the research activities in reaction optimization and material robustness testing [WIL].

At first, research activities using the high throughput approach will be limited to water electrolysis. Parallel to this, the extended application for CO_2 reduction to CO or formic acid

and more complex products such as ethylene is theoretically considered. Thereby, an extended field of application is already prepared to a certain extent. With consideration of the safety standards and avoidance of chemical corrosion activities, the investigation of further electrochemical processes such as N_2 reduction, chlor-alkali electrolysis or redox flow batteries can be imagined with system adaptations of small to medium complexity.
In addition to the increased number of processes, technical system extensions are possible. Since the reactor design is modular, the adaptation of the design of individual reactor modules is easy to implement. Such an adaptation is benefited by the use of additive manufacturing processes for the individual modules. The design can be adjusted to enable the incorporation of multiple temperature probes into each cell. This enables the high-throughput test system to be extended from point temperature measurement to segmented temperature measurement in order to implement a higher resolution of this online process parameter and to investigate the area effects. Furthermore, the system can be extended by additional reference electrodes per cell. Therefore, more data can be obtained by simultaneously studying anode and cathode reaction, the electrolyte solution or membrane effects [EME, XIE, CAH]. Due to the compression force executed onto the planar outer cell surface and the robust design, the developed cell reactor is able to support further increased process pressures. The application of electrochemical high-pressure processes is thus conceivable regarding the cell reactor. However, other system components would have to be adapted in order to be able to run high-pressure processes.
Elaborations in this publication show that performing parallelized experiments significantly reduces the laboratory time. This shifts the bottleneck of the entire work cycle from experimental screening execution to one of the numerous other steps: Scientific planning, material synthesis, material characterization, setup and cleaning of experiments, and data acquisition, analysis, or visualization. To further increase the effective experimental throughput in this research field, these steps also need to be accelerated. [DAR] Design of experiment approaches could be applied to increase the significance of each individual experiment. Furthermore, computer scripts could automate the data analysis of the very large, accumulating data sets and thereby accelerate the data analysis considerably. Another approach with great time-saving potential for the overall work cycle would be the development of complementary high-throughput technologies for electrode and material preparation.

References

[BER] Bergh, Sam, et al. "Combinatorial heterogeneous catalysis: oxidative dehydrogenation of ethane to ethylene, selective oxidation of ethane to acetic acid, and selective ammoxidation of propane to acrylonitrile." Topics in Catalysis 23.1 (2003): 65-79.
[BIN] Cao, Bing, et al. "How to optimize materials and devices via design of experiments and machine learning: Demonstration using organic photovoltaics." ACS nano 12.8 (2018): 7434-7444.
[CAH] Cahan, B. D., and J. S. Wainright. "AC impedance investigations of proton conduction in Nafion™." Journal of the Electrochemical Society 140.12 (1993): L185.
[CHE] On-Line Inductively Coupled Plasma Spectrometry of Pt/C layer dissolution for fuel cells, Encyclopedia of Interfacial Chemistry, S. Cherevko, K. Mayrhofer, (2018), 326–335, Elsevier 2018
[COA] https://www.coatema.de/de/produkte/laboranlagen/testsolution
[DAR] Dar, Yadunandan L. "High-throughput experimentation: A powerful enabling technology for the chemicals and materials industry." Macromolecular rapid communications 25.1 (2004): 34-47.
[EME] Emeji, Ikenna Chibuzor, et al. "Electrochemical Cells." Nanostructured Metal-Oxide Electrode Materials for Water Purification. Springer, Cham, 2020. 65-84.

[FZJ] Schalenbach, Maximilian, B. Hecker, et al. "Ionic transport modeling for liquid electrolytes-Experimental evaluation by concentration gradients and limited currents." Electrochemical Science Advances (2022): e2100189.
[HOO] Hoof, Lucas, et al. "Hidden parameters for electrochemical carbon dioxide reduction in zero-gap electrolyzers." *Cell Reports Physical Science* 3.4 (2022): 100825.
[HSV] Hagemeyer, Alfred, and Peter Strasser. "High-Throughput Screening in Heterogeneous Catalysis." (2004).
[IMM] Ziogas, Athanassios, et al. "Novel Flexible Electrochemical Microreactor and its Validation by Three Model Electrosyntheses." Chemie Ingenieur Technik 92.5 (2020): 513-524.
[IRE] IRENA: Green Hydrogen Cost Reduction, Lecture at World Electrolysis Congress 31 May 2022 Düsseldorf, Germany
[KLE] Klein, Jens, et al. "Accelerating lead discovery via advanced screening methodologies." Catalysis today 81.3 (2003): 329-335.
[LAZ] Lazaridis, Timon, et al. "Capabilities and limitations of rotating disk electrodes versus membrane electrode assemblies in the investigation of electrocatalysts." Nature Catalysis 5.5 (2022): 363-373.
[LOP] López-Fernández, Ester, et al. "Recent advances in alkaline exchange membrane water electrolysis and electrode manufacturing." Molecules 26.21 (2021): 6326.
[MET] https://www.metrohm.com/en_gb/products/electrochemistry/multichannel-line.html
[MID] Zheng, Qinghe, et al. "Part I: A Comparative Thermal Aging Study on the Regenerability of Rh/Al2O3 and Rh/Ce x O y-ZrO2 as Model Catalysts for Automotive Three Way Catalysts." Catalysts 5.4 (2015): 1770-1796.
[MKI] Haas, Alfred, Christoph Hauber, and Marius Kirchmann. "Time-resolved product analysis of dimethyl ether-to-olefins conversion on SAPO-34." ACS Catalysis 9.6 (2019): 5679-5691.
[MKO] hte company, internal project information
[MUE] Muench, Falk, et al. "Nucleation-Controlled Solution Deposition of Silver Nanoplate Architectures for Facile Derivatization and Catalytic Applications." *Advanced Materials* 30.51 (2018): 1805179.
[NIT] Nitopi, Stephanie, et al. "Progress and perspectives of electrochemical CO2 reduction on copper in aqueous electrolyte." Chemical reviews 119.12 (2019): 7610-7672.
[PA1] patent granted: WO 2021/048375A1
[PA2] patent filed 2021
[PA3] patent filed 2021
[PGA] Gazdzicki, Pawel, et al. "Impact of platinum loading on performance and degradation of polymer electrolyte fuel cell electrodes studied in a rainbow stack." Fuel Cells 18.3 (2018): 270-278.
[PTQ] Accelerated catalyst screening and scale-up for aromatics alkylation, B. Mutz, P. Kolb, A. Higelin, PTQ Q1 (2021), www.digitalrefining.com
[RAE] Jovanovic, Sven, et al. "An electrochemical cell for in operando 13 C nuclear magnetic resonance investigations of carbon dioxide/carbonate processes in aqueous solution." Magnetic Resonance 2.1 (2021): 265-280.
[ROD] Roduner, Emil. "Selected fundamentals of catalysis and electrocatalysis in energy conversion reactions—a tutorial." Catalysis Today 309 (2018): 263-268.
[SIE] https://assets.siemens-energy.com/siemens/assets/api/uuid:3d4339dc-434e-4692-81a0-a55adbcaa92e/200915-whitepaper-h2-infrastructure-en.pdf
[SMA] Martens, Sladjana, et al. "A comparison of rotating disc electrode, floating electrode technique and membrane electrode assembly measurements for catalyst testing." Journal of Power Sources 392 (2018): 274-284.
[SMO] Smolinka et al., Electrochemical Power Sources, Hydrogen Production by Water Electrolysis, Elsevier (2022), ISBN 978-0-12-819424-9
[SSK] Kocha, Shyam S., and Bruno G. Pollet. "Advances in rapid and effective break-in/conditioning/recovery of automotive PEMFC stacks." Current Opinion in Electrochemistry 31 (2022): 100843.
[STR] Strasser, Peter, et al. "High throughput experimental and theoretical predictive screening

of materials− a comparative study of search strategies for new fuel cell anode catalysts." The Journal of Physical Chemistry B 107.40 (2003): 11013-11021.
[SUN] https://www.sunfire.de/en/news/detail/demo4grid-project-partners-successfully-install-a-3-2-mw-pressurized.
[THY] https://miningconstruction-sadc.com/thyssenkrupp-uhde_-green-hydrogen/
[WAN] Wang, Shan, Aolin Lu, and Chuan-Jian Zhong. "Hydrogen production from water electrolysis: Role of catalysts." Nano Convergence 8.1 (2021): 1-23.
[WEC] World Electrolysis Congress 30th May 2022, Masterclass "Traditional and Disruptive Electrolysis Technologies for Green Hydrogen", Stephen B. Harrison
[WI1] https://de.wikipedia.org/wiki/Tafel-Gleichung
[WI2] https://commons.wikimedia.org/wiki/Category:Nyquist_plots
[WI3] https://en.wikipedia.org/wiki/Cyclic_voltammetry
[WIL] Wills, Alfie G., et al. "High-throughput electrochemistry: state of the art, challenges, and perspective." Organic Process Research & Development 25.12 (2021): 2587-2600.
[XIE] Xie, Zhong, et al. "Discrepancies in the measurement of ionic conductivity of PEMs using two-and four-probe AC impedance spectroscopy." Journal of the Electrochemical Society 153.10 (2006): E173.
[YAN] Yang, Hongzhou, et al. "Performance and long-term stability of CO2 conversion to formic acid using a three-compartment electrolyzer design." Journal of CO2 Utilization 42 (2020): 101349.
[ZHI] Yan, Zhifei, et al. "Renewable electricity storage using electrolysis." *Proceedings of the National Academy of Sciences* 117.23 (2020): 12558-12563.
[ZHO] Zhao, Xue, et al. "Comprehensive understanding of the thriving ambient. electrochemical nitrogen reduction reaction." Advanced Materials 33.33 (2021): 2007650.

Activated Metal Foams – Attractiveness and Challenges in Industrial Hydrogenations

J. Bauer[1], J. Metternich[2], R. Franke[2], M. Roos[2], H. W. Zanthoff[2]
[1] Spark e-Fuels GmbH, Berlin, Germany
[2] Evonik Operations GmbH, Marl, Germany

Abstract

Hydrogenation reactions are core technology for upgrading chemicals, e.g. isononanal (INAL) hydrogenation to isononanol (INA). Optimization of existing catalysts and related processes is therefore continuously performed to obtain improvements towards higher raw material and energy effectiveness. In the present paper a new class of highly active INAL hydrogenation catalysts based on activated Nickel foam doped with Molybdenum (Metalyst® MC 981 from Evonik Operations GmbH) is discussed.
This catalyst, when applied as cuboidal particle fixed bed, exhibits at least threefold higher reaction rates compared to a conventional Ni-Cu supported catalyst (Specialyst® 103 from Evonik Operations GmbH). Selectivities observed in INAL hydrogenation are comparable for both catalyst systems. Additionally, side reactions like the formation of aldol condensates were strongly minimized over the activated Nickel foam-based catalyst. Also, the conversion of side products in the feed stream from the oxo-process is diminished over this type of catalyst. This allows the decoupled optimization of the hydrogenation process in two consecutive steps, which could lead to further improvements in technical application.
Long term experiments up to 3000 h showed stable operation in a two-step operation with a recycle reactor containing the Metalyst® MC 981 foam catalyst in the first step and the conventional granular Specialyst® 103 catalyst in the second single throughflow step.

Introduction

Hydrogenation reactions are core technology for upgrading chemicals, e.g. in food, specialty chemicals, petrochemicals, pharmaceuticals, and dye industries [1]. For example, aldehydes obtained from the oxo process (hydroformylation of primary olefins) are hydrogenated to obtain the respective alcohols. According to the carbon chain length the alcohols are used in a wide variety of different applications, for example as plasticizers for plastics (e.g. PVC), as detergents or as raw materials for specific syntheses.
In industrial applications hydrogen is used in gaseous form and reacts with the liquid substrate in the presence of solid catalysts to form the desired products in high selectivity. Some exceptions are, for example, enantiomeric hydrogenations [2], where homogeneous catalysts are applied. Typical active catalytic metals in heterogeneous hydrogenations are Cu, Ni, Co, Rh, Ru, Pd or Pt, depending on the substrate and the functional groups to be hydrogenated.

Hydrogenation reactions usually exhibit complex reaction kinetics and are often accompanied by mass and heat transport limitations. This offers a large playground for reactor and catalyst improvements towards higher raw material and energy efficiency. Besides activity of a new catalyst material and its selectivity in the hydrogenation reaction, secondary effects are important factors towards industrial application: Long-term stability, behaviour in side reactions and the possibility to use the catalyst as a drop-in solution in existing plants affect the economic attractiveness of such process improvements.

Hydrogenation of oxo process long chain aldehydes have already been subject of mechanistic and kinetic studies due to their industrial importance [3, 4]. The reaction is typically performed

in heterogeneously catalyzed continuous processes over oxide supported mixed metal catalysts mainly based on Ni, e.g. modified Ni-Cu/Al_2O_3, which are used in the form of shaped bodies in fixed beds [5]. Also, Ni based Raney-type catalysts are already known to be effective in aldehyde hydrogenation [6].
Commonly applied temperatures are in the range of 120°C to 200°C and pressures within a range from 25 to 350 bars. Due to the strong exothermicity, the main reaction occurs in circulation mode with dilution of fresh feed by product stream to reduce reaction rates and consequently minimize hot spots and increase catalyst lifetimes.

Lower temperatures are proposed to minimize undesired catalyst aging by fouling due to side-product formation [7]. However, the low activity of typical oxidic supported Ni fixed bed catalysts requires temperatures at which these side reactions cannot be avoided completely, so that the catalysts must be removed and replaced in industrial environment after limited lifetime.

Therefore, continuous research is performed to obtain improved catalysts for industrial application. A relatively new class of hydrogenation catalysts are active metal/support catalysts based on 3D metal foams [8]. These open cellular metal foams have been proven to be advantageous compared to classical fixed bed catalysts or even oxidic foam materials [9,10]. The main benefits reported are mechanical strength combined with low weight, significantly improved mass and heat transfer properties and higher selectivity in catalytic reactions.

It was aim of the present study to investigate the performance of activated Ni foam catalysts (Metalyst® MC 9 series*) from Evonik Operations GmbH) in batch and continuous operation in the hydrogenation of Isononanal (INAL) to Isononanol (INA) in comparison to a classical fixed bed catalyst under technically relevant conditions.

*) This catalyst technology is manufactured under a license from Alantum Europe GmbH [8].

Metal Foams

Metal foams gained significant industrial interest starting with the beginning of the 21st century and are well known for application in batteries (electrodes), heat exchangers, filters, energy absorbers, flame arrestors or biomedical implants. However, the high cost of the material has limited its use so far to advanced technologies. For their application as chemical catalysts on industrial scale, so far only few examples exist, such as steam methane reforming (SMR), partial oxidation of methanol to formaldehyde or Biogas desulfurization [11].

The metal foam catalyst technology discussed in the presented paper with its conceptionally high flexibility in material design allows the structuring of the internal reaction space of existing plants, without necessarily having to touch outer reactor geometries, downstreaming or infrastructure with simultaneous efficiency improvements.

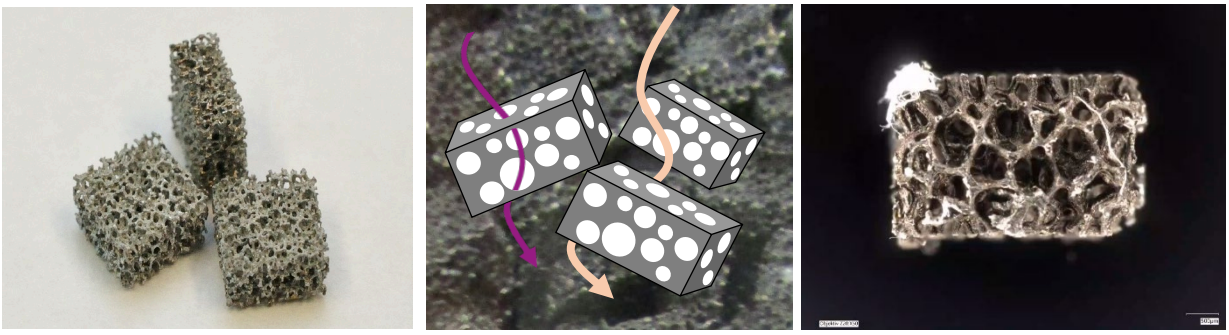

Figure 1 (a) Cuboidal open foam catalyst particles (b) flow patterns through a foam catalyst

bed and (c) OM view of foam carrier material in the submicron region.

Experimental

Foam catalyst (Metalyst® MC 981)

The Ni based metallic foam catalyst Metalyst® MC 981 (Evonik Operations GmbH) was used in the present study. It has been manufactured under a license from Alantum Europe GmbH [8]. The preparation method is described in [12].
Ni foam as roll material with a thickness of 1,9 mm was sprayed with polyethyleneimine binder solution, coated with commercially available aluminum powder (particle size <150 µm, $d_{50} \approx 68$ µm) and subjected to heat treatment in absence of oxygen at up to 715°C. The mass ratio of Ni foam and aluminum powder was chosen such that the ratio of aluminum to the total mass of the resulting supported alloy was 28±2%. After cooling, the material was comminuted with a laser into cuboidal particles having outer dimensions of 4 mm x 4 mm x 1,9 mm. The resulting bulk material was activated by treatment with a 10 wt.-% NaOH solution at 60°C for 60 min. The resulting catalyst was washed with demineralized water and ammonium chloride solution until pH 7,5-8 had been attained.
The resulting activated Ni foam was impregnated with a 55,4 wt.-% solution of ammonium heptamolybdate at room temperature for several hours until the molybdenum was completely deposited on the foam material. The catalyst obtained was washed twice with demineralized water.
The resulting catalyst Metalyst® MC 981 contained more than 87 wt.-% Ni, 12 wt.-% aluminum and <1 wt.-% molybdenum.

It should be mentioned that the activated Ni foam-based catalyst Metalyst® MC 981 is not pyrophoric, but self-heating in air due to its relatively high metal surface area. It reacts easily with oxygen forming NiO in an exothermic reaction. However, when kept wet the catalysts can be handled as safely as a commonly used oxidic supported catalyst material but advantageously without formation of Ni containing dust.

No further activation or reduction of the activated foam catalysts is necessary after being transferred into the reactor.

Granular catalyst (Specialyst® 103)

A Ni-Cu supported granular catalyst Specialyst® 103 (Evonik Operations GmbH) was used as reference material for comparison with the catalytic foam material. The preparation method is described in [13].
An extruded Al_2O_3 carrier material (d = 1,2 mm, BET surface: 260 m^2/g) was impregnated with an aqueous solution of copper(II)hydroxide carbonate, nickel hydroxycarbonate paste, ammonium carbonate and ammonia. The resulting material is dried in air <100°C and is subsequently calcined in air at 450°C. The resulting pre-catalyst contains 6,5 – 7,0 wt.-% copper and 2,8 – 3,3 wt.-% nickel.

The pre-catalyst is transformed into the active catalyst after transferring it into the reactor by reduction in hydrogen flow at T_{Red} = 180°C (heating rate from RT in 30 K steps with 1 Nl/min off gas).

Pressure drop

The pressure drop of the foam material was investigated in a glass reactor (h= 240 cm, d_i= 8 cm) at atmospheric pressure and temperatures between 20°C and 60°C. INAL was used as liquid feed, for biphasic flow N_2 was added instead of hydrogen. Pressure drop was determined at flow rates between 200 and 600 $Lmin^{-1}$.

Non-activated Nickel-foam material was used for the pressure drop measurement to decrease hazardous potential.

Hydrogenation tests

The catalytic performance of the catalysts applied in this study was investigated for isononanal (INAL) hydrogenation to isononanol (INA) in lab scale fixed bed reactor setups which allowed operation in batch and continuous mode.

The batch operation setup consisted of a packed bed reactor containing the investigated catalyst Metalyst® MC 981 or Specialyst® 103 (catalyst volume: 50 ml) with an external recycle loop with a pump and a heat exchanger to regulate the temperature in the reactor. A gas/liquid separator was applied to remove unreacted hydrogen gas at the reactor outlet. Recycle liquid feed rate amounted to 45 l/h; pressure amounted to 26 bar.

The continuous setup consisted of a first hydrogenation step similar to the batch reactor setup, but with a higher total possible catalyst volume of 200 ml, and a second hydrogenation step also with a fixed bed reactor which always contains Specialyst® 103 catalyst (Volume: 100 ml) connected to the liquid outlet of the first hydrogenation step.
To avoid hot spot formation the first reactor was run in a recycle mode with an external recycle loop with cooling device. Additionally, due to the higher activity of Metalyst® MC 981 (see results section "Batch tests"), only 100 ml of catalyst were applied compared to 200 ml for the Specialyst® 103 catalyst. The recycle stream was kept constant at 25 L/h. Hydrogen and fresh feed were mixed before the entrance to the fixed bed reactor. Surplus hydrogen was removed at the reactor outlet in a continuous off-gas stream. Hydrogen partial pressure was regulated so that a constant off gas flow of 1L/min was obtained. Temperature in the first reaction step was varied from 130°C to 170°C, while the reactor temperature of the second step was kept constant at 180°C.

The liquid reactor outlet streams of both reactor steps were frequently sampled and analyzed by gas chromatography. A FFAP CP Wax 58 capillary column (250°C, L=25 m, ID: 320 µm, FT: 0,2 µm) and a HP-5HP-5 capillary column (325 °C: L=30 m, ID: 320 µm, FT:0.25 µm) were used for separation of the components in the product mixtures. The feed and product compositions contain >100 components. Therefore, the components are lumped to product groups (aldehydes, alcohols, esters, ethers, hydrocarbons, formates, acetales, aldol condensates, etc.) for ease of discussion.

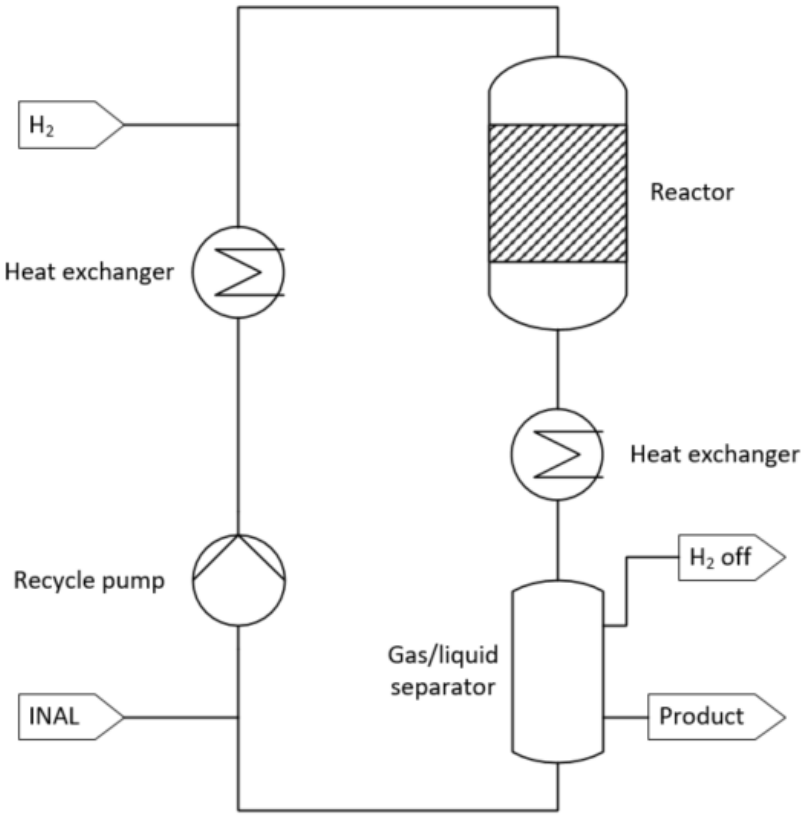

Figure 2 Lab scale set-up for catalyst testing in INAL hydrogenation in the batch mode

In the experiments performed (batch and continuous operation) real product streams from a hydroformylation production plant were used. These INAL feeds already contained side components which must be considered in the evaluation of the catalyst performance. A typical feed composition is given in Table 1.

Table 1 Typical feed composition for INAL hydrogenation (from Co based oxo process) [13]

component	HC	ZL	AL	FOR	OL	Ether	Ester	Acetale	H_2O
content (wt-%)	5,5	0,1	69,2	0,3	21,7	0,0	0,8	1,6	0,7

With HC = hydrocarbon, ZL = undefined, AL = aldehyde, FOR = formate, OL = alcohol

These side components can also react over the applied catalysts, some leading to the formation of INA (e.g. ether cleavage). Depending on feed composition and catalyst applied this might lead to total INA selectivities above 100 % with respect to the amount of INAL in the feed.

Results and Discussion

Physico-chemical properties of the applied Ni foam-based catalyst Metalyst® MC 981

580 µm pore size foam material was used throughout this study. Other pore sizes were tested, but lower catalytic performance was observed in INAL hydrogenation. Depending on the outer particle geometry -larger pore sizes can result in lower amount of active material is available in the reactor, whereas small pore sizes can lead to diversion of the liquid flow around the

particles, thus resulting in suboptimal utilization of the active centers inside the catalyst pores. (see reaction section). These results are not reported here.
The applied Metalyst® MC 981 catalyst has a total porosity of 0,925 with a bulk density of 0.451 g cm^{-3} in a packed bed.

Pressure drop investigations

One of the advantages of open cellular foams is their lower pressure drop in packed beds compared to granular material. The reason is that the liquid will not only move around the particles as in granular packed beds but can flow through the open cellular structure as well. This, however, makes a prediction of pressure drop more difficult, as pressure drop not only depends on the particle´s outer geometry, but also on the inner foam structure (mainly pore size).

Pressure drop is an important parameter in process design and performance of trickle bed reactors as it affects the energy requirements and hence the operating cost and sizing of the reactor [14]. Various hydrodynamic factors influence the two-phase pressure drop of a trickle bed reactor, including gas flow rate, liquid flow rate, surface tension of the liquid phase, viscosity of the liquid phase, and bed characteristics such as porosity and sphericity of the packing material. In the present paper, we only report on the pressure drop of liquid flow through the foam filled tubular reactor.
The pressure drop of the 580 µm pore size Metalyst® MC 981 and Specialyst® 103 catalysts are shown in *Figure 3* for different temperatures. The granular material exhibited 8 to 10 times higher pressure drop compared to the foam catalyst. For both materials pressure drop decreased with increasing temperature. This can be explained by the lower viscosity of the fluid with increasing temperature. The pressure drop of the liquid flow in the glass reactor tube without catalytic material was less than <1 mbar and can therefore be neglected.

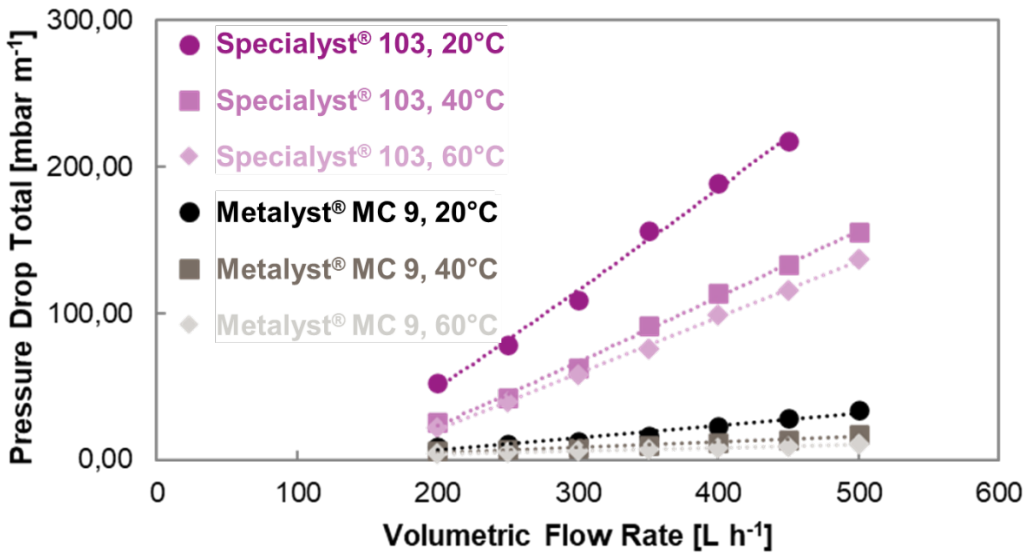

Figure 3 Pressure drop for liquid flow of INAL in dependence of liquid flow rate and temperature for the non-activated catalyst material Metalyst® MC 9 and Specialyst® 103 in a fixed bed (bed height: 204 cm, d = 8 cm)

Pressure drop was also investigated for biphasic flow INAL/N_2 at 20°C. It can be depicted from Figure 4 that in presence of additional N_2 flow (volume fraction: 70 % INAL, 30 % N_2) the pressure drop is again diminished by approx. 15 % and another 50 % when larger gas flows than typical under trickle bed conditions are used.

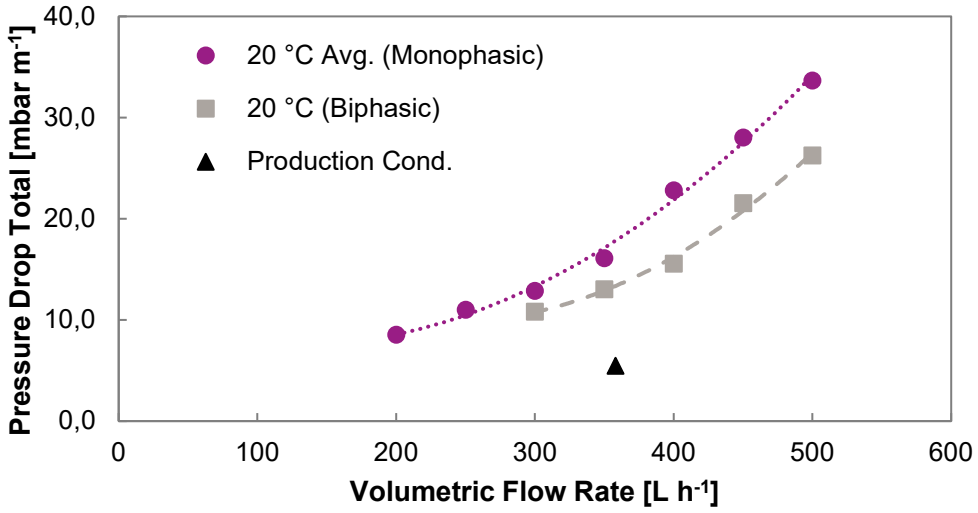

Figure 4 Comparison of pressure drop from monophasic and biphasic flow (volume fraction: 70 % INAL, 30 % N2) over non-activated Metalyst® MC 9 in a fixed bed (bed height: 204 cm, d = 8 cm)

As mentioned above, the pressure drop has been evaluated applying the non-activated catalyst foam material of Metalyst® MC 981. It might be expected that due to the higher surface roughness of the activated catalyst surface the pressure drop under real reaction conditions could be slightly higher than observed in this study. However, the roughness effect is proposed to be small and should be lower than 5 %. This value was adapted from differences in pressure drop for smooth and rough (1 µm) micro channels [15].

In conclusion, the Metalyst® MC 981 catalyst exhibits a significantly lower pressure drop (8 to 10 times) than the granular Specialyst® 103. Similar behavior, however, is already known from research on other catalytic open foam fixed bed, e.g. for gas flows [16].

Catalytic investigations

Batch-Tests

The performance of the Metalyst® MC 981 foam catalyst was investigated for the hydrogenation of INAL in batch mode to obtain information about the activity of the foam catalyst material compared to conventional granular Specialyst® 103 catalyst and the respective selectivity behavior.

Temperature dependence

The reaction rate of Metalyst® MC 981 and Specialyst® 103 catalysts in INAL hydrogenation were investigated at reaction temperatures between 130°C and 180°C at a pressure of 26 bar. Figure 5 shows the conversion vs. reaction time behavior for Metalyst® MC 981 (at T_R= 130 and 150°C) and the reference catalyst Specialyst® 103 (at T_R= 130, 150 and 180°C).
The newly developed Ni foam based catalyst Metalyst® MC 981 shows complete INAL conversion after1,1 h reaction time at 150°C and after 1,5 h reaction time at T_R= 130°C. When applying the same catalyst volume of Specialyst 103, 6,0, 3,5 and 1,5 h at 130°C, 150°C and 180°C, respectively, are required for complete conversion of INAL. Thus, an increase in operation temperature of 50 K over Specialyst 103 is necessary to obtain conversion rates comparable to the results achieved with Metalyst® MC 981. This correlates to an approx. 2 to 3 times higher volumetric reaction rate for Metalyst® MC 981. Based on catalyst mass even higher differences between the reaction rates of the two catalysts occur.

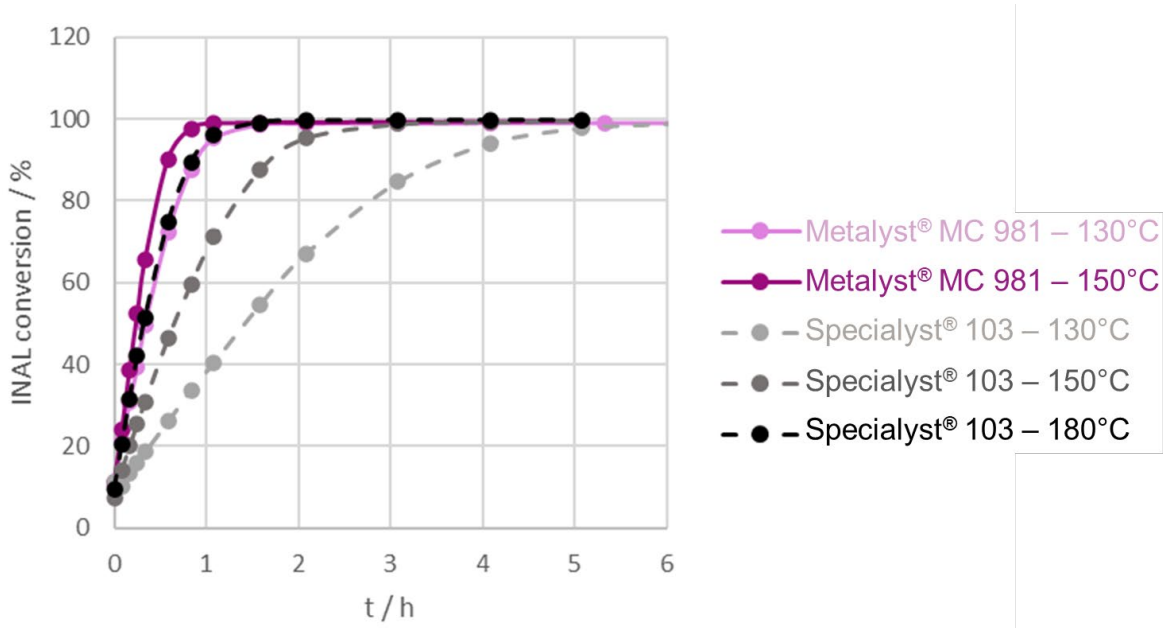

Figure 5 Temperature dependence of conversion of INAL vs reaction time over Metalyst® MC981 (lines) and Specialyst® 103 (dotted lines) catalyst in a fixed bed recycle reactor (batch mode) (V_{cat} = 50 ml; T_R= 130 – 180°C; P = 26 bar)

Selectivity behavior

The conversion of INAL vs. reaction time for the conventional Specialyst® 103 catalyst and the innovative Metalyst® MC 981 at the same reaction temperature of T_R= 150°C are presented in Figure 6(a). After 1 h of reaction already complete conversion was obtained for Metalyst® MC 981, whereas approx. 3 h were necessary for Specialyst® 103. The analysis of the product selectivities at 99 % conversion (T_R= 150°C) for Specialyst® 103 and Metalyst® MC 981 (after 1 h reaction time for Metalyst® MC 981 and 3 h for Specialyst 103) shows that over Metalyst® MC 981 approx. 2/3 less undesired side products are formed compared to the reaction over Specialyst® 103. The cleavage of acetals and esters is much less pronounced over the Metalyst® MC 981 catalyst (-1,92 % vs. – 3,35 %) under these conditions.

In conclusion Metalyst® MC 981 is a highly active hydrogenation catalyst which transforms INAL into INA with very high selectivity. Conversion of side products usually present in the hydrogenation feed are minimized to cleavage of formats to a low extent under the conditions applied.

Mass transport limitation effects

The linear fluid velocity over the catalyst bed of Metalyst® MC 981 particles was modified by changing the recycle flow rate between 30 L/h and 60 L/h. No significant change in reaction rates could be observed, indicating that no film diffusional limitation occurs.
When modelling the temperature dependence of the hydrogenation reaction applying a simple first order reaction rate, the activation energy $E_{a,eff}$ obtained was significantly lower ($E_{a,eff}$ = 17±1 kJ/mol) than calculated for the Specialyst® 103 ($E_{a,eff}$ = 40 kJ/mol). This indicates that the reaction rates achievable over the Ni foam-based catalyst Metalyst® MC 981 are most probably limited by pore diffusional effects under the reactions conditions chosen. This has to be considered for further reactor design.

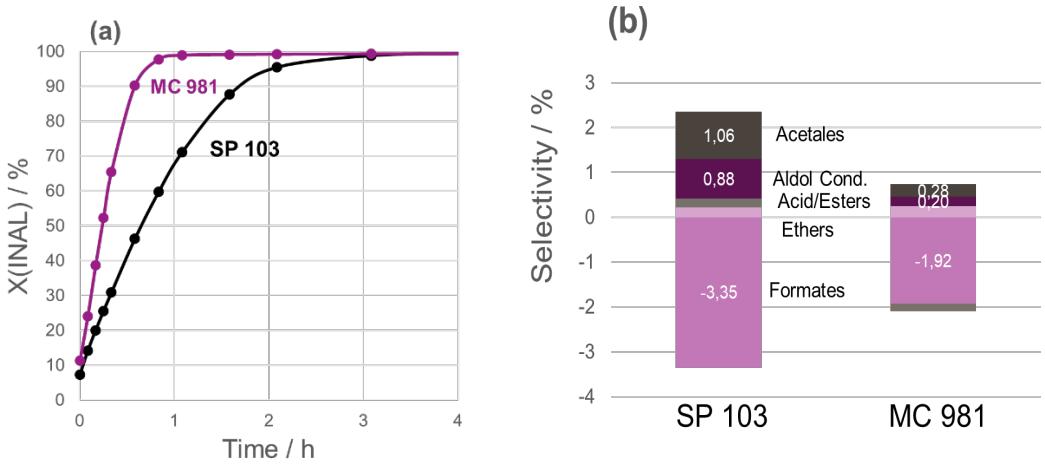

Figure 6 (a) INAL conversion vs. reaction time and (b) side product selectivities at 99 % conversion for Metalyst® MC 981 foam (purple) and Specialyst® 103 (SP 103, black) (T_R= 150°C, P = 25 bar, each 50 ml catalyst) in batch operation mode

Continuous Operation

Hydrogenation reactions often suffer from deactivation effects of the catalysts applied. Multiple reasons for deactivation are conceivable, e.g. poisoning by undesired feed components, restructuring of the catalyst surface over time, leaching to name a few of the most important. Therefore, it is important to investigate the long-term stability of the catalysts under reaction conditions.

A long-term study was performed in the described continuous reactor setup for over 3000 h applying the reference catalyst a well as the Metalyst® MC 981 in the first hydrogenation step. During this trial several reaction parameters like feed quality and feed rate, as well as reaction temperature in the first and second hydrogenation step were changed.

Figure 7 shows the INAL conversion for the applied conditions. The purple curve gives the conversion in the first hydrogenation step containing the Metalyst® MC 981 catalyst, whereas the black curve gives the total INAL conversion for both hydrogenation steps with Metalyst® MC 981 in the first recycle reactor and Specialyst® 103 in the tubular finishing reactor.
The fluctuations in the purple curve are due to changes in reaction parameters (T, mass flow, feed quality), which are marked by the grey lines in the graph. Complete INAL conversion was consistently achieved at the outlet after the two-step hydrogenation reaction. However, a slow decrease in conversion can be observed for Metalyst® MC 981 used in the first hydrogenation step.

A possible deactivation pathway of the hydrogenation catalyst is the poisoning by components of the utilized INAL feed, e.g. contaminants from the oxo process step, or reaction products immediately formed at the reactor entrance at high INAL concentrations (e.g. high boilers formed by aldol condensation of the aldehyde [7,17]). Therefore, the deactivation rate of the catalysts used was compared based on the continuous long-term experiments with respect to the cumulated amount of INAL fed to the reactor over time.

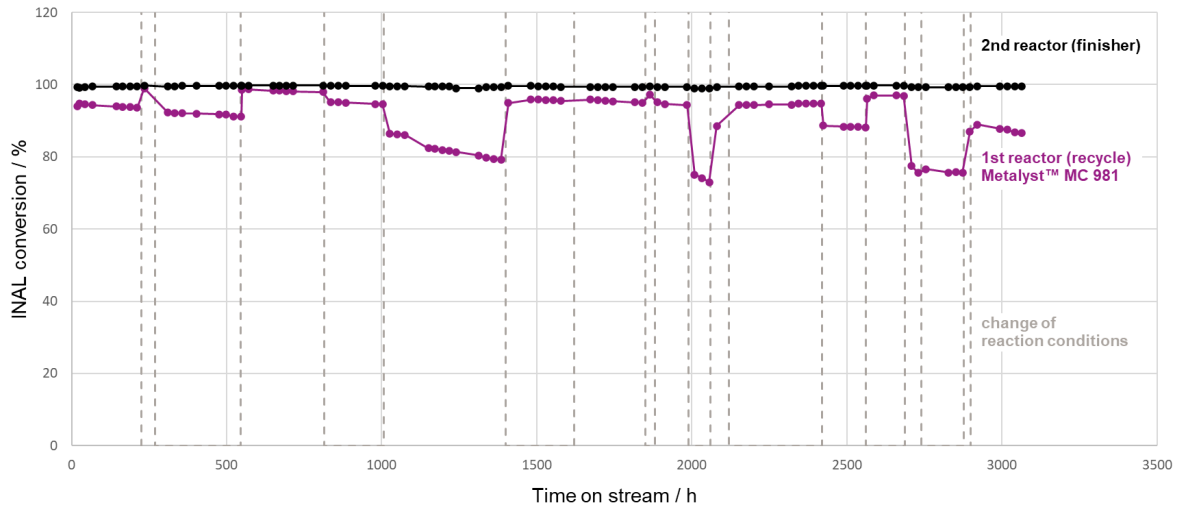

Figure 7 Performance of the activated Nickel foam catalyst Metalyst® MC 981 in INAL hydrogenation to INA under various operating conditions during a time-on-stream of 3000 h.

A linear deactivation behavior was observed with respect to the amount of INAL fed to the reactor for both investigated catalysts, i.e. Specialyst® 103 and Metalyst® MC 981. Furthermore, the rate of deactivation for both catalysts are similar. The results, however, do not allow to elucidate the reason for the deactivation.

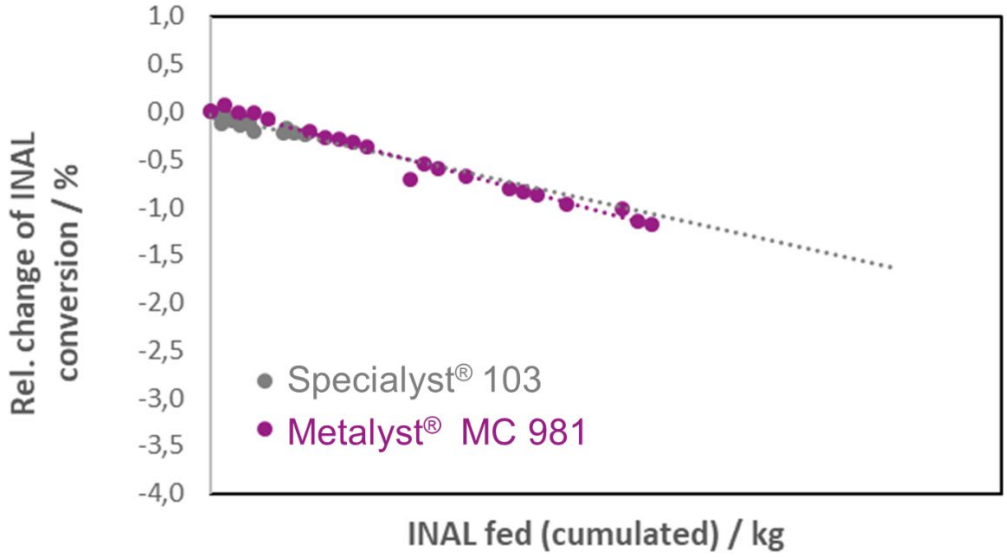

Figure 8 Comparison of deactivation of Specialyst® 103 and Metalyst® MC 981 catalyst in dependence of cumulated INAL fed into the reactor

Conclusions

An activated Ni foam-based catalyst doped with Molybdenum (Metalyst® MC 981, Evonik Operations GmbH) was developed and applied under technically relevant conditions in the hydrogenation of isononanal (INAL) to isononanol (INA). When applied as cuboidal particle fixed bed, the catalyst exhibited excellent performance in the desired hydrogenation step. At least threefold higher reaction rates compared to a conventional Ni-Cu supported catalyst (Specialyst® 103, Evonik Operations GmbH) were observed. Selectivity of the INAL

hydrogenation was comparable in both catalyst systems. Additionally, side reactions like formation of aldol condensates were strongly minimized over the activated Ni foam-based catalyst. Also, the conversion of side products in the feed stream from oxo-process were diminished over this type of catalyst. This allows for separate optimization of the reaction in two consecutive steps, which could lead to further improvements in industrial applications.
Long-term experiments up to 3000 h demonstrated high process stability in a two-step operation with a recycle reactor containing the Metalyst® MC 981 foam catalyst in the first step and the conventional granular Specialyst® 103 catalyst in the second single throughflow step. By analyzing the recycle step it was observed, that the foam catalyst slightly deactivates over time and in linear correlation with respect to the amount INAL fed to the reactor. The speed of deactivation is comparable to that of the conventional Specialyst® 103 catalyst.
Summarizing: Metalyst® MC 981 exhibited superior performance compared to the incumbent catalyst mainly due to its unique physico-chemical properties (porosity and pressure drop) and its significantly higher catalytic activity.

References

1 Anand, S.; Pinheiro, D.; Devi, K.R.S.; Asian J. Org. Chem. 10(12), 3068, (2021).
2 Handbook of Homogeneous Hydrogenation, Ed. J.G. de Vries, J.E. Cornelis, Verlag Wiley-VCH, Weinheim, Germany, (2007)
3 Argyle M., Bartholomew C., Catalyst, 5, 145, (2015).
4 Mann, R. Catal. Today, 1997, 37, 331-349.
5 Vargas, J.M.; Agosto, M.; Riley, K.L.; Exxon Chem. Pat. Inc., US 5,399,793 B (1995)
6 Bonnier, J.M.; Damon, J.P.; Masson, J.; Appl. Catal. 30, 181 (1987)
7 (a) Reinsdorf, A.; PhD Thesis, University of Bayreuth (2017)
(b) Reinsdorf, A.; Korth, W.; Jess, A.; Klasovsky, F.; DGMK conference "Catalysis – Novel Aspects in Petrochemistry and Refining", Berlin (2016)
8 Radivojevic, D., Naumann, D., Saberi, S., Bae, J., Poss, R.; Alantum Europe GmbH, EP 2,764,916 B1 (2014)
9 Lali, F., Böttcher, G., Schöneich, P.-M., Haase, S., Hempel, S., Lange, R., Chem. Eng. Res. Des. 94, 365, (2015)
10 Cimino, S.; Cepollaro, E.M., Lisi, L., Fasolin, S., Musiani, M.,Vázquez-Gómez, L., Catalysts 11, 13, (2021)
11 Walther, G.; Gaitzsch, U.; Büttner, T.; Kieback, B.; Weißgärber, T.; Kolvenbach, R.; Lincke, M.; International Powder Metallurgy Congress and Exhibition Euro PM2017, Milan, Italy, 1.-5.10.2017 (2017)
12 Roos, M.; Poss, R.; Berweiler, M.; Göttlinger, M.; Wieland, S.; Franke, R.; Altmann, L.; Evonik Operations GmbH, US 11,401,224 B2 (2022)
13 Klasovsky, F.; Franke, R.; Becker, M.; Quandt, T.; Geilen, F.; EP 3,037,400 B1 (2015)
14 Bansal, A.; Wanchoo, R.K.; Sharma, S.K.; Chem. Eng. Commun. 195(9), 1085, (2008)
15 Dzarma, G.W.; Adeyemi, A.B.; Taj-Liad, A.A.; Int. J. Novel Research Eng. Sci. 7(1), 1, (2020)
16 George, G.R.; Bockelmann, M.; Schmalhorst, L.; Gerstle, A.; Beton, D.; Torkuhl, L.; Lindermeir, A.; Wehinger, G.D.; Reaction Engineering Conference 2022, Würzburg, Poster
17 Reinsdorf, A.; Korth, W.; Jess, A.; Terock, M.; Klasovsky, F.; Franke, R.; J. Catal. (2016)

Supported Catalytically Active Liquid Metal Solutions (SCALMS) as Novel Materials for Dynamic Single Atom Catalysis

N. Taccardi, M. Haumann, P. Wasserscheid
Friedrich-Alexander-Universität Erlangen-Nürnberg (FAU)
Lehrstuhl für Chemische Reaktionstechnik (CRT)

Abstract

Supported Catalytically Active Liquid Metal Solution (SCALMS) systems represent a new concept for promoting chemical reactions in a clean and sustainable manner through catalysis. In SCALMS materials, a matrix metal is doped with small amounts of (precious or non-precious) active metal.[1] The resulting is deposited in the form of very small droplets onto a porous support material. Given the right composition, these alloys become liquid at reaction temperature. We found that under these conditions single atoms of the active metal, stabilized at the liquid alloy interface, act as highly active and dynamic single catalytic sites with often unique reactivity and performance.[2] Due to the single atom nature, the SCALMS concepts allows for a very effective use of the dissolved precious metal component.

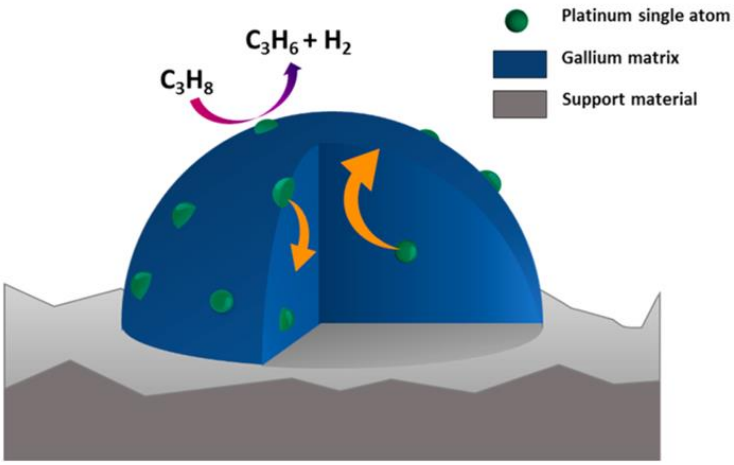

In addition, the highly dynamic nature of the liquid alloy interface prevents classical deactivation pathways, such as coking and agglomeration (sintering).[3] With these unique benefits, we could show that SCALMS systems are highly promising catalyst systems for i) the dehydrogenation of short (propane, butane) and long (heptane, methylcyclohexane) hydrocarbons, ii) the selective oligomerization of propene and butene,[4] iii) dry reforming of methane. We are convinced that further progress in SCALMS materials development will directly lead to energy and emission reductions, and thus to greener and more benign processes.

References

[1] N. Taccardi et al. Nature Chem. 2017, 9, 862.
[2] N. Raman et al. ACS Catal. 2019, 9, 9499.
[3] O. Sebastian et al. ChemCatChem 2020, 12, 4533.
[4] A. Søgaard et al. Cat. Sci. Technol. 2021, 11, 7535.

Artificial Photosynthesis: The Role of Photocatalysis in the Energy Transition

M. Tommasi[1], F. Conte[1], G. Ramis[2], I. Rossetti[1]
[1] Chemical Plants and Industrial Chemistry Group, Dip. Chimica, Università degli Studi di Milano, CNR-SCITEC and INSTM Unit Milano-Università, Italy; [2] Dip. Ing. Chimica, Civile ed Ambientale, Università degli Studi di Genova and INSTM Unit Genova, Genoa, Italy

Abstract

Artificial photo-synthetic approaches are gaining spreading interest in order to exploit solar light for the production of fuels. Different applications are proposed, among which the most explored are the production of H_2 and the reduction of CO_2 and, much more recently, attention is also paid to the photosynthesis of ammonia. Despite the enormous progresses in the field of materials development and characterization, which allowed to understand the main phenomena driving photo-catalysed up-hill reactions, the productivities achieved still do not justify the scale up of the processes to relevant scales and efficiencies are still very low, calculated over natural irradiance, in most cases much lower than 1%.
In this work we focus on a multiscale approach to improve the conversion and productivities, with special reference to the photoreduction of CO_2, developing a coupled strategy to optimize materials, conditions and irradiance. On the materials scale, TiO_2 has been extensively used as photocatalyst, being an inexpensive and non-toxic semiconductor, with manufacturing at industrial scale and recyclability options, but it is absorbing UV radiation, only, ca. 5% of sunlight. Furthermore, photogenerated electrons and holes must survive enough to migrate to the photocatalyst surface and react with the adsorbed species, but unfortunately the charge recombination rate in titania is quite fast. The metal-free polymeric catalyst, graphitic carbon nitride (g-C_3N_4) is a relatively novel material, characterized by wider absorbance in the visible region. Its junction with a second semiconductor or with metals can also improve the lifetime of the photogenerated charges. In this paper only TiO_2 catalysts have been tested due to the need of a large batch of reproducible materials for testing of different operating conditions, though visible responsive and stable g-C_3N_4, g-C_3N_4@TiO_2, WO_3@TiO_2 and g-C_3N_4@ WO_3 demonstrated superior performance under visible irradiation.
From the process conditions side, we developed and innovative photoreactor operating at high pressure, up to 20 bar, which is unprecedented in photocatalytic applications, where transparent windows are needed. This allows to boost the solubility of CO_2 in water when operating the reactor as tri-phase liquid/gas/solid device, and improves the surface adsorption over the catalyst. The best productivity for HCOOH so far achieved with this system at 18 bar, pH = 14 and by using Na_2SO_3 as hole scavenger was ca. 1.4 g/h g_{cat}, boosted to ca. 2 g/h g_{cat} when complex hole scavengers mixtures are tested, which showed a still unexplained synergistic effect. Such productivity is orders of magnitude higher than literature values.
Finally, the coupling with concentrating solar devices as a follow up of this study will make available a higher irradiance, further boosting the productivity.

Introduction

The exploitation of renewable energies plays a key role to reduce the emission of CO_2, mitigate the climate change and provide a clean environment as well as clean energy for the population. Despite the great disadvantage of unpredictability and intermittency, a source that can be considered theoretically infinite is sunlight: it is free, more or less equally distributed around the globe and during the capture and storage of the sun energy, no CO_2 is actually emitted.
The main way in which the solar energy is exploited by nature is photosynthesis which is a process that converts the carbon dioxide present in the atmosphere into sugar-based biomass. With the development of photovoltaic panels research tried to imitate this process with less

success, with an efficiency that ranges between 10 and 20% [1]. When speaking about the energy produced through photovoltaic panels at a large scale, there is another problem: the electricity generated with this process needs to be consumed right away because batteries and accumulators that can be used to store energy at a small scale (even though they reduce the efficiency of the overall process) cannot be currently applied to a commercial large scale.
A different option to exploit solar light is the production of solar fuels through photocatalysis. Heterogeneous photosynthetic processes, in particular, make use of solid semiconductors that are activated through the absorption of a photon with energy higher than their band gap [2], This generates an electron-hole couple, so that each separated charge may be exploited to promote reduction or oxidation reactions with redox couples present in the reaction environment. It is particularly interesting for photosynthetic applications, where solar light can be used to achieve the reduction of water to H_2 or of CO_2 to various solar fuels. The concept is very promising, but many challenges still limit the potential for exploitation, among which: i) the limited lifetime of the photopromoted charges, that relax faster than the reactive events; ii) limited sensitivity of the main photocatalysts to solar light harvesting; iii) scale-up challenges due to limited radiation distribution and reactor design issues.
In this paper we will deepen the first issue, by improving the charges lifetime through selection of an appropriate hole scavenger (HS), i.e. a compound acting as electron donor to the semiconductor, preventing the relaxation of the photopromoted electron for a sufficient time, to allow it to promote the reduction reaction. The focus for application is the photoreduction of CO_2, which is carried out in an innovative photoreactor, operating up to 20 bar pressure to boost CO_2 absorption in aqueous medium and surface adsorption over the catalyst surface. To compare the performance of different HS we have used the most worldwide employed photocatalyst, titanium dioxide, in commercial nanosized form [3,4]. Titania shows some great advantages since it is abundant, inexpensive [5], non-toxic to humans (though recently WHO has labeled titanium dioxide as potential carcinogen when used as food additive [6]), resistant to photocorrosion when used in solution with water [7] and with an already assessed recyclability [8].
Despite all the good properties, titanium dioxide deserves some big issues, including a relatively large band gap and a high recombination rate of the promoted photocharges. These are two critical problems because they depress the efficiency of the process [9,10]. Anatase shows a band gap equal to 3.23 eV and this induces an absorption threshold of 387 nm [11]. This represents a critical aspect for the use of TiO_2 which is poorly activated by the sunlight since the UV portion of the total sun radiation is around 5%.
On the other hand, CO_2 is very inert due to its very stable oxidation state. Our aim is to use of solar energy to convert CO_2 into solar fuels like formic acid and methanol. CO_2 photoreduction allows to remove carbon dioxide from atmosphere and to produce a valuable product. The data related to thermodynamics can be found in literature [12–14], from which it is possible to glean some general information. The transfer of more electrons to achieve a more reduced product is harder, so on a kinetic basis, formic acid is the easier product of CO_2 reduction, followed by formaldehyde, methanol and lastly methane. However, because the reaction occurs at a lower potential, methane and methanol are the preferred products from a thermodynamic perspective. These results, however, do not account for several factors, including pH, the phase, the type of catalyst, the interaction between CO_2 and titania, CO_2 and a metallic co-catalyst, or titania and metal [14].
The multi-electron water splitting and CO_2 reduction reactions are reported in Equations 1 to 6, together with the Gibbs free energy variation ΔG_0 and the standard redox potential ΔE_0. All the reactions have extremely positive ΔG_0 values, which makes CO_2 reduction a highly endoergonic process that is very challenging at room temperature. The ΔG_0 values also suggest that the water splitting cannot store as much energy as the CO_2 reduction reactions, which become therefore particularly intriguing as energy storage strategy [15].
Due to the larger reduction potential of 1.9 V compared to a conventional hydrogen electrode, the reaction by one electron to generate a CO_2 radical is highly unfavorable for the reduction of CO_2. In contrast, multi-electronic processes are more advantageous since they require significantly less energy for each electron transfer than mono-electron processes do.

$$(Eq.1) \quad H_2O(l) \rightarrow H_2(g) + \frac{1}{2}O_2(g) \qquad \Delta G^0 = 237\frac{kJ}{mol} \qquad \Delta E^0 = 1.23\,V$$

$$(Eq.2) \quad CO_2(g) \rightarrow CO(g) + \frac{1}{2}O_2(g) \qquad \Delta G^0 = 257\frac{kJ}{mol} \qquad \Delta E^0 = 1.33\,V$$

$$(Eq.3) \quad CO_2(g) + H_2O(l) \rightarrow HCOOH(l) + \frac{1}{2}O_2(g) \qquad \Delta G^0 = 286\frac{kJ}{mol} \qquad \Delta E^0 = 1.48\,V$$

$$(Eq.4) \quad CO_2(g) + H_2O(l) \rightarrow HCHO(l) + O_2(g) \qquad \Delta G^0 = 522\frac{kJ}{mol} \qquad \Delta E^0 = 1.35\,V$$

$$(Eq.5) \quad CO_2(g) + 2H_2O(l) \rightarrow CH_3OH(l) + \frac{3}{2}O_2(g) \qquad \Delta G^0 = 703\frac{kJ}{mol} \qquad \Delta E^0 = 1.21\,V$$

$$(Eq.6) \quad CO_2(g) + 2H_2O(l) \rightarrow CH_4(g) + 2O_2(g) \qquad \Delta G^0 = 818\frac{kJ}{mol} \qquad \Delta E^0 = 1.06\,V$$

Additionally, every step required to convert CO_2 to CO, HCOOH, hydrocarbons, or alcohols has low kinetic barriers. Proton-assisted multielectron transfer is a different and preferable method to reduce CO_2 compared to the mono-electron technique. Through multi-electron transfer procedures, H_2CO_3 and the carbonate ions in the solution can be reduced to a range of products, including CH_3OH, HCOOH, and HCHO.
In a previous investigation we have concluded that the mechanism shown here below is the most likely to occur at pH=14 (starting from the carbonate ion, , which is the one leading to the highest overall productivity and energy stored for CO_2 photoreduction) or at neutral pH, starting from absorbed CO_2 [16,17]:

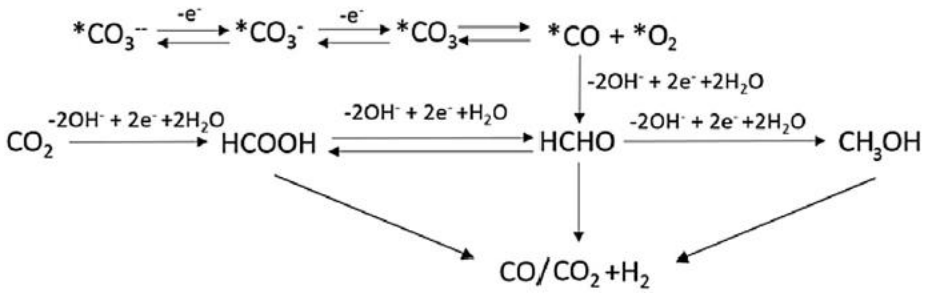

Reaction conditions and catalyst formulation greatly affect both the yield and the products distribution obtained from the photoreduction process.
Here below a short list of the main influencing factor is summarized, besides the trivial effect of the photocatalyst formulation [18–21]:

- *Partial pressure of CO_2* ➔ Increased CO_2 partial pressure enhances CO_2 absorption, adsorption, and diffusion into the photocatalyst's pores as well as its concentration in solution [13]; the use of a high pressure photoreactor for the first time led to unprecedented productivity even with very simple photocatalysts such as TiO_2.
- *Temperature* ➔ it plays a double role: on one side it increases the reaction kinetics and desorption of products while on the other it reduces the solubility of CO_2 in water, which is already very low (about 2 g/L). Coupling an increase of temperature with a higher pressure allows to explore unconventionally high temperatures (80-120°C), boosting activity.
- *pH* ➔ this parameter influences the solubility of CO_2. Higher pH translates into higher CO_2 solubility and, as a consequence, higher productivity. In addition, OH^- ions can lead to the formation of $OH^{\cdot}$ radicals, which are strongly oxidizing species that can

oxidise back the reaction products.

- *Photoreactor configuration* ➔ influences the mixing, the catalyst dispersion and the light irradiation profile.
- *Hole scavenger* ➔ CO_2 is reduced by the photopromoted electron and, to close the circuit, holes must be saturated by a proper electron donor. Water oxidation (reported in Eq. 1-6 as basic example) is a slow multielectron process. Sacrificial hole scavengers are usually employed.

In this paper we are summarising the effect of some operating parameters based on previous investigations. The core of the manuscript will then be the study of the effect of hole scavengers for this application, which is very rarely discussed in the literature.

Experimental

Samples of commercial P25 TiO_2 by Evonik were used as reference material, to ensure a reproducible large batch of photocatalyst.
All the experiments have been performed in an innovative high-pressure batch photoreactor, sketched in Fig. 1 [22]. The high-pressure (up to 20 bar) allows to improve the CO_2 solubility, in water which at atmospheric pressure is quite poor (around 2 g/L at 25°C). In addition, the CO_2 solubility decreases at higher temperature, which can be however beneficial to improve the kinetics of the reactions.

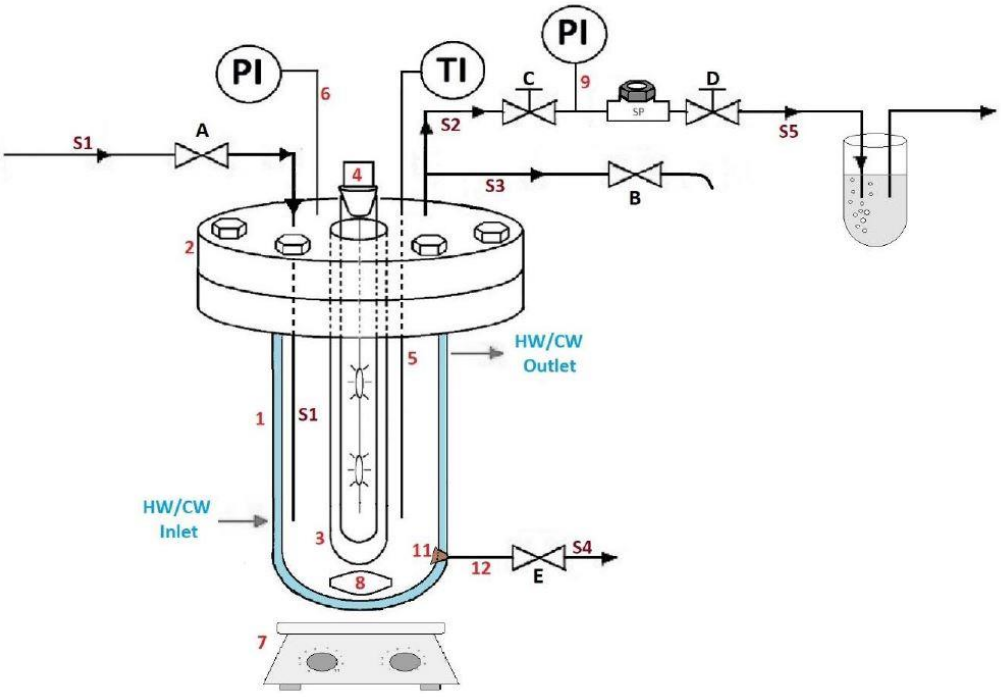

Fig. 1 Scheme of the high-pressure batch photoreactor.

The reactor consists of a jacketed cylinder-shaped vessel (1) made of AISI 316 stainless steel with an internal gross volume of 1.7 L and an internal net volume of 1.3 L, decreased due to the presence of the quartz candle. The external jacket is used to heat (or cool) in order to maintain the desired reaction temperature during the different experiments. The top of the reactor consists of a flange closure (2) that is tightened by screwing some bolts. Between the two flange sides, a silicon gasket is placed in order to ensure a tight seal and avoid gas leaks. The use of a gasket is fundamental, especially when performing experiments at 20 bar of pressure. During the experiments, the reaction mixture is kept under stirring through the help

of a spinner (8) and of a magnetic stirrer (7) operated at 400 rpm in order to ensure a homogeneous dispersion of the solid catalyst in the liquid phase. At the bottom of the reactor is also present a valve that allows the discharge of the reactor at the end of the experiments. A quartz candle (3) is placed in the axis of the reactor. The latter, which contains the UV-lamp (4), is allowed to resist to the pressure inside the reactor, protects the radiation source while allowing the UV-radiation to pass.
The UV-lamp used for the photoreduction is usually a medium Hg Pressure lamp with a power of 125W. The radiation sources are two light bulbs that emit in the range of 254-364 nm. When operated the lamps heat up, needing cooling through a flux of air. A newer design is composed of LED lamps, either UV or visible (emitting in the blue), which do not need cooling and have a much lower power consumption.
The gas inlet and the gas outlet are placed in the upper part of the reactor. In particular, the gas inlet metal pipe (S1) is immersed inside the reaction liquid so that the gases can bubble up when the high-pressure reactor is being loaded. The outlet is placed in the upper section of the flange. Another AISI 316 stainless steel pipe closed at the bottom and present inside the reactor is used for the thermocouple insertion (5). The head of the reactor also is connected to a manometer which allows us to measure the pressure inside the reactor (6). The discharge of the gas and liquid phase of the reactor is performed respectively through the (S2) and (S3) line. The (S2) line which allows the discharge of the gaseous product is connected to a sampling loop that allows the sampling of the gas to be analyzed. The last part of the gas line, called (S5) is the purging line, equipped with a bubble counter filled with silicon oil. The (S3) line is used for the discharge of the liquid product that are analyzed through HPLC.

The reactor is filled with 1.2 L of an aqueous solution of hole scavenger (typically 1.66 g/L, if not specified else), with the desired amount of catalyst (typically 0.031 g/L) and the pH is kept neutral or, eventually, NaOH is added (pH = 7 or 14). The pressure is set with pure CO_2, bubbled into water and typical operating conditions are either 8 or 18 bar, 80°C.
Once the pressure has reached equilibrium, the lamp is turned on. Each experiment is carried out for 24 or 6 h. After testing, the lamp is turned off, the reactor is cooled to ambient temperature and three consecutive gas samplings are collected for GC analysis. Three liquid samples of 10 mL each are collected, centrifugated at 10,000 rpm for 15 minutes to perform the iodometric titration (to quantify HS conversion when sodium sulphite is used) and the HPLC analysis to determine the amount of liquid products obtained.
The analysis of the gaseous compounds is done with a GC Agilent 7890A equipped with two columns (HP PlotQ and MS, both 30 m long), two detectors (FID and TCD) and a sampling loop of 250 µL.
The HPLC analyses on the liquid mixture were performed with a Jasco instrument, including an injection sampling loop of 20 µl, a precision pump (PU-4180), a polymeric column (SepaChrom Benson Polymeric BP-OA BL0053 2000-0) with a stationary phase of PS-DVB sulphonated gel (dimension 300 x 7.8 mm) immersed in a thermostated bath. The liquid is analyzed through a UV-Vis Detector and a Refractive Index (RI) detector. The wavelength of the UV-Vis detector is fixed at 210 nm in order to analyze with more accuracy the amount of formic acid obtained from the analysis.
The power of the lamp has been mapped with the help of a photoradiometer (model Delta OHM HD2102.2, LP 471A-UV probe). Lamp power have been measured at three different heights: the first measure in correspondence of Bulb A, the second at Bulb B, while the third measure has been taken in the middle between Bulbs A and B. For each height, eight different positions have been checked (from I to VIII) around the lamp, each one at three different distances from the axis: distance (a) corresponds to the inner wall of the steel photoreactor, distance (c) corresponds to the outer wall of the quartz tube that protects the lamp inside the reactor, while distance (b) is taken exactly in the middle between (a) and (c). Collected data are reported in Table 1 and Fig. 2.
A non completely homogeneous distribution of the light radiation inside the reactor is due to various factors including the inherent geometry of the bulbs, the geometry of the reactor, the presence of electrical cables connecting the two bulbs, and the presence of two steel tubes around the quartz candle.

LAMP POWER			
Lamp A	**a**	**b**	**c**
	W/m2	W/m2	W/m2
I	29,00	59,00	117,00
II	50,00	106,00	205,00
III	123,00	212,00	404,00
IV	117,00	222,00	456,00
V	143,00	275,00	601,00
VI	134,00	263,00	563,00
VII	137,00	221,00	313,00
VIII	82,00	110,00	208,00
Middle	**a**	**b**	**c**
	W/m2	W/m2	W/m2
I	23,00	32,00	17,00
II	30,00	30,00	25,00
III	70,00	61,00	30,00
IV	64,00	49,00	17,00
V	56,00	44,00	8,00
VI	54,00	42,00	12,00
VII	32,00	39,00	15,00
VIII	53,00	42,00	36,00
Lamp B	**a**	**b**	**c**
	W/m2	W/m2	W/m2
I	37,00	71,00	102,00
II	44,00	60,00	82,00
III	112,00	153,00	162,00
IV	95,00	153,00	181,00
V	123,00	143,00	173,00
VI	94,00	139,00	191,00
VII	68,00	90,00	131,00
VIII	57,00	82,00	116,00
Average	**a**	**b**	**c**
	W/m2	W/m2	W/m2
	76,13	112,42	173,54

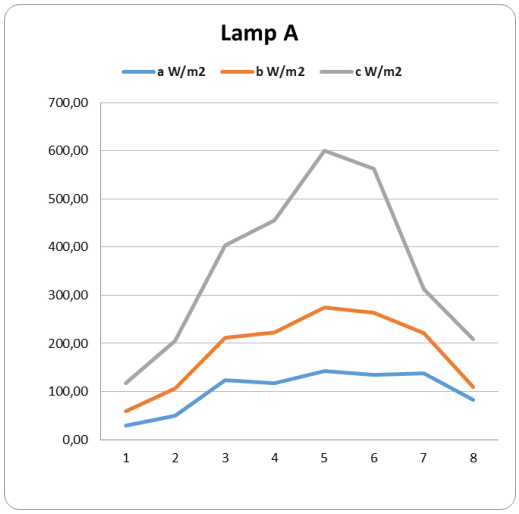

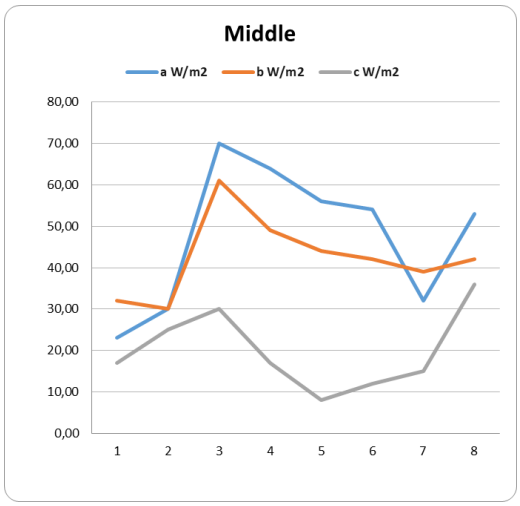

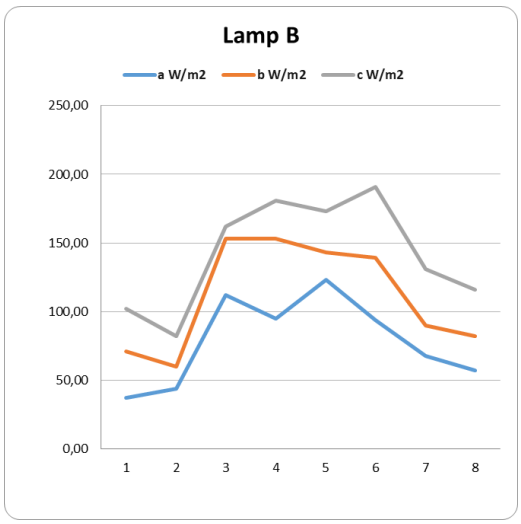

Table 1 and **Fig. 2:** Lamp power mapping datasheet and Irradiance graph.

Results and discussion

Through the preliminary set up of the apparatus, the following dependence on the operating conditions has been found. The productivity of every product increased as catalyst concentration in the reactor decreased. This has been explained as the result of improved light distribution throughout the reaction solution. The optimal value of catalyst concentration has been found out to be 0.031 g/L for TiO_2 P25 as catalyst as reported in Fig. 3 [17].

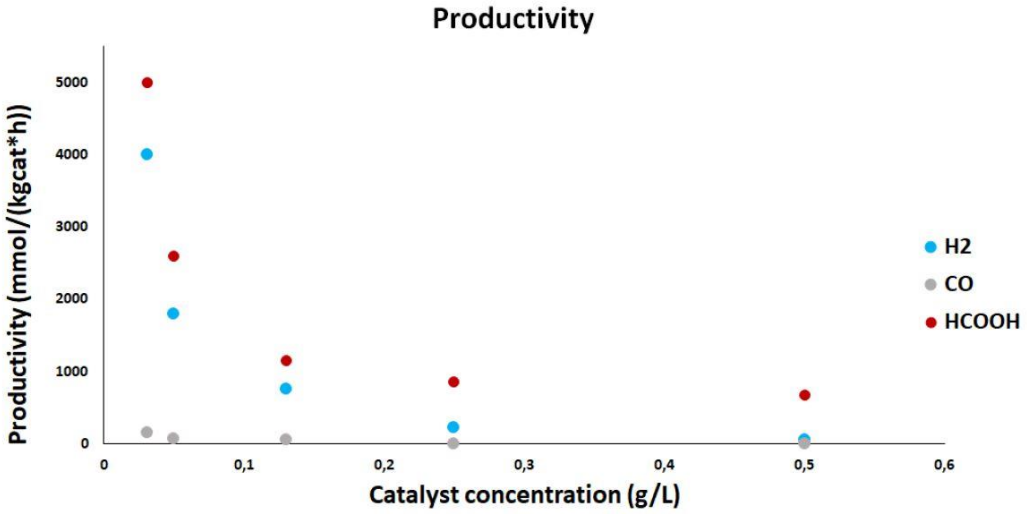

Fig. 3 Productivity vs. catalyst concentration. Catalyst TiO_2 P25, HS Na_2SO_3 1.66 g/L, pH=14, T = 80°C, P=8 bar.

From the photoreduction of CO_2 performed in aqueous phase the two main products obtained are formic acid and methanol, depending on the operating conditions, particularly on pH. HCOOH is a substance widely used in the textile, leather and rubber industry, as well as a reagent in many processes. At the moment it is obtained through the hydrolysis of formamide and the oxidation of hydrocarbons. Its production is roughly 840 ktons/year with a selling price of 870 $/ton in 2020. CH_3OH is widely used in the production of formaldehyde, dimethyl ether and as solvent or reagent. Currently its production derives from the use of syngas (produced from coal or methane). Methanol can also be used in the energy sector, blended with gasoline or to feed DMFC (direct methanol fuel cells) that are used for power production [23]. For this reason, there is a strong incentive in the development of a green methanol production process. Its production is roughly 110 million tons per year with a selling price that in 2020 was equal to 340 $/ton.
Through this process, HCOOH was obtained with much higher productivity than methanol, which, combined to its higher value, suggests focusing on formic acid as primary target product for CO_2 photoreduction.
The presence of a hole scavenger is essential to lower the rate of electron and hole recombination and, consequently, to increase the reaction rate. An inorganic HS was originally selected by us, sodium sulfite, to avoid interference with the detection of organic products of CO_2 photoreduction and to allow an easier interpretation of the reaction mechanism. In its absence, a negligible productivity has been achieved. In Fig. 4 results of experiments performed with different hole scavenger concentration are summarized. Since the formation of the gas phase photoreforming products (H_2, CO) begins only after full sulphite consumption, after which the products of CO_2 photoreduction start to consume as HS themselves [16], the use of higher quantity of HS (3.34 and 6.68 g/L) prevented the consumption of the formic acid produced.

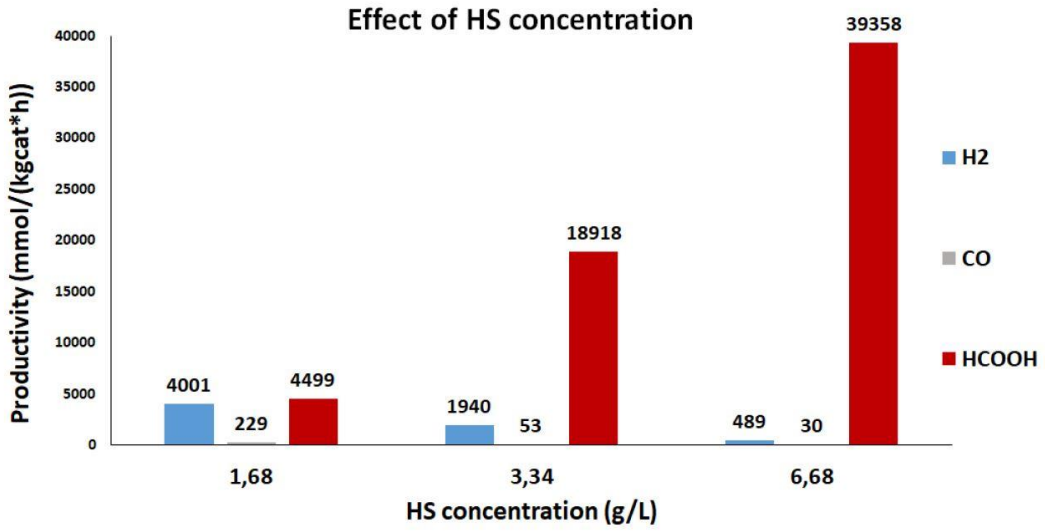

Fig. 4 Productivity vs. concentration of HS (Na_2SO_3), reaction time 24h, catalyst TiO_2 P25, pH =14, T = 80°C, P=8 bar.

This point is particularly intriguing and seems the key to achieve realistic productivity for this reaction. Given the primary role that is played by the HS in the photoreduction process, in this paper different hole scavengers have been screened in order to determine their influence on the type of products obtained and on their productivity, a topic scarcely investigated in the literature.

Effect of hole scavenger

The tests have been carried out on the commercial benchmark material, P25 TiO_2, to ensure homogeneous materials properties for a large experimental campaign. 6 h reaction time has been selected to avoid the complete oxidation of the hole scavenger, which would lead to the consumption of the organic products as hole scavengers themselves due to consecutive photoreforming. The base concentration of Na_2SO_3 has been used, 1.66 g/L, to avoid excess consumption of reactants and highly concentrated solutions, while keeping the same molar concentration for the different scavengers.

The productivity of P25 at neutral pH was 541 mmol/kg_{cat}h, 484 mmol/kg_{cat}h and 323 mmol/kg_{cat}h respectively for formic acid, formaldehyde and methanol. The test performed at basic pH despite not producing methanol, showed a much higher productivity of formic acid way higher equal to 16884 mmol/kg_{cat}h, while the productivity of formaldehyde did not change appreciably (512 mmol/kg_{cat}h) (Fig. 5). This result is in line with the one reported in a previous study [9] that was performed with longer reaction time.

Sodium sulfite has been selected as hole scavenger due to two main features: it is easy to oxidize and inexpensive. It increased the lifetime of the photoexcited electrons very effectively, but this molecule is produced through a synthetic route, with no current production possibilities starting from a renewable resource, and during the use as HS, the produced sulphate accumulates inside the reactor and its separation or regeneration is not easy.

For this reason, in this work we searched for alternative hole scavengers to further increase the productivity of the photoreduction process and that can be also produced through the use of renewable resources or recovered from waste streams.

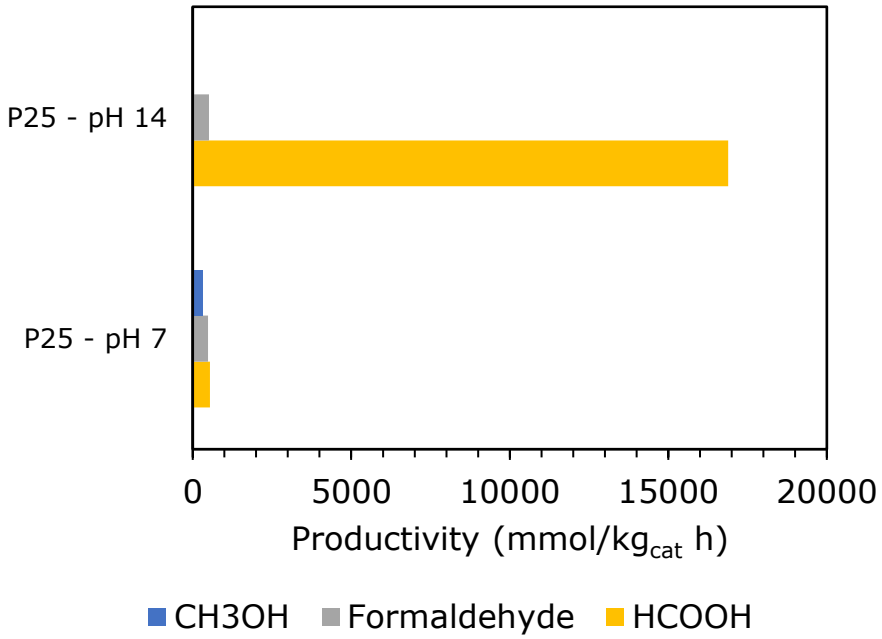

Fig. 5 Photoreduction of CO_2 with TiO_2 P25, Na_2SO_3 as hole scavenger at pH 7 and 14. 6 h reaction time.

Different HS have been tested to find out a possible alternative to sodium sulfite. The tests performed with different hole scavengers can be divided in three groups: ammonia-based HS (such as ammonia and urea), organic HS with alcoholic function (like methanol, ethanol and polyalcohols such as glycerol) and organic HS with amine function (such as tri-ethanolamine). All the tests have been performed using the same molar amount of hole scavenger, 15.8 mmol, corresponding to the amount of Na_2SO_3 added in the standard tests (1.66 g/L).

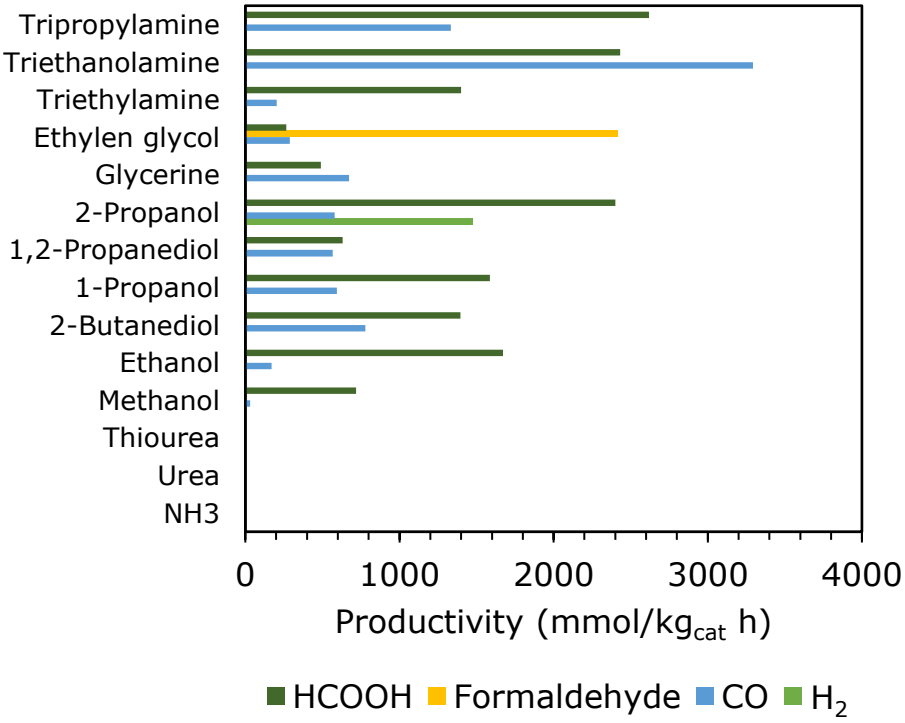

Fig. 6 Productivity obtained by testing different HS. Catalyst TiO_2 P25, pH 14, 8 bar, 80°C, 6 h reaction time.

Fig. 6 reports the productivity of formic acid and formaldehyde for each test, besides the productivity of CO and H_2, possibly obtained by consecutive or parallel photoreforming.

Ammonia (NH_3) was firstly selected as promising candidate, since its selective oxidation produces molecular nitrogen which, being a gas easily released, would have solved the problem of accumulation of the oxidized scavenger in the photoreactor [24]. Also, being ammonia itself a gas, it would also employable, in perspective, in a continuous gas phase system, which cannot make use of liquid HS. The photooxidation of ammonia is also reported in the literature, though partially successful at much lower ammonia concentration [25,26].
For this application, the productivity obtained with the use of ammonia was extremely low, both towards liquid and gaseous products. Increasing the pressure up to 18 bar and the quantity of HS used were also ineffective attempts. Further tests, performed with a combination of ammonia and sodium hydroxide did not show any change in the productivity. Other authors suggested that ammonia combines preferably with hydroxyl radical generated by the UV-light instead than with the photogenerated holes on the surface of the catalyst [27,28]. This leads to holes accumulation, lowers the efficiency of the photocatalyst and leads, as a consequence, to a lower productivity.
Urea has been also tested as hole scavenger being cheap, non-toxic and a possible ammonia source, but unfortunately the productivity was negligible also in this case. The same holds for thiourea. As in the case of ammonia, urea and thiourea react more easily with the hydroxyl radicals present in the aqueous solution rather than with the photogenerated holes on the catalyst surface [29], demonstrating ineffective as direct hole scavengers.

Various alcohols have been tried, starting from methanol to more complex polyalcohols like ethylene glycol and glycerol which can represent a greener alternative since they can be already produced from natural sources. Results obtained from the tests are reported in Table 2.

HS	**H_2 (mmol/kg_{cat}h)**	**CO (mmol/kg_{cat}h)**	**HCHO (mmol/kg_{cat}h)**	**HCOOH (mmol/kg_{cat}h)**
Methanol	0	32	0	718
Ethanol	0	171	0	1671
2-Butanediol	0	779	0	1396
1-Propanol	0	594	0	1587
1,2-Propanediol	0	566	0	631
2-Propanol	1478	579	0	2401
Glycerol	0	673	0	491
Ethyleneglycol	0	288	2420	265
Triethylamine	0	204	0	1400
Triethanolamine	0	3293	0	2432
Tripropylamine	0	1334	0	2618

Table 2 Productivity obtained with different HS (15.8 mmol), TiO_2 P25, pH 14, 6 h, 80 °C and 8 bar.

Methanol led to the worst results, with a productivity of 718 mmol/kg_{cat}h and 32 mmol/kg_{cat}h respectively of HCOOH and CO. Ethanol and 1-propanol showed higher and similar productivity for formic acid (1671 mmol/kg_{cat} h and 1587 mmol/kg_{cat} h) with 1-propanol evidencing a 3-fold increase in the productivity of CO (594 mmol/kg_{cat} h vs. 171 mmol/kg_{cat} h). The productivity increased again with the increase in the number of C atom: 2-butanol compared to 2-propanol showed a higher productivity of CO (779 mmol/kg_{cat} h vs. 579 mmol/kg_{cat} h), but half the productivity of formic acid and no hydrogen present, compared with 2-propanol, which led to a H_2 productivity of 1478 mmol/kg_{cat} h. Alcohols overall may lead to a parallel direct photoreforming to produce H_2 as competitive reaction. By looking to the products

distribution it cannot be excluded the coexistence of both reactions, though alcohols have a non negligible contribution of direct photooxidation to CO (and CO_2 which is not quantified being the major component in the gas phase).
The productivity overall increased with increasing the number of carbon atoms in the scavenger molecule. Some authors suggest that alcohols are effective as hole scavenger only after they are activated from hydroxyl radical, as in the case of ammonia [30]. This could explain why the productivity increased substantially when using a secondary alcohol which is more stable, compared to a primary alcohol, once activated by the hydroxyl radical.
Among the polyalcohols, ethylene glycol achieved a quite low productivity of formic acid and carbon monoxide (below 300 $mmol/kg_{cat}\,h$), but surprisingly an interesting amount of formaldehyde produced. 1,2-propandiol and glycerol showed similar productivity of both formic acid (631 $mmol/kg_{cat}\,h$ vs 491 $mmol/kg_{cat}\,h$) and carbon monoxide (566 $mmol/kg_{cat}\,h$ vs 673 $mmol/kg_{cat}\,h$).

Organic molecules with amine functional group have been also tested, since they can be produced from the fermentation of proteins and free amino acids [31], while being also present in industrial wastewaters. Triethanolamine for example is used in the manufacture of surface active agents, waxes, polishes, detergent builders, herbicides, demulsifies, cement additives, and cutting oils. Moreover, in general, alkanolamines are good inhibitors of the corrosion of ferrous metals and for this reason they are widely used in coolant systems and other specific applications [32]. Finally, alcanolamines are proposed as valuable compounds for CO_2 capture processes, so that if successful as hole scavengers a direct photoconversion of the absorbed CO_2 / alkanolamine stream can be considered.
Triethylamine as HS returned similar results than alcohols, with a productivity of HCOOH and CO respectively of 1400 $mmol/kg_{cat}\,h$ and 204 $mmol/kg_{cat}\,h$. Results were much more interesting when tripropylamine and triethanolamine were used. In particular, the latter showed an incredibly high CO productivity (3293 $mmol/kg_{cat}\,h$) compared to the 1334 $mmol/kg_{cat}\,h$ of the tripropylamine. Also, the productivity of formic acid was quite high for both HS, ca. 2500 $mmol/kg_{cat}\,h$, very similar to the one obtained with the use of 2-propanol.
This activity difference between triethylamine and tripropylamine is hard to explain but in literature is reported that triethylamine reacts on the titanium dioxide surface and there is a high chance that the same concept is applied also to propylamine [33].
The high productivity obtained with the use of triethanolamine, especially for what concerns the carbon monoxide, has also been reported by some authors [34] who observed a similar productivity trend when testing these different amines and explained that triethanolamine can interact stronger with hydroxylic groups present on the titania surface. This stronger adsorption leads to an increase in the productivity.

2-propanol as HS
Overall, 2-propanol was the most promising substitute HS, though not reaching the same HCOOH productivity than sodium sulphite, and thus it has been further investigated. The results are reported in Table 3.

Fig. 7 shows the results obtained with 2-propanol as HS after 6 and 24 hours reaction time. The experiment was performed at 18 bar and from the 6 hours test the majority of the products obtained were carbon monoxide, formic acid and acetic acid. Acetic acid should be the product of the oxidation of ethanol and in theory the oxidation of a secondary alcohol, like 2-propanol, should lead to the formation of acetone. This means that acetone should be further oxidized and decarbonised. It is suggested that acetone can be adsorbed on the titanium dioxide surface by interacting with the surface oxygen. This adsorption leads to the formation of a ketene intermediate which undergoes the elimination of a methyl radical [35]. This last step leaves an acetate adsorbed on the titania surface which can then be released as acetic acid. When increasing the reaction time, the productivity of CO, HCOOH decreased while the one of acetic acid increased and also the H_2 productivity increased greatly. The latter is likely formed by the photoreforming of the organic products formed upon photoreduction of CO_2, that start to act as hole scavengers or by the photoreforming of the primary HS itself. The

conversion of 2-propanol also increased from 10.8% to 36.4%.
Fig. 8 shows the results in the same conditions of Figure 7 except for the pressure that was decreased from 18 to 8 bar. Productivity increased as well as the conversion of HS which raised from 19.6% and 68.7% respectively after 6 and 24 hours reaction time. The productivity trend was the same. In particular, the productivity of acetic acid results tripled when decreasing the pressure.

Hole Scavenger	**mmol HS**	**t (h)**	**T (°C)**	**P (bar)**	**HS Conv. (%)**	**H_2**	**CO**	**HCOOH**	**CH_3COOH**
2-prop	15.8	6	80	18	**10.8**	0	396	660	1539
		24	80		**36.4**	509	265	542	2049
2-prop	15.8	6	80	8	**19.6**	1478	579	2401	4535
		24	80		**68.7**	1780	400	1364	6066
2-prop	15.8	6	30	8	**18.0**	787	203	1870	4291
		24	30		**49.7**	1201	166	1058	4555
2-prop	7.9	6	80	8	**25.9**	884	435	2153	3888
		24	80		**86.7**	1500	419	1159	4804
2-prop + Na_2SO_3	15.8 + 15.8	6	80	8	**5.5**	1495	118	45870	0
		12	80		**18.4**	2435	508	19884	0

Table 3 Productivity (mmol/h kg_{cat}) and HS conversion. Tests with 2-propanol as HS, 0.031 g/L TiO_2 P25, pH 14, various temperature, pressure and reaction time as indicated.

These tests show an inverse trend in productivity with respect to Na_2SO_3 as HS: with the latter the productivity increases by increasing pressure, while using 2-propanol as HS, the productivity increases as pressure decreases.
Two different adsorbed species were found over the TiO_2 surface, in particular 2-propanol and 2-propoxyde [36,37]. The decomposition reaction of the adsorbed species over TiO_2 can proceed through the dehydrogenation or the dehydration. In the photocatalytic oxidation of 2-propanol, only acetone was found as dehydrogenation product of 2-propanol and 2-propoxide. The mechanism regarding the dehydrogenation of 2-propanol and the further oxidation of acetone is still not clear. Bickley et al. suggest that formic acid and acetaldehyde are intermediates of the photocatalytic oxidation of acetone [38]. Other authors, such as Rochester [39] indicate the formation of carboxylate species as results, which could directly lead to the formation of acetic acid. Other authors report that the photocatalytic oxidation of 2-propanol is affected by different factors, including the competitive surface adsorption of the different products in the solution [37,40]. This suggests that in our case, when the operative pressure is increased, the CO_2 solubility is increased and this increases the competition for surface adsorption with the 2-propanol present in solution, causing a decrease in the overall productivity of the catalyst.
A test at lower temperature has been also performed. Fig. 9 reports the productivity obtained at 30°C and 8 bar, which was only a little bit smaller than the one obtained at 80 °C. Also, the conversion of 2-propanol was a lower, 18.0% and 49.7%, respectively after 6 and 24 hours, vs. 19.6% and 68.7% achieved at 80 °C. So the effect of temperature was not as important for 2-propanol as when using sodium sulfite as HS, while pressure played a much bigger role. This is likely due to the fact that the majority of the products obtained during the test performed with 2-propanol as hole scavenger come from the photooxidation of isopropanol and of the acetone that is produced.
Given the relatively low conversion of the HS, an experiment with half the quantity of 2-propanol has been also performed (Table 3). The overall productivity was lower for every compound considered. However, what is interesting to notice is that for the first time the

productivity of the carbon monoxide and of the formic acid was higher after 24 hours compared to 6 hours. The conversion of HS after 6 and 24 hours was equal respectively to 26% and 86.7%.
A test was finally performed by using sodium sulfite and 2-propanol in combination (1:1 mol/mol). From the results reported in Fig. 10 it can be noticed that the productivity of the formic acid was increased by ten times. The conversion of sodium sulfite was completed in 12 hours while the conversion of 2-propanol raised from 5.5% to 18.4% respectively after 6 and 12 hours. Acetone was detected among the products in this analysis, suggesting that the hypothesized mechanism was correct. The presence of a HS extremely easy to oxidize, such as sodium sulfite, prevented the further conversion of acetone to acetic acid. It is important to notice the synergic effect when both HS are used together. In this last test the productivity of formic acid after 6 hours was equal to 45870 mmol/kg_{cat}h compared to the benchmark productivity of P25 in the same conditions with Na_2SO_3 as HS which was equal to 13889 mmol/kg_{cat}h [41]. Acetone was identified as a primary degradation intermediate for 2-propanol oxidation and subsequently acetic acid and formic acid were identified as secondary products. A blank test was performed without CO_2 added to the reactor and by using nitrogen to set the pressure. No relevant productivities were detected, except for small amounts of hydrogen and acetone, deriving from the direct photoreforming of 2-propanol.

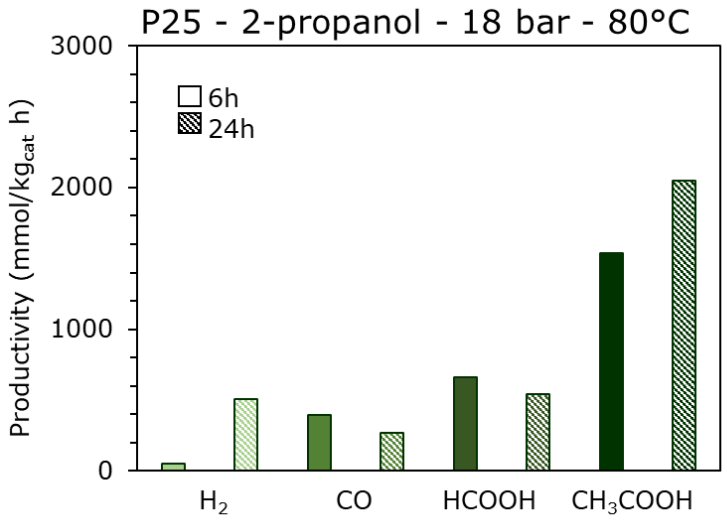

Fig. 7 Products distribution for photoreforming of CO_2 with TiO_2 P25 using 2-propanol as HS at 18 bar, 80°C.

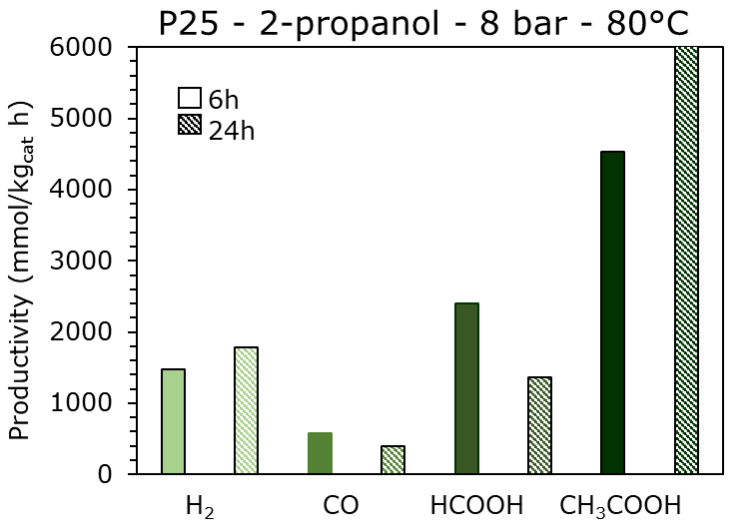

Fig. 8 Products distribution for photoreforming of CO_2 with TiO_2 P25 using 2-propanol as HS at 8 bar, 80°C.

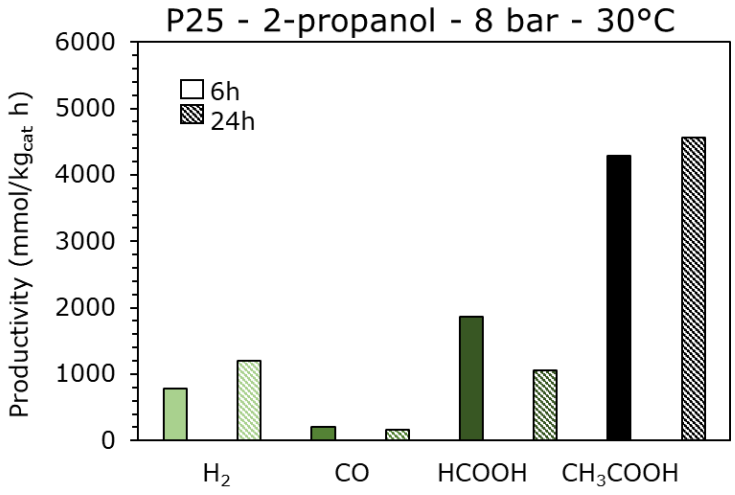

Fig. 9 Products distribution for photoreforming of CO_2 with TiO_2 P25 using 2-propanol as HS at 8 bar, 30°C.

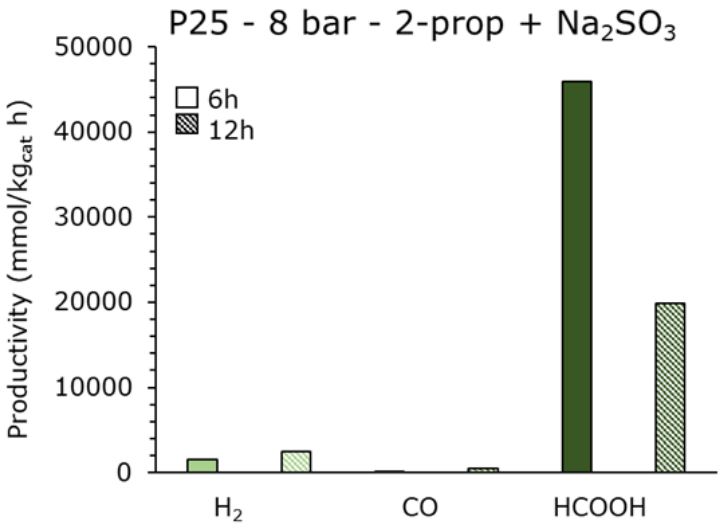

Fig. 10 Products distribution for photoreforming of CO_2 with TiO_2 P25 using 2-propanol and sodium sulphite (1:1 mol/mol) as HS at 8 bar, 80°C.

Conclusions

The photoreduction of CO_2 is an intriguing photosynthetic approach to exploit solar light and store it in form of solar fuels. This is particularly relevant since this reaction converts a powerful greenhouse gas, that represents a paradigm in the energy transition. Nevertheless, insufficient productivity has been reported till now in the literature to become relevant for scale-up. The photoreduction of CO_2 has been investigated here through an innovative photoreactor, which allows to operate at high pressure and temperature, achieving higher productivity with respect to literature data. Specific attention was focused on the test of different hole scavengers.
Various tests were carried out using commercial titania P25 in combination with various organic and inorganic hole scavengers. The results obtained showed that the choice of the HS was not simple and have underlined the difficulty to find renewable alternatives to the sodium sulfite (Na_2SO_3) currently in use. Ammonia, which was one of the most ideal HS, did not show any activity, probably due to the reaction mechanism underpinning its oxidation. P25 performances when using alcohols, vary greatly depending on the HS used. In particular, 2-propanol shifted the products distribution towards acetic acid and for this reason its effect has been deepened. Tests have shown that the presence of acetic acid is related to the conversion of the intermediate acetone. As suggested by some authors, acetone can be adsorbed on the titanium dioxide surface and may lead to the formation of a ketene intermediate which undergoes the ejection of a methyl radical, leaving an acetate adsorbed. The latter can be further released as acetic acid. Tests have highlighted the reverse influence of the pressure on the productivity. In particular the productivity increased when the pressure was decreased with this HS, in contrast with sodium sulphite.
Overall, as high as 2 kg HCOOH were obtained per kg of TiO_2 per h, which is an extremely promising result, attained when exploiting a synergy between sodium sulphite and 2 propanol as scavengers. Further investigations are in progress to understand the mechanism of this synergistic action.

Acknowledgements

Fondazione Cariplo (Italy) is gratefully acknowledged for funding this research through the grant "2021-0855 SCORE – Solar energy for circular CO_2 photoconversion and chemicals regeneration", in the frame of the 2021 call on circular economy (I. Rossetti and G. Ramis).
This research is also part of the project "One Health Action Hub: University Task Force for the resilience of territorial ecosystems", supported by Università degli Studi di Milano – PSR 2021

- GSA - Linea 6 (I. Rossetti).
Finally, this research is part of the activities of the Centro Nazionale Agritech – Spoke 8: New models of circular economy in agriculture through waste valorization and recycling (I. Rossetti).

References

1. Green, M.A.; Emery, K. Solar cell efficiency tables (version 3). *Prog. Photovoltaics Res. Appl.* **1994**, *2*, 27–34, doi:10.1002/pip.4670020105.
2. Xie, S.; Zhang, Q.; Liu, G.; Wang, Y. Photocatalytic and photoelectrocatalytic reduction of CO2 using heterogeneous catalysts with controlled nanostructures. *Chem. Commun.* **2015**, *52*, 35–59, doi:10.1039/C5CC07613G.
3. Fujishima, A.; Rao, T.N.; Tryk, D.A. Titanium dioxide photocatalysis. *J. Photochem. Photobiol. C Photochem. Rev.* 2000.
4. Zhang, J.; Zhou, P.; Liu, J.; Yu, J. New understanding of the difference of photocatalytic activity among anatase, rutile and brookite TiO2. *Phys. Chem. Chem. Phys.* **2014**, *16*, 20382–20386, doi:10.1039/c4cp02201g.
5. Donald, V.B. Titanium Dioxide: Commodity Or Speciality? *Pigment Resin Technol.* **1994**, *23*, 10–15, doi:10.1108/eb043098.
6. Grande, F.; Tucci, P. Titanium Dioxide Nanoparticles: a Risk for Human Health? *Mini-Reviews Med. Chem.* **2016**, *16*, 762–769, doi:10.2174/1389557516666160321114341.
7. Izumi, Y. Recent Advances (2012-2015) in the photocatalytic conversion of carbon dioxide to fuels using solar energy: feseability for a new energy. In *Advances in CO2 capture, sequestration and conversion*; American Chemical Society: Washington, 2015; p. 46.
8. König, B. *Chemical Photocatalysis*; 2020; ISBN 9783110576764.
9. Galli, F.; Compagnoni, M.; Vitali, D.; Pirola, C.; Bianchi, C.L.; Villa, A.; Prati, L.; Rossetti, I. Applied Catalysis B : Environmental CO 2 photoreduction at high pressure to both gas and liquid products over titanium dioxide. *"Applied Catal. B, Environ.* **2017**, *200*, 386–391, doi:10.1016/j.apcatb.2016.07.038.
10. Pomilla, F.R.; Brunetti, A.; Marcì, G.; García-López, E.I.; Fontananova, E.; Palmisano, L.; Barbieri, G. CO2 to Liquid Fuels: Photocatalytic Conversion in a Continuous Membrane Reactor. *ACS Sustain. Chem. Eng.* **2018**, *6*, 8743–8753, doi:10.1021/acssuschemeng.8b01073.
11. Yan, H.; Wang, X.; Yao, M.; Yao, X. Band structure design of semiconductors for enhanced photocatalytic activity: The case of TiO2. *Prog. Nat. Sci. Mater. Int.* **2013**, *23*, 402–407, doi:10.1016/j.pnsc.2013.06.002.
12. Abdullah, H.; Khan, M.M.R.; Ong, H.R.; Yaakob, Z. Modified TiO2 photocatalyst for CO2 photocatalytic reduction: An overview. *J. CO2 Util.* **2017**, *22*, 15–32, doi:10.1016/j.jcou.2017.08.004.
13. Ola, O.; Maroto-Valer, M.M. Review of material design and reactor engineering on TiO2 photocatalysis for CO2 reduction. *J. Photochem. Photobiol. C Photochem. Rev.* **2015**, *24*, 16–42, doi:10.1016/j.jphotochemrev.2015.06.001.
14. Li, K.; An, X.; Park, K.H.; Khraisheh, M.; Tang, J. A critical review of CO2 photoconversion: Catalysts and reactors. *Catal. Today* **2014**, *224*, 3–12, doi:10.1016/j.cattod.2013.12.006.
15. Li, X.; Wen, J.; Low, J.; Fang, Y.; Yu, J. *Design and fabrication of semiconductor photocatalyst for photocatalytic reduction of CO 2 to solar fuel*; 2014; Vol. 57; ISBN 4084301400031.
16. Bahadori, E.; Tripodi, A.; Villa, A.; Pirola, C.; Prati, L.; Ramis, G.; Rossetti, I. High pressure photoreduction of CO2: Effect of catalyst formulation, hole scavenger addition and operating conditions. *Catalysts* **2018**, *8*, 430, doi:10.3390/catal8100430.
17. Bedendi, M.; Rossetti, I.; Ramis, G. Design of photocatalytic processes for solar fuels production through CO2 photoreduction, University of Milan, 2019.

18. Conte, F.; Villa, A.; Prati, L.; Pirola, C.; Bennici, S.; Ramis, G.; Rossetti, I. Effect of Metal Cocatalysts and Operating Conditions on the Product Distribution and the Productivity of the CO 2 Photoreduction. *Ind. Eng. Chem. Res.* **2022**, *61*, 2963–2972, doi:10.1021/acs.iecr.1c02514.
19. Conte, F.; Tripodi, A.; Rossetti, I.; Ramis, G. Feasibility Study of the Solar-Promoted Photoreduction of CO2 to Liquid Fuels with Direct or Indirect Use of Renewable Energy Sources. *Energies* **2021**, *14*, 2804, doi:10.3390/en14102804.
20. Bahadori, E.; Tripodi, A.; Villa, A.; Pirola, C.; Prati, L.; Ramis, G.; Dimitratos, N.; Wang, D.; Rossetti, I. High pressure CO 2 photoreduction using Au/TiO 2 : unravelling the effect of co-catalysts and of titania polymorphs. *Catal. Sci. Technol.* **2019**, *9*, 2253–2265, doi:10.1039/C9CY00286C.
21. Bahadori, E.; Tripodi, A.; Villa, A.; Pirola, C.; Prati, L.; Ramis, G.; Rossetti, I. High Pressure Photoreduction of CO2: Effect of Catalyst Formulation, Hole Scavenger Addition and Operating Conditions. *Catalysts* **2018**, *8*, 430, doi:10.3390/catal8100430.
22. Rossetti, I.; Villa, A.; Pirola, C.; Prati, L.; Ramis, G. A novel high-pressure photoreactor for CO2 photoconversion to fuels. *RSC Adv.* **2014**, *4*, 28883–28885, doi:10.1039/c4ra03751k.
23. Rice, C.; Ha, S.; Masel, R.I.; Wieckowski, A. Catalysts for direct formic acid fuel cells. *J. Power Sources* **2003**, *115*, 229–235, doi:10.1016/S0378-7753(03)00026-0.
24. Tan, J.Z.Y.; Maroto-Valer, M.M. A review of nanostructured non-titania photocatalysts and hole scavenging agents for CO2 photoreduction processes. *J. Mater. Chem. A* **2019**, *7*, 9368–9385, doi:10.1039/c8ta10410g.
25. Bahadori, E.; Conte, F.; Tripodi, A.; Ramis, G.; Rossetti, I. Photocatalytic Selective Oxidation of Ammonia in a Semi-Batch Reactor: Unravelling the Effect of Reaction Conditions and Metal Co-Catalysts. *Catalysts* **2021**, *11*, 209, doi:10.3390/catal11020209.
26. Conte, F.; Pellegatta, V.; Tripodi, A.; Ramis, G.; Rossetti, I. Photo-Oxidation of Ammonia to Molecular Nitrogen in Water under UV, Vis and Sunlight Irradiation. *Catalysts* **2021**, *11*, 975, doi:10.3390/catal11080975.
27. Ren, H.T.; Liang, Y.; Han, X.; Liu, Y.; Wu, S.H.; Bai, H.; Jia, S.Y. Photocatalytic oxidation of aqueous ammonia by Ag2O/TiO2 (P25): New insights into selectivity and contributions of different oxidative species. *Appl. Surf. Sci.* **2020**, *504*, doi:10.1016/j.apsusc.2019.144433.
28. Lee, J.; Park, H.; Choi, W. Selective photocatalytic oxidation of NH3 to N2 on platinized TiO2 in water. *Environ. Sci. Technol.* **2002**, *36*, 5462–5468, doi:10.1021/es025930s.
29. Park, S.; Lee, J.T.; Kim, J. Photocatalytic oxidation of urea on TiO 2 in water and urine: mechanism, product distribution, and effect of surface platinization. *Environ. Sci. Pollut. Res.* **2019**, *26*, 1044–1053, doi:10.1007/s11356-017-8380-3.
30. Guzman, F.; Chuang, S.S.C.; Yang, C. Role of methanol sacrificing reagent in the photocatalytic evolution of hydrogen. *Ind. Eng. Chem. Res.* **2013**, *52*, 61–65, doi:10.1021/ie301177s.
31. Visciano, P.; Schirone, M. Update on Biogenic Amines in Fermented and Non-Fermented Beverages. *Foods* **2022**, *11*, 353, doi:10.3390/foods11030353.
32. Weavers, L.K.; Hua, I.; Hoffmann, M.R. Degradation of triethanolamine and chemical oxygen demand reduction in wastewater by photoactivated periodate. *Water Environ. Res.* **1997**, *69*, 1112–1119, doi:10.2175/106143097x125849.
33. Huang, A.; Cao, L.; Chen, J.; Spiess, F.J.; Suib, S.L.; Obee, T.N.; Hay, S.O.; Freihaut, J.D. Photocatalytic degradation of triethylamine on titanium oxide thin films. *J. Catal.* **1999**, *188*, 40–47, doi:10.1006/jcat.1999.2617.
34. Horikoshi, S.; Watanabe, N.; Mukae, M.; Hidaka, H.; Serpone, N. Mechanistic examination of the titania photocatalyzed oxidation of ethanolamines. *New J. Chem.* **2001**, *25*, 999–1005, doi:10.1039/b102186i.
35. Henderson, M.A. Photooxidation of acetone on TiO 2(110): Conversion to acetate via methyl radical ejection. *J. Phys. Chem. B* **2005**, *109*, 12062–12070, doi:10.1021/jp0507546.

36. Siemer, N.; Lüken, A.; Zalibera, M.; Frenzel, J.; Muñoz-Santiburcio, D.; Savitsky, A.; Lubitz, W.; Muhler, M.; Marx, D.; Strunk, J. Atomic-Scale Explanation of O 2 Activation at the Au-TiO 2 Interface. *J. Am. Chem. Soc.* **2018**, *140*, 18082–18092, doi:10.1021/jacs.8b10929.
37. Song, R.; Luo, B.; Geng, J.; Song, D.; Jing, D. Photothermocatalytic Hydrogen Evolution over Ni2P/TiO2 for Full-Spectrum Solar Energy Conversion. *Ind. Eng. Chem. Res.* **2018**, *57*, 7846–7854, doi:10.1021/acs.iecr.8b00369.
38. Burek, B.O.; Bahnemann, D.W.; Bloh, J.Z. Modeling and Optimization of the Photocatalytic Reduction of Molecular Oxygen to Hydrogen Peroxide over Titanium Dioxide. *ACS Catal.* **2019**, *9*, 25–37, doi:10.1021/acscatal.8b03638.
39. Burek, B.O.; Timm, J.; Bahnemann, D.W.; Bloh, J.Z. Kinetic effects and oxidation pathways of sacrificial electron donors on the example of the photocatalytic reduction of molecular oxygen to hydrogen peroxide over illuminated titanium dioxide. *Catal. Today* **2019**, *335*, 354–364, doi:10.1016/j.cattod.2018.12.044.
40. Wang, Z.; Huang, J.; Amal, R.; Jiang, Y. Solid-state NMR study of photocatalytic oxidation of acetaldehyde over the flame-made F-TiO2 catalyst. *Appl. Catal. B Environ.* **2018**, *223*, 16–21, doi:10.1016/j.apcatb.2017.04.011.
41. Wu, J.J.; Yang, J.S.; Muruganandham, M.; Wu, C.C. The oxidation study of 2-propanol using ozone-based advanced oxidation processes. *Sep. Purif. Technol.* **2008**, *62*, 39–46, doi:10.1016/j.seppur.2007.12.018.

Aquivion® PFSA-based Spray-freeze Dried Composite Catalysts for the One-pot Domino Reaction from Furfural to γ-valerolactone

A. Allegri[1], C. Oldani[2], A. S. Cattaneo[2], A. Brigliadori[3],
I. Zanoni[3], G. Fornasari[1], S. Albonetti[1,3]
[1]Department of Industrial Chemistry – University of Bologna, Bologna, Italy
[2]Solvay Specialty Polymers SpA, Bollate, Italy
[3]National Research Council ISTEC-CNR, Faenza, Italy

Abstract

Among the various molecules that can be obtained from lignocellulosic biomasses, furfural has been regarded as one of the most promising for the substitution of non-renewable carbon feedstock, thanks to the wide range of possible reactions it can undergo and the plethora of possible applications of its derivatives.[1] The aim of this study was to investigate the possibility of the one-pot domino reaction from furfural to γ-valerolactone represented in Figure 1.

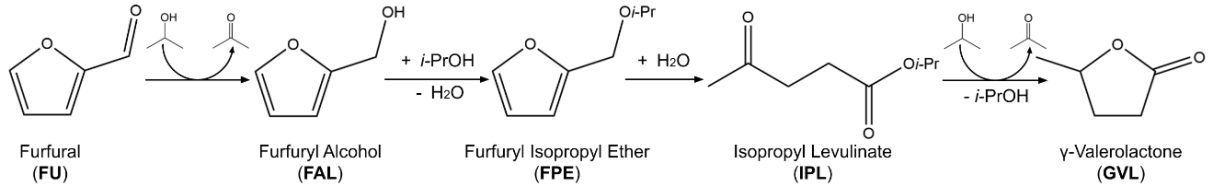

Figure 1. Studied reaction scheme.

In order to develop a sustainable process for the one-pot production of γ-valerolactone (GVL) from biomass-derived furfural (FU), both Lewis and Brønsted acidity are required. Lewis acidity is needed to promote catalytic transfer hydrogenation, while Brønsted acidity are necessary to convert furfuryl alcohol (FAL) to isopropyl levulinate (IPL). [1],[2] The materials utilized to carry out the process are zirconia and Aquivion® PFSA, the most recent commercially available fluorinated acid polymer. [3]

To combine the two phases, spray-freeze drying was employed. [4] Such technique allowed for the preparation of a range of composite materials with a varying polymer content, obtaining a high surface area and a good dispersion of the phases. The prepared materials were characterized by means of SEM, TGA, MAS NMR and porosimetry, then tested as catalysts in the conversion of biomass-derived furfural and furfuryl alcohol to isopropyl levulinate and γ-valerolactone. By examining the produced species in the reaction mixture at different reaction times and temperatures by means of GC-MS, insight was provided into the different produced intermediates and their associated reaction pathways. The optimization of the Lewis/Brønsted acidity ratio led to a further improvement of the reaction outcome, with a GVL yield above 40% after 2h at 180°C, through a four-step one-pot domino reaction. The optimized catalysts were then tested in a continuous-flow fixed-bed reactor, and the influence of reaction parameters on the outcome was once again investigated.

References

[1] Grazia, L., *Green Chem.* **2017**, *19*, 4412-4422.
[2] Vásquez, P. B., *ACS Sustain. Chem. Eng.* **2019**, *7*, 8317–8330.
[3] Andreoli, S., *Appl. Catal. A Gen.* **2020**, *597*, 117544-117552.
[4] Lolli, A., *Catal. Today* **2019**, *334*, 193–202.

Enhancement of Fischer-Tropsch-Synthesis due to Periodical Draining of Wax-filled Catalyst Pores by Hydrogenolysis

C. Unglaub, J. Thiessen, A. Jess
University Bayreuth, Chair of Chemical Engineering, Bayreuth

Fischer-Tropsch reactors operated in the steady state suffer from low pore effectiveness and high methane selectivity caused by internal mass transfer limitations due to accumulation of long chain hydrocarbons inside the catalyst pores. Therefore, an alternating process of Fischer-Tropsch synthesis and subsequently drainage of the pores with hydrogenolysis is proposed. Frequent cracking of the accumulated waxes within the partially filled pores, realized by a switch from synthesis gas (H_2, CO) to hydrogen, result in higher overall catalyst productivity and in a more favourable product distribution. The influence of filling time on drainage time and product distribution was experimentally investigated at 240 °C. Alternating drainage of the pores with a hydrogen partial pressure of just 1bar during hydrogenolysis resulted in an improvement of up to 90% concerning carbon monoxide conversion rate (with 2 hours FTS) and in an improvement of 120% concerning production of non-methane products (with 2 hours FTS).

Introduction

Since energy from renewable sources like wind or solar are seasonal and fluctuating, the future employment of clean energy depends on cheap and efficient storage techniques to become more demand oriented temporally and locally. But, most storage strategies suffer from low energy density, bad long term stability or high conversion losses in the case of liquefied or adsorbed hydrogen [1]. Thus, for applications like jet fuel which require high energy density and easy long term storage under standard conditions, chemical conversion of hydrogen to methanol, ammonia or linear alkanes becomes feasible. Linear alkanes benefit from an especially high energy density (diesel oil 36 GJm^{-3}) caused by utilizing additional carbon atoms, justifying the additional work for conversion [2, 3]. The concept of chemical energy storage using carbon capture and conversion (CCC) processes comprises generation of syngas using CO_2 and H_2 (e.g. from water electrolysis) by the reverse water-gas shift reaction and then subsequent production of hydrocarbons by Fischer-Tropsch synthesis to produce (aviation) fuel and other chemicals like lubricants [4–6].

Fischer-Tropsch synthesis can generally be grouped into two operation modes. The low-temperature (LTFT, 200 °C - 240 °C) process, which employs mainly cobalt catalysts and has high selectivity to linear high molecular mass paraffins and the high-temperature (HTFT, 300 °C - 350 °C) process which produces mainly gasoline and low molecular mass olefins using iron catalysts. Long chain paraffins obtained from LTFT have to be processed further to diesel oil by mild hydrocracking to achieve a diesel fuel selectivity up to 80% [3, 7]. Since hydrocarbon chains are formed by successive incorporation of carbon units and hydrogen into a hydrocarbon chain, the Fischer-Tropsch-Synthesis can be seen as a polymerization reaction of some sort and can be therefore represented by [8]:

$$CO + 2H_2 \rightarrow (-[CH_2]-) + H_2O \qquad (1)$$

As any polymerization reaction follows the three distinguishable reaction steps of initiation, propagation and termination, the product distribution can be estimated by the Anderson-Schulz-Flory distribution using the probability of chain growth α (equation (2). Chain growth probability usually depends on reactant concentration, catalyst and temperature, whereby already small deviations of the value of α can cause a severe shift of product selectivity [8, 9].

$$w_n = n_n(1-\alpha)^2\,\alpha^{n-1} \qquad (2)$$

During the initial phase of FTS at representative industrial process conditions and for technical relevant particle diameters, long chain hydrocarbon products will condense in the reactor and fill the porous system of the catalyst. The initial period of accumulation of these waxes is assumed to be rather short, but can cause severe problems. First, by accumulating long chain paraffins in the pores of the catalyst the internal mass transport is limited ($D_{gas} \approx 150\ D_{liq}$) resulting in a lower overall activity [10]. Second, the diffusion coefficient of H_2 in long chain paraffins is twice as high as the diffusion coefficient of CO, leading to a higher H_2/CO-ratio towards the catalyst core, which can result in a higher methane selectivity and lower chain growth probability [9, 11–15]. For product optimization towards fuel like kerosene or diesel, a chain growth probability of at least 0.85 is needed and should be obtained at any time (cobalt, LTFT) [15]. In general, the accumulation of wax inside the pores of the catalyst is considered as harmful on both catalyst activity and process selectivity [16].

Hydrogenolysis (HGL) is characterized, at least concerning alkanes, as the breaking of C-C bonds in presence of hydrogen, leading to alkanes of lower molar mass by eliminating short chain alkanes, mainly methane. Since hydrogenolysis is often referred to as parasitic and unwanted, most publications focus on how to avoid or minimize it [17]. The first step is the dissociative adsorption of hydrogen and the initial break of C-H bonds before C-C bond rupture of the alkane backbone occurs on the catalyst surface and subsequently carbon-hydrogen bonds reform. The reaction is highly dependent on hydrogen pressure and therefore a reaction order of -2 to -3 with regard to hydrogen is often reported [18–20]. The dependency of reaction rate on hydrogen pressure decreases with increasing temperature because at higher temperature less hydrogen is adsorbed on the catalyst surface than at lower temperature resulting in less hindrance of the initial C-H bond rupture. Also, alkanes with more carbon atoms have more attractive interaction with the catalyst, which facilitate activating the dehydrogenation and stabilize a transition state. Thus, the overall reaction rate of hydrogenolysis increases with chain length of the alkane and the maximum of the reaction rate shifts to higher hydrogen pressures [19, 21, 22].

The process outlined in this publication consists of an alternation between Fischer-Tropsch-Synthesis and subsequent draining of the catalyst pores by cracking of accumulated long chain hydrocarbons by hydrogenolysis in order to reduce mass transport limitations and therefore improve activity and product selectivity towards the C_5-C_{20} fraction. Process cycle times are under investigation in order to evaluate the best set of parameters for optimal enhancement of process activity and selectivity.

Catalyst preparation

In this publication a platinum promoted 20 wt.-% cobalt-Al_2O_3 catalyst is used. The catalyst was synthesized by wet impregnation of 5 x 5 mm Al_2O_3 tablets from Sasol using cobalt(II)nitrate-hexahydrate and tetraamineplatinum(II)nitrate. After impregnation and drying at ambient conditions, the catalyst was calcined by heating in

air with a heating rate of 3 K/min to 340 °C and a three hour hold at that temperature. A more detailed description of the catalyst synthesis can be found in [23]. Thereby, two subsequent impregnation steps were employed to reach the metal content of 20 wt.-%. Further characteristic values of the catalyst are presented in Table 1.

Table 1: Characteristic values of used cobalt catalyst.

Support	Al_2O_3
Cobalt content / wt%.	21.5
Platinum content / wt%.	0.04
BET surface area / m^2g^{-1}	148
Specific pore Volume / cm^3g^{-1}	0.39
Mean pore diameter / nm	7.9
Porosity	0.58
Geometry	5 x 5 mm

Experimental setup

All experiments were conducted in a continuous flow fixed-bed reactor, heated by an oil thermostat. The reactor was built as a single pellet string reactor, where the diameter of the reactor is smaller than two times the diameter of the used catalyst pellet ($d_{pellet} > 0.5\ d_{reactor}$) allowing a reliable determination of the axial position of each individual catalyst pellet. For quick and easy exchange of the catalyst bed, the pellets were placed in an aluminium inlay with an inner diameter of 8 mm. Then, the inlay was placed inside the reactor. A more detailed description of the whole reactor concept can be found elsewhere [23].

Since FTS is strongly exothermic, particular care has to be taken to achieve isothermal conditions, especially when using a hot-start procedure. The catalyst bed inside the aluminium inlay was diluted with stainless steel grist of a diameter of around 1mm. To prevent the catalyst pellets from floating, the pellets were weighted down by 5mm stainless steel beads placed between every catalyst particle. Also, the aluminium inlay used proved to be very efficient in discharging the heat of reaction.

General proceedings

Prior to any FTS run, the catalyst was activated by reduction with hydrogen (15 bar, 290°C, 16h). After reduction the catalyst was preconditioned with 10 l_{STP}/h syngas (H_2/CO = 2/1) at 15 bar and 190°C for 2 h, then 200°C for another 2 h, followed by 210 °C and 220 °C for 1 h each. At 240°C the synthesis was performed for 1-2h until initial methane production reached steady state. After that the catalyst pores were drained by hydrogenolysis (p_{H2} = 1 bar, p_{total}= 15bar, rest N_2). During experiments presented here, no deactivation of the catalyst occurred. Also, a high number of cycles between pore filling with FTS and pore draining with HGL did not cause any deactivation. Every Fischer-Tropsch sequence was started with completely empty catalyst pores, by replacing the H_2 feed by syngas (H_2/CO = 2/1; p = 15bar; "hot-start" conditions). Performing a hot start means to expose a completely empty catalyst to syngas at designated reaction temperature. This leads to an extremely reactive synthesis and is considered as the most critical part of the whole operation. Initially, the methane selectivity was high and the reactor temperature rose by 5 °C for about 20 minutes at 240 °C set temperature.

Carbon monoxide consumption and methane selectivity of the FTS were continuously monitored with a gas analyser and a gas flow meter. The amount of catalyst and volume

flow of syngas was always adjusted to obtain a steady state CO conversion of around 15% at reaction temperature. To start the HGL reaction, the syngas feed was stopped and immediately replaced by a mixture of nitrogen and hydrogen (p_{H2} = 1 bar, p_{total}= 15 bar, V = 45 l_{STP} /h). The pore draining reaction was considered as complete when the methane concentration in the off gas fell below 0.5 mmol$(kg_{Kat}s)^{-1}$. To purge the system and make sure no traces of FT – product remained, pure hydrogen (p = 15 bar) was flowed through the reactor prior to the following FTS run. Liquid products of FTS were collected using cooling traps at 0 °C and -72 °C which were then analysed by gas chromatograph. Gaseous products of FTS were contained inside a gas collection tube and measured also with GC. But, since reaction times could be very short not always enough liquid specimen was available for experimental determination of chain growth probability. Thus, for calculation of chain growth probability correlation of Rose was used [24]. For this correlation, only selectivity of gaseous products in the range from C_2 to C_5 is needed to calculate α_{FTS}. The correlation is validated for chain growth probability between 0.6 and 0.9.

The pore filling degree, the ratio of wax volume in the pores to the pore volume of the catalyst, of the catalyst pellets after FTS was measured using a thermo-balance (TG). For this, the reactor was cooled as fast as possible and then flushed with hydrogen, before the catalyst pellets were removed from the reactor. Then hydrogenolysis of the wax in the pores was conducted with pure hydrogen at atmospheric pressure, until the mass in the thermo-balance was constant. For calculating the pore filling degree (F_{FTS}) from the mass change during HGL, equation (3) was used:

$$F_{FTS} = \frac{\Delta m_{TG}}{m_{cat,pellet} * v_{s,pore} * \rho_{wax}} \quad (3)$$

The density was calculated with the density correlation from Seyer [25]. The composition of the accumulated wax in the pores after FTS was measured by extracting the wax with toluene in a soxhlet-extractor for 48h at 73 °C. After extraction the samples were measured using a gas chromatograph. Gaseous products of hydrogenolysis were collected using a 10 l inert foil gas sampling bag and liquid samples were collected using a cooled (0 °C) scrubber filled with toluene and a cooling trap (-72 °C). These specimens were also analysed by GC.

Filling of Catalyst Pores during Fischer-Tropsch-Synthesis

All FTS experiments started with completely drained pores. The pores were always drained at a hydrogen partial pressure of 1bar at 240 °C.

The key parameters of Fischer-Tropsch-Synthesis over pore filling time are depicted in Figure 1. The initial phase of the FTS holds some uncertainties of measurement due to back-mixing of the product stream with the gas already in the exhaust part of the reactor setup at the beginning of the experiment. Pöhlmann [10] showed with measurements in a magnetic suspension balance that the first layer of paraffins (F_{mono} = 0.2) builds up fast in comparison with the rest of the pore filling. Measurements of pore filling degree (Figure 1 B) support the presumption of extremely fast creation of a paraffin monolayer, as values for F are already well above 0.35 after only 1h. In further course of the synthesis, the rate of pore filling slows down noticeably which is related to the decrease of the chain growth probability with increasing filling time and pore filling degree. At 240°C filling of the catalyst pores isn't even fully completed after 72h time on stream.

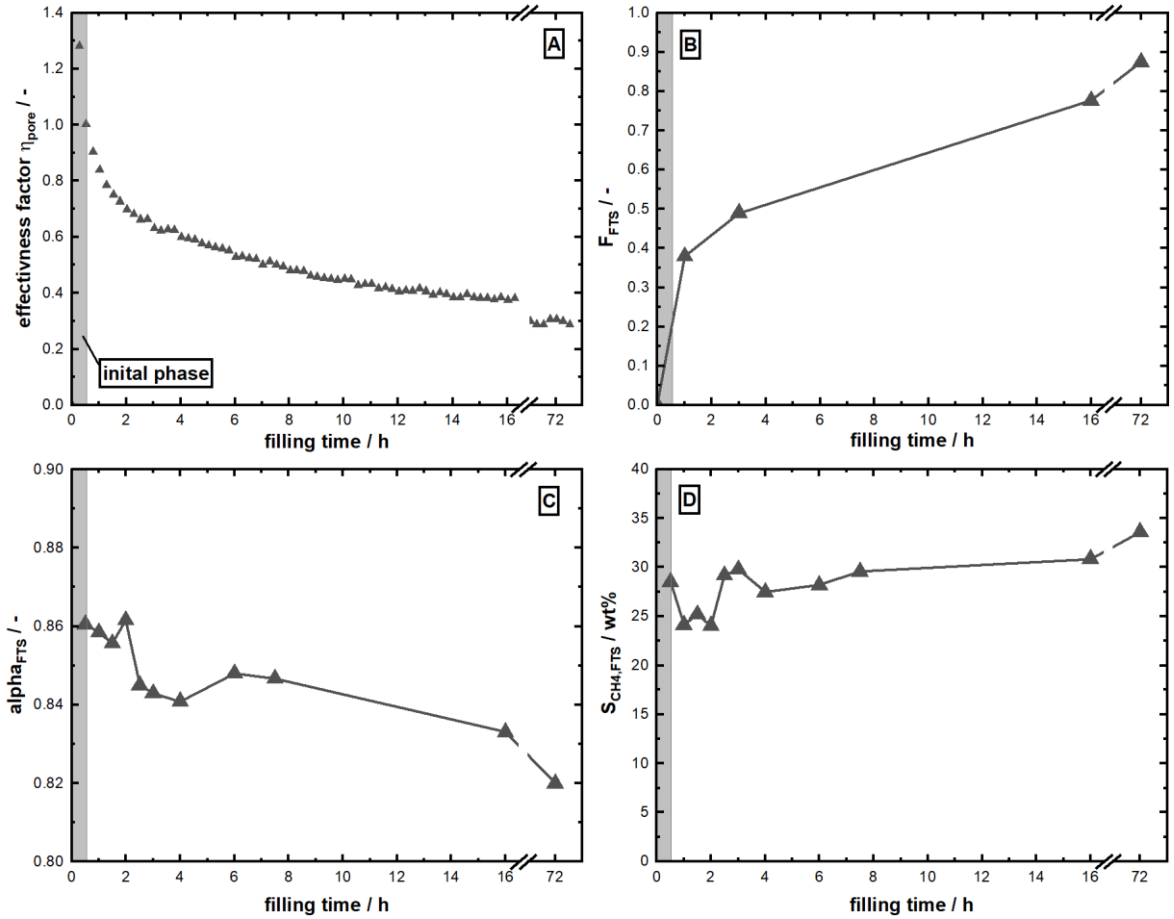

Figure 1: Progress of key figures during transient FTS at 240 °C ($V_{syngas,240\ °C}$ = 30 $l_{STP}(g_{cat}h)^{-1}$; p_{total} = 15bar; H_2/CO = 2/1). A) Decline of effectiveness factor over pore filling time; B) Growth of pore filling degree over pore filling time; C) Dependency of chain growth probability of pore filling time; D) Methane selectivity over pore filling time.

Decreasing chain growth probability α means the product spectrum of the hydrocarbons shifts to shorter chain length and thus to less wax which can be deposited inside the catalyst pores is produced. A large quantity of hydrocarbon residue causes high diffusion resistance and due to the different diffusion coefficients of H_2 and CO the H_2/CO ratio shifts to values >2 towards the catalyst core. Thus, methane selectivity increases, α decreases with increasing time on stream and the pore effectiveness factor decreases as diffusion resistance increases. According to measurements made by Pöhlmann [10], the pore filling degree has no linear influence on catalyst activity. The first negative influence becomes visible at a pore filling degree of F = 0.5 and about F > 0.8 is needed to fill the transport pores in the catalyst and thus to substantially hinder the reaction.

Chain length shifts to higher values over time on stream, as the formation rate of the (very) high carbon number products is slower as for shorter hydrocarbons, and it takes some time for the equilibrium of hydrocarbon formation and evaporation to be established. This effect can be seen in Table 2.

Hydrogenolysis of long chain hydrocarbon deposits of Fischer-Tropsch-Synthesis

Since it is mostly seen as unwanted side reaction and is not of commercial interest, hydrogenolysis of long chain hydrocarbons is scarcely investigated and therefore not very well understood. Thus, it should be noted that the pore draining by hydrogenolysis is here assumed to be the result of the combination of two processes: 1) Formation of predominantly methane and to a smaller extent ethane and propane, thus shortening the hydrocarbon chain lengths. 2) the evaporation of the corresponding alkane, which has a higher vapour pressure due to the shortened chain length. The proceeding of the reduction of pore filling degree over time at 240 °C is shown in Figure 2.

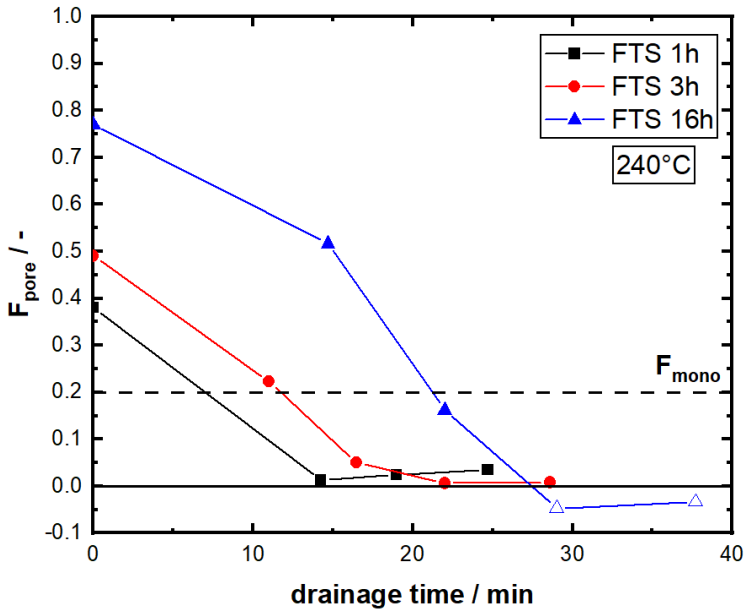

Figure 2: Decline of pore filling degree over drainage time for 240 °C ($V_{HGL,total}$ = 45 l_{STP}/h; p_{H2} = 1bar; p_{total} = 15bar)

Hydrogenolysis was performed starting from different pore filling degrees according to the time the catalyst was filled. Pore drainage progresses swiftly until the pores are fully drained. At 240 °C the pores can be fully drained and no deviations between the different initial filling degrees are noticeable. It was shown in the previous section that longer pore filling times result in higher pore filling degree and composition of product waxes in the catalyst pores shift to higher chain length, but these changes appear as too slight to cause any difference in pore drainage. All subsequently performed Fischer-Tropsch experiments showed no degradation in activity.

The distribution of hydrogenolysis products derived from cracking long chain hydrocarbons possesses a specific shape, also reported by other researchers [26, 27]. The most abundant product of hydrogenolysis at 240 °C for all measurements is methane. The selectivity to other light alkane products of cleavage of the terminal or near-terminal bonds is comparably low, leading to the conclusion that cracking of the long chain alkanes happens predominantly but not exclusively by successive methane elimination. Product selectivity decreases further until a local minimum is reached at a carbon number of 7. After that selectivity increases again with increasing carbon number up to a local maximum at C_{11}-C_{12}. This maximum becomes less

pronounced with higher pore filing degree. Methane selectivity decreases with decreasing pore filling degree and the location of the local minimum remains unchanged. Products with a higher chain length than C_{21} were found in none of the measurements made. Product selectivities of all HGL experiments made can be found in Table 2.

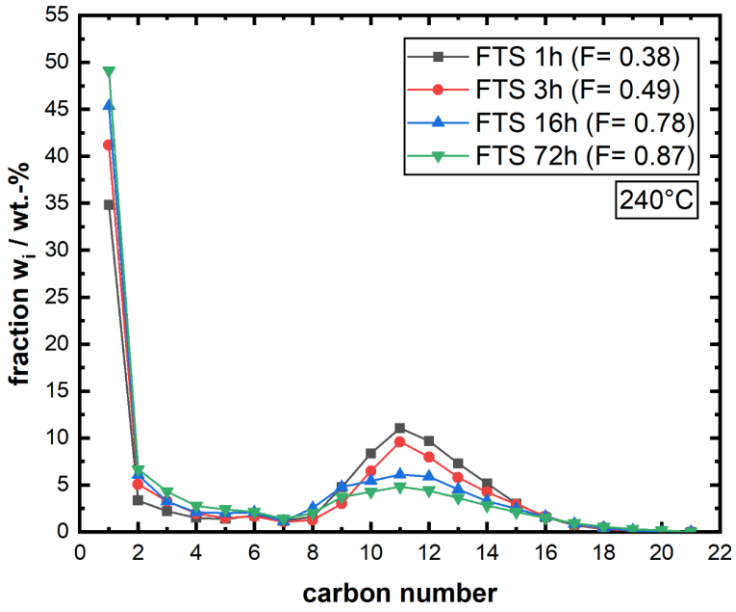

Figure 3: Typical distribution of products of hydrogenolysis at 240 °C after various Fischer-Tropsch synthesis time. Selectivity of methane and kerosene fraction (C9-C17) at different temperatures and pore filling degrees.

Methane selectivity of the hydrogenolysis reaction depends only slightly on pore filling degree. Selectivity towards C_9-C_{17} decreases to the same extent as methane selectivity increases, whereas selectivity to C_2-C_8 remains mainly unchanged. C_9-C_{17} selectivity also decreases with increasing pore filling degree. These results support the assumption mentioned earlier that the product distribution is the result of methane rupture and evaporation of the longer chain residues, once their vapour pressure is high enough. It is known from literature that longer chain alkanes tend to have higher methane selectivity with increasing chain length, due to better stabilization of the transition state, but correlation is not strong [22]. Nevertheless, it can be stated that the hydrogenolysis of Fischer-Tropsch waxes results in products with substantially shortened alkane chains and show only slight dependency on pore filling degree, which suggests that variation of pore filling time doesn't affect the alternating process by much.

Table 2: Overview of pore filling degree and mean carbon number obtained after different pore filling and product distribution of hydrogenolysis derived from the wax residues at a process temperature of 240 °C.

Filling time / h	1	3	16	72
F_{FTS} / -	0.38	0.49	0.78	0.87
C_{mean} / -	26.5	31.1	36.0	37.1
$S_{CH4,HGL}$ / mol/mol	0.31	0.43	0.45	0.49
$S_{C2\text{-}C8,HGL}$ / mol/mol	0.12	0.14	0.18	0.21
$S_{C9\text{-}C17,HGL}$ / mol/mol	0.55	0.38	0.36	0.28

Alternating drainage of the catalyst pores with hydrogenolysis after Fischer-Tropsch-Synthesis

The knowledge of pore filling behaviour during transient FTS and following hydrogenolysis of the condensed long chain hydrocarbons, gained in the previous sections is used to enhance overall performance of the Fischer-Tropsch synthesis. Hereby, pore filling time and drainage time could be identified as the two most influential factors. Here, the hydrogenolysis was conducted at the same temperature than the Fischer-Tropsch synthesis to reduce the number of applied parameters. The drainage time depends on temperature and pore filling degree, and the pore filling degree depends on filling time and process temperature as well. The higher the pore filling degree the longer the drainage time. For better mathematical description and a better theoretical understanding Duerksen [28] introduced the Process Enhancement (PE) factor:

$$PE_{CO} = \frac{\int_0^{t_{FTS}} r_{CO}\, dt}{(t_{FTS} + t_{HGL}) * r_{CO,steady-state}} \qquad (4)$$

PE factors >1 are desirable because when PE factor reaches unity the productivity of the alternating process equals the productivity of the steady-state process. Since drainage time has to be considered as down time, where no products are formed, the duration of drainage must be as short as possible. The shorter the drainage time t_{HGL} the higher the PE factor and for $t_{HGL} \rightarrow 0$, $PE_{CO} \rightarrow {\eta_{pore}}^{-1}$. Obviously, pore filling degree influences drainage time but activity is not as dependent on it up to a certain point. More specifically, the catalyst pores fill up quickly after FTS is started, but activity degrades faster only at high pore filling degrees, leading to the conclusion that the alternating process works best within a certain time range of Fischer-Tropsch-Synthesis. For $t_{FTS} \rightarrow 0$, also $t_{HGL} \rightarrow 0$ and so does the PE factor, since no reaction takes place.

In Figure 4 the progress of drainage time is depicted in context of FTS pore filling time at 240°C. The drainage time reaches a plateau after a certain time of Fischer-Tropsch synthesis, since pore filling happens quickly after the start of the FTS. As a certain pore filling degree is reached, the deposition rate of wax slows down and becomes insignificant for increase of drainage time. At 240 °C the increase of pore filling degree is comparatively slow and hydrogenolysis is fast, so the plateau is reached quickly and therefore basically no difference in drainage time of 8h of FTS and 16h of FTS is visible.

By solving equation (4) for the drainage time t_{HGL}, the set of curves of given process enhancement factors, presented in Figure 4, could be calculated. These curves give an idea of the theoretical drainage time needed for a particular filling time, for achieving a certain PE factor. Shape and curvature depend solely on CO consumption and pore effectiveness factor during Fischer-Tropsch synthesis. Interestingly, in order to achieve high PE, only certain filling times appear to be suitable. Long FTS time on stream makes achieving a high PE factor impossible, because theoretically negative drainage time would be necessary. The higher the desired PE factor the narrower the field of possible cycle times becomes. A pore filling time of around 2 to 3 hours seems to be suitable for the process at 240°C.

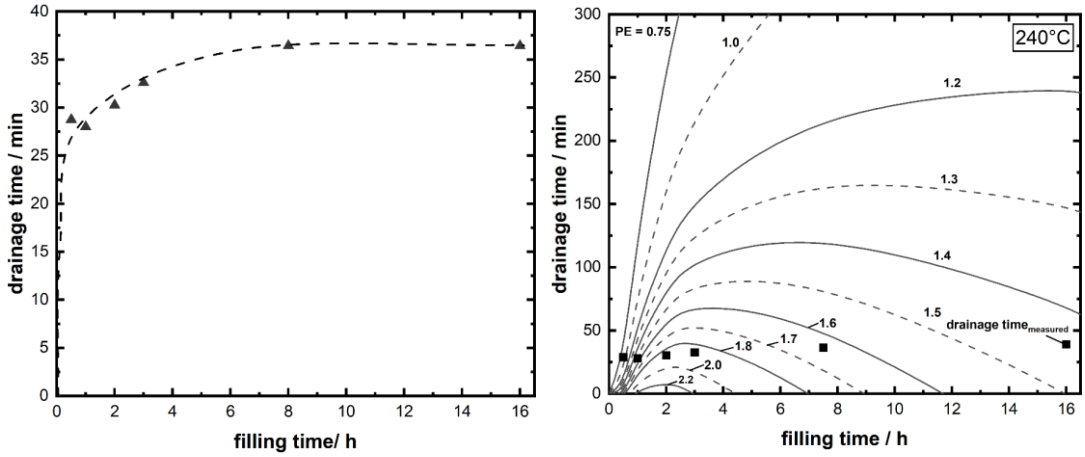

Figure 4: Left) Progress of the necessary drainage measured over different pore filling times at 240°C. Right) Theoretically calculated drainage time over given Process Enhancement (CO) factors as function of pore filling time.

Since hydrogenolysis produces mainly methane, the risk that improvements made in reaction activity come along with worse reaction selectivity is high. Therefore, the Process Enhancement factor (PE_{CO}) is extended to PE_{C2+}, which also takes methane selectivity into account:

$$PE_{C2+} = \frac{\int_0^{t_{FTS}} r_{CO}\,dt - (\int_0^{t_{FTS}} r_{CH4,FTS}\,dt + \int_0^{t_{HGL}} r_{CH4,HGL}\,dt)}{(t_{FTS} + t_{HGL}) * (r_{CO,steady-state} - r_{CH4,steady-state})} \quad (5)$$

For calculation of production rate of C_{2+} compounds (any FTS-product except for methane) during a cycle of pore filling and draining the amount of methane produced during FTS and HGL is subtracted from the amount of total used carbon monoxide during FTS and then divided by rate of C_{2+} production at steady state.

It is not surprising that the curves of PE_{C2+} factor (Figure 5) are similar to PE_{CO} curves. High process enhancement factors are not achievable for any pore filling times. The desired cycle time for best process enhancement lies between 2 and 3 hours, too.

Conclusion and Outlook

A potential improvement of Fischer-Tropsch synthesis by alternating pore draining with hydrogenolysis is investigated and discussed. The highest measured process improvement regarding the CO conversion activity (PE) was measured for a pore filling time between 2 and 3 hours and amounted to 1.9. The highest value measured regarding activity of production of products longer than methane (PE_{C2+}) was 2.2 obtained also for a pore filling time of 2 and 3 hours. Thus, the assumption made by Duerksen [28] was confirmed, that higher temperature leads to higher improvement factors. But, this work clearly shows the potential of the alternating pore draining, because improvement of catalyst productivity is clearly visible. Since deterioration of Fischer-Tropsch activity is a result of wax accumulation and catalyst geometry, the alternating drainage appears as a feasible and easy option for enhancement. Increase of hydrogenolysis rate can be done by increase of reaction temperature. But, an even higher

reaction temperature than 240 °C may cause unfeasibly high methane selectivity during FTS. Thus, a process with low FTS temperature and high HGL temperature is desirable, or the introduction of a more active metal on the catalyst which possesses higher activity to hydrogenolysis than cobalt. But, improvement of hydrogenolysis with a bimetallic catalyst without altering the Fischer-Tropsch synthesis for the worse might be challenging.

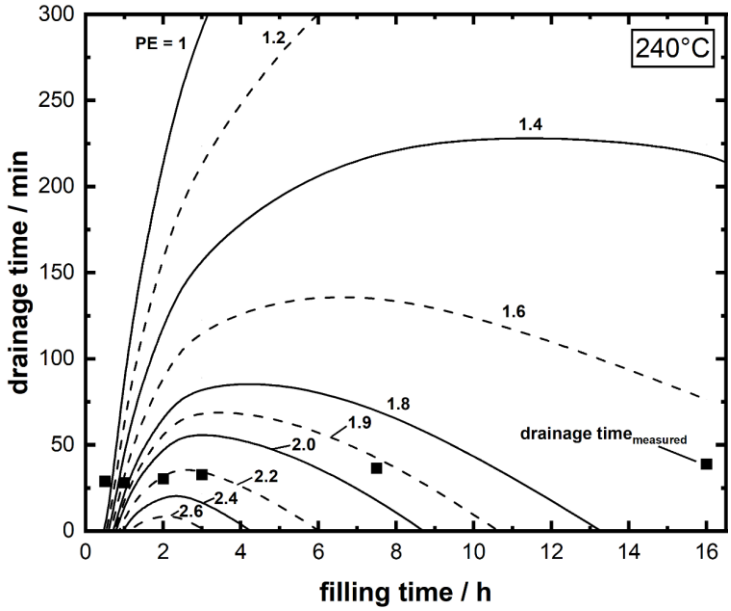

Figure 5: Theoretically calculated drainage time over given Process Enhancement factors (C_{2+}) as function of pore filling time. Measured drainage times indicated with symbols.

References

1. Müller, K.: Technologien zur Speicherung von Wasserstoff. Teil 1: Wasserstoffspeicherung im engeren Sinn. Chemie Ing. Techn. **91**(4), 383–392 (2019). doi: 10.1002/cite.201800043
2. Müller, K.: Technologien zur Speicherung von Wasserstoff. Teil 2: Irreversible Konversion und Technologievergleich. Chemie Ing. Techn. **91**(4), 393–402 (2019). doi: 10.1002/cite.201800044
3. Kaiser, P., Unde, R.B., Kern, C., Jess, A.: Production of Liquid Hydrocarbons with CO 2 as Carbon Source based on Reverse Water-Gas Shift and Fischer-Tropsch Synthesis. Chemie Ing. Techn. **85**(4), 489–499 (2013). doi: 10.1002/cite.201200179
4. Jess, A., Kaiser, P., Kern, C., Unde, R.B., Olshausen, C. von: Considerations concerning the Energy Demand and Energy Mix for Global Welfare and Stable Ecosystems. Chemie Ing. Techn. **83**(11), 1777–1791 (2011). doi: 10.1002/cite.201100066
5. Jiang, Z., Xiao, T., Kuznetsov, V.L., Edwards, P.P.: Turning carbon dioxide into fuel.

Philosophical transactions. Series A, Mathematical, physical, and engineering sciences **368**(1923), 3343–3364 (2010). doi: 10.1098/rsta.2010.0119
6. Schulz, H.: Short history and present trends of Fischer–Tropsch synthesis. Applied Catalysis A: General **186**(1-2), 3–12 (1999). doi: 10.1016/S0926-860X(99)00160-X
7. Gregor, J.H.: Fischer-Tropsch products as liquid fuels or chemicals. Catal Lett **7**(1-4), 317–331 (1991). doi: 10.1007/BF00764512
8. Jess, A., Wasserscheid, P.: Chemical technology. An integral textbook. Wiley-VCH, Weinheim (2013)
9. Vervloet, D., Kapteijn, F., Nijenhuis, J., van Ommen, J.R.: Fischer–Tropsch reaction–diffusion in a cobalt catalyst particle: aspects of activity and selectivity for a variable chain growth probability. Catal. Sci. Technol. **2**(6), 1221 (2012). doi: 10.1039/C2CY20060K
10. Pöhlmann, F., Kern, C., Rößler, S., Jess, A.: Accumulation of liquid hydrocarbons in catalyst pores during cobalt-catalyzed Fischer–Tropsch synthesis. Catal. Sci. Technol. **6**(17), 6593–6604 (2016). doi: 10.1039/c6cy00941g
11. Rößler, S., Kern, C., Jess, A.: Accumulation of liquid hydrocarbons during cobalt-catalyzed Fischer–Tropsch synthesis - influence of activity and chain growth probability. Catal. Sci. Technol. **9**(15), 4047–4054 (2019). doi: 10.1039/c9cy00671k
12. van der Laann, G.P., Benackers, A.A.C.M.: Kinetics and Selectivity of the Fischer–Tropsch Synthesis: A Literature Review. Catalysis Reviews **41**(3-4), 255–318 (1999). doi: 10.1081/CR-100101170
13. Anderson, J.R. (ed.): Catalysis. Science and technology, vol. 1. Springer, Berlin (1981)
14. Huff, G.A., Satterfield, C.N.: Liquid accumulation in catalyst pores in a Fischer-Tropsch fixed-bed reactor. Ind. Eng. Chem. Proc. Des. Dev. **24**(4), 986–995 (1985). doi: 10.1021/i200031a015
15. Pöhlmann, F., Jess, A.: Interplay of reaction and pore diffusion during cobalt-catalyzed Fischer–Tropsch synthesis with CO 2 -rich syngas. Catalysis Today **275**, 172–182 (2016). doi: 10.1016/j.cattod.2015.09.032
16. Dry, M.E.: The Fischer–Tropsch process: 1950–2000. Catalysis Today **71**(3-4), 227–241 (2002). doi: 10.1016/S0920-5861(01)00453-9
17. Bond, G.C.: Metal-catalysed reactions of hydrocarbons. Fundamental and applied catalysis. Kluwer Academic/Plenum Publishers, New York (2005)
18. Guczi, L., Frennet, A., Ponec, V.: Kinetics of Hydrocarbon Reactions on Metals. Acta Chim. Acad. Sci. Hung(112), 127–151 (1983)
19. Bond, G.C., Cunningham, R.H.: Alkane Transformations on Supported Platinum Catalysts. Journal of Catalysis **166**(2), 172–185 (1997). doi: 10.1006/jcat.1997.1490
20. Paal, Z.: Hydrogen effects as a possible cause of inverse arrhenius plots. Journal of Catalysis **91**(1), 181–182 (1985). doi: 10.1016/0021-9517(85)90299-4
21. Hibbitts, D.D., Flaherty, D.W., Iglesia, E.: Effects of Chain Length on the Mechanism and Rates of Metal-Catalyzed Hydrogenolysis of n -Alkanes. J. Phys. Chem. C **120**(15), 8125–8138 (2016). doi: 10.1021/acs.jpcc.6b00323
22. Flaherty, D.W., Iglesia, E.: Transition-state enthalpy and entropy effects on reactivity and selectivity in hydrogenolysis of n-alkanes. J. Am. Chem. Soc. **135**(49), 18586–18599 (2013). doi: 10.1021/ja4093743
23. Schurm, L., Kern, C., Jess, A.: Accumulation and distribution of higher hydrocarbons in the pores of a cobalt catalyst during low-temperature Fischer–Tropsch fixed-bed synthesis. Catal. Sci. Technol. **11**(18), 6143–6154 (2021). doi: 10.1039/d1cy01305j
24. Rose, A.: Nano-carbon supported cobalt catalysts in Fischer-Tropsch synthesis. Dissertation Universität Bayreuth (2013)
25. Seyer, W.F., Patterson, R.F., Keays, J.L.: The Density and Transition Points of the n-Paraffin Hydrocarbons. J. Am. Chem. Soc. **66**(2), 179–182 (1944). doi: 10.1021/ja01230a004
26. Kulikova, M.V., Dement'eva, O.S., Kuz'min, A.E., Chudakova, M.V.: Fischer–Tropsch synthesis and hydrogenolysis of long-chain alkanes over cobalt-containing nanosized catalysts in a slurry reactor. Pet. Chem. **56**(12), 1140–1153 (2016). doi: 10.1134/S0965544116120082

27. Nakagawa, Y., Oya, S.-I., Kanno, D., Nakaji, Y., Tamura, M., Tomishige, K.: Regioselectivity and Reaction Mechanism of Ru-Catalyzed Hydrogenolysis of Squalane and Model Alkanes. ChemSusChem **10**(1), 189–198 (2017). doi: 10.1002/cssc.201601204
28. Duerksen, A., Thiessen, J., Kern, C., Jess, A.: Fischer–Tropsch synthesis with periodical draining of a liquid-filled catalyst by hydrogenolysis. Sustainable Energy Fuels **4**(1), 90 (2020). doi: 10.1039/C9SE01269A

Accumulation of Higher Liquid Hydrocarbons in the Pores of a Cobalt Catalyst during the Initial Non-stationary Phase of Fixed-bed Fischer-Tropsch Synthesis

L. Schurm, A. Jess
University Bayreuth

Abstract

The Fischer-Tropsch synthesis (FTS) could play a major role in the energy transition from fossil fuels to carbon neutral alternatives as part of the Power-to Liquid concept by converting the fluctuating electrical power coming from renewable resources via intermediate steps to hydrocarbons or e-Fuels. The low temperature fixed-bed FTS is normally operated at steady state, but the investigations for the necessary operation at non-stationary conditions are comparably few. An alternative application of non-stationary operation could be the alternating operation of FTS with hydrogenolysis. During FTS the pores of the catalyst are filled with liquid waxes resulting in diffusional limitations and reducing pore and process efficiency. The hydrogenolysis is used to crack the waxes and empty the pores. While the hydrogenolysis can be seen as downtime product wise, the increased pore efficiency could ultimately lead to an enhancement of the overall process.
Therefore, the filling process of the catalyst during the non-stationary start-up is investigated in a single pellet string reactor to approximate the fixed bed behaviour on a laboratory scale. The results of the filling degree over the bed length for different temperatures and the hydrocarbon distribution are presented. Additionally, the CO-conversion and chain growth probability were measured at the reactor outlet and correlated to the filling process. A model was adopted and adjusted to describe the overall filling process.

Introduction

The ever-increasing emissions of anthropogenic CO_2 of the last decades have led to a severe negative impact on nature and the climate change.[1] Inevitably, a societal and political desire and necessity was established and is more than ever present for an energy transition from fossil to sustainable energy resources, e.g. wind or solar energy. One major challenge of these renewable sources for supplying, storing and using electric energy is the fluctuating productivity.[2] Several different promising concepts are investigated and tested revolving around this topic. One possibility in storing the excess electrical energy is the production of chemical liquids including dimethyl ether, methanol or Fischer-Tropsch fuels in the Power-to-Liquid (PtL) concept. An advantage of this concept is the compatibility to existing infrastructure and transportation, especially high energy density demanding sectors as commercial aircraft or ships which are challenging to electrify.[3] Thus the production of e-fuels can be seen as necessary to achieve an energy transition in a short to medium time frame.[4] Another advantage is the possible incorporation in the value chain of the chemical industry. For the PtL concept hydrogen is generated by water electrolysis and additionally a carbon capture technology is applied. For the Fischer-Tropsch synthesis (FTS) CO_2 captured from exhaust gas or from atmosphere can be transformed to CO in the reverse water gas shift reaction[5,6] or biomass is converted to CO,[7] instead of using traditional fossil feedstocks like coal or natural gas for CO generation.
The main products of FTS are n-paraffins formed by a surface reaction similar to the polymerization of methylene monomer units produced by the reagents carbon monoxide and hydrogen:

$$n\ CO + 2\ n\ H_2 \rightarrow (\text{-}CH_2\text{-})_n + n\ H_2O \qquad (1)$$

Additionally, olefins, iso-paraffins and oxygenated hydrocarbons can be formed during the reaction. The amount of these products depends strongly on the catalyst used and the reaction conditions. Industrial relevant catalysts consist either of iron or cobalt as the active metal on a support.[8] A side reaction during FTS is the water gas shift reaction which is more relevant for iron.

$$CO + H_2O \rightleftharpoons CO_2 + H_2 \quad (2)$$

The Fischer-Tropsch synthesis is normally operated at 200-350 °C and in a pressure range of 0.5-3 MPa. The FTS can be divided into the low temperature FTS operated at 200-240 °C aiming for high molecular weight linear products and the high temperature FTS at 300-350 °C with low molecular weight products and higher extents of olefins and oxygenates.[9] The mole fraction x_i of the hydrocarbon with chain length i can, due to the similarity to a polymerisation reaction, be described mathematically by the Anderson-Schulz-Flory (ASF) distribution with the chain growth probability α:[10]

$$x_i = (1 - \alpha)\, i^{\alpha - 1} \quad (3)$$

Even though, typically, on cobalt catalysts the selectivity towards methane is higher than predicted by the ASF. The FTS is normally operated at steady state conditions and is the focus in literature, but the fluctuating energy supply in PtL could make a dynamically operated FTS more beneficial.[2] Therefore a better understanding of non-stationary behaviour of FTS is necessary and the focus of this study. A separate study in this project investigates the enhancement of the overall FTS process by a periodic filling of the catalyst during FTS and an emptying under hydrogenolysis conditions. During low temperature FTS in a fixed bed the higher hydrocarbons or liquid waxes accumulate inside the pores of the catalyst. This introduces diffusional limitations for the reactants and lowers the pore and process efficiency. Even though the hydrogenolysis can be seen as downtime with respect to the production of FTS products, the emptying of the pores by cracking the waxes lead to an increase in pore efficiency for the subsequent FTS. In conclusion, the challenge of a flexible operation of the plant could even result in the usage of synergetic effects to obtain a more effective process. Those desirable effects are recently getting more in the focus of research but are still scarce in industry.[11]

For this concept the non-stationary start-up of the low temperature FTS is particularly important and is investigated in the following to obtain a basic understanding of this complex system. The filling process inside single catalyst pellets as well as the overall behaviour of the fixed-bed is examined. The final goal will be a model describing the filling process to facilitate a precise and desirable process control for a periodic operation.

Experimental

Experimental Setup

The experiments were performed in a single pellet string reactor (SPSR). Its characteristic can be described as a fixed-bed reactor with the additional restrain that the particle diameter must be smaller than two times the reactor diameter. Therefore, no particle/pellet can pass each other in the reactor resulting in a fixed order and exact location of each pellet.
A more detailed description of the reactor setup and the catalyst synthesis and characterisation can be found in Schurm et al..[12] The catalyst can be summarised as a 5x5 mm cylindrical Al_2O_3 pellet impregnated with 10 wt.% of the catalytically active cobalt and with platinum as a promoter for reduction. The literature regarding SPSR claims that the SPSR often has similar behaviour to an industrial fixed-bed with a high ratio of d_r to d_p, at least in comparison to standard laboratory reactors with small to medium d_r to d_p>2.[13–15] An overview of the SPSR implemented in the plant is given in Figure 1.

When the desired reaction time is reached, the reactor is cooled down from reaction temperature to 60 °C in roughly 15 min. Additionally, the synthesis gas stream is turned off. At 60 °C the pressure is released from the reactor and afterwards flushed for 2 minutes with nitrogen. Then the reactor is opened and the pellets are removed for further analysis. The sequencing of the reactor shut down is chosen to minimize the possibility of evaporation of hydrocarbons inside the pores.

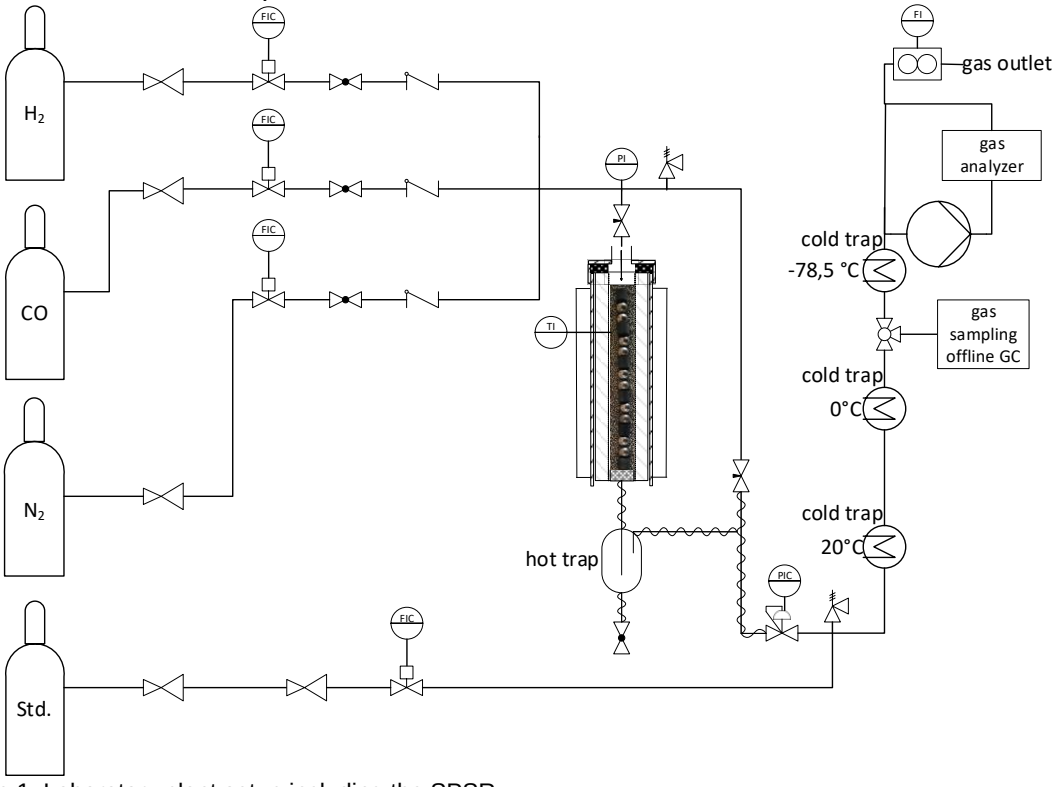

Figure 1: Laboratory plant setup including the SPSR.

Determination of the filling degree

The filling degree was obtained by simply weighing the pellets before the experiment and directly after their removal from the reactor with a fine scale and applying equation 4.

$$F = \frac{V_{HC}}{V_{pore}} = \frac{\rho_{HC,avr}(T_{reac})\, m_{HC,total}}{V_{s,pore}\, m_{cat,0}} \quad (4)$$

The pore filling degree F is defined by dividing the volume of the hydrocarbons inside the pores V_{HC} with the overall volume of the pores V_{pore}. The pore volume is obtained by multiplying the catalyst mass before the experiment $m_{cat,0}$ with the average specific pore volume $V_{s,pore}$ of the catalyst. Due to the lack of significant amounts of micropores of the catalyst, the specific pore

volume can either be measured by water pycnometry or by superimposing the results of nitrogen adsorption pycnometry and mercury porosiometry. Both methods yielded similar results, but the values of the water pycnometer were used because of its greater sample size. The volume of hydrocarbons V_{HC} at reaction temperature is calculated with the product of the density of the hydrocarbon with the average chain length of the mixture at reaction temperature $\rho_{HC,avr}(T_{reac})$ and the mass of all hydrocarbons $m_{HC,total}$. The average chain length is approximated with the hydrocarbon distribution obtained by the extraction of pellets. The mass of hydrocarbons is calculated by the difference between the mass of the catalyst after the reaction $m_{cat,end}$ and the mass of reduced catalyst which is approximated by multiplying the oxidized catalyst mass from the beginning with an average reduction factor l_{red} estimated in separate reduction experiments. l_{red} is 3.1% for the catalyst and the reduction conditions used in this work and includes the loss of oxygen from reduction and the loss of physi- and/or chemisorbed water.

$$m_{HC,total} = m_{cat,end} - m_{cat,0}\left(1 - \frac{l_{red}\,[\%]}{100}\right) \tag{5}$$

The results for the filling degree were compared and validated with calculations from cracking the hydrocarbons in filled catalysts in a thermobalance and by a correlation including the difference in BET surface area from empty and (partially) filled catalysts.

To assign the measured filling degrees to a certain reaction time, a well-defined starting point for the reaction has to be chosen. The reactor is heated up and the reaction and filling process starts before reaching the reaction temperature. This effect is rather small due to the exponential dependency of the reaction rate with the temperature. Nonetheless heating to higher temperatures takes longer and makes the choice of the starting point difficult for comparing results at different temperatures. For this reason, different heating ramps for different temperatures were chosen in order to ensure a constant heating time of 10 min for the heating medium. The well-defined starting point is when the heating medium reaches reaction temperature. Unfortunately, the packed bed has not reached the reaction temperature at this point in time because of heat transfer limitations, but reaches isothermal conditions after a few minutes. The thermocouple placed inside the packing has no fixed position between different experiments resulting in small derivations of the temperature profiles and it is assumed to be unsuitable as reference for a well-defined starting point.

The position of pellet z in the fixed-bed is described by the normalized bed length L with the total number of pellets z_{total} as follows:

$$L = \frac{z - 1}{z_{total} - 1} \tag{6}$$

Determination of hydrocarbon distribution inside the pores

20 ml of Toluene are heated to 78 °C in a flask. After reaching the temperature, the pellet is added and the flask is closed and the extraction proceeds for two days. After cooling down cyclooctane is added as internal standard, mixed and a sample is taken and measured in a GC. Paraffins and olefins with the same chain length are lumped up to one pseudo-species, because the concentration of olefins is very low and often not detectable and the model assumes only paraffinic hydrocarbons.

Determination of the chain length probability α

Under steady state conditions and a sufficient reaction time the chain growth probability can normally be determined by analysing the liquid samples from the cooling traps and the gas phase. At non-stationary conditions the reaction time is not long enough to form a suitable liquid sample size and additionally hydrocarbons are accumulating partially inside catalyst pores, resulting in a non-representative product composition at the reactor outlet and in the cooling traps for an ASF distribution. Alternatively, α can be solely determined by the gas phase sample with hydrocarbons up to butane which do not accumulate inside the reactor due to their

high saturation pressures. Assuming only the Fischer-Tropsch main reaction is occurring, the combined selectivity for hydrocarbons with a chain length of five or greater S_{C5+} can be described by equation 7. Methane is assumed to be a separate reaction and is therefore excluded from FTS.

$$S_{C5+} = 1 - \sum_{i=2}^{4} w_{C,i} \tag{7}$$

Here, $w_{C,i}$ is the carbon weight fraction of the hydrocarbon with chain length i. The selectivity can be determined experimentally by applying equation 8,

$$S_{C5+} = \frac{\Delta \dot{m}_{C,CO} - \sum_{i=1}^{4} \dot{m}_{C,i}}{\Delta \dot{m}_{C,CO} - \dot{m}_{C,CH_4}} \tag{8}$$

where $\Delta \dot{m}_{C,CO}$ is the difference in the inlet and outlet carbon related carbon monoxide mass flow representing the overall consumed mass flow of carbon originating from carbon monoxide. The ASF weight distribution without methane is described in equation 9 with the derivation originating from the molar distribution.[8]

$$w_i = i\,(1-\alpha)^2 \alpha^{i-2} \tag{9}$$

Finally, inserting equation 9 in equation 7 results in a correlation between the chain growth probability and the C_{5+}-selectivity.

$$S_{C5+} = 1 - (1-\alpha)^2\,(1 + 2\alpha + 3\alpha^2) \tag{10}$$

Equation 10 is implicit regarding α, so the experimentally determined selectivity is interpolated for a sufficient small step size to obtain the chain growth probability. The overall calculation requires a 100% closed carbon mass balance which is neither guaranteed nor confirmable during the non-stationary start-up. This requires an especially precise measurement of CO-conversion. For non-stationary conditions the residence time (which changes with conversion and reaction time) from reactor outlet to the gas analysis has to be considered to assign measured volume flows and CO concentrations to each other. This introduces an additional uncertainty and therefore the results of α must be handled with observation and assumed to be not exact all the time.

Experimental results

In this section the results of experiments for 190 °C and 220 °C are shown depending on the subject. The slower reaction rate at 190 °C displays a better time resolution and the high reaction rate at 220 °C shows mass transfer limitations clearer.

The non-stationary pore filling process

In Figure 2 the filling degree over the normalized bed length is shown for different reaction times at 190 °C. Overall the reproducibility of the experiments is reasonably good (see the 6 h experiment in Figure 2) has to be considered that only single pellets are analysed at a certain location. Therefore, no statistical averaging of fluctuations in cobalt loading, specific pore volume, BET surface area, porosity, tortuosity, particle length, diameter and outer surface are present which all affect the pore filling process. While it was analysed that the fluctuation of each parameter itself is rather small and unavoidable in heterogenous catalysis, the total influence of all parameters on the pore filling process and degree can add up to higher extends. Additionally, the resulting gas phase at each location is never exactly the same, except for the first particle. The occasionally occurring outliers do not affect the clear trend of each experiment over the normalised bed length L observable in the experiments.

The experimental filling degrees greater one can be explained by the waxes trickling down the bed after reaching a pore filling degree of one. The waxes are pushed out of the pores by newly produced HC's and a certain amount remains on the outer surface area of the catalyst.

Before the removal of the catalyst, the reaction is stopped by lowering the temperature. This results in an increase of the hydrocarbon density and a decrease of occupied volume by the HC's. The arising vacant volume is filled by the wax on the outer surface area via capillary forces. The suction of waxes results in a higher mass of HC in the pores at lower temperatures. In combination with the correction by the density at reaction temperature in equation 4 filling degrees slightly greater one are possible and reasonable.

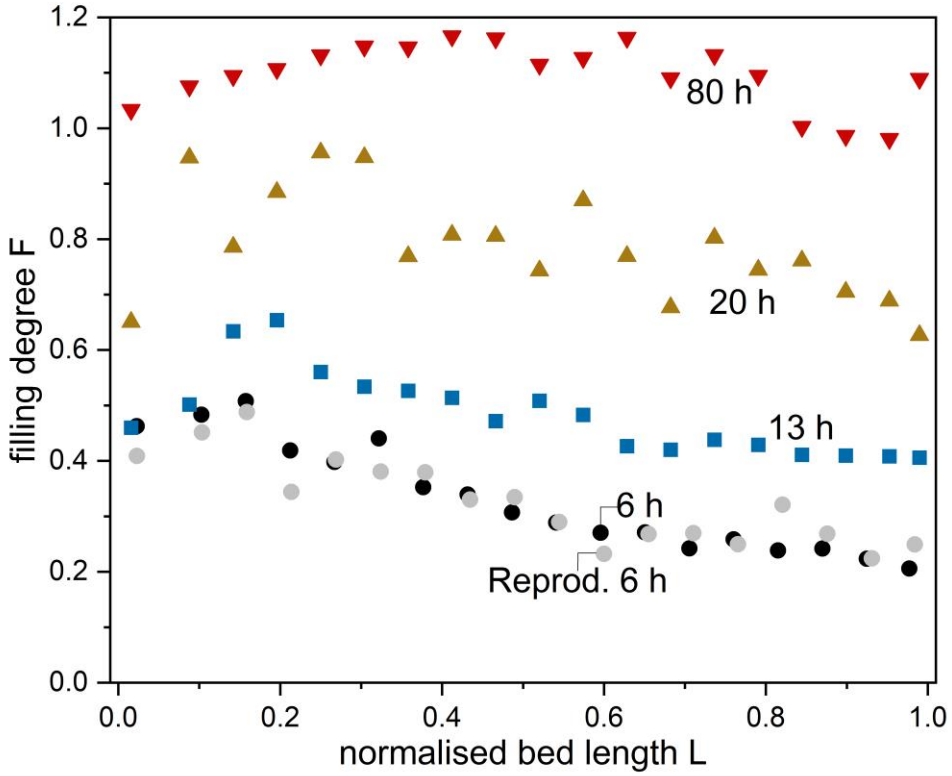

Figure 2: Filling degree over the normalized bed length for different reaction times. One data point is obtained from averaging four pellets. Reaction conditions: T=190 °C, p_{tot}= 1 MPa, H_2/CO=2, $V_{STP,in}$= 3.5 l/h, m_{cat}=10 g, d_p= 5 mm, 74 pellets, $X_{CO,stat.}$=12 %.

For partially filled pellets the expected slight increase of the filling degree with bed length caused by the increase in partial pressure of hydrocarbons resulting in an inhibited evaporation is not observable. Instead the overall trend is a slight decrease of the filling degree over the bed length. A possible explanation could be a (reversible) deactivation of the catalyst with bed length, most likely through the increased water partial pressure, the by-product of the FTS. A tendency at the beginning of the bed for a slight increase with bed length is observable before the decrease begins indicating that the deactivation could start only at a certain point or water partial pressure. While the parameters were chosen that no deactivation should occur at stationary conditions with a stationary CO-conversion of 12 %, the partially filled particles have significant greater CO-conversions (see Figure 4) and water partial pressure. Additionally, it is unclear how the wax film and its thickness (correlating to the filling degree) influences the deactivation behaviour.

In Figure 3 the filling degree over the normalized bed length at 220° C is depicted. To compare the different temperatures the volume flow was kept the same and the catalyst mass was changed to obtain the same stationary CO-conversion. Overall the increased temperature causes a significantly higher reaction rate and only a slight increase in evaporation resulting in shorter filling times. At this reaction temperature the expected slight increase in filling degree with the bed length is observable. However, additional experiments show that the different

behaviour with bed length is caused by the change in catalyst mass or number of pellets instead of the temperature. This effect is not fully understood yet, but is most likely due to the change in total external surface area and therefore the ratio of evaporation and production rate of products and partial pressures.

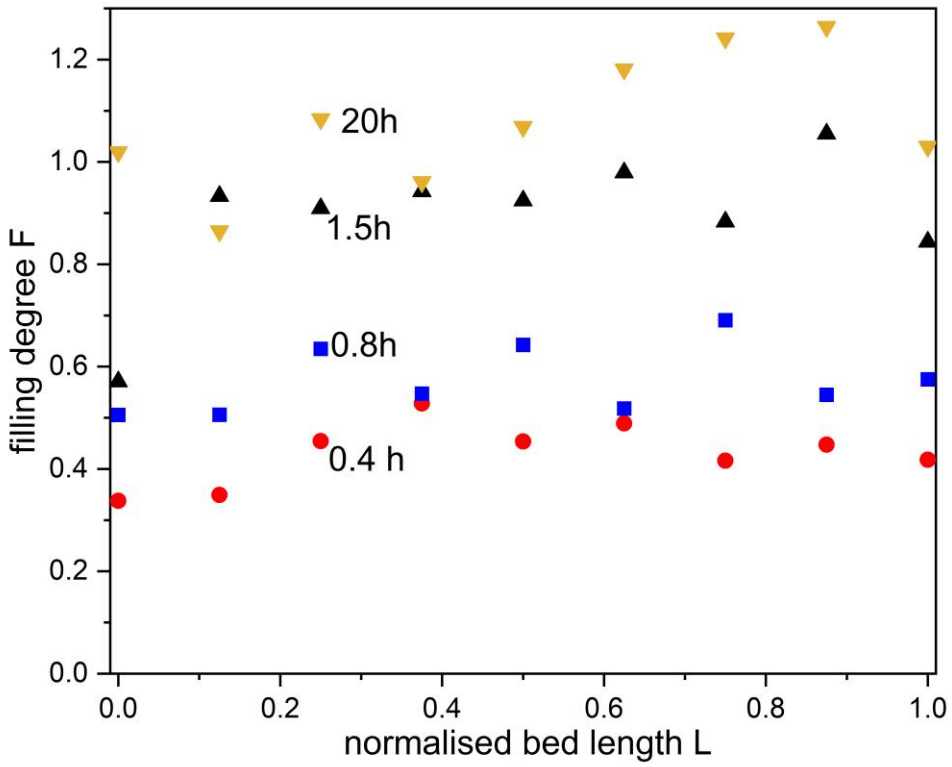

Figure 3: Filling degree over the normalized bed length for different reaction times. One data point is obtained from one pellet. T=220 °C, p_{tot}= 1 MPa, H_2/CO=2, $V_{STP,in}$= 3.5 l/h, m_{cat}=1.25 g, d_p= 5 mm, 9 pellets, $X_{CO,stat.}$=12 %.

Non-stationary CO-reaction rate and catalyst effectiveness

In Figure 4 the CO reaction rate, average filling degree of the bed and the methane selectivity over the reaction time are shown. At the beginning the increase of reaction rate is caused by the heat up of the reactor and a short non-isothermal period. Afterwards the reaction rate decreases rapidly as the average filling degree of the catalyst bed and the methane selectivity increase.

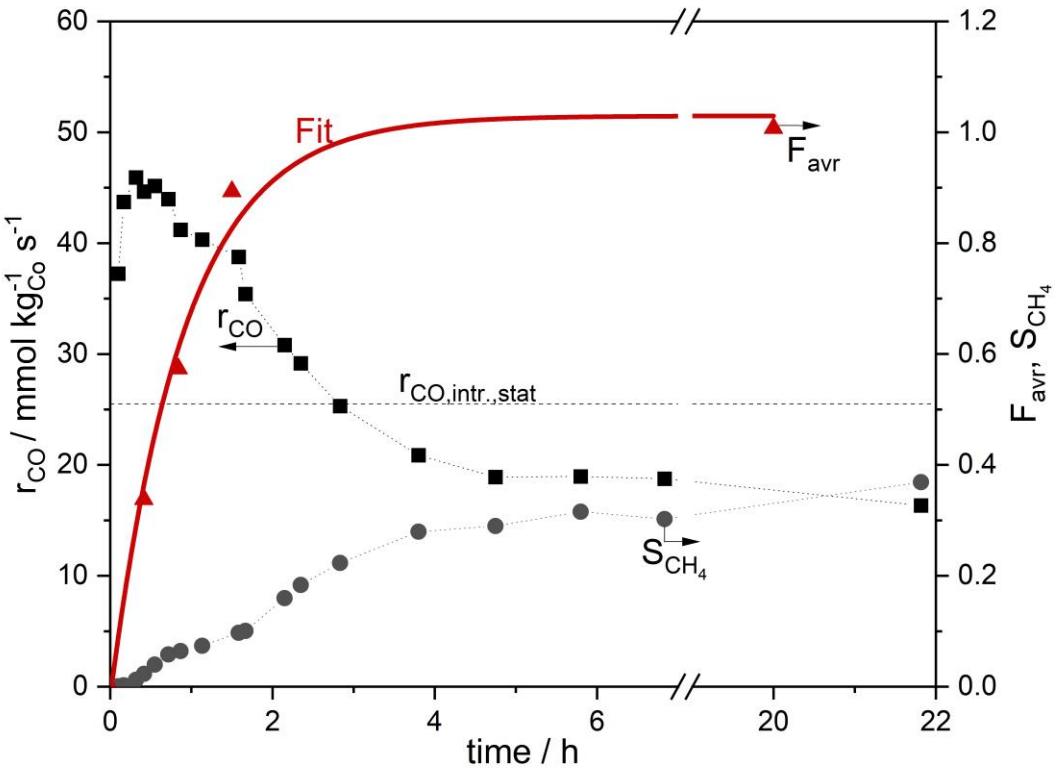

Figure 4: Carbon monoxide reaction rate, filling degree and methane selectivity over time. Dotted lines only for visual guidance, solid line fitted function. Reaction conditions: T=220 °C, p_{tot}= 1 MPa, H_2/CO=2, V_{STP}= 3.5 l/h, m_{cat}=1.25 g, d_p= 5 mm, 9 Pellets, $X_{CO,stat.}$=12%. $r_{CO,intr,.sta.}$ is the intrinsic reaction rate in steady state, measured with finely ground catalyst (d_p < 150µm).

All values can only be measured directly over time. But in fact, a lot of values depend on the filling degree, which again depends on time. Therefore, only the data points for the filling degree are fitted over time in order to be able to plot the other values over the filling degree by assigning the fitted filling degrees for the same points in time. The necessity of the fit arose from the high experimental effort of determining the filling degree resulting in a low time resolution (4 data points) compared to the other values. The resulting graph is plotted in Figure 5 and the reaction rate is changed to the stationary catalyst effectiveness factor by applying equation 14. Three zones are observable in the graph:

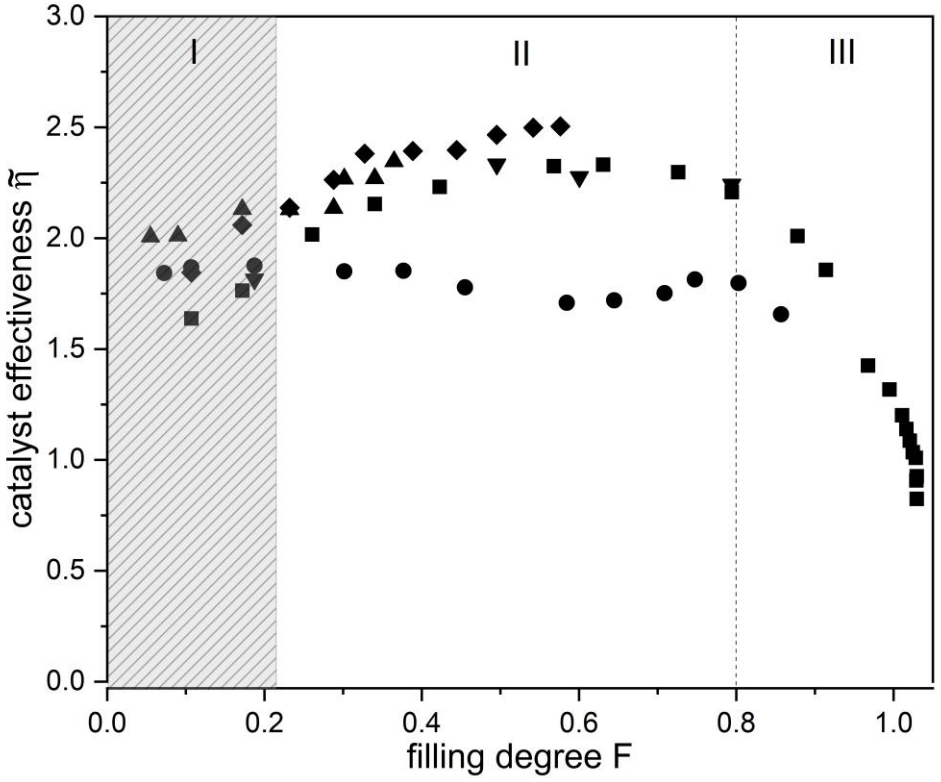

Figure 5: Catalyst effectiveness of the fixed-bed over the filling degree. Different symbols are obtained from different catalyst beds. Reaction conditions: T=220 °C, p_{tot}= 1 MPa, H_2/CO=2, $V_{STP,in}$= 3.5 l/h, m_{cat}=1.25 g, d_p= 5 mm, 9 pellets, $X_{CO,stat}$.=12%.

The first shaded zone up to a filling degree of 0.2-0.3 is regarded as invalid for evaluation due to non-isothermal conditions caused by the initial heating of the reactor. The catalyst is exposed to the raw gas phase in the beginning for a filling degree of zero. At this point the concentration of educts is the highest and consequently the catalyst activity, reaction rate and efficiency should be the highest in theory as well. This is not depicted by the non-isothermal experimental results. In the second zone from a filling degree of around 0.3-0.85 a catalyst effectiveness compared to stationary conditions of roughly two is present. Afterwards in the third zone the catalyst effectiveness factor is decreasing rapidly and reaches 0.5 for a filling degree of one. This result indicates that mass transfer limitations only occur for a filling degree greater 0.85. A possible explanation is that the macropores of the catalyst act as transport pores and assuming pores are filled completely from small to big pore radii these macropores are filled last. The catalyst support is produced by pelletizing smaller particles obtained from precipitation. For this catalyst it would make sense, that the macropores, which represent the gaps between the agglomerated small particles, are the transport pores to the mesopores inside the small particles. The macropore volume fraction of 12 % is very close to the gas filled pore volume fraction (1-F) at the point of beginning mass transfer limitation. This would further support the theory. The unexpected high catalyst effectiveness factor of 1.5-2 in the second zone could be explained by cavities of the steric hindered liquid molecules inside the partially filled pores enhancing reagent gas solubility. This is one explanation in literature for the significantly higher solubility of gases and especially hydrogen in liquids inside partially filled mesoporous structures compared to the solubility in the bulk liquid, at least at moderate tempeartures.[16–19]

Non-stationary product selectivity

The product selectivity in FTS can be categorized as follows:

- the chain growth probability α
- the methane selectivity (and the ethane selectivity) not following α
- the ratio of olefinic to paraffinic products
- the amount of oxygenated products

For non-stationary conditions and the catalyst used in the experiments no oxygenated products were detectable. The olefinic products were only detectable reliably with good time resolution in the gas phase for small chain lengths.
In Figure 6 the ratio of olefins to paraffins (O/P-ratio) for the predominantly gaseous products with a chain length of 2-6 are depicted over the reaction time. Independent on time an overall decrease in the O/P-ratio with increasing chain length is observable, with the exception of ethane which also does not follow the ASF distribution. At first, dependent on time for all chain lengths the O/P-ratio increases over a far longer period of time than the heating up procedure. At roughly 10h the ratios start to decrease which lies in the vicinity of reaching a filling degree corresponding to a theoretical monolayer filling. With more time on stream and higher filling degrees the ratio further decreases. The decrease of the O/P ratio with increasing filling degree could possibly have two reasons. Firstly, the residence time inside the pores is increased due to slower diffusion in the forming liquid phase and readsorption of olefins could occur more frequently. Secondly, the surface concentration of hydrogen could increase relative to CO leading to lesser olefin formation.

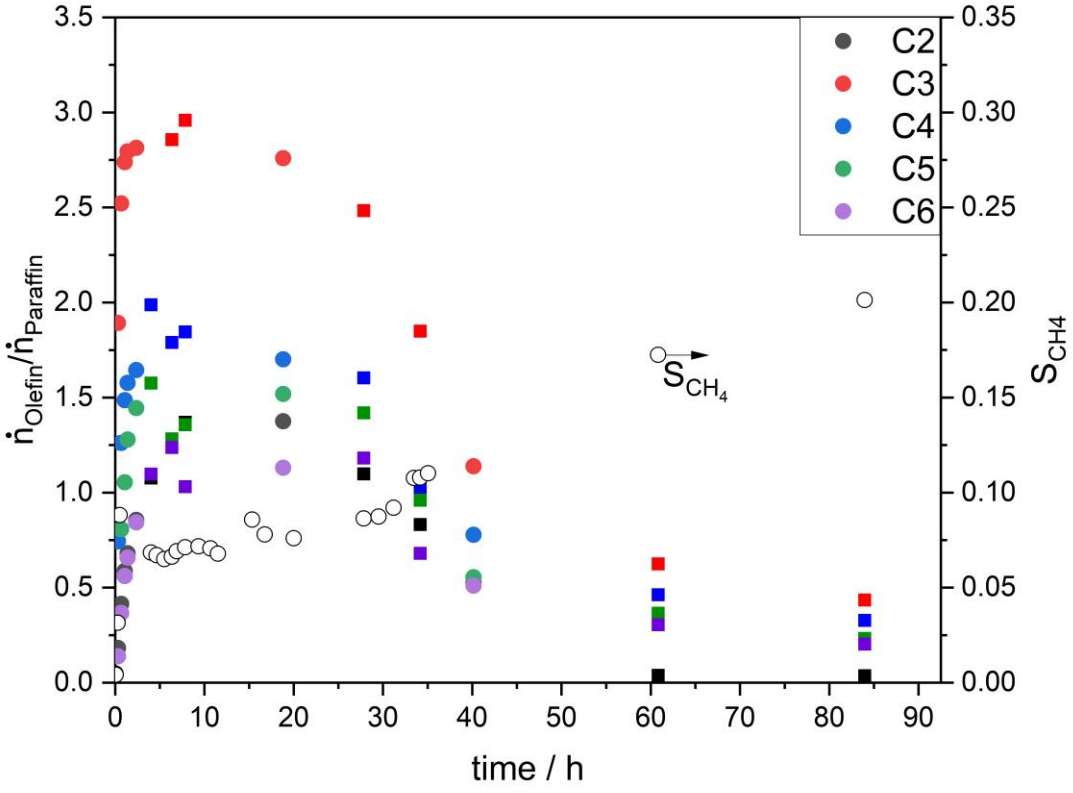

Figure 6: Olefin to paraffin ratio in the gas phase for hydrocarbons with a chain length of 2-6 and the selectivity of methane over the time. Colors are used for different chain lengths and symbols for different fixed-beds. Reaction conditions: T=190 °C, p_{tot}= 1 MPa, H_2/CO=2, $V_{STP,in}$= 3.5 l/h, m_{cat}=10 g, d_p= 5 mm, 74 pellets, $X_{CO,stat.}$=12%.

There are two additional correlations indicating that the second theory and the increase in H_2/CO surface concentration could be the (main) parameter for the change in O/P-ratio. The

methane selectivity has an inverse trajectory after 10 h compared to the O/P-ratio and increases with increasing filling degree. This suggests an increase in the H_2/CO surface concentration ratio, the predominant parameter influencing the methane selectivity for the same catalyst. The catalyst efficiency factor indicates stronger diffusional limitations only after a filling degree of 0.8. At this filling degree the slope of the decrease of the O/P-ratio is rather small compared to lower filling degrees, indicating that the mass transfer is less relevant for this behavior.

In f the chain growth probability determined from the gas phase is depicted for 190 °C and 220 °C in dependency of the pore filling degree. As mentioned in the experimental part the exact determination is rather difficult resulting in a high variance of values. Nonetheless an overall trend can be postulated. At 220 °C the chain growth probability starts roughly at 0.92 and decreases slowly up to a filling degree of 0.85-0.9. Afterwards the decrease is rapid and nearly approaches the intrinsic value. For 190 °C the intrinsic value is already 0.89 resulting in a fairly steady behavior of the chain growth probability over the filling degree. For 200 °C and 210 °C a similar course to 220 °C is observable approaching their respective steady state values (data not shown). This would indicate that the direct effect of the temperature on α is less pronounced as the literature proposes and the ratio of H_2/CO is the more dominant factor. The temperature indirectly affects the ratio by altering the solubility, diffusion and reaction rate of both gases resulting in an apparently high influence on α.

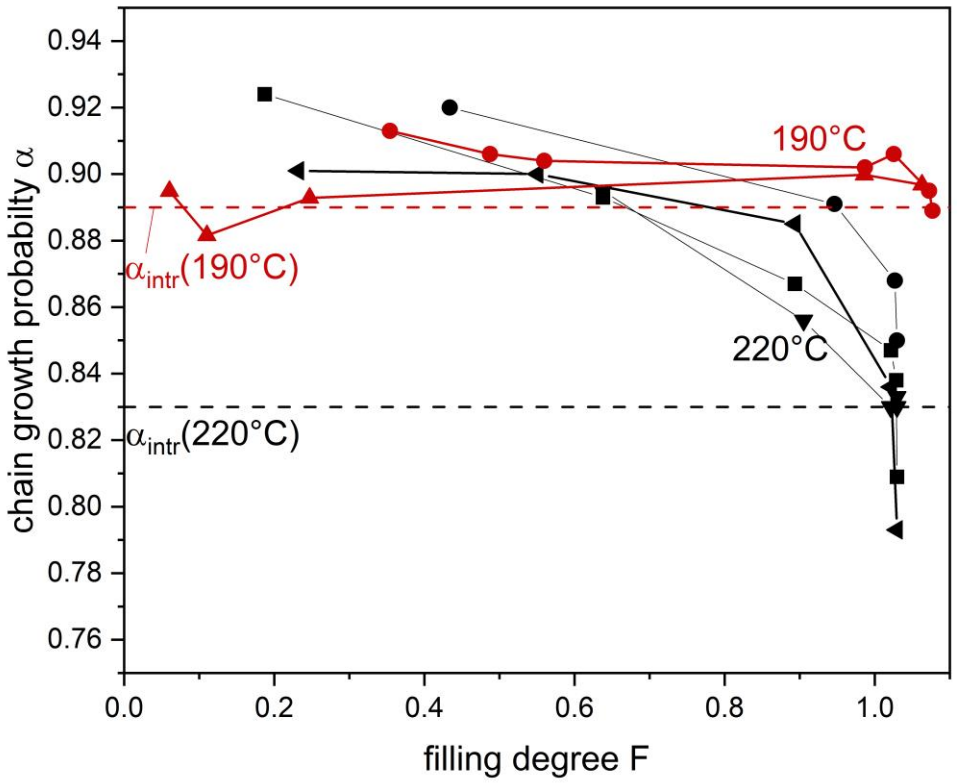

Figure 7: Chain growth probability over the filling degree for 190 °C and 220 °C. Different symbols are experiments with different catalyst beds. Reaction conditions: T=190-220 °C, p_{tot}= 1 MPa, H_2/CO=2, $V_{STP,in}$= 3.5 l/h, m_{cat}=1.25-10 g, d_p= 5 mm, 9-74 pellets, $X_{CO,stat.}$=12%. %. α_{intr} is the intrinsic chain growth probability in steady state, measured with finely ground catalyst (d_p < 150µm).

Beside the products leaving the reactor, a fraction of the hydrocarbons accumulates in the pores of the catalyst. In Figure 8 the mole fraction of hydrocarbons is showed for different normalized bed lengths L at a reaction time of 0.42 h and different reaction times for the

beginning of the bed (L=0). Nearly all distributions show a gaussian peak with tailing at long chain lengths. The maximum of the distribution starts at a chain length of 21 and shifts with the bed length to smaller chain lengths and increases slightly. At all positions hydrocarbons with a chain length of 9 or smaller are not detectable. The increasing partial pressure of light to medium hydrocarbons with increasing bed length reduces their evaporation leading to this shift. In comparison to the saturation pressure the increase in partial pressure at these conditions is nearly neglectable for hydrocarbons with a chain length of 9 or smaller.
The maximum shifts to longer chain lengths with increasing time on stream. Longer hydrocarbons do not evaporate but have lower production rates. Thus, their fraction increases with more time on stream. Additionally, the CO-conversion decreases leading to smaller production rates of all hydrocarbons reducing their partial pressures and increasing the evaporation of small to medium hydrocarbons.

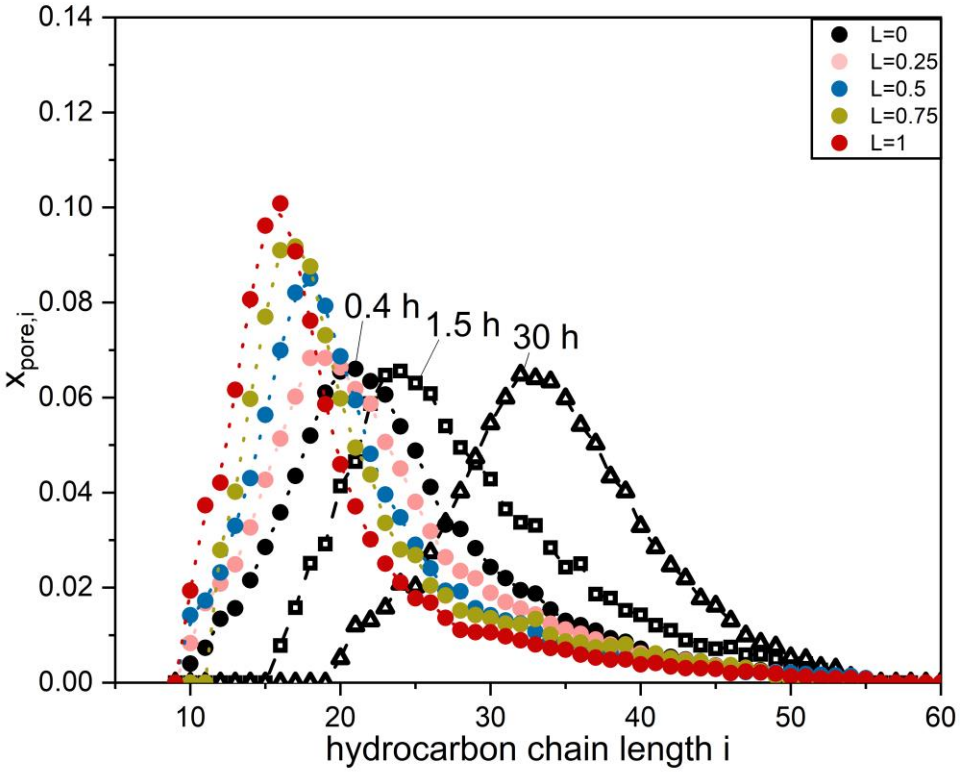

Figure 8: Distribution of mole fractions of hydrocarbons inside the catalyst pores for 220 °C. Different colors are used for different bed lengths Different symbols are experiments with different catalyst beds and reaction times at L=0. Reaction conditions: T=220 °C, p_{tot}= 1 MPa, H_2/CO=2, $V_{STP,in}$= 3.5 l/h, m_{cat}=1.25 g, d_p= 5 mm, 9 pellets, $X_{CO,stat}$.=12%.

Modelling

In the first part the basic model concept is explained which is derived from a model for only a single pellet and validated experimentally up to a temperature of 200 °C and CO-conversions of practically zero.[20] The single pellet model is expanded to a SPSR model by modelling single pellet as a consecutive series. In the second part the results of the model are compared to the experimental results and further model modifications are introduced to match them better.

Basic model concept

The catalyst pellet is balanced as a whole for each hydrocarbon with chain length i up to 60. The change of the molar amount of each HC over time inside the pores is the difference

between the FTS production rate $\dot{n}_{syn,i}$ and the evaporation rate $\dot{n}_{vap,i}$. This differential equation was adopted from Rössler et al.[20] for a single pellet with the additional implementation of the partial pressure. For the SPSR the gas phase composition is calculated behind the pellet and is the input matrix for the following pellet.

$$\frac{dn_i}{dt} = \dot{n}_{syn,i} - \dot{n}_{vap,i} \tag{11}$$

The amount of synthesized HC can be described by the product of the intrinsic CO consumption rate $r_{CO,C_{2+},intr}$ to products with a chain length of two or greater (this can be described as the total consumption rate of CO excluding the CO reacting to methane as well), the molar carbon fraction $x_{SF,C,i}$ according to the Schulz-Flory distribution and the catalyst efficiency $\tilde{\eta}$.

$$\dot{n}_{syn,i} = r_{CO,C_{2+},intr.}\, x_{SF,C,i}\, \tilde{\eta} \tag{12}$$

The reaction rate is based on a Langmuir-Hinshelwood approach suggested by Yates and Satterfield.[21] The kinetic parameters can be found in Pöhlmann et al..[22] The kinetic approach was validated for the catalyst used in this work for different temperatures at a syngas ratio of H_2/CO=2.

$x_{SF,C,i}$ is the carbon normalized Anderson-Schulz-Flory distribution without methane which has to be used instead of the normal ASF distribution in order to maintain the carbon balance in the system. α is the chain growth probability.

$$x_{SF,i,C} = \frac{(1-\alpha)i^{\alpha-2}}{\sum_{i=2}^{60}(1-\alpha)i^{\alpha-2}\, i} \tag{13}$$

The pore effectiveness factor η is described by the ratio of the CO reaction rate to either the intrinsic reaction rate or the reaction rate at the outer rim of the catalyst. In both cases the intention is to compare the measured value to a reaction rate without any mass transfer limitations.
For non-stationary conditions the phases involved change from gas-solid to gas-liquid-solid with an undefined transient gas-liquid monolayer-solid phase change in-between. Hence the reaction rate on the outer rim of the catalyst changes with the phases making it unsuitable for the definition in this specific case. For that reason, the intrinsic reaction rate at stationary conditions $r_{CO,intr.,stat.}$ is used which is measured for completely liquid filled small catalyst particles (d_p<150 µm) to exclude mass transfer limitations.

$$\tilde{\eta} = \frac{r_{CO}}{r_{CO,intr.,stat.}} \tag{14}$$

For equation 14 the usual pore efficiency factor η is modified to the catalyst (stationary) efficiency factor $\tilde{\eta}$ with the specification of the reaction rate to stationary conditions to account for efficiency factors greater one which would lie above the intuitive maximum pore efficiency factor of one. Initially the model of Pöhlmann et al.[22] was adopted for $\tilde{\eta}$.

The expression for evaporation is given in equation 15 where Sh is the Sherwood number, ε_p the porosity of the catalyst pellet, A_{ext} the external surface area, d_p the specific diameter, $D_{FSG,i}$ the gas diffusion coefficient according to Fuller-Schettler-Giddings, $x_{pore,i}$ the mole fraction of in the liquid inside the pores, $p_{vap,eff,i}$ the effective vapor pressure and p_i the partial pressure.

$$\dot{n}_{vap,i} = \frac{Sh\, \varepsilon_p\, A_{ext}}{d_p\, R\, T} D_{FSG,i}(x_{pore,i}\, p_{vap,eff,i} - p_i) \tag{15}$$

The effective vapor pressure for the hydrocarbons inside this catalyst is derived from a correlation of the adsorption isotherms described by Rössler et al..[23]

Modelling results

In Figure 9 the average filling degree of the bed at 220 °C over the reaction time is illustrated. The SPSR model clearly underpredicts the measured filling degrees. The model only assumes the intrinsic reaction rate as the maximal rate for empty pores. The experimental data show significantly higher rates for the beginning of the reaction. Therefore, for now the reaction rates were fitted to the experimental values and applied in the model. This leads to an increase of the filling degree, but is still far away from matching the experimental data. A second observation in the experiments is the increased chain growth probability for not completely filled pores. Thus, the fit of the chain growth probability over the filling degree for the experimental data was used in the model instead of the constant intrinsic one. This results in a large increase of the filling degree and has an even bigger impact than the increased reaction rate. In fact, the chain growth probability is by far the most influential parameter in the whole model and this is the only option in the model to be able to come close to the experimental data. Consequently, it could be comprehended as a validation of the uncertain experimental determination of the chain growth probability. While the model still underpredicts the filling degree, a clear improvement is observable.

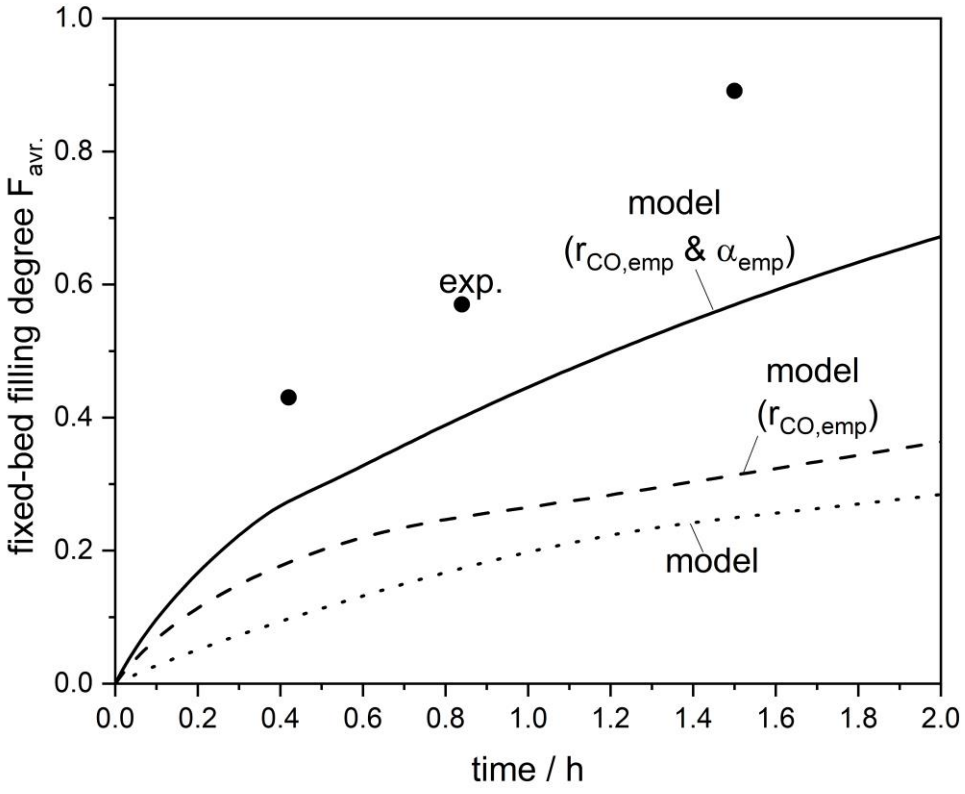

Figure 9: Average filling degree of the fixed-bed in the SPSR over the reaction time. Model results for the adopted single pellet model and the implemented experimental observations. Reaction conditions: T=220 °C, p_{tot}= 1 MPa, H_2/CO=2, $V_{STP,in}$= 3.5 l/h, m_{cat}=1.25 g, d_p= 5 mm, 9 pellets, $X_{CO,stat.}$=12%.

In Figure 10 the hydrocarbon distribution inside the first and last pellet are illustrated for the two reaction times of 0.84 h (partially filled) and 30 h (completely filled). The modelled values underpredicts the average chain length and shifts the distribution to smaller chain lengths compared to the experiments. An increased reaction rate and therefore filling degree in the model shift it slightly to the right. The addition of the empirical chain growth probability causes a necessary significant increase in hydrocarbons with a chain length >40 to match the experimental results better, especially for the short reaction times. This broadening of the distribution results in a decrease of the maximum. Good agreement with the experimental data

is obtained for the first pellet with the changes in the model for 30 h. For 0.84 h the adjusted model improved the result but there is still a discrepancy to the experimental data, most likely caused by a mismatch of the evaporation behavior. For the pellet at L=1 for 0.84 h a similar trend to L=0 is observable. Only for 30 h a different behavior is observable and the distribution is shifted to the right of the measured values and the evaporation of medium hydrocarbons (~C15-C25) could be overestimated.

Overall the modifications improved the model regarding the filling degree and the hydrocarbon distribution. The qualitative changes are represented by the model so the basis of the model seems to represent the behavior of the reaction. Nonetheless there are still discrepancies to the experimental data indicating that some effects are not or incorrectly included. Current investigations show a far greater influence of the volume flow or gas velocity and water could have a greater influence than expected. Implementing these effects in the future could yield a satisfying model.

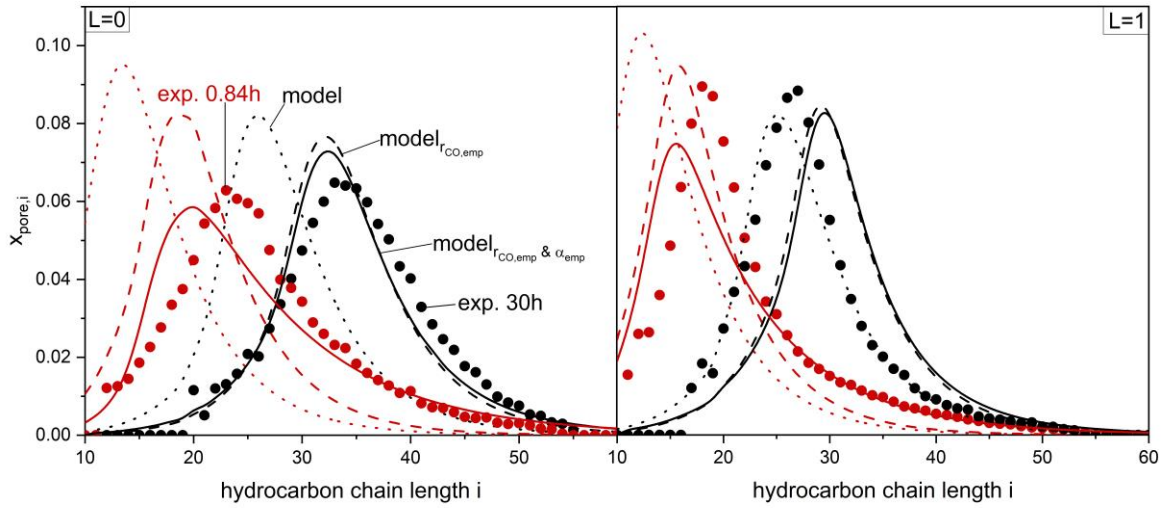

Figure 10: Left: Experimental and modelled distribution of the mole fraction of hydrocarbons with chain length i for 0.84 h and 30 h reaction time for the beginning of the fixed-bed L=0. Right: Same graph for the end of the fixed-bed L=1. Reaction conditions: T=220 °C, p_{tot}= 1 MPa, H_2/CO=2, $V_{STP,in}$= 3.5 l/h, m_{cat}=1.25 g, d_p= 5 mm, 9 pellets, $X_{CO,stat.}$=12%.

Conclusions

The results of experiments conducted in a single pellet string reactor for the non-stationary start-up of Fischer-Tropsch synthesis can be summarized to a few insightful conclusions:

- The increase in bed length increases the filling degree slightly due to the higher partial pressure of hydrocarbons up to certain point. Increasing the bed length further results in an inhibition of the filling process.
- The product selctivities change with the filling degree. The chain growth probability starts higher than the intrinsic one and decreases with filling degree, just as the olefin to paraffin ratio
- The reaction rate is far higher than the intrinsic stationary reaction rate up to high filling degrees, only dropping under it for nearly fully filled pores indicating mass transfer limitations only apply for high pore filling degrees for this catalyst. This could be caused by the filling of transport macropores.
- The hydrocarbon distribution inside catalyst pores shifts to higher chain lengths with reaction time for all bed lengths. For a certain reaction time the distribution shifts to smaller chain lengths and the maximum increases with increasing bed length.

It was attempted to model the experimental results by a series of single pellets to obtain the SPSR behavior. The model does not describe the behavior sufficiently for the SPSR and clearly underpredicts the filling degree. The experimental observation of the increased reaction

rate and chain growth probability for not completely filled pores was implemented in the model resulting in far better results.
There is still a discrepancy which will be addressed in the future. The experimental data suggest two additional effects the model does not account for enough. Firstly, the volume flow or gas velocity has a far greater effect on the filling process than the model assumes. Secondly, up to now, the accumulation of water was assumed to be neglectable due to the high saturation pressure (e.g. 2.36 MPa at 220 °C). But current investigations indicate an unexpected high content of water on the catalyst, especially with increasing bed length and at low reaction times. This increases the filling degree and could influence the reaction rate.

Notations

Latin

A_{ext}	external surface area, m^2
d_p	pellet diameter, m
$D_{FSG,i}$	diffusion coefficient according to Fuller-Schettler-Giddings, $m^2\ s^{-1}$
F	filling degree
L	normalized bed length
l_{red}	mass loss degree of reduction, %
$m_{cat,0}$	mass of empty catalyst before reaction, g
$m_{cat,end}$	mass of wax filled catalyst after reaction, g
$m_{Hc,all}$	mass of all liquid HC in catalyst, g
p_i	partial pressure, MPa
$p_{vap,eff,i}$	effective saturation pressure inside the pores of HC with chain length I, MPa
R	universal gas constant, $J\ mol^{-1}\ K^{-1}$
S_{C5+}	selectivity to HC's with chain length 5 and higher for the FTS
Sh	Sherwood number
T	temperature, K
V_{HC}	Volume of liquid hydrocarbons, m^3
V_{pore}	pore volume, m^3
$V_{s,pore}$	specific pore volume, $m^3\ kg^{-1}$
$V_{STP,in}$	Input volume flow at standard temperature pressure, $l\ h^{-1}$
w_i	mass fraction of hydrocarbon with chain length i
$X_{CO,stat}$	stationary CO-conversion, %
x_i	mole fraction of hydrocarbon with chain length i according to ASF distribution
$x_{pore,i}$	mole fraction of hydrocarbon with chain length i inside the catalyst pores
z	pellet number in the fixed-bed

Greek

α	chain growth probability
ε_p	pellet porosity
η	pore efficiency
$\tilde{\eta}$	catalyst efficiency
ρ	density, $kg\ m^{-3}$

Abbreviations

ASF	Anderson-Schulz-Flory
BET	Brunauer-Emmett-Teller
FTS	Fischer-Tropsch synthesis
O/P	olefin to paraffin ratio
PtL	Power-to-Liquid
SPSR	single pellet string reactor

Conflicts of interest

There are no conflicts of interest to declare.

Acknowledgements

The authors gratefully acknowledge the financial support of this work by the German Research Foundation (DFG Je 257/23-2).

References

1 Gallo, A. B.; Simões-Moreira, J. R.; Costa, H.; Santos, M. M.; Moutinho dos Santos, E. *Renewable and Sustainable Energy Reviews* 65, 800 (2016).
2 Wentrup, J.; Pesch, G. R.; Thöming, J. *Renewable and Sustainable Energy Reviews* 162, 112454 (2022).
3 European Commission. *Communication from the comission to the european parliament, the council, the european economic and social committee and the committee of the regions.*: *The 2015 International Climate Change Agreement: Shaping international climate policy beyond 2020* (2013).
4 Willner, T.; Lucka, K. *Fortschrittliche alternative flüssige Brenn- und Kraftstoffe für Klimaschutz im globalen Rohstoffwandel*: *Positionspapier des temporären ProcessNet Arbeitskreises "Alternative Brenn- und Kraftstoffe"* (2016).
5 Gao, R.; Zhang, C.; Jun, K.-W.; Kim, S. K.; Park, H.-G.; Zhao, T.; Wang, L.; Wan, H.; Guan, G. *Journal of CO2 Utilization*, 101619 (2021).
6 Kaiser, P.; Unde, R. B.; Kern, C.; Jess, A. *Chem. Ing. Tech.* 4, 489 (2013).
7 Rauch, R.; Hrbek, J.; Hofbauer, H. *WIREs Energy Environ* 4, 343 (2014).
8 Jess, A.; Wasserscheid, P. *Chemical technology*: *From principles to products*, Second edition; Wiley-VCH, 2020.
9 Choudhury, H. A.; Chakma, S.; Moholkar, V. S., 383.
10 Maitlis, P. M.; Klerk, A. d. *Greener Fischer-Tropsch processes for fuels and feedstocks*; Wiley-VCH, 2013.
11 Kalz, K. F.; Kraehnert, R.; Dvoyashkin, M.; Dittmeyer, R.; Gläser, R.; Krewer, U.; Reuter, K.; Grunwaldt, J.-D. *ChemCatChem* 1, 17 (2017).
12 Schurm, L.; Kern, C.; Jess, A. *Catal. Sci. Technol.* 18, 6143 (2021).
13 Sie, S. T. *AIChE J.* 12, 3498 (1996).
14 Hipolito, A. I.; Rolland, M.; Boyer, C.; Bellefon, C. de. *Oil Gas Sci. Technol.* 5, 689 (2010).
15 Fernengel, J.; Bolton, L.; Hinrichsen, O. *Chem. Eng. J.* 373, 1397 (2019).
16 Miachon, S.; Syakaev, V. V.; Rakhmatullin, A.; Pera-Titus, M.; Caldarelli, S.; Dalmon, J.-A. *Chemphyschem* 1, 78 (2008).
17 Clauzier, S.; Ho, L. N.; Pera-Titus, M.; Farrusseng, D.; Coasne, B. *J. Phys. Chem. C* 20, 10720 (2014).
18 Coasne, B.; Farrusseng, D. *Microporous and Mesoporous Materials* 288, 109561 (2019).
19 Pera-Titus, M.; El-Chahal, R.; Rakotovao, V.; Daniel, C.; Miachon, S.; Dalmon, J.-A. *Chemphyschem* 12, 2082 (2009).
20 Rößler, S.; Kern, C.; Jess, A. *Catal. Sci. Technol.* 15, 4047 (2019).
21 Yates, I. C.; Satterfield, C. N. *Energy Fuels* 1, 168 (1991).
22 Pöhlmann, F.; Kern, C.; Rößler, S.; Jess, A. *Catal. Sci. Technol.* 17, 6593 (2016).
23 Rößler, S.; Kern, C.; Jess, A. *Catal. Sci. Technol.* 8, 1902 (2019).

Fischer-Tropsch Synthesis Based Maritime Fuel Production with Syngas containing O_2

A. Herbers, C.Kern, A. Jess
Universität Bayreuth

Abstract

New emission regulations lead to a demand for renewable fuel sources. In particular, the shipping sector needs clean and pollution-free alternatives with regard to sulfur oxide emission. As battery-powered solutions are inapplicable due to their low energy density, economic production of high-density synthetic fuels attends the focus of today's research. This work presents a new process to produce synthetic maritime fuel by Fischer-Tropsch synthesis (FTS) based on "green" syngas. Here, syngas is generated from CO_2 and H_2O using renewable energy. In this syngas production process molecular oxygen is a byproduct that can not be completely removed. Hence, the FTS is run with traces of O_2. For safety reasons the O_2-content has to be limited to a maximum of 2 vol.-%. Based on this syngas generation process by renewables a high-quality maritime fuel is obtained at low temperature Fischer-Tropsch synthesis (LTFTS) reaction conditions (10-30 bar, 180-230 °C).

At LTFTS conditions, gravimetric measurements with 5x5 mm $Co/Pt/Al_2O_3$ catalyst-particles in a magnetic suspension balance indicate that the catalyst stays active as long as H_2 is present in the system. Oxygen is converted to H_2O and CO_2 in varying proportions, based on composition and reduction degree of the catalyst. The water produced adsorbs reversibly on the catalyst surface at the reaction conditions.

Furthermore, under LTFTS conditions experiments performed in a technical tube reactor with $Co/Pt/Al_2O_3$ catalyst particles show no influence on the product distribution of C_{2+} products. Moreover, methane selectivity decreases because of the adsorbed water on the catalyst surface.

The experimental data indicate that reaction temperature and O_2 content in the gas phase have no effect on the product distribution. On the other hand, higher total pressure and CO concentration yield higher CO_2 selectivity. Finally, the variation of the H_2 concentration shows no influence on the reaction outcome. These described effects allow the conclusion that the CO surface coverage on the catalyst - that is based on the CO gas concentration - is the main factor for product distribution of the products resulting from the reaction with oxygen.

Optimizing the reaction conditions promises a 65 wt.-% yield of high quality maritime fuel.

Production of Anhydrous Formaldehyde with Co-generation of Hydrogen

M. Kamienowska[1,2], K. Niedermeier[2], M. Bender[1], Th. Wetzel[2]
[1]BASF SE, Ludwigshafen, Germany, [2]Karlsruhe Institute of Technology, Karlsruhe, Germany

Abstract

In response to the evolving needs of the chemical industry, enhancing the efficiency of its processes has become a matter of the utmost importance. For this reason, there has been ongoing research into more high-performing production routes, one of which is the direct dehydrogenation of methanol to formaldehyde. As stated in literature [1,2], sodium vapour is one of the most potent catalysts for the synthesis of anhydrous formaldehyde with the co-generation of highly valuable hydrogen gas [3]. Nonetheless, no further scaling-up has been implemented to this point. Thus, a mini-plant called MEDENA ('Methanol dehydrogenation with evaporated sodium [Na] as catalyst') is assembled. The MEDENA setup aims to develop an economical and sustainable solution to obtain water-free formaldehyde. This contribution will outline the influence on the chemical reaction efficiency of different reactor types, including the insertion of ceramic sponges in the apparatus with their various dimensions and porosities and their enhancing effect on the mixing of the gases and the heat transfer. Furthermore, for the purpose of providing a continuous sodium vapour supply for the reaction, this work will elaborate on the experimental demonstration of the catalyst dosing system, which may be used to provide a controlled amount of evaporated sodium as well as a constant catalyst distribution over time.

Literature

[1] S. Ruf and G. Emig, "Pure dehydrogenation of methanol to formaldehyde a homogeneously sodium-catalysed vapour-phase reaction," *Applied Catalysis A: General*, vol. 161, no. 1, pp. L19–L24, Nov. 1997, doi: 10.1016/S0926-860X(97)00127-0.

[2] A. Meyer and A. Renken, "Sodium compounds as catalysts for methanol dehydrogenation to water-free formaldehyde," *Chemical Engineering & Technology*, vol. 13, no. 1, pp. 145–149, 1990, doi: 10.1002/ceat.270130120.

[3] A. Kovač, M. Paranos, and D. Marciuš, "Hydrogen in energy transition: A review," *International Journal of Hydrogen Energy*, vol. 46, no. 16, pp. 10016–10035, Mar. 2021, doi: 10.1016/j.ijhydene.2020.11.256.

Acknowledgements

This research is part of the NAMOSYN project, which is funded by the Federal Ministry of Education and Research under grant number 03SF0566K0.

Hydrogenative Depolymerization of Polyurethanes Catalyzed by Manganese- and Ruthenium Pincer Complexes

T. Schaub
BASF SE

Abstract

Polyurethanes (PU) are the 6th most commonly used polymer accounting for almost 8% of annually produced plastic materials. Due to the high possibility to tune polyurethane properties it can be found in different classes of plastics, such as elastomers, hard foams, soft foams, adhesives, fibers and others and thereby has countless applications. Chemical recycling, namely decomposing polymers into their monomers, offers a sustainable loop of plastic production, since the monomers obtained by this means can be used to prepare polymers without loss in properties, thus creating an ideal, circular polymer economy. One option to achieve this is the Hydrogenation of spend Polyurethanes to the monomeric units as polyols and polyamines to be reused to produce new polyurethanes. The key to success to allow this recycling concept is the use of suitable hydrogeneration catalysts. We developed systems based on homogeneous Ruthenium- and Pincer-Complexes which allow this hydrogenation in combination with elevated temperatures (up to 200 °C) as well as appropriate solvents to ensure a sufficient solubility of the polymers. A wide range of polyurethane samples of varying polyol and isocyanate compositions, some of which featuring significant amounts of urea functionalities, were successfully depolymerized, releasing polyetherols and diaminotoluene (TDA) as well 4,4´-methylenedianiline (MDA).

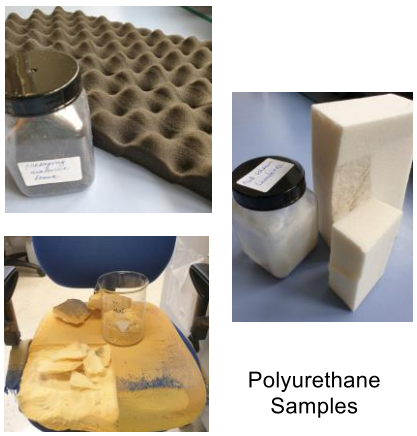

References: a) V. Zubar, A. Haedler, M. Schütte, A.S.K. Hashmi, T. Schaub, *ChemSusChem*, **2022**, *15*, e202101606; b) W. Zhou, P. Neumann, M. Al Batal, F. Rominger, A.S.K. Hashmi, T. Schaub, *ChemSusChem*, **2021**, *14*, 4176-4180.

Synthesis of Stable Zinc Oxide Based Catalysts for Carrying out Direct Dehydrogenation of Methanol to Obtain (a) Anhydrous Formaldehyde and (b) Highly Selective Hydrogen as By-product

A. G. Chowdhury[1], D. Deutsch[1], U. Arnold[1], J. Sauer[1], M. Bender[2]
[1] Institute of Catalysis Research and Technology (IKFT), Karlsruhe Institute of Technology (KIT), Eggenstein-Leopoldshafen
[2] BASF SE, Ludwigshafen am Rhein

Abstract

There is a growing demand for renewable hydrogen in recent years with climate change attaining one of the highest priorities in today's industrialized societies. In industry, a significant amount of hydrogen is used in the methanol (CH_3OH) production. Successively, the produced methanol is used to manufacture formaldehyde (HCHO), which is one of the most extensively used raw materials for further synthesis of many other types of chemicals. However, most of these synthesis routes require its anhydrous form. Therefore, the currently and most widely used industrial oxidative dehydrogenation processes are disadvantageous, because of the formation of water during the manufacturing process. Not only is the separation chemistry of formaldehyde-water-methanol mixture a complex unit operation, but it is also relatively energy intensive [1]. Moreover, the hydrogen used in the beginning of the supply chain to produce methanol is lost, since it reacts to water.
The topic of direct dehydrogenation is therefore of real interest, because the two main products, viz. anhydrous monomeric formaldehyde and hydrogen are commercially of great interest. Zinc oxide (ZnO) is known to catalyze the direct methanol dehydrogenation [2–4]. However, the volatilization of ZnO at high temperatures is a major problem leading to a significant drop in the catalyst activity over time [3]. In this investigation, we initially compare the dehydrogenation chemistry of ZnO catalyst to the methanol pyrolysis, wherein the formed hydrogen and water was also quantified. To the best of our knowledge, a very few number of studies have been published till date catering to quantification of the trace amount of water formed during the dehydrogenation reaction [5]. All types of ZnO catalysts yielded a maximum of 0.8 vol% water inside the investigated temperature range. Experiments were carried out to stabilize activity of the catalyst with help of mild oxidizing agents, one of them being carbon dioxide (CO_2). Although a minimal stabilizing effect was observed, it did not completely hinder the catalyst deactivation. Consequently, focus was laid upon binding the ZnO chemically to silica support matrix by applying different manufacturing as well as heat-treatment (calcination) methods. A Time On Stream (TOS) study revealed a higher stability of the new catalyst, which surpasses stability of the ZnO catalyst with a constant methanol conversion and formaldehyde selectivity.

Introduction

A major task undertaken by the global political committees is to set the goal of a net-zero emission society by 2050 [6, 7]. For chemical industry, which is the third largest direct CO_2 emitter [8], this could mean recycling the emitted CO_2, where various basic chemicals (with C,H & O in their structure) can be manufactured in combination with H_2. For example, methanol (CH_3OH) is currently synthesized from CO_2, CO and H_2 at pressures from 50 to 100 bar and temperatures between 200 and 300 °C using $Cu/ZnO/Al_2O_3$ as catalyst. From which, approximately 30% caters to the single major usage, i.e., the production of formaldehyde [9]. The IEA predicts an increased CO_2 footprint in methanol production from 222 Mt/p.a. in 2020 to 269 Mt/p.a. by 2025 [8]. Therefore, manufacturing methanol completely with the help of recycled CO_2 would have a significant impact on the chemical sector alone in directly diminishing the GHG emissions. Although, recycling CO_2 is not just the only way of increasing sustainability and energy efficiency of industrial processes. During production of formaldehyde from methanol, one of the major side-products is water [1]. Currently industrially practiced processes include the silver contact process (with silver catalyst) and the formox process (iron oxide-molybdenum oxide catalyst). In both processes, synthesis happens by means of two different routes, viz. through

a. partial oxidation of methanol

$$CH_3OH + ½\ O_2 \rightarrow HCHO + H_2O$$

b. direct dehydrogenation of methanol

$$CH_3OH \rightarrow HCHO + H_2$$

The partial oxidation route drastically reduces energy efficiency of the process because, the energy dense hydrogen used in manufacturing methanol in the beginning is thereby lost and converted to its more stable form, water. Consequently, the topic of direct dehydrogenation of primary alcohols and alkanes is of a significant relevance in process industry, due to the fact that the dehydrogenation chemistries are usually moderate to high endothermic reactions requiring relatively high temperatures [10]. It is important to mention here that, provisions have to be made to install a consecutive utility plant for anhydrous formaldehyde, since the molecule is very reactive and also unstable outside a specific range of temperature [11]. Hereby, one can imagine a manufacturing plant for generation of in-situ anhydrous formaldehyde from methanol and its subsequent utilization in the next step for manufacturing widely used formaldehyde derivatives like trioxane [12].
Pure zinc oxide is one of the very few materials known to be active towards the direct dehydrogenation chemistry of primary alcohols and alkanes [4, 13]. Recently, a paper has been published, where application of bulk gallium oxide (Ga_2O_3) material enabled a direct dehydrogenation of methanol, with an initial formaldehyde selectivity of 77% alongside a methanol conversion of 72% [14]. However, in case of bulk ZnO these values are much lower with initial selectivity of being 75% with only 10% methanol conversion [15]. Moreover, the high temperatures and a reducing atmosphere causes a relatively fast deactivation of both the above-mentioned catalysts in a very short time. In case of ZnO, the catalyst is reduced to metallic zinc, which then accumulates at the colder reactor outlet, thus leading to loss of active zinc species from the catalyst bed [15]. Previous efforts show that, manufacturing ZnO from different precursors, viz. zinc acetate, zinc nitrate or zinc chloride, led to different BET surface areas along with different activities [13]. Apart from application of different manufacturing techniques, efforts were undertaken to physically support bulk ZnO with typical support materials such as silica, alumina or titanium, to circumvent the volatility problem. Here, silica was the most effective support material with a significant improvement in catalyst activity as well its stability [16, 17].
In this study, we initially investigated the zinc oxide catalyst by physically supporting it with fumed silica. Although, in a harsh reductive environment the catalyst suffered serious deactivation, again due to catalyst volatility at high temperatures. Experiments were focused on in-situ re-oxidation of the reduced metallic zinc with help of CO_2 and O_2. Application of minimal O_2 in feed produced relatively high amounts of water as by-product, whereas application of CO_2 as a mild oxidizing agent was observed to slow down the zinc reduction (for one specific CO_2:CH_3OH concentration and reaction temperature), similar to investigations from Jung and his coworkers [3].
Since these measures did not lead to a complete overall stability of any manner, diverse efforts were undertaken to chemically bind the catalyst material to its support. Here, the interaction of zinc oxide with different support materials is a topic, which has been extensively investigated in past. Various applications of zinc silicate [18–20], zinc aluminate [21–25] as well as zinc titanate [26–28] as a spinel material can be found, primarily all across photo catalysis and in the electronics industry. Zinc titanate ($ZnTiO_3$) is a well-known sorbent candidate for high temperature hydrogen sulfide (H_2S) removal from exhaust gases of a coal gasifier [29]. Since temperatures of the exhaust gases are as high as 650 °C, a stable form of zinc oxide has to be implemented. Therefore, by chemically binding TiO_2 to ZnO matrix, the reduction of zinc oxide could be hindered significantly. Analogous to this, volatility problem of the bulk ZnO can also be positively influenced by understanding its interactions with the SiO_2 material. Such an effect is also known as strong metal-support interaction and is a well-researched field of study

in the branch of material science [30]. There are various phases of zinc silicate, which exist in resonance to the base material depending on formation and concentration of ZnO and SiO_2. Two of these are; zinc metasilicate/bisilicate ($ZnSiO_3$) and willemite or zinc orthosilicate/monosilicate (Zn_2SiO_4). Some of these are even found naturally in the ore and mines of zinc [31]. Presence of impurities inside their structures enable physical and chemical properties of the material to vary largely, in some cases leading to a wider band of emission spectrums, an enhanced thermal and electrical conductivity or in some cases very good dielectric properties have also been observed [32]. The structure of zinc silicate material allows its widespread usage as a host matrix for various dopants. Although, manufacturing these materials in laboratory could be a very challenging task. Sagou and coworkers have made constant efforts in 1980s to manufacture the zinc silicate in Zn_2SiO_4 structural form [13, 16]. In one study they reported an amount of 43.1 wt% of Zn and 21.2 wt% Si in the catalyst matrix by performing ICP elemental analysis [33]. This suggests that the material manufactured had a chemical formula of $Zn_1Si_{1.14}O_{3.38}$, rather than the targeted Zn_2SiO_4 catalyst.
Out of the various available synthesis methods, during this study we have applied the sol-gel method to synthesize all the zinc silicate materials [34]. Thereby, usage of different calcination methods and temperatures enabled varied structure specific characteristics of the same material. Simultaneous to the catalyst activity tests, characterization of the material was executed. XRD and EDX techniques were used to investigate phase structures and surface elemental composition respectively, thereby disclosing some physical characteristics of the material. Physisorption experiments were also undertaken for measuring BET surface area. For investigation of chemical properties, bulk composition was characterized with the help of ICP-OES method before and after the reaction, to quantify the loss of zinc from catalyst matrix. During some experiments, deposition of carbonaceous species was also observed. Here TGA method with synthetic air (20.5% O_2) was implemented to burn off the coke and determine the amount during a specific TOS. The synthesis and characterization methods have been described in detail in the following sections of this investigation.

Experimental section

Catalyst preparation

ZnO nanopowder (Sigma-Aldrich, <100 nm particle size) was directly obtained for catalytic tests, where the powder was calcined at 600 °C in static air for 5 hours. Before application on the fixed bed, 5 wt% of the powder was mixed with fumed silica (SiO_2, Sigma-Aldrich), pressed and sieved. The sieve fraction in between 400 – 600 µm was used throughout all experiments, even for the zinc silicate trials. A single ZnO catalyst was tested during this study, whose sample name was ZnFS/SA1.
For preparation of zinc silicate materials, the following chemicals were exactly used as they were commercially procured without undergoing any pre-treatment; zinc nitrate hexahydrate ($Zn(NO_3)_2.6H_2O$, Sigma-Aldrich, reagent grade 98%) and tetraethyl orthosilicate (TEOS, Sigma-Aldrich, for synthesis) were used as precursors for obtaining zinc silicate based catalyst. The molar ratio of Zn to Si was fixed at 2. The zinc precursor was dissolved in a round bottom flask using ethanol as solvent. To this, the required amount of TEOS was fed in, while constantly stirring the solution inside the flask. All steps were performed in room temperature. After this, the pH of the solution was adjusted to 4, with help of nitric acid to activate the sol [35]. The solution was then allowed to stand at room temperature. Evaporation of the solvent took place at ambient temperature and with the help of natural air convection [32]. After a couple of days, the formed gel turned into a white powder, which is also known as gel desolvation effect [10]. This was thoroughly washed and then dried for 12 hours at 120 °C. To undertake calcination, two types of ovens were utilized, viz. ovens with static & dynamic airflow. The prepared zinc silicate was calcined at 450 °C, 750 °C and 950 °C in both oven types to observe various material characteristics. Here the rate of heating was 5 °C/min with 5 hours of dwell time for the observed calcination temperatures. The various zinc silicates were named with the prefix, ZnSi. This was followed by the abbreviations SA or DA, which depicted the type of calcination procedure, viz. Static Airflow or Dynamic Airflow respectively. Lastly, numbers 2 to 5 represent the different end temperatures during each calcination procedure.

Catalyst characterization

Phase composition of differently calcined zinc silicate catalysts was determined by means of XRD with Cu-Kα (40mA, 45 kV) as the source of X-ray. Peak positions and profiles were then determined and fitted with the help of X'Pert Highscore software.
N_2 physisorption measurements were performed using a Quantachrome Novawin analyser. Prior to the measurements, samples were degassed to 130 °C with 20 h holding time. During the measurement, adsorption and desorption isotherms were recorded and the BJH fitting was applied to determine surface areas of all the tested catalysts.
In order to quantify elements on the surface of the material, SEM and EDX measurements were carried out with the help of a Zeiss V16 microscope. Thereafter, PhiZAF method was used to quantify the recorded maps. The software also automatically calculated atom percentages (at%) of respective elements from the measured weight percentages (wt%).
For characterization of chemical composition of the catalyst bulk, ICP-OES measurements were undertaken. An Anton Paar Multiwave 3000 instrument was used for sample preparation, where a maximum amount of 500 mg of sample was completely digested in concentrated hydrogen fluoride solution (40%). An Agilent 725 ICP-OES Spectrometer was then used to detect the ions, which were generated by ionizing the solution with help of an argon plasma. Here the flow rate of Ar was maintained at 15 l/min.
Lastly, TGA analyses of carbon deposited on the materials were performed to estimate the amount of carbon formed per unit time. Here, synthetic air (20.5% O_2) was used to heat 30 mg of sample at a rate of 10 °C min^{-1}. Here the end temperature was maintained throughout at 1000 °C.

Catalyst activity

The testing of catalysts was executed inside a fixed bed of quartz glass tube with 9 mm inside and 12 mm outside diameter. Temperature at the bed was measured directly with a thermoelement protected by a thin tube of quartz glass. A typical experiment always comprised 250 mg of catalyst material. The weighed catalyst was sandwiched in between two plugs of quartz wool and placed in isothermal zone of an electric oven. The oven was purchased from Horst GmbH, which served as the heating device for the reactor. The device had a total length of 550 mm, with a single heating zone, which was 450 mm long.
A specific amount of liquid methanol was fed by overpressure (under He 6.0), where the flow was measured with a Cori-flow mass flow meter (MFM). At downstream the MFM was attached to an evaporator, which was supported with a N_2 mass flow controller (MFC) used also as the process carrier gas (purity: 5.5). All instruments were purchased from Wagner Mess- und Regeltechnik. A second MFC was assigned to feed either CO_2 or synthetic air (purity of both gases: 5.5) into the feed. Actual amount of the flowing gas was dependent on upstream pressure of the MFC and the conversion factors were calculated with help of the online available Fluidat Software from Bronkhorst.
A gas chromatograph (GC) model 7890 from Agilent equipped with two thermal conductivity detectors (TCD) was used to determine and quantify the effluent gases. The dosing took place by generation of under pressure on the analytic bypass line, which then forced the gases to flow through sample loops inside the GC. After sufficient purging with effluent gas from the process outlet, samples were released into two channels of the GC. The back TCD detector was supplied with Ar (purity: 6.0) as carrier gas to detect the permanent gas species (H_2, CO, CH_4 and CO_2), whereas He (purity: 6.0) was used in the front detector.
Calibration of water was carefully carried out with the help of a humidity measurement device and a psychometric chart. After complete calibration of main components of air, the value of relative humidity was used to determine humidity ratio. This furthermore revealed the concentration of water in a specific volume of air. This process was repeated three times at three different times of a day. The resulting correlation factor of these calibration points was 0.99959, which showed good accuracy of calibration.
A typical experiment was approached as follows, where an inert gas feed (N_2), was used in the beginning not only to purge the system, but also simultaneously to heat up reactor and the catalyst bed. After steady state, a specific stream of methanol was fed in. During all the tests,

amount of methanol was kept constant at 5 vol%. For parameter optimization, temperature programmed experiments were carried out by varying the temperatures from 400 to 750 °C.

Results and discussion

Catalyst characterization

From Table 1 it can be interpreted, that the different methods and temperatures of calcination had different effects on the catalyst characteristics. The zinc silicate powder, ZnSi/SA2 calcined at the lowest temperature showed the highest BET surface area just after the ZnO catalyst, ZnFS/SA1. This was expected, because thermal treatment at higher temperatures lead to sintering of the material and smaller pores merge and create larger pores inside the matrix [32]. It is also worth mentioning, that apart from the usage of an acid in sol-gel method instead of a base, the dynamic airflow method proved to be a better method for preparing catalysts with a higher pore volume.

Table 1: Sample nomenclature with measured physical properties of the various zinc oxide catalysts.

Samples	**Calcination temperature, dwell time / °C, h**	**S(BET) / $m^2 \cdot g^{-1}$**	**Zn in bulk / wt%** *(fresh)*	**Zn on surface / wt%** *(fresh)*	**Zn:Si / ratio of at%** *(fresh)*	**Zn in bulk / wt%** *(spent)*
ZnFS/SA1	550, 5	154.4	4.3	2	0.1	0.08
ZnSi/SA2	450, 5	58.4	57.5	65.7	3.3	40.6
ZnSi/SA3	750, 5	18.3	58.4	80.3	2	53.3
ZnSi/SA4	950, 5	8.5	56.6	71.3	1.3	53.5
ZnSi/DA5	900, 5	12.8	57.1	83.6	2.5	54.5

The usage of an acid increases the hydrolysis rate of sol, which not only leads to a lesser branched gel formation, but it is also related to more pore volume [10]. The later phenomenon can be explained through an uneven heat and mass transport in case of the static air type of oven, where achieving a steady state requires more time and it is prone to small disruptions caused due to changes in air pressure of its surroundings [36]. The surface weight percentages of zinc was higher than those in material bulk. In the bulk, zinc silicate material largely corresponds to the targeted Zn_2SiO_4. The theoretical weight percentages of Zn, Si and O are 58.68%, 12.6% and 28.72%, respectively. Table 1 shows, that the samples prepared through sol-gel procedure exhibit a maximum deviation of 3.5% from the targeted material after performing calcination. On, the other hand, the wt% of Zn on the surface measured with the help of EDX method, showed a maximum deviation 42% for the ZnSi/DA5 catalyst. The EDX measurements also showed that ZnFS/SA1 and ZnSi/DA5 had a rather inhomogeneous distribution of the active component (Zn) in their structures, which can be seen from the Figure 1. The figure shows presence of Zn, Si, O and C elements on the material surface represented by the various colors. In case of both the catalysts, the distribution of Zn was rather uneven, comprising of small dense patches. Here, it is important to note, that only one measurement for each of these catalyst was carried out. Hence, it also explains the huge deviation of almost 40% in the surface Zn wt% for the ZnSi/DA5 catalyst material. However, contrary to the material manufactured by Sagou [13], this was already a huge improvement in regards to synthesis of the targeted catalyst material. Results of the bulk material chemical composition was also supported by observing the different phases of zinc silicate material, where a higher calcination temperature of the material not only increased the material crystallinity, but also the more phases of the desired Zn_2SiO_4 could be observed at 950 °C and above [34]. Please refer to the Figure *2* for information on these XRD analyses.

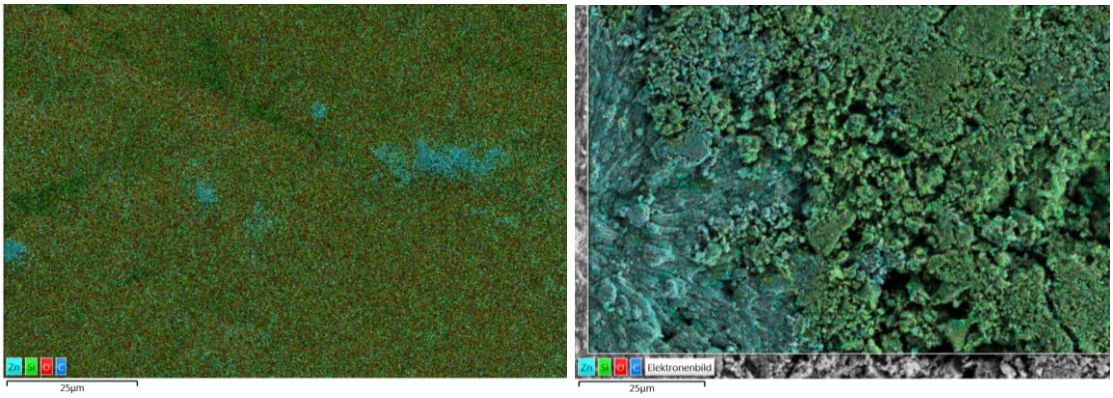

Figure 1: EDS (energy-dispersive X-ray spectroscopy) measurements superimposed on the SEM images to look at the elemental composition on the surface of ZnFS/SA1 (on the left) and ZnSi/DA5 (on the right).

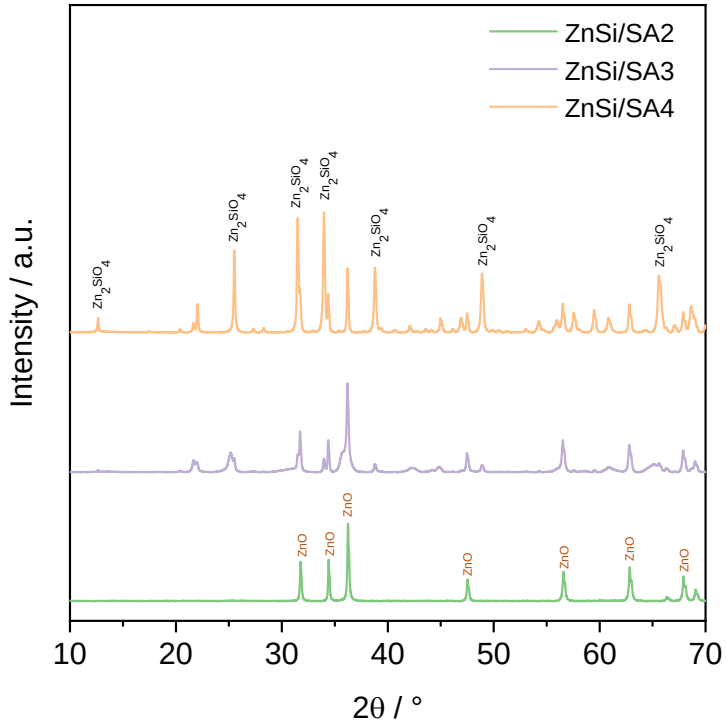

Figure 2: XRD patterns of zinc silicate samples calcined in static air oven at temperatures of 450, 750 and 950 °C.

Catalyst activity

ZnFS/SA1 was the first catalyst to be tested for looking at the products of methanol dehydrogenation chemistry. Figure *3* shows a typical product spectrum obtained with the pure ZnO material. An expected increase in the methanol conversion was represented through this test, until the temperatures were high enough for a fast ZnO reduction leading to a fall in the methanol conversion. By the end of experiments, accumulation of metallic zinc could be observed, proving the volatility of zinc oxide in a reducing atmosphere. Apart from that, Figure 4 shows the main products of direct dehydrogenation. Here, it can be seen that the catalytic yield of anhydrous formaldehyde throughout the investigated temperature ranges (400 – 700 °C) always exceeded the HCHO yield from the methanol pyrolysis process, which is normally performed at 700 – 950 °C. During methanol pyrolysis, significant conversions of methanol

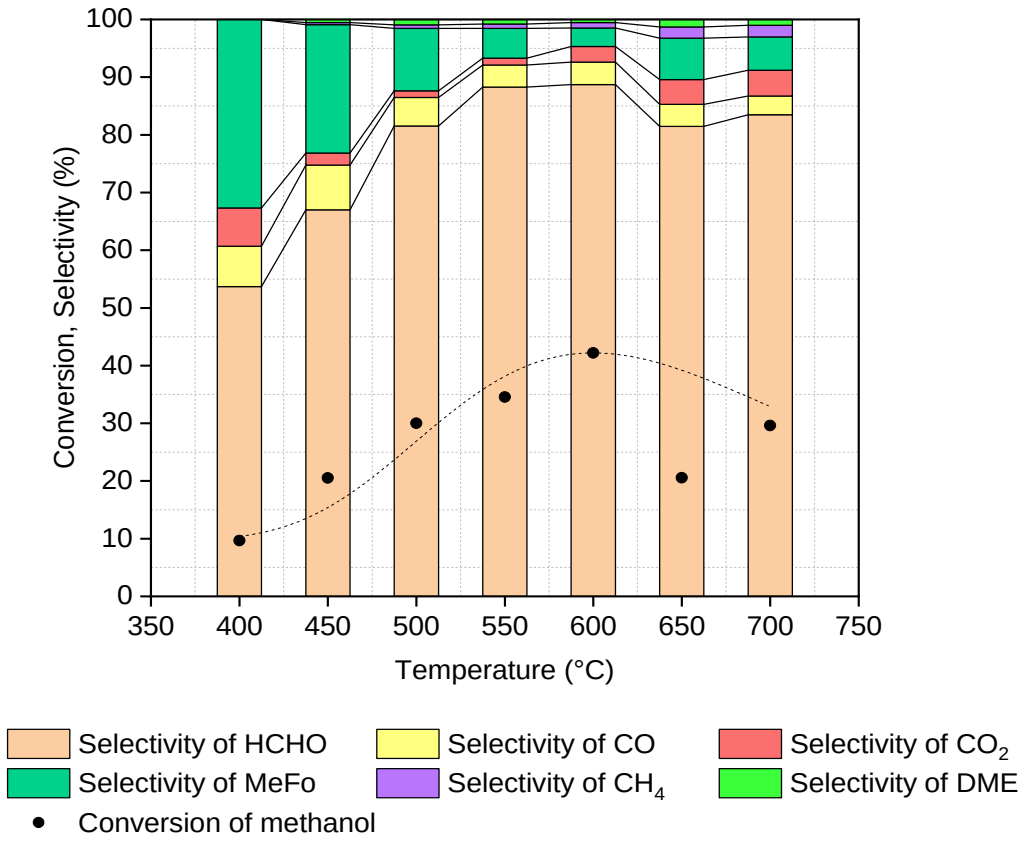

Figure 3: Conversion and selectivity of methanol and its various reaction products respectively versus reaction temperature for the ZnFS/SA1 catalyst system.

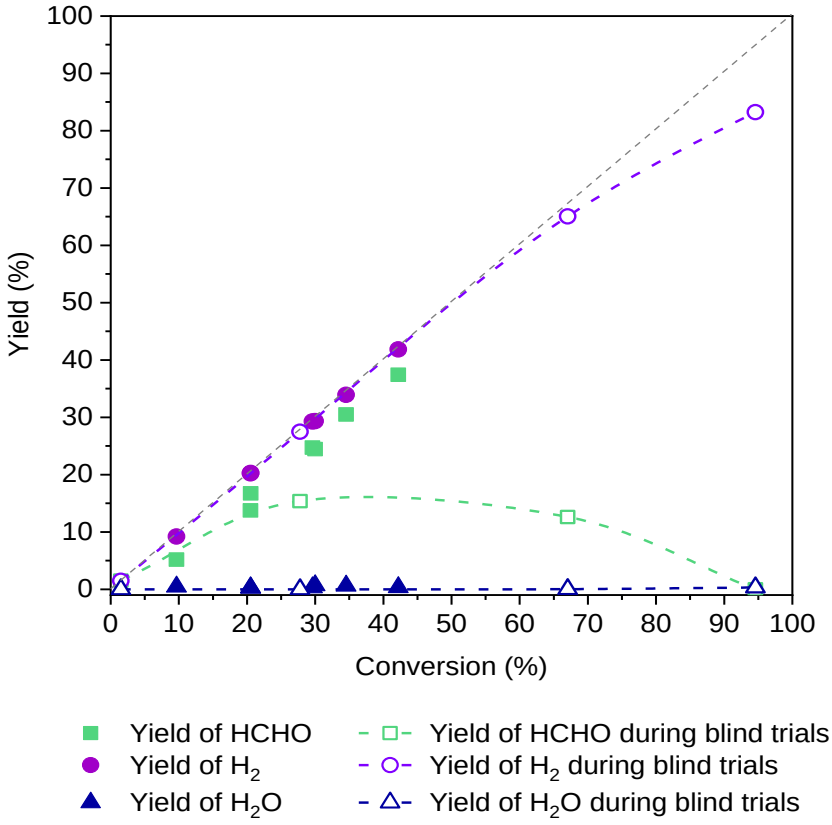

Figure 4: A comparison of conversion of methanol versus yield of formaldehyde, hydrogen and water in between methanol pyrolysis and ZnFS/SA1 catalyst system.

only appear at temperatures exceeding 700 °C [37]. The selectivity of hydrogen in comparison to water for both the systems was almost 99%, with a maximum yield of 0.8% water for the ZnFS/SA1 catalyst. Through bulk elemental analysis, it was observed that, the spent ZnFS/SA1 catalyst had lost 98.13 wt% of zinc from its matrix after 8 hours of TOS. As a corrective measure, a certain amount of O_2 was introduced in the feed along with methanol and N_2 carrier gas. The ratio of O_2:CH_3OH was varied in the between 3.3, 2 and 1. All three feeds yielded water as product for a WHSV of 364.6 h^{-1} in the temperature range of 400 – 750 °C. Naturally, the highest amount of water was produced in an oxygen rich feed mixture (O_2:CH_3OH = 3.3) and at 750 °C, where the oxidation of H_2 took place majorly in the gas phase [38].
Since, trials with oxygen led to water formation, CO_2 was introduced into the feed, as a mild oxidizing agent. Addition of CO_2 was carried out mainly for two temperatures of interest, viz. 500 and 550 °C, indicated in the Figure *5* with blue and red lines. Below this temperature, methyl formate (MeFo) dominated the product spectrum, whereas above 550 °C, deactivation of the ZnO was rather accelerated (also in presence of CO_2). CO_2:CH_3OH ratio in the feed was varied once to 0.8 and then to 1.4. Again, full deactivation of the catalyst could not be completely hindered. Moreover, the reduction could only be slowed down at a temperature of 500 °C and a feed ratio of 0.8. The trend of these observations was in resonance with other investigations, where influence of CO_2 showed to diminish the reduction effect of ZnO [3, 39]. There were two major conclusions resulting from these investigations. The first that, CO_2 clearly blocks the catalytically active adsorption sites by occupying them, suggesting a probable interaction with ZnO. This can be proved through a lower initial methanol conversion in the presence of CO_2 (irrespective of its ratio to methanol) in comparison to when it was absent. Additionally, the second observation suggests that, CO_2 had a stabilizing effect on the ZnO catalyst. This effect is well known, but the exact reason is not quite understood, especially in the field of methanol dehydrogenation.

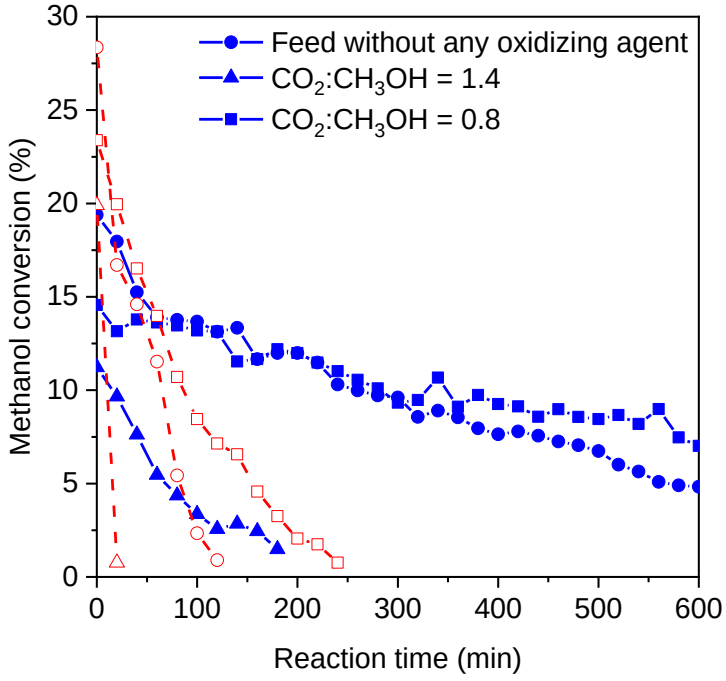

Figure 5: Reaction time versus methanol conversion at two different CO_2:CH_3OH ratio and temperature (500 °C (blue lines) and 550 °C (red dotted lines)).

In propane dehydrogenation chemistry, CO_2 addition also shows a stabilizing effect, which can be attributed to less coke formation and therefore the catalyst remains relatively longer active [40]. Here, a Boudouard reaction is assumed to be taking place which would then explain the stabilizing effect of CO_2 [41].

c. Boudouard reaction

$$CO_2 + C \leftrightharpoons 2CO$$

The deactivation at 550 °C was fast, showing rather an adverse effect of CO_2 addition. Notably, here the worst performance was observed in presence of a CO_2 rich mixture where, not only the stability of catalyst was negatively affected, but also conversion of methanol was the lowest. Presumably, here the CO_2 not only blocked active ZnO sites to make a different chemistry, but a higher temperature caused a much faster ZnO to Zn reduction. Although a fitting explanation would only be possible through scrutinizing the amounts of different effluent gases. Moreover, presence of two C-species as raw material, made the analytical assessment more challenging. The pronounced concentration of CO and the diminished amount of CO_2 in effluent gases could therefore be roughly co-related to not only a bourdard reaction, but rather to a resulting oxidation reaction of Zn to ZnO [42].

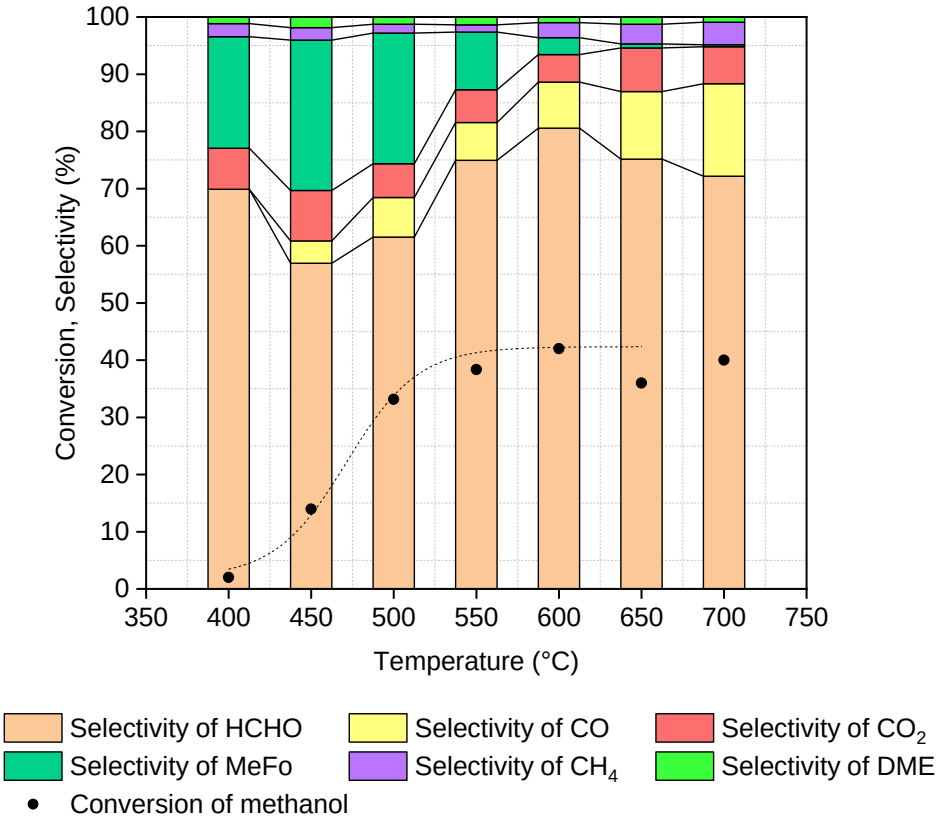

Figure 6: Temperature versus conversion and selectivity of various reaction products for the ZnSi/DA5 catalyst.

The ZnSi/SA2 system deactivated almost as fast as the ZnFS/SA1. From the XRD measurement in Figure *2* the reason becomes quite evident, where deactivation happens because of the ZnO in lattice structure, which lies freely without being bound to the silica. Moreover, the ZnSi/SA2 system had lost 30% Zn after 8 h TOS, whereas the ZnSi/SA3 had only lost 8.7%. The least reducible catalyst were the ones calcined at and above 900 °C. In Figure *6*, the activity of ZnSi/DA5 catalyst is depicted. Experiments with other zinc silicate catalysts showed the same product composition, however ZnSi/DA5 appeared to be the most stable and active of all. Thereby, comparing the product spectrum of the physically and chemically bounded supports (ZnFS/SA1 and ZnSi/DA5), one can clearly see that silica interacts with ZnO in a manner that the chemistry was not completely changed. The formation of small amounts of dimethyl ether (DME) was probably due to presence of a small density of acidic sites present in silica [43]. It is well known, that a direct dehydrogenation of methanol on

ZnO catalyst is associated with formation of formate species [44]. The presence of basic sites lead to higher electro positivity, thereby favouring methyl formate and CO formation [15]. The trend here was same for both catalysts, where methyl formate formation was less pronounced at higher temperatures. The hypothesis from Sagou et al. is as follows; at higher temperatures, the formaldehyde route is favoured and this is also easily desorbed from surface [13]. Although, the presence of a nearby adsorbed hydrogen leads to formation of CO_2 and H_2, thereby extracting oxygen from the catalyst matrix. This was assumed to be the culprit reaction behind a fast ZnO deactivation mechanism [45]. Further characterization and in-situ or ex-situ investigations are required to thoroughly understand the individual adsorption/desorption steps taking place on and inside the catalyst surface and bulk, respectively. The methanol conversion of ZnSi/DA5 was slightly lower compared to ZnFS/SA1 catalyst for the similar temperature region. The absence of free ZnO species can be the reason, which could explain this effect.

Initially, the reason for deactivation of the catalyst was unknown, since no single deactivation mechanism could be ascertained. Because of change in colour of the catalyst powder from white to black, we could confirm deposition of carbonaceous species. Therefore, TGA experiments were executed, where the deposited carbon was burnt away in presence of oxygen. After 8 h of TOS, there was 5.2% carbon deposits on the ZnSi/DA5 surface. Although, this measurement was performed, keeping a dehydrogenation chemistry in mind (where coking is a common phenomenon), it was assumed not to be the only reason for decrease in the catalyst activity. As discussed before, ICP-OES measurements enabled some insight about the loss of Zn, which occurred in every catalyst system. For the ZnSi/DA5 catalyst discussed here in detail, this value was only 4.5% after 8 h of TOS. Irrespective of this fact, the activity as well as catalyst lifetime was still not anywhere close to a practicable usage in industry. From Figure *7*, some very interesting observations could be made about these three catalyst systems, viz. ZnFS/SA1, ZnSi/SA4 & ZnSi/DA5.

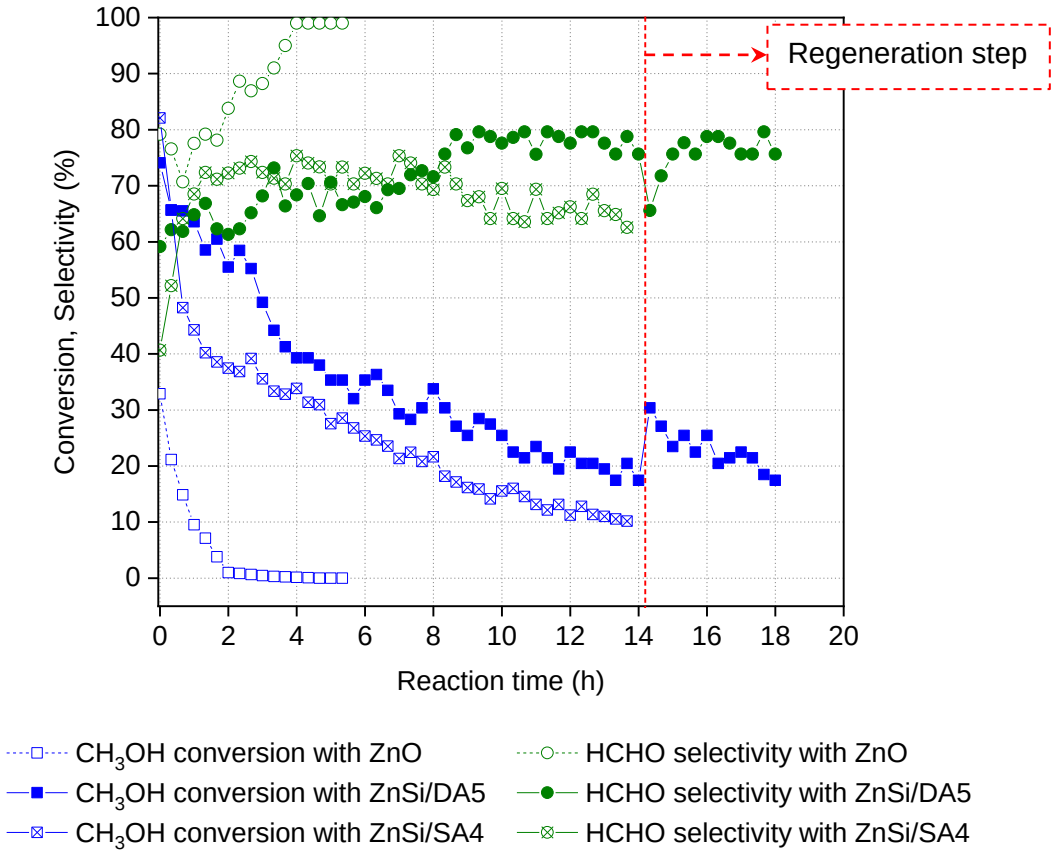

Figure 7: TOS experiments with zinc oxide and zinc silicate catalysts.

It shows reaction time in hours on the x-axis versus conversion of methanol along with formaldehyde selectivity on the y-axis. The reaction temperature was fixed at 550 °C for this experiment. Out of all the effluent gases, only formaldehyde selectivity has been depicted in the diagram. The ZnFS/SA1 catalyst completely loses its activity in just two hours from the start of experiment. The ZnSi/SA4 and ZnSi/DA5 catalyst on the other hand show relatively more stability reaching almost stable conversions of 10% and 20% respectively. A common phenomenon observed for both of these systems was the initial drop in methanol conversion. This was possibly because of the presence of free ZnO, which was then quickly reduced (similar to that of ZnFS/SA1) to zinc metal found in the end of reaction. After this stage, the ZnSi/SA4 catalyst showed a slow and steady fall in conversion. The selectivity of formaldehyde was same throughout with an average around 68%. After a steep fall in methanol conversion in the beginning, there was a rather slow and steady fall in the activity until 10 h of TOS for the ZnSi/DA5 catalyst. The catalyst was observed to be stable after this point. An attempt was made to burn away the coke, which had accumulated on the catalyst surface and at the bulk with time. Regeneration step composed of treating the system with synthetic air for couple of minutes. After this, the methanol stream was turned on again. The attempt was not successful to fully restore the previous activity of catalyst, where within two hours the methanol conversion dropped back to 20%. This furthermore concluded, that the deactivation of the catalyst was not just because of coking, but rather a mixture of Zn loss and coking both. Comparing the ZnSi/SA4 and ZnSi/DA5 catalysts, we also conclude that the material calcined by dynamic flow of air had more pore volume and this was also the probable reason for its slightly higher activity to decompose methanol.

Conclusion and comments on the potential scope of zinc silicate catalyst

From the study of the aforementioned catalyst systems, rough comments can be delivered regarding the potential scope of zinc oxide catalyst system. The zinc oxide catalyst is one of the very few materials, which bring about the direct dehydrogenation of methanol with formation of trace amount of water. The high volatility of the material leads to its fast deactivation, where a mild oxidizing agent like CO_2 was helpful in slowing down this process either by prevention of coke formation or by re-oxidation of zinc, which could not be completely understood within the scope of this investigation. More experiments are required to comprehend this effect. Nevertheless, application of an acidic environment to the sol-gel method and then calcining the material in dynamic airflow at 900 °C or higher yielded a zinc silicate material, which showed a relatively high stability (with loss of only 4.5 wt% Zn in 8 h TOS). A steady methanol conversion of 20% was achieved accompanied with 80% formaldehyde selectivity in a completely reductive atmosphere. Therefore, this study lays down the first impressions of a material manufactured at one specific $ZnO:SiO_2$ ratio, to achieve approximately a higher Zn_2SiO_4, zinc silicate phase, which is known to be the more stable material for the methanol dehydrogenation chemistry.

References

1. Adam, W. Franz Helmut, Kronemayer, P. Daniel, D.P. Roman, R. Gänther, D. Walter, O.G. Armin, H. Albrecht (eds), Ullmann's Encyclopedia of Industrial Chemistry (Wiley-VCH Verlag GmbH & Co. KGaA, Weinheim, Germany, 2000)
2. S. Danwittayakul, J. Dutta, International Journal of Hydrogen Energy **37**, 5518 (2012)
3. K.-D. Jung, O.-S. Joo, S.-H. Han, S.-J. Uhm, I.-J. Chung, Catal Lett **35**, 303 (1995)
4. D. Kaiser, L. Beckmann, J. Walter, M. Bertau, Catalysts **11**, 869 (2021)
5. C.J. Baranowski, J. Brandon, A.M. Bahmanpour, O. Kröcher, ChemCatChem **13**, 3864 (2021)
6. D. Welsby, J. Price, S. Pye, P. Ekins, Nature **597**, 230 (2021)
7. S. Fankhauser, S.M. Smith, M. Allen, K. Axelsson, T. Hale, C. Hepburn, J.M. Kendall, R. Khosla, J. Lezaun, E. Mitchell-Larson, M. Obersteiner, L. Rajamani, R. Rickaby, N. Seddon, T. Wetzer, Nat. Clim. Chang. **12**, 15 (2022)
8. Tiffany Vass, Peter Levi, Alexandre Gouy, Hana Mandová, Direct CO2 emissions from primary chemical production in the Net Zero Scenario, 2015-2030,

https://www.iea.org/reports/chemicals (2021)
9. U. Mondal, G.D. Yadav, Green Chem. **23**, 8361 (2021)
10. G. Ertl, Handbook of heterogeneous catalysis (Wiley-VCH; Chichester : John Wiley, Weinheim, 2008)
11. S. Ruf, A. May, G. Emig, Applied Catalysis A: General **213**, 203 (2001)
12. Michael Haubs, Klaus Kurzm, Jurgen Lingnau, Process for the production of trioxane (2017)
13. M. Sagou, T. Deguchi, S. Nakamura, in Successful Design of Catalysts Future Requirements and Development, Proceedings ofthe Worldwide Catalysis Seminars, July, 1988, on the Occasion of the 30th Anniversary of the Catalysis Society of Japan (Elsevier, 1989), p. 139
14. M. Merko, G.W. Busser, M. Muhler, ChemCatChem **14** (2022)
15. A. Musˇicˇ, J. Batista, J. Levec, Applied Catalysis A: General **165**, 115 (1997)
16. Masakazu Sagou, Process for producing formaldehyde (1985)
17. M.A. Tadashi Yao, Production of formaldehyde
18. V.V. Baghramyan, A.A. Sargsyan, N.V. Gurgenyan, N.B. Knyazyan, V.V. Arutyunyan, E.M. Aleksanyan, N.E. Grigoryan, A.A. Saakyan, Theor Found Chem Eng **52**, 873 (2018)
19. M.F. Casula, D. Loche, S. Marras, G. Paschina, A. Corrias, Langmuir : the ACS journal of surfaces and colloids **23**, 3509 (2007)
20. S. Zhang, L. Hou, M. Hou, H. Liang, Materials Letters **156**, 82 (2015)
21. S. Battiston, C. Rigo, E.C. Da Severo, M.A. Mazutti, R.C. Kuhn, A. Gündel, E.L. Foletto, Mat. Res. **17**, 734 (2014)
22. M. Fabián, P. Bottke, V. Girman, A. Düvel, K.L. Da Silva, M. Wilkening, H. Hahn, P. Heitjans, V. Šepelák, RSC Adv. **5**, 54321 (2015)
23. M. Nadjafi, A.M. Kierzkowska, A. Armutlulu, R. Verel, A. Fedorov, P.M. Abdala, C.R. Müller, J. Phys. Chem. C **125**, 14065 (2021)
24. B.R. Strohmeier, Surface Science Spectra **3**, 128 (1994)
25. L. Su, L. Miao, J. Miao, Z. Zheng, B. Yang, R. Xia, P. Chen, J. Qian, Journal of Asian Ceramic Societies **4**, 185 (2016)
26. C.-T. Wang, J.-C. Lin, Applied Surface Science **254**, 4500 (2008)
27. F. Pinzari, Reac Kinet Mech Cat **134**, 23 (2021)
28. C.-L. Wang, W.-S. Hwang, H.-L. Chu, H.-H. Ko, C.-S. Hsi, W.-L. Li, K.-M. Chang, M.-C. Wang, Metall and Mat Trans A **45**, 2689 (2014)
29. K. Jothimurugesan, S.K. Gangwal, Ind. Eng. Chem. Res. **37**, 1929 (1998)
30. Y. Ogura, T. Asai, K. Sato, S. Miyahara, T. Toriyama, T. Yamamoto, S. Matsumura, K. Nagaoka, Energy Technol. **8**, 2000264 (2020)
31. M.A. Simonov, P.A. Sandomirskii, Y. Egorov Tismenko, N.V. Belov, Doklady Akademii Nauk SSSR **237**, 581 (1977)
32. B.C. Babu, S. Buddhudu, Physics Procedia **49**, 128 (2013)
33. H.F. Masakazu Sagou, Process for producing formaldehyde (1988)
34. M. Takesue, H. Hayashi, R.L. Smith, Progress in Crystal Growth and Characterization of Materials **55**, 98 (2009)
35. R.K. Iler, The chemistry of silica: Solubility, polymerization, colloid and surface properties, and biochemistry / Ralph K. Iler: Solubility, polymerization, colloid and surface properties, and biochemistry / Ralph K. Iler (Wiley, New York, Chichester, 1979)
36. Friederike C. Jentoft, Thermal Treatment of Catalysts: Modern Methods in Heterogeneous Catalysis Research: Modern Methods in Heterogeneous Catalysis Research (2003)
37. T.S. Norton, F.L. Dryer, Int. J. Chem. Kinet. **22**, 219 (1990)
38. H. Hashemi, J.M. Christensen, S. Gersen, P. Glarborg, Proceedings of the Combustion Institute **35**, 553 (2015)
39. D. Weibel, Z.R. Jovanovic, E. Gálvez, A. Steinfeld, Chemistry of materials : a publication of the American Chemical Society **26**, 6486 (2014)
40. Y. Ren, F. Zhang, W. Hua, Y. Yue, Z. Gao, Catalysis Today **148**, 316 (2009)
41. P. Chen, H.-B. Zhang, G.-D. Lin, Q. Hong, K.R. Tsai, Carbon **35**, 1495 (1997)

42. V. Abdelsayed, M.W. Smith, D. Shekhawat, Applied Catalysis A: General **505**, 365 (2015)
43. A.M. Bahmanpour, F. Héroguel, C.J. Baranowski, J.S. Luterbacher, O. Kröcher, Applied Catalysis A: General **560**, 165 (2018)
44. S. Akhter, Journal of catalysis **85**, 437 (1984)
45. J.M. Vohs, M.A. Barteau, Surface Science **176**, 91 (1986)

Selective Cobalt Catalyzed Synthesis of Acetaldehydedimethylacetale (AADMA)

K. A. Sheikh[1,2], T. A. Zevaco[1], J. Jelic[1], F. Studt[1], M. Bender[2]
[1]Karlsruher Institut für Technologie (KIT), Eggenstein-Leopoldshafen, [2]BASF SE, Ludwigshafen am Rhein, Germany

Abstract

Acetaldehydedimethylacetale (AADMA) is an important material for the synthesis of many kind of pharmaceuticals, fragrances and like the structurally related dimethoxymethane, it can be used as diesel additive to enhance fuels' cetane numbers. Structurally very similar tri-alkoxy alkanes are known to reduce soot emissions during the combustion process of diesel fuels, as known for most oxygenates.[1] The synthesis of AADMA from synthesis gas and methanol has been investigated rather sporadically. Most publications limit themselves to the homogenous route. Walter Reppe, a pioneer in high-pressure chemistry, first patented the direct synthesis of AADMA in 1953 in his publication "oxygen containing organic compounds". Wherein they reported that using Cobalt bromide or Cobalt iodide at elevated pressures led to high methanol conversions and selectivities of up to 77% towards AADMA.[2] Further optimizing this process led to a patent in 1955, where the addition of quartenary alkyl ammonium or phosphonium salts allowed to steer the reaction towards AADMA or other side products like acetic acid, methyl acetate or acetaldehyde by changing the ligand.[3] Long residence times were the major drawback of this reaction. In 1981 Korff et al. further optimized the process by using simple ligands like triphenylphosphine, reducing remarkably the residence times down to 1 h by promoting the catalyst with hydrogen iodide and nickel(II)salts.[4]

We herein present an experimental and theoretical investigation of the above-mentioned reaction using synthesis gas and methanol to generate AADMA. After screening several noble metal-promoted cobalt catalysts, we chose the gold-promoted cobalt catalyst for further investigation of this reaction. It showed enhanced activity (X_{CO} = 42%) at relatively low temperatures (T = 150 °C), pressures and displaying good selectivities towards AADMA (S_{AADMA} = 75%). Variation of reaction control, temperatures, solvents, pressures and CO to H_2 ratios gave interesting insight into the mechanism of the reaction. Furthermore, a broad study on the homogenous route has been conducted as well as a comparison with the results of the heterogeneous catalysts, giving a better understanding of ancillary processes like leaching and partial deactivation of the catalyst.

References:

[1] aJ. Waller Francis, L. Weist Jr Edward, M. Brown Dennis, J. A. Tijm Petrus, AIR PROD & CHEM, US, **1999**; bN. Miyamoto, H. Ogawa, T. Arima, K. Miyakawa, *Improvement of Diesel Combustion and Emissions with Addition of Various Oxygenated Agents to Diesel Fuels*, Society of Automotive Engineering, Inc., **1996**; cC. Morley, D. Reinalda, S. Rigutto Marcello, SHELL INT RESEARCH, GB, **2002**.
[2] D. R. Reppe Walter, D. R. Friederich Herbert, BASF AG, DE, **1953**.
[3] R. Walter, F. Herbert, BASF AG, US, **1955**.
[4] J. Korff, M. A. X. Fremery, J. Zimmermann, UNION RHEINISCHE BRAUNKOHLEN, US, **1981**.

Optimization of the Oxidative Dehydrogenation of Methanol to Formaldehyde: A Combined Theoretical, Experimental and Simulative Approach

F. Eichner[1], P. Münzer[1], J. Jelic[1], S. Behrens[1], J. Sauer[1], F. Studt[1], M. Bender[2]
[1]Karlsruhe Institute of Technology (KIT), Institute of Catalysis Research and Technology (IKFT), Eggenstein-Leopoldshafen / Germany, [2]BASF SE, Ludwigshafen am Rhein / Germany

Abstract

With production capacities exceeding 30 million tons per annum,[1] formaldehyde is one of the most important platform molecules in today's chemical industry and is also a key intermediate in the production of synthetic fuels like oxymethylene ethers. One of the major industrial synthesis routes for formaldehyde is the oxidative dehydrogenation (ODH) of methanol over polycrystalline silver catalysts.[2] Hydrogen is a valuable byproduct of this process. Within this study, we address various approaches at different scale to identify optimization potentials in methanol ODH.

As a basis for comparison to the industrial process, methanol ODH over polycrystalline silver catalysts was studied in an electrically heated, continuous flow reactor at temperatures between 773 K and 953 K. By optimizing the reaction parameters, distinct trends in hydrogen formation could be identified and used to increase the hydrogen yield. Our experiments showed that the selectivity to hydrogen was increased and the selectivity to water reduced by increasing the molar ratio of methanol to oxygen in the feed, while the selectivity of the main product formaldehyde remained constant.

To compare the activity of silver and copper species in methanol ODH, Strong Electrostatic Adsorption (SEA) was applied to manufacture supported coinage-metal catalysts. The catalysts were extensively characterized before and after reaction by XRD, TEM/EDX, SEM/EDX and N_2 physisorption. All systems were stable under methanol ODH conditions for more than 400 min TOS.

To enhance the understanding of the underlying reaction mechanism in methanol ODH, density functional theory calculations were applied to generate Gibb's free energy reaction diagrams. Methanol partial oxidation and direct dehydrogenation were compared on both silver and copper surfaces. The results indicated that the energy barriers for methanol partial oxidation were very low for silver and slightly higher for copper catalysts. On the other hand, the process of direct methanol dehydrogenation was highly energy demanding over silver while copper was shown to exhibit lower methanol dissociation barriers.

By process simulation and economic evaluation, various separation procedures for hydrogen from the off-gas of the silver process were evaluated on the process scale. In addition, the effect of changes in inert gas circulation on the hydrogen separation efficiency were studied. The results indicated that the separation of hydrogen from the off-gas of the industrial methanol ODH process could be economically beneficial, especially if the process was adapted to facilitate hydrogen separation without changing the catalytic performance.

1 Merchant Research&Consulting Ltd., https://mcgroup.co.uk/news
2 G.J. Millar and M. Collins, Ind. Eng. Chem. Res. 2017, 56, 9247–9265.

Catalyst Recycling by a Crystallisation of the Ethylene Carbonate-based Catalyst Phase in the Hydroformylation of 1-Octene

J. T. Vossen[1,2], N. Hülsken[1,2], A. J. Vorholt[1] W. Leitner[1,2]
[1]Max Planck Institute for Chemical Energy Conversion, Mülheim an der Ruhr, Germany
[2]Institute for Technical and Macromolecular Chemistry, RWTH Aachen University, Aachen, Germany

Abstract

The hydroformylation reaction is one of the most important and most used homogeneously catalysed processes.[1] Olefins react to aldehydes using transition metal complexes such as rhodium carbonyls modified with phosphine ligands. The recycling of such catalysts and their removal from the product are a focus in research and industry.[2] A method to achieve this is through multiphase catalysis. A well-known system for the hydroformylation of short chain olefins such as ethylene and propylene is the Rhône Poulenc/Ruhrchemie process using water soluble ligands, resulting in the separation of a pure product phase from the catalyst phase.[3] However, this method is not suitable for long chain olefins.[3] Less polar solvents need to be applied for the catalyst phase such as glycols and carbonates.[4] Using two solvents with a smaller polarity gap a thermomorphic multicomponent systems (TMS) may form. In these systems, the solvents are miscible at increased temperatures and turn biphasic again after the reaction at low temperatures.[5]
Herein, we present the development of an ethylene carbonate-based catalyst recycling system using Rh/sulfoXantphos as a water-soluble catalyst in the highly selective hydroformylation of 1-octene. The catalyst was recycled by a crystallisation of the entire catalyst phase. Ethylene carbonate and the reaction product nonanal form a reaction induced TMS System which is of disadvantage in the reaction as it causes a precipitation of the catalyst with increasing yield. Modifications have been investigated in order to increase the phase change temperature to remain in the biphasic regime. The addition of less polar solvents to the catalyst phase such as *n*-decane or the addition of water to the catalyst phase result in a slower but improved reaction system with an increased yield which is well recyclable.

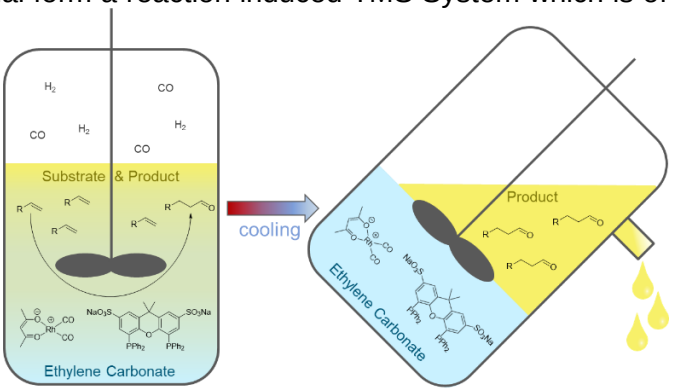

References

[1] P. W. N. M. van Leeuwen, C. Claver, *Rhodium Catalyzed Hydroformylation*, Kluwer Academic Publishers, New York, Boston, Dordrecht, London, Moscow, **2002**.
[2] B. Cornils, W. A. Herrmann, I. T. Horváth, W. Leitner, S. Mecking, H. Olivier-Bourbigou, D. Vogt, *Multiphase Homogeneous Catalysis, Vol. 1*, Wiley-VCH Verlag GmbH & Co. KGaA, Weinheim, **2005**.
[3] C. W. Kohlpaintner, R. W. Fischer, B. Cornils, *Appl. Catal. A: Gen.* **2001**, *221*, 219.
[4] M. Strohmann, J. T. Vossen, A. J. Vorholt, W. Leitner, *Green Chem.* **2020**, *22*, 8444.
[5] J. Bianga, K. U. Künnemann, T. Gaide, A. J. Vorholt, T. Seidensticker, J. M. Dreimann, D. Vogt, *Chem. Eur. J.* **2019**, *25*, 11586.

Effect of Liquid-liquid Interfacial Area on Multiphase Catalysis

M. Schrimpf,[1] K. E. Naße,[1] A. J. Vorholt,[1] W. Leitner[2]
[1]Max Planck Institute for Chemical Energy Conversion, Mülheim an der Ruhr, Germany
[2]Institute of Technical and Macromolecular Chemistry, RWTH Aachen University, Aachen, Germany

Abstract

The investigation of liquid–liquid interfaces are interesting to investigate, especially for understanding the effect on mass transport between both phases at different parameter and the correlated transport limitations. With a photo–optical probe (also called a borescope) with automated image analysis, we were able to investigate the interface of the liquid phases. The borescope and evaluation algorithm analyze the liquid droplets exclusively without the interference of possible gas bubbles in the emulsion.

This photo-optical probe was applied in multiphase catalysis. A well-known example of multiphase catalysis is the Ruhrchemie/Rhône–Poulenc process for the hydroformylation of short chain alkenes, which are transformed to aldehydes with synthesis gas. In this system, the catalyst is immobilized with a water-soluble ligand in a polar aqueous phase. The product forms a second organic, non-polar phase and can be easily separate afterwards.

For long chain alkenes the reactivity is much lower due to the transport limitation between the phases and the poor solubility of the alkenes in water. There are different approaches in research to improve this limitation. By adding additives such as amphiphilic ligands or by intensifying the stirring for increasing the liquid–liquid interface with various stirrer or reactor designs. Nevertheless, it is still debated where the reaction takes place, at the interface of the polar water phase and non-polar organic phase or with substrate dissolved in the catalyst bulk phase.

The use of borescopy allowed us to investigate the interfacial area in the aqueous multiphase hydroformylation of 1-octene. Different parameters (ligand concentration, nonanal concentration, stirrer speed and catalyst concentration) were tested. A significant influence on the interfacial area by the ligand concentration as well as the product nonanal concentration were found. An up to 5-fold increase in interfacial area was measured. That means, the interfacial area changes constantly during the reaction while nonanal is being produced.

References:

[1] M. Schrimpf, P. A. Graefe, A. E. Kaczyna, A. J. Vorholt, W. Leitner, Ind. Eng. Chem. Res. 2022, 61, 2701−2713.
[2] M. Schrimpf, P. A. Graefe, A. Holl, A. J. Vorholt, W. Leitner, ACS Catal. 2022, 12, 7850−7861.
[3] H. Warmeling, R. Koske, A. J. Vorholt, Chem. Eng. Technol. 2017, 40, No. 1, 186–195.
[4] H. Warmeling, D. Hafki, T. von Söhnen, A. J. Vorholt, Chemical Engineering Journal 326 (2017) 298–307.
[5] H. Warmeling, D. Janz, M. Peters, A. J. Vorholt, Chemical Engineering Journal 330 (2017) 585–595.

Intensified Production of 5-hydroxymethylfurfural and Furfural from Biomass in Multiphase Systems

N. Thanheuser,[1,3] J. Esteban,[2] A. J. Vorholt,[1] W. Leitner[1,3]
[1]Max Planck Institute for Chemical Energy Conversion, Mülheim an der Ruhr, Germany
[2]Department of Chemical Engineering, The University of Manchester, Manchester, United Kingdom
[3]Institut für Technische und Makromolekulare Chemie, RWTH Aachen, Aachen, Germany

Abstract

The valorization of lignocellulosic biomass derived sugars has gained more interest for the production of chemicals. 5-hydroxymethylfurfural (HMF) and furfural are highly valued building blocks that can be obtained by the dehydration of glucose, fructose and xylose. To prevent the formation of undesired humins and other by-products that occur in monophasic systems, a multiphase approach can be followed, whereby a reaction with *in situ* extraction takes place. With regard to Green Chemistry, the choice of solvents is a matter of interest. Therefore, environmental, health and safety (EHS) as well as the performance of the chosen solvent have to be considered. Several solvent selection guides have been established taking the EHS parameters into account. To assess the performance, the Conductor-like Screening MOdel for Real Solvents (COSMO-RS) is a proven tool for screening different candidates based on structural information of the molecules. COSMO-RS screenings among a pool of selected solvent candidates gave methyl propionate and ethyl acetate as best performing extraction phases. In addition, methyl isobutylketone (MIBK) also showed a promising performance with the advantage of not undergoing hydrolysis under the typical acidic conditions of the reaction. Dehydration reactions were conducted in a biphasic system with MIBK as extracting phase, with ethylene diaminetetraaceticacid (EDTA) as a catalyst due to its thermomorphic behaviour at temperatures above 140 to 170 °C. In addition, autocatalytic reactions are very promising although they are less productive, since catalyst removal is no longer needed as a further workup step. Furthermore, highly advantageous partition coefficients for furfural in MIBK and water can be observed, emphasizing the suitability of MIBK for this reaction setup.

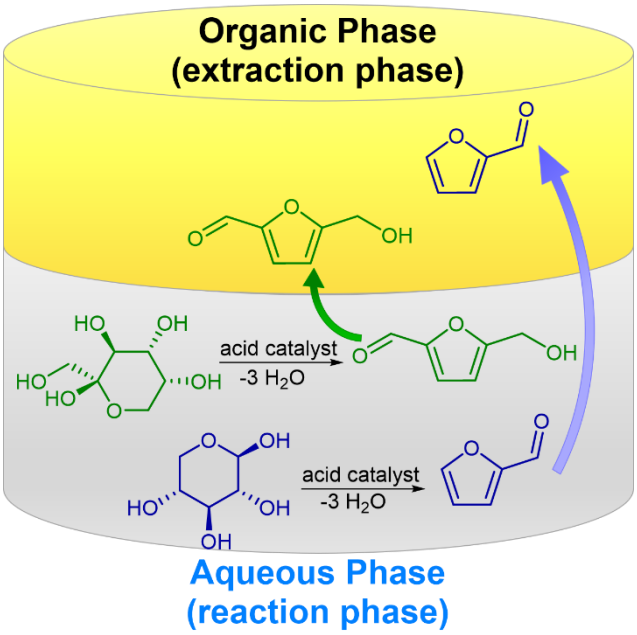

Sodium Methoxide as a Low-cost Glycolysis Catalyst for Chemical Recycling of Post-consumer PET Waste

S. Javed, J. Fisse, D. Vogt
Laboratory of Industrial Chemistry, TU Dortmund University

Abstract

Glycolysis of post-consumer polyethylene terephthalate (PET) waste is a promising chemical recycling technique, back to the monomer, bis(2-hydroxyethyl terephthalate) (BHET). This work presents sodium methoxide (MeONa) as a low-cost catalyst for this purpose. It was shown, not surprisingly, that PET conversion increases with the glycolysis temperature. At a fixed temperature of 190 °C, the response surface methodology (RSM) based on the Box-Behnken design was applied. Four independent factors, namely the molar ratio of PET: MeONa (50-150), the molar ratio of ethylene glycol to PET (EG: PET) (3-7), the reaction time (2-6 h), and the particle size (0.25-1 mm) were studied. Based on the experimental results, regression models as a function of significant process factors were obtained and evaluated by analysis of variance (ANOVA), in order to predict the depolymerization performance of MeONa in terms of PET conversion. The coefficient of determination, R^2 of 92%, indicated the adequacy of the predicted model. Afterward, the regression model was validated and optimized within the design space. The regression model suggested the influence of various interacting parameters on glycolysis performance. A Van 't Hoff plot confirmed the endothermic nature of the depolymerization reaction. The ceiling temperature was calculated from Gibbs' free energy. Kinetic investigations revealed that depolymerization reaction follows a pseudo-first-order reversible reaction. The reaction enthalpy of the glycolysis reaction was found to be 109 $kJ \cdot mol^{-1}$ and the activation energy for MeONa was estimated as 130 $kJ \cdot mol^{-1}$. The catalytic depolymerization efficiency of MeONa was compared to that of zinc and cobalt acetate. All compared catalysts gave virtually complete conversion. However, sodium methoxide is advantageous because it is much cheaper and environmentally benign than heavy metal salts. These findings will undoubtedly provide insight into the economical upscaling of PET recycling to meet future recycling demands of a circular economy.

Electronic Effect of Polymeric Stabilisers on the Catalytic Activity of Supported Au Nanoparticles for the Selective Oxidation of HMF

F. Liuzzi,[1] A. Allegri,[1,2] S. Scurti,[1] N. Dimitratos,[1,2] D. Caretti,[1] S. Albonetti[1,2]
[1]Department of Industrial Chemistry "Toso Montanari", University of Bologna
[2] CIRI-FRAME, University of Bologna, Bologna, Italy

Abstract

It is widely documented that the catalytic activity of supported metal nanoparticles (NPs) is correlated to their size and shape,[1] consequently, stabilising molecules are usually employed during their preparation to control these properties. However, these capping agents can significantly affect catalytic activity. Indeed, the accessibility to active sites can be partially blocked by the polymer, and the stabiliser steric and electronic properties can influence the reaction mechanism. Therefore, the complete understanding of NPs stabiliser role is becoming more and more important for catalyst design. Several works have shown how removing the stabiliser influences the catalytic performances, but only few have paid attention to the effect that these molecules have on the catalytic properties.
In our previous work[2], we have shown how different stabilising agents can affect Au-NPs activity in the selective oxidation of 5-hydroxymethyl-furfural (HMF) to produce 2,5-furan-dicarboxylic acid (FDCA), modifying their dimensions and gold exposure.
The main purpose of this work was to study the effect of the charge transfer caused by the electronic properties of polymeric stabilisers on Au nanoparticles activity, using HMF oxidation as a model reaction. In particular, a series of gold-based catalysts prepared via sol-immobilization and supported on active carbon, (Au/AC) were tested. To study the influence of different stabiliser electronic properties on catalytic performances, two polymers with different functional groups, poly-vinyl alcohol (PVA) and poly-vinylamine (PVAm), and a series of co-polymers PVA-co-PVAm, with different PVA/PVAm ratio, were synthesised and employed as NPs stabilisers. In fact, these polymers have similar structures, but the amino group is a stronger electron-donor than the hydroxyl group, thus the charge transfer between the stabilizer groups and the metal surfaces is different. A study on the reaction intermediates has demonstrated that a different reaction mechanism, already observed on calcined Pd-Au bimetallic nanoparticles,[3] takes place on the PVAm-stabilised catalyst. The strong electron-donor nature of the poly-vinylamine affects the catalyst properties, leading to a dramatic change in the NPs activity, altering the reaction mechanism. The gold NPs are partially charged by the stabiliser and their role of electron-acceptor is inhibited. However, decreasing the number of electron-donor groups, it was possible to observe a variation of the reaction mechanism and an improvement in the catalytic performances. This study highlighted the importance of considering the stabiliser presence during the catalyst design.

References

1. C. Megías-Sayago, A. Lolli, D. Bonincontro, A. Penkova, S. Albonetti, F. Cavani, J. A. Odriozola, S. Ivanova, ChemCatChem 2020, 12 (4), 1177-1183
2. S. Scurti, A. Allegri, F. Liuzzi, E. Rodríguez-Aguado, J.A. Cecilia, S. Albonetti, D. Caretti, N. Dimitratos, Catalysts 2022, 12, 323
3. A. Lolli, S. Albonetti, L. Utili, R. Amadori, F. Ospitali, C. Lucarelli, F. Cavani, Appl. Catal. Gen. 2015, 504, 408-419.

Catalyst Recycling by a Self-Separation of the Product Phase in the Production of Formic Acid from Carbon Dioxide

K.R. Ehmann,[1,2] A. Nisters,[1,2] A. J. Vorholt,[1] W. Leitner[1,2]
[1]Department of Molecular Catalysis, Max Planck Institute for Chemical Energy Conversion, Mülheim an der Ruhr, Germany
[2]Institute for Technical and Macromolecular Chemistry, RWTH Aachen University, Aachen, Germany

Abstract

Climate change is recognized as a global topic since several years. Besides the transition from fossil resources to sustainable energy, the production of chemicals from biomass and carbon dioxide is considered an important pillar to deal with this challenge. Carbon dioxide hydrogenation to formic acid is one possible reaction to introduce carbon dioxide as C_1 building block into the chemical value chain. For homogeneously catalyzed reactions the separation of the product and the catalyst under retention of the catalyst's performance remains a major challenge. One approach towards facile catalyst recycling are liquid-liquid biphasic systems. Using a second solvent for the extraction of the product from the reaction mixture during catalysis, the catalyst and product phase can easily be separated. However, the requirement of a stabilizing amine during the reaction results in the need for the separation of two components (solvent and amine) from the product phase during down-stream processing. Therefore, in the present study, we present a Ru-phosphine catalyzed reaction system comprising only a hydrophobic solvent as the catalyst phase and *N*-methyldiethanolamine as a base. Separation of the reaction mixture into a pure formic acid/amine product and a recyclable catalyst phase occurs in this reaction system spontaneously by the formation of formic acid/formate. The optimization of the reaction conditions enabled a TON of 1590 in a single reaction and a TTON of 5590 after four recycling runs.

Figure 1 Illustration of the reaction system with self-separating product phase

Semi-Hydrogenation of Poly-Unsaturated Fatty Acid Derivatives in Multiphase Catalysis for Chemical Feedstock Supply

M. Spiekermann, F. Lehmann, T. Seidensticker
Laboratory of Industrial Chemistry, TU Dortmund University, Dortmund, Germany

Abstract

Dwindling fossil resources increase the demand for sustainable alternatives, i.e. oleochemicals.[1] Increasing the degree of saturation to mono-unsaturated fatty acid derivatives paves the way for various chemical reactions like epoxidation. The major part of these reactions depends on mono-unsaturated oleochemicals independent of the terminal functionalization of the molecule to ensure a stable catalyst or a high selectivity to the desired product.[2] Most promising results in terms of heterogeneous catalysis have utilized Pd catalysts at reaction temperatures of 80°C and 75 atm Hydrogen or needed high catalyst loading of 4,94 wt.% with reaction times over 1 hour.[3] This research focuses on an approach that utilizes a multiphasic reaction system which consists of a polar solvent containing a transition metal and a non-polar substrate phase. The non-polar phase only consists of the fatty substrate and is solvent free. Hydrogen at different pressures is provided as gas phase. Intense stirring is key to ensure proper phase interaction.[4] The catalyst shows high activity already at temperatures up to 50°C and high selectivity to the monounsaturated fatty compound in the mixture. Optimization of reaction conditions led to reaction times below 15 minutes. First tests were performed using a mixture of fatty acid methyl esters (FAMEs). After promising results reactions were performed using refined soybean oil that was esterified with methanol. Since the reaction performance is already on a high level, whilst utilizing a multiphasic approach, the separation of the reaction mixture should be the less demanding task which makes this approach more viable for industrial application.

References:

[1] A. Behr, T. Seidensticker, *Einführung in die Chemie nachwachsender Rohstoffe*, Springer, Berlin, Heidelberg, **2018**.
[2] U. Biermann, U. T. Bornscheuer, I. Feussner, M. A. R. Meier, J. O. Metzger, *Angewandte Chemie (International ed. in English)* **2021**, *60*, 20144.
[3] a) D. Adu-Mensah, D. Mei, L. Zuo, Q. Zhang, J. Wang, *Fuel* **2019**, *251*, 660; b) Jakkrapong Jitjamnong, Natthida Numwong, Narinphop Chuaykarn, Chatrawee Direksilp, Nonlapan Khantikulanon, *Chiang Mai Journal of Science* **2021**, *48*, 580.
[4] A. Behr, N. Döring, S. Durowicz-Heil, B. Ellenberg, C. Kozik, C. Lohr, H. Schmidke, *Fat Sci. Technol.* **1993**, *95*, 2.

Opportunities and Potential of Electrocatalytic Energy Transition and Challenges in the Development of a new High-throughput Technology

D. Dogan, B. Hecker, H. Tempel, R.-A. Eichel
Institute of Energy and Climate Research (IEK-9) – Forschungszentrum Jülich GmbH

Abstract

The energy transition and the associated reduction in greenhouse gas emissions require various key strategies, in particular the reduction of energy demand by improved energy efficiency and lower energy consumption. An important driver in the optimization of energy efficiency is the improvement of heterogeneous catalysts. Moreover, it is inevitable to replace fossil energy carriers with chemical energy carriers produced by green electrical power. This will significantly increase the importance of electrocatalysis in the future.

One reason that existing alternative green processes or systems are slowly establishing themselves is the lower overall efficiency from energy production to the point of utilization compared to existing processes. Thus, electrocatalysis research has become increasingly important in recent years. The application of high-throughput technologies has already achieved success in other research fields in the past decades and thereby is also a promising approach for electrocatalyst research.

Reducing greenhouse gas emissions to zero is not feasible. In fact, the objective is to reduce greenhouse gas emissions to net zero. This indicates that processes emitting greenhouse gases will continue to exist in the future. However, these gases must be captured and stored or catalytically converted, either directly coupled to the process or offsite. The electrocatalytic reduction of CO_2 to valuable basic chemicals for the industry could play an important role in this context.

This poster will highlight current research efforts in electrocatalytic CO_2 reduction and the potential of these processes for the energy transition. Furthermore, the opportunities and challenges in the development of a high-throughput test system for electrocatalysis research are discussed. For the plant operation of this innovative research system, processes with different technology readiness levels are planned. In addition to research in electrochemical CO_2 reduction, the system is designed to optimize water electrolysis for the production of green hydrogen.

DME as a Global Point-to-Point H_2 Carrier: Process Intensified DME Production - The INDIGO Technology

A. Schaadt[1], M. Semmel[1], O. Salem[1], C. Hebling[1]
[1] Fraunhofer Institute for Solar Energy Systems ISE, Freiburg, Germany

Abstract

Studies estimate that by 2050, the European energy market alone will need 550 to 1800 TWh of hydrogen and PtX products annually from which the major part is imported from areas with high renewable energy potential. In the PtX context, dimethyl ether (DME) is a promising product and energy carrier with diverse possible applications in different sectors. DME has a nominal hydrogen storage capacity of 26.1 wt.-%, high gravimetric and volumetric energy density and is environmentally benign. This qualifies DME as a very attractive H_2 carrier for the global envisaged sustainable energy trade. Due to its relatively low vapor pressure of 0.6 MPa at 25 °C, DME is easily liquefied and a promising substitute or blending agent for LPG. Globally, almost 90% of the current annual production of 5 Mt DME is used for LPG blending, predominantly in China. Currently, DME is produced based on fossil feedstock as natural gas or coal. The shift to renewable feedstock from CO_2 and hydrogen will allow emerging pathways for the production of DME to achieve economic competitiveness. PtX processes boundary conditions require advanced strategies matching with the feedstock fluctuations. Focus is hereby put on a process intensification approach based on reactive distillation and its influence on the overall process enhancements. To enable this new process concept, new catalysts are required. Results of a catalyst screening and kinetic measurements incl. kinetic fitting are presented. Finally, a potential estimation of the new DME production pathway will be given.